Multimodal Characterisation of Silicates: Combining Fluorescence Imaging, Spectroscopy, and Molecular Simulations

PhD Thesis

Daniel Doveiko

Photophysics Group
Department of Physics
University of Strathclyde, Glasgow

October 7, 2025

Abstract

Silica-based nanomaterials are central to catalysis, coatings, and sustainable technologies, yet their rapid and reliable characterisation remains challenging. Traditional methods such as nuclear magnetic resonance (NMR) spectroscopy using the ^{29}Si isotope provide limited structural information, while scattering and microscopy techniques are complex and unsuitable for routine or industrial use. This thesis addresses this gap by developing a fluorescence-based nanometrology platform that combines advanced spectroscopy and microscopy with computational modelling, offering a scalable framework for particle sizing and mechanistic insight.

Molecular dynamics (MD) simulations and density functional theory (DFT) calculations were used to investigate the interactions of Rhodamine 6G (R6G) with silica nanoparticles (SNPs). Adsorption strength was found to depend on nanoparticle curvature, crystallinity, and pH, with larger SNPs and hydroxyl-rich surfaces favouring stable binding. Crucially, adsorption occurred even at the isoelectric point, highlighting the role of van der Waals forces beyond electrostatics. Simulations also showed R6G dimerisation, which quenches fluorescence, occurs primarily in solution rather than on the silica surface due to structural constraints, providing a molecular-level explanation for how adsorption and aggregation influence fluorescence.

Experimental validation used time-resolved fluorescence anisotropy and fluorescence recovery after photobleaching (FRAP). Anisotropy-based methods yielded reliable hydrodynamic radii for sodium silicate systems, agreeing with small-angle X-ray scattering (SAXS), and demonstrated the influence of dye flexibility on size determination. FRAP

proved particularly powerful, resolving distinct particle populations in complex colloids and detecting changes in viscosity, dye concentration, and aggregation. Larger SNPs consistently exhibited stronger dye binding and more stable fluorescence, confirming computational predictions.

This work unites modelling and experiment to create a multiscale fluorescence-based nanometrology approach. Compared with dynamic light scattering (DLS), transmission electron microscopy (TEM), or SAXS, the platform offers rapid, non-invasive, and sample-efficient characterisation. Its ability to probe both average and spatially resolved particle sizes provides new insights into colloidal stability and structural evolution. Beyond advancing fluorescence imaging as a nanometrology tool, the results highlight broader opportunities for integrating simulation and spectroscopy in the study of soft matter and industrially relevant materials.

Publications

List of Publications Relevant to this Thesis:

- **Daniel Doveiko**, Karina Kubiak-Ossowska and Yu Chen, "Impact of the Crystal Structure of Silica Nanoparticles on Rhodamine 6G Adsorption: A Molecular Dynamics Study" *ACS Omega*, 9 (3), 4123-4136 (2024).

- **Daniel Doveiko**, Alan R. G. Martin, Vladislav Vyshemirsky, Simon Stebbing, Karina Kubiak-Ossowska, Olaf Rolinski, David J. S. Birch and Yu Chen, "Nanoparticle Metrology of Silicates Using Time-Resolved Multiplexed Dye Fluorescence Anisotropy, Small Angle X-ray Scattering, and Molecular Dynamics Simulations" *Materials*, 17(7):1686 (2024)

- **Daniel Doveiko**, Karina Kubiak-Ossowska and Yu Chen, "Estimating Binding Energies of π-Stacked Aromatic Dimers Using Force Field-Driven Molecular Dynamics" *International Journal of Molecular Sciences*, 25(11):5783 (2024)

- **Daniel Doveiko**, Karina Kubiak-Ossowska and Yu Chen, "Binding Energy Calculations of Anthracene and Rhodamine 6G H-Type Dimers: A Comparative Study of DFT and SMD Methods" *Journal of Physical Chemistry A*, 129 (12), 2946–2957 (2025), **Selected as Front Cover of the Issue**

- **Daniel Doveiko**, Lisa Asciak, Simon Stebbing, Wenmiao Shu, Karina Kubiak-Ossowska, David J. S. Birch and Yu Chen, "Quantitative Nanometrology of Binary Particle Systems Using Fluorescence Recovery After Photobleaching: Ap-

plication to Colloidal Silica" *Langmuir*, 41 (29), 19173–19182 (2025) **Selected as Front Cover of the Issue**

- **Daniel Doveiko**, Karina Kubiak-Ossowska and Yu Chen, "Nanoparticles as adsorbents for hydrophobic molecules: Exploring size, pH, and structural dependencies" *J. Chem. Phys.*, 163 (2), 024708 (2025)

List of Publications not relevant to this Thesis:

- Olga Adamczyk, Magdalena Szota, Kamil Rakowski, Magdalena Prochownik, **Daniel Doveiko**, Yu Chen and Barbara Jachimska, "Bovine Serum Albumin as a Platform for Designing Biologically Active Nanocarriers—Experimental and Computational Studies" *International Journal of Molecular Sciences*, 25(1):37 (2023)

- Ziao Jiao, Mingliang Pan, Khadija Yousaf, **Daniel Doveiko**, Michelle Maclean, David Griffin, Yu Chen and David Day Uei Li, "Smartphone-based optical sectioning (SOS) microscopy with a telecentric design for fluorescence imaging" *Journal of Microscopy*, 296, 10–23 (2024)

- Magdalena Szota, Urszula Szwedowicz, Nina Rembialkowska, Anna Janicka-Klos, **Daniel Doveiko**, Yu Chen, Julita Kulbacka and Barbara Jachimska, "Dendrimer Platforms for Targeted Doxorubicin Delivery—Physicochemical Properties in Context of Biological Responses" *International Journal of Molecular Sciences*, 25(13):7201 (2024)

Conference Proceedings

- **Daniel Doveiko**, Simon Stebbing, Yu Chen, Vladislav Vyshemirsky, David J. S. Birch, Olaf Rolinski, "Sodium silicate particle size measurements using time-resolved fluorescence anisotropy" *SUPA Annual Gathering 2023*, Glasgow, UK *Poster Presentation*

- **Daniel Doveiko**, Karina Kubiak-Ossowska, Yu Chen, "Impact of the Crystal Structure of Silica Nanoparticles on Rhodamine 6G Adsorption" *ARCHIE-WeSt AI Showcase 2023*, Glasgow, UK *Poster Presentation*

- **Daniel Doveiko**, Simon Stebbing, Yu Chen, David J. S. Birch, Vladislav Vyshemirsky, Olaf Rolinski, "Sodium silicate particle size measurements using time-resolved fluorescence anisotropy" *66th International Open Readings Conference for students of Physics and Natural Sciences (2023)*, Vilnius, Lithuania *Oral Presentation* **Award for best oral presentation in "Spectroscopy, Methods and Devices for Physical Diagnostics"**

- **Daniel Doveiko**, Karina Kubiak-Ossowska and Yu Chen, "Impact of the crystal structure of silica nanoparticles on Rhodamine 6G adsorption" *67th International Open Readings Conference for students of Physics and Natural Sciences (2024)*, Vilnius, Lithuania *Oral Presentation*

- **Daniel Doveiko**, Alan R. G. Martin, Vladislav Vyshemirsky, Simon Stebbing, Karina Kubiak-Ossowska, Olaf Rolinski, David J. S. Birch and Yu Chen,

"Nanoparticle metrology of silicates using time-resolved multiplexed dye fluorescence anisotropy" *PCCP 25th Anniversary Symposium (2024)*, Amsterdam, Netherlands *Poster Presentation*

- **Daniel Doveiko**, Karina Kubiak-Ossowska and Yu Chen, "Impact of the Crystal Structure of Silica Nanoparticles on Rhodamine 6G Adsorption" *Methods in Molecular Simulation Summer School 29th edition (2024)*, Newcastle upon Tyne, UK *Poster Presentation*

- **Daniel Doveiko**, Karina Kubiak-Ossowska and Yu Chen, "Interaction of Fluorescent Dye Rhodamine 6G with Silica Nanoparticles" *Methods in Molecular Simulation Summer School 29th edition (2024)*, Newcastle upon Tyne, UK *Oral Presentation*

- **Daniel Doveiko**, Karina Kubiak-Ossowkska and Yu Chen "Binding Energy Calculations of Anthracene and Rhodamine 6G H-type using DFT and SMD Methods" *ARCHIE WeSt Showcase Meeting (2024)* Glasgow, UK *Poster Presentation*

- **Daniel Doveiko**, Lisa Asciak, Simon Stebbing, Wenmiao Shu, Karina Kubiak-Ossowska, David J.S. Birch and Yu Chen "Nanometrology of Binary Systems Using Fluorescence Recovery After Photobleaching" *SUPA Physics and Life Sciences Theme Meeting 16th January 2025* Glasgow, UK *Oral Presentation*

- **Daniel Doveiko**, Karina Kubiak-Ossowkska and Yu Chen "Binding Energy Calculations of Anthracene and Rhodamine 6G H-type using DFT and SMD Methods" *6th CCPBioSim/CCP5 Multiscale Modelling Conference (2025)*, Manchester, UK *Poster Presentation*

- **Daniel Doveiko**, Karina Kubiak-Ossowska and Yu Chen, "Interaction of Fluorescent Dye Rhodamine 6G with Silica Nanoparticles" *ARCHIE WeSt Showcase Meeting (2025)* Glasgow, UK *Oral Presentation*

Abbreviations

AO   Atomic Orbital

BOA   Born-Oppenheimer Approximation

BSSE   Basis Set Superposition Error

CCSD(T)   Coupled Cluster Singlet Doublet Perturbed Triplets

CLSM   Confocal Laser Scanning Microscope

COM   Centre of Mass

COSX   Chains of Sphere

CPCM   Conductor-Like Polarizable Continuum Solvation Model

cSNP α-Cristobalite Structured Silica Nanoparticles

CW   Continuous Wavelength

DFT   Density Functional Theory

DLS   Dynamic Light Scattering

FCS   Fluorescence Correlation Spectroscopy

FF   Force Field

FFT   Fast Fourier Transform

FRAP	Fluorescence Recovery After Photobleaching
FTIR	Fourier Transform Infrared Spectroscopy
GBM	Gradient Boosting Machine
GFP	Green Fluorescent Protein
GGA	General Gradient Approximation
GPU	Graphics Processing Unit
GUI	Graphical User Interface
HF	Hartree-Fock
HO	Harmonic Oscillator
HPC	High-Performance Computer
ICP-OES	Inductively Coupled Plasma Optical Emission Spectroscopy
IRF	Instrumental Response Function
LDA	Local Density Approximation
LED	Light Emitting Diode
LJ	Lennard-Jones
MCA	Multi Channel Analyser
MD	Molecular Dynamics
ML	Machine Learning
MM	Molecular Mechanics
NMR	Nuclear Magnetic Resonance Spectroscopy
NP	Nanoparticle

PAH	Polycyclic Aromatic Hydrocarbons
PBC	Periodic Boundary Conditions
PDB	Protein Data Bank
PES	Potential Energy Surface
PME	Particle Mesh Ewald
PMT	Photomultiplier
qSNP	α-Quartz Structured Silica Nanoparticles
RB	Rhodamine B
RESP	Restrained Electrostatic Potential
R6G	Rhodamine 6G
RI	Resolution of the Identity
ROI	Region of Interest
RSH	Range-Separated Hybrid
S/N	Signal to Noise Ratio
SAXS	Small Angle X-ray Scattering
SCF	Self-Consistent Field
SMD	Steered Molecular Dynamics
SNP	Silica Nanoparticle
SPAD	Single Photon Avalanche Diode
SPE	Single Point Energy
TAC	Time-to-Amplitude Converter

TCSPC	Time Correlated Single Photon Counting
TEM	Transmission Electron Microscopy
TISE	Time-Independent Schrödinger Equation
UV-Vis	Ultraviolet to visible
vdW	van der Waals
XC	Exchange-Correlation
ZPE	Zero Point Energy

Contents

List of Figures

xxv

List of Tables

xxxi

Acknowledgements

During the last four years, I've met a lot of wonderful people, without whom this journey of mine would have been very different, and most likely unsuccessful.

First, I would like to thank my supervisors, Dr Yu Chen and Dr Karina Kubiak-Ossowska.

Dr Yu Chen – thank you for trusting my instincts and allowing me to venture into many things independently. Your calm and open-minded approach gave me the space to explore ideas freely, even the crazy ones, and that made a huge difference in how I grew as a researcher. You gave me the confidence to think outside the box and trust my gut.

Dr Karina Kubiak-Ossowska – thank you for not kicking me out after our countless disagreements over all the simulations and computational methods I insisted on trying. Through it all, you listened, challenged me, and helped sharpen my thinking. Our back-and-forths weren't always easy, but they were always constructive, and I'm genuinely grateful for your patience and perseverance.

Also, let's not forget my original supervisor – Dr Olaf Rolinski. It was short, but sweet, and I hope that you're enjoying your retirement. While you mentored me during my undergraduate years, I'm especially thankful for the opportunity to start my PhD with you. You were the one who first believed I could take on something of this scale, and I'll always appreciate that vote of confidence.

I would also like to thank Prof David Birch for co-writing the proposal that launched this project with Olaf, and for all the invaluable advice throughout my PhD. It wouldn't

Finally, to my wife Margarita and our sons, Dominik and Alexander – thank you for keeping me sane and believing in me, especially during the hardest parts.

Margarita – thank you for travelling with me to all the conferences, for keeping me sane there, and for letting me show you at least a few new places along the way. The tulip festival in Amsterdam will always be one of my favourite memories. Thank you for taking time off work while I travelled to concerts and headbanged to Slayer – that gave me, the so-needed change of surroundings to help me clear my head at least a little bit. There were more lows than highs along the way – as there often are during a PhD – and you stood beside me through all of it. Thank you for telling me to go to sleep when I clearly needed it, and for all the evenings we spent curled up watching endless serials – Netflix, Disney – whatever gave us some comfort and escape. You gave me balance when I couldn't find it myself. I cannot express how sorry I am that I took four years of your youth chasing this PhD. I know it wasn't easy, and I know the sacrifices you made. I couldn't have done this without you, and I will never forget the support, love, and quiet strength you gave me every single day.

Dominik and Alexander – thank you for turning my world around when you were born. You pulled me out of the tunnel vision of this PhD and reminded me to slow down, take a breath, and just *be* your dad. You gave me reasons to smile when I had nothing left to give, and helped me see that time, real joyful time, is the most precious thing we have. You reminded me what life is really about, and that there is more to success than just publishing papers or finishing chapters.

Love you.

Chapter 1

Introduction

Sodium silicates, or *waterglass*, have been known since at least the early Roman Empire, with Pliny the Elder documenting the accidental discovery by Phoenician mariners who observed transparent streams of liquid formed by combining sand and soda during meal preparation [1, 2]. This substance, later recognised as sodium silicate, became more widely understood through the work of alchemists and scholars during the 17th and 18th centuries, including Goethe [3]. However, it was Johann Nepomuk von Fuchs [4] who coined the name "waterglass" and highlighted its industrial potential.

Since then, sodium silicates have grown into one of the most widely used industrial chemicals, with applications spanning detergents [5], adhesives [6], sealants [7], catalysts, and more. In 2022, the global sodium silicate market size was valued at $11.25 billion, growing at a compound annual growth rate of 4.2% [8]. Other derivatives, such as zeolites and precipitated silica, are anticipated to drive the demand even further. Moreover, the ability of sodium silicate to transform into silica gel expands its applications to such fields as catalysis [9], drug delivery [10], and final polishing of silicon wafers used in the semiconductor industry [11, 12].

Figure 1.1: Pliny's account of Phoenician mariners, often cited as the earliest description of sodium silicate ("water glass") formation. Reproduced from [13] with permission from Elsevier.

The widespread success and versatility of waterglass stem from several factors, including its relatively low cost, abundance, alkalinity, buffering capacity, emulsifying properties, non-toxicity, and ability to regulate viscosity [13,14]. Given the versatility of sodium silicate applications, gaining insight into its properties is essential in achieving better control over the production process and overall sustainability.

1.1 Unravelling the Chemistry of Sodium Silicates

Though widely used today, sodium silicates have long been a subject of scientific intrigue. Their complex chemistry, consisting of water, anionic silicate species, and sodium cations in dynamic equilibrium, has sparked curiosity for centuries. Despite their early discovery and use, the exact nature of silicate species in waterglass remained speculative for years, with many dismissing their study as impractical [15]. As methods advanced, however, a clearer picture emerged. Early pioneers, such as Lentz in 1964 [16], challenged outdated theories and unveiled the true structure of silicate

anions in alkaline solutions, revealing that they are not monomeric as once thought.

Raman spectroscopy further disproved prior assumptions, confirming that silicon in these ions is coordinated with four oxygen atoms, not six [17]. Since the 1970s, Nuclear Magnetic Resonance (NMR) spectroscopy has become the main tool used to characterise sodium silicates, allowing the identification of many distinct silicate species present [18–20]; however, it does not provide any quantitative data about the sizes of the species. In ^{29}Si NMR spectroscopy, each silicate species has assigned "Q-units", depending on their connectivity. This was first introduced by Engelhardt et al. [21], where five main classes of NMR signals have been identified and labelled as Q^n, where Q represents the fourfold coordinated silicon atom and n indicates the number of neighbouring silicon atoms linked through an oxygen atom. While NMR sounds like an ideal method for sodium silicate analysis, it requires expensive and sophisticated laboratory equipment with properly trained personnel. Furthermore, the experiments are notoriously slow and require sample preparation, such as dilution and ^{29}Si enrichment. These factors, combined with the potential challenges in spectrum assignment, make NMR less practical, particularly for industrial application. Nevertheless, over time, ^{29}Si NMR spectroscopy has identified more than fifty distinct silicate species, significantly enriching our understanding of silicate chemistry [13].

1.2 From Monomers to Colloids: Speciation in Sodium Silicate Solutions

The chemistry of sodium silicate is highly dependent on its composition, particularly the SiO_2:Na_2O molar ratio, which dictates the size and complexity of the silicate species. Sodium silicate solutions contain a dynamic mixture of monomeric, oligomeric, and polymeric silicate species, held in equilibrium by sodium cations that balance the negative charges on the silicate anions. At low SiO_2:Na_2O ratios (below 1.6), the solutions are dominated by small species such as monomers (Q^0) and dimers (Q^1). As the ratio increases to between 2.0 and 3.0, larger cyclic and branched silicate structures (Q^2 and Q^3) become more prominent, forming more complex oligomers and small clusters.

When the SiO_2:Na_2O ratio exceeds 3.0, highly polymerised species (Q^4) emerge, forming dense colloidal particles and three-dimensional networks characteristic of silica gels. This increasing polymerisation reflects the condensation of silicate species, where silicon atoms become increasingly connected through bridging oxygen atoms. The transition from small soluble species to colloidal particles is confirmed by small-angle X-ray scattering (SAXS) and dynamic light scattering (DLS), which reveal that particle sizes grow from a few nanometres at low ratios to over 100 nm at higher ratios [22, 23].
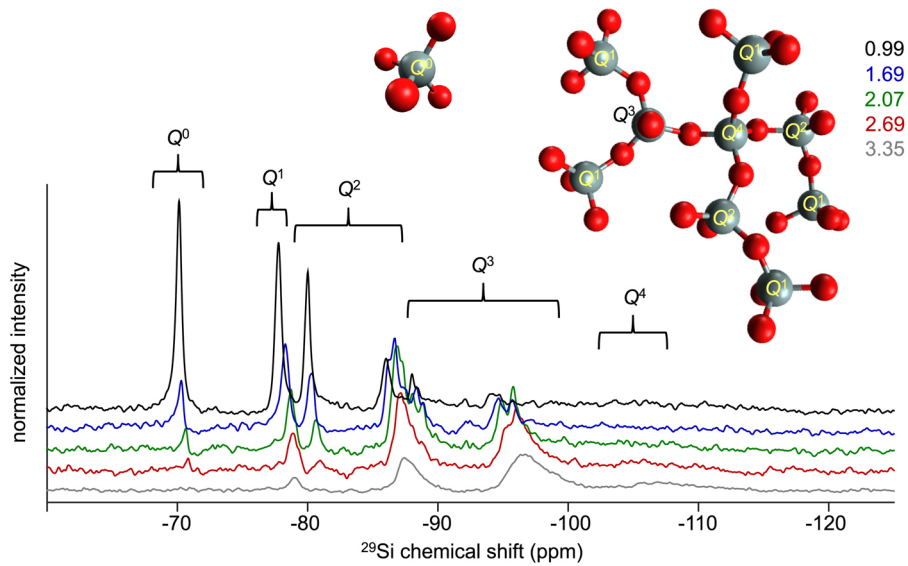
Figure 1.2: ^{29}Si NMR spectra of sodium silicate solutions with varying SiO_2:Na_2O ratios, showing Q^n species assignments. Reproduced from [24].

Spectroscopic techniques such as Raman and Fourier Transform Infrared Spectroscopy (FTIR) further support this trend, showing shifts in vibrational modes associated with increasing Si–O–Si connectivity as the ratio rises [25–27]. However, sodium cations play a crucial role in this process. By balancing the negative charges of silicate anions, they influence the degree of polymerisation and the stability of the species in solution. Lower sodium content promotes condensation and gelation, while higher sodium concentrations stabilise smaller species and prevent aggregation [28]. This delicate balance underlies the complex behaviour of sodium silicate solutions and their versatility in industrial applications.

1.3   Beyond Conventional Characterisation of Sodium Silicates

Still, despite decades of research, much of the chemistry, stability, and speciation of sodium silicates remains unclear. The process of transforming waterglass into silica gel, essential for a variety of industries, is similarly underexplored. Some even argue that the preparation of silica gels has become more of an art than a science, guided more by tradition than fundamental principles [29]. A deeper understanding of waterglass, from its speciation to condensation and gelation mechanisms, is crucial for optimizing its use in advanced applications. However, gaps in knowledge persist, and the limitations of current methods hinder further progress. There remains a pressing need for more refined techniques to fully unlock the potential of sodium silicates and bridge these knowledge gaps. Therefore, an inexpensive, simple, and non-invasive technique to characterize sodium silicates is urgently needed. Commonly used techniques such as transmission electron microscopy (TEM) and DLS, while managing to capture the polydispersity of the samples, require complex sample preparations which can potentially alter the silicate speciation or are not sensitive to sizes below 10 nm [30, 31]. Other techniques, such as SAXS, are completely inappropriate for industrial applications due to their high running costs and complexity. Additionally, contaminants must be accounted for, as metal ions tend to act as aggregation seeds, thus further impacting the size of individual species [32].

Rhodamine 6G (R6G) has been successfully employed as a fluorescent label to investigate silica colloids and to monitor sol–gel transitions in sodium silicate systems [33–35]. R6G, also known as Rhodamine 590, is a xanthene dye frequently used in dye lasers and as a fluorescent tracer [36]. It exhibits exceptional photostability in various solvents and a wide pH range while maintaining a high quantum yield [37]. Its chemical structure, consisting of a xanthene core with three aromatic rings in a single plane, its hydrophobicity, and cationic charge allow it to easily bind to a wide range of compounds, such as silica nanoparticles [38], sodium silicates [39], gold nanoparti-

cles [40, 41], titanium dioxide nanocomposites [42], and graphene [43, 44]. Additionally, R6G can be used as a sensor for mercury (II) detection in water [45] and for the specific and sensitive detection of nitrite [46]. The dye can be used to label silica nanoparticles electrostatically [35], and then time-resolved anisotropy measurements can be used to obtain the average particle size in sodium silicate, which showed perfect agreement with SAXS-obtained results [39]. However, the demonstrated anisotropy approach is incapable of assessing the size distribution and is limited to average size only.
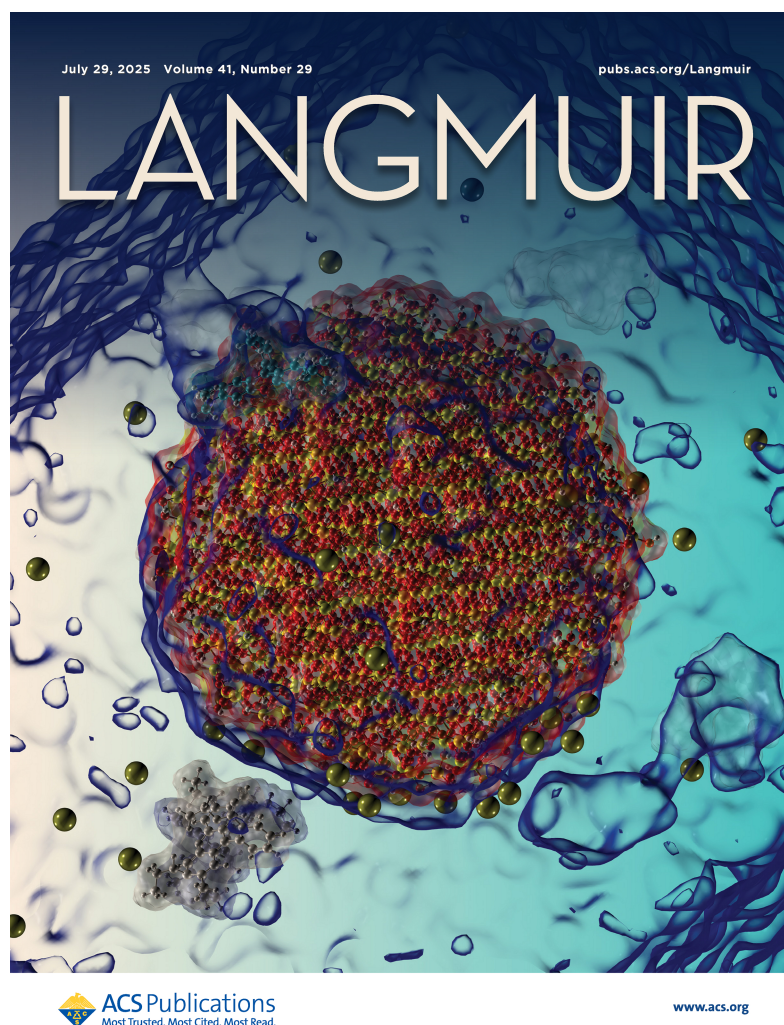
Figure 1.3: Front cover image of *Langmuir*, July 29, 2025, Vol. 41, Issue 29. Artistic representation of Rhodamine 6G adsorption onto a silica nanoparticle. Reproduced with permission from ACS. © American Chemical Society.

1.4   From Atoms to Clusters: Modelling Sodium Silicates

The complexity of sodium silicate solutions extends beyond what experimental techniques alone can capture. Molecular modelling has become a powerful tool for understanding the complex behaviour of silicate-based systems at the molecular level [47–52]. Over the past three decades, computational studies have provided valuable insights into the mechanisms driving silica polymerisation, complementing experimental data where direct observation is challenging and often impossible. These models cover a broad range of scales, from quantum mechanical (QM) methods at the atomic level to larger-scale molecular dynamics (MD) and mesoscale models. However, the detail each model can capture is often limited by the length and timescale it can handle, making it necessary to choose the right approach for the system of interest carefully.

Silicate polymerisation, which is essential in forming higher order structures in high ratio silicates and central to the sol–gel process, has been extensively studied using *ab initio* methods [47,53–55]. These studies suggest an ionic two-step mechanism involving penta-coordinated silicon intermediates. In the first step, a negatively charged silica oxygen attacks the silicon atom of another monomer, forming a penta-coordinated intermediate. In the second step, a water molecule is released, leading to condensation. Trinh et al. [47] showed that the ionisation of silanol groups promotes condensation, while White et al. [49] demonstrated that the Gibbs free energy of deprotonation and dimerization reactions depends strongly on the pH of the solution.

MD simulations have provided further insights into the kinetics of polymerisation. Trinh et al. and Pavlova et al. explored the early stages of condensation, showing that energy barriers for silica polymerisation are significantly higher in water than in the gas phase, highlighting the crucial role of the surrounding solvent [48, 56]. The influence of sodium ions has also been investigated, with findings suggesting that sodium disrupts hydrogen bonding between water molecules, inhibiting silica dimerization and trimerization.

On a larger scale, MD simulations have tracked the formation and growth of silicate clusters. Rao and Gelb simulated the polymerisation of hundreds of silicate

monomers at high temperatures and observed the formation of elongated clusters, indicating that more refined reactive potentials may be needed to accurately capture these processes [57]. Kamińska et al. proposed a four-step mechanism involving the formation of small species, growth into larger clusters, dissolution of intermediates, and eventual stabilisation in equilibrium with smaller species [58].

Despite these advances, challenges remain. QM methods are limited to small systems, while MD simulations are constrained by computational cost, simulation time, and the accuracy of the force fields used to describe silicate interactions. Developing reliable force fields for silicate systems is particularly challenging due to the complex nature of Si–O bonding and the influence of solvent and counterions [59]. While classical force fields can capture general trends, they often struggle to accurately reproduce reaction barriers and local structural details, highlighting the need for more refined models. Coarse-grained and kinetic Monte Carlo (kMC) models provide alternatives, allowing the study of larger systems over longer timescales, but integrating these approaches with atomistic models remains a challenge. As computational power and modelling techniques continue to improve, molecular modelling is expected to uncover even deeper insights into the dynamics of silicate solutions.
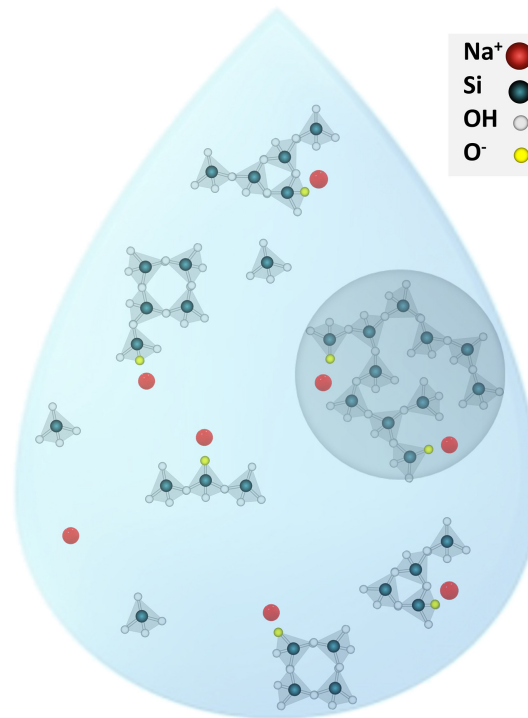
Figure 1.4: Schematic illustration of silicate species and sodium ions in a droplet of sodium silicate solution. The grey sphere indicates a colloidal particle that may form in concentrated solutions. Reproduced from [13] with permission from Elsevier.

1.5 From Photons to Particles: Fluorescence in Silicate Characterisation

Understanding the influence of sodium ions and the dynamics of silicate clustering naturally raises the question of how to characterise these processes, particularly the size of silicate species. This is where fluorescence-based methods come into play. By directly probing the motion and interaction of silicate species in solution, fluorescence techniques can provide a direct measure of size distribution, complementing the structural insights gained from MD simulations. Fluorescence techniques predominantly involve the emission of light by fluorescent molecules (or fluorophores) following their absorption of light at shorter wavelengths. These techniques can be classified into steady-state and time-resolved methods. Steady-state fluorescence techniques measure

the time-averaged intensity of emitted light under continuous excitation, providing insights into the concentration, environmental characteristics, and interactions of fluorescent molecules. On the other hand, time-resolved techniques, such as time-resolved fluorescence anisotropy and fluorescence correlation spectroscopy (FCS), analyse the dynamics of fluorescence emission, providing insights into molecular motion, particle size, and interaction kinetics. Due to their high sensitivity, these techniques can detect subtle changes in molecular environments, making them ideal for studying complex systems like silicate solutions.

Among these methods, Fluorescence Recovery After Photobleaching (FRAP) stands out [60]. FRAP was first introduced by Daniel Axelrod in 1976 as the method used to measure the diffusion of fluorescently labelled particles attached to the cell membranes [60]. Since then, it has been widely used to study various biological systems and the photobleaching properties of fluorescent molecules [61]. Since the rise of the popularity of confocal laser scanning microscopes (CLSM), FRAP has become one of the main tools for studying diffusion in cells and other biological systems, protein diffusion and their interactions by labelling them with extrinsic fluorophores [62,63]. FRAP is a technique used to measure the lateral mobility of fluorescently labelled molecules within a specific region of interest. In a typical FRAP experiment, a defined area of a sample is rapidly photobleached using a high-power laser, which irreversibly bleaches the fluorophores in that region. The recovery of fluorescence is then monitored over time as unbleached molecules from the surrounding area diffuse into the bleached region. By analysing the recovery curve, key parameters such as the diffusion coefficient, mobile fraction, and binding interactions of the labelled molecules can be extracted, providing valuable insights into the dynamic properties of the system under study. The main advantages of FRAP are its non-invasiveness, high specificity, and relative experimental simplicity. However, despite its advantages, there are some limitations. The recovery of fluorescence in a region of interest is often assumed to follow simple diffusion models, which may not always be accurate in more complex systems [64,65]. For example, in systems with membrane microdomains or highly viscous environments, diffusion may be hindered, leading to deviations from ideal recovery curves [64,66,67].

Additionally, FRAP measurements can be influenced by factors such as bleaching effi-
ciency, fluorophore concentration, and the intensity of the laser, all of which need to be
carefully controlled to obtain reliable results [60, 68, 69]. Furthermore, while FRAP is
powerful, its interpretation often relies on assumptions of homogenous recovery, which
may not hold in all cases [70]. Despite these challenges, FRAP remains a widely used
and valuable tool for studying molecular dynamics in living cells [63, 64, 71].

1.6   Towards a Fluorescence-Based Metrology of Silicates

This thesis aims to apply FRAP for measuring the size distribution of sodium sili-
cates, a key step towards developing an application in nanometrology. By leveraging
the principles of FRAP in the context of nanoparticle diffusion, this research aims to
contribute to the precision measurement of nanomaterials, which could have significant
implications for various fields, including materials science and nanotechnology.

When utilised for sodium silicate characterisation, fluorescence methods, particu-
larly FRAP, present notable advantages compared to traditional techniques. In contrast
to NMR, which is costly and time-consuming, FRAP is faster, straightforward to exe-
cute, and doesn't necessitate intricate sample preparation. Additionally, FRAP can be
customized to observe the diffusion of labelled silica nanoparticles across various me-
dia, enabling the direct measurement of particle dynamics and size distribution *in situ*.
The technique's capacity to monitor particle diffusion over time renders it especially
beneficial for characterising silicates at different processing stages, eliminating the need
for complicated sample handling. Furthermore, FRAP can be combined with other
fluorescence techniques, like fluorescence lifetime imaging (FLIM), to yield detailed in-
sights into the local environment of silicate particles, including their interactions with
solvents, surfactants, or other additives.

However, a key challenge in applying fluorescence-based methods to sodium silicates
is that silicate species are non-fluorescent. To address this, fluorescent dyes need to
be introduced to label the silicate particles. The success of this approach depends on
how the dye interacts with the silicate network, which could alter diffusion and size

distribution. Therefore, exploring these interactions at the molecular level is crucial; since this is impossible to study experimentally, computational methods must be used.

The first half of the results chapter of this thesis (Chapters 6 and 7) focuses on MD and density functional theory (DFT) simulations to study the binding modes, stability, and structural effects of fluorescent dye R6G on silica nanoparticles. The second half (Chapters 8, 9, and 10) applies this knowledge to guide fluorescence experiments, developing a FRAP-based method to measure the size of silicate species.

- **Chapter 2** outlines the theoretical foundation of MD and DFT simulations. It describes the key principles behind MD, including force fields, potential energy functions, and integration methods, and discusses how these simulations provide atomic-level insight into molecular interactions.

- **Chapter 3** introduces DFT as a complementary approach for refining interaction parameters and understanding electronic structure.

- **Chapter 4** outlines the theoretical background of fluorescence, covering the key principles behind fluorescence emission, quenching, and the factors that influence fluorescence behaviour in solution.

- **Chapter 5** describes the fluorescence techniques used in this research, including steady-state fluorescence measurements, time-correlated single photon counting (TCSPC), anisotropy decay analysis, and FRAP.

- **Chapter 6** explores the adsorption dynamics of R6G onto silica nanoparticles (SNPs), examining the effects of crystal structure, particle size, and pH on adsorption stability. It discusses how molecular dynamics simulations provide insight into the adsorption mechanisms, highlighting the role of electrostatic interactions, van der Waals forces, and surface ionization in determining the stability and mobility of the dye-SNP complex.

- **Chapter 7** examines the dimerisation dynamics of R6G in the presence and absence of SNPs, focusing on the role of π-π stacking interactions and the competition between adsorption and dimer formation. Using a combination of steered

molecular dynamics (SMD) and DFT calculations, the chapter explores the stability, binding energies, and molecular conformations of R6G dimers, highlighting the influence of SNP size, surface charge, and solution pH on dimerisation behaviour.

- **Chapter 8** presents a novel approach to nanoparticle metrology of sodium silicates using time-resolved multiplexed dye fluorescence anisotropy, complemented by SAXS. It explores the adsorption behaviour of R6G on silicate nanoparticles, detailing the influence of dilution, temperature, viscosity, and dye aggregation on fluorescence anisotropy measurements, while validating the results through SAXS and molecular dynamics simulations presented in Chapter 6.

- **Chapter 9** explores the use of FRAP to measure the size distribution of colloidal SNPs in binary mixtures. It describes how LUDOX HS40 and AS40 colloids were labelled with R6G and measured using FRAP under different mixture ratios and dye concentrations. The chapter discusses the analysis of FRAP recovery curves using different fitting models and how machine learning (ML) techniques were used to improve the accuracy of size estimation. The results demonstrate that FRAP can successfully distinguish between different nanoparticle sizes in mixed systems, offering a simple and effective alternative to more complex methods like SAXS or TEM.

- **Chapter 10** applies the FRAP-based methods established in Chapter 8 to sodium silicates, exploring whether particle sizes differ for silicates prepared from different materials but with identical ratios. The chapter compares FRAP results with industry-standard NMR measurements, evaluating the strengths of FRAP in characterising complex silicate systems. The findings reveal variability in silicate particle sizes and demonstrate FRAP's potential as a reliable and insightful alternative to NMR.

- **Chapter 11** summarises the key findings of the study and outlines directions for future research, including potential improvements to the FRAP methodology

and its broader application to diverse silicate systems.

1.7 Research Hypothesis and Objectives

Hypothesis

The central hypothesis of this thesis is that FRAP can resolve particle size distributions in sodium silicate solutions that remain inaccessible to conventional techniques such as NMR. Specifically, it is proposed that silicate solutions of identical molar ratios may nevertheless display very different particle sizes, influenced not only by stoichiometry but also by preparation route, impurities, and processing conditions. By directly probing diffusion, FRAP provides a simple, non-invasive, and scalable approach to nanometrology that complements or surpasses traditional methods.

A critical requirement for this approach is the ability to label silicate particles with a fluorescent probe. In this work, R6G is used due to its straightforward electrostatic adsorption onto silica surfaces, which avoids the need for complex covalent functionalisation or chemical modification. The central assumption is that the adsorption behaviour of R6G governs the sensitivity and reliability of fluorescence-based size measurements. To underpin this, MD and DFT simulations are employed to elucidate the stability, orientation, and aggregation behaviour of R6G at silica interfaces and in solution, ensuring that experimental fluorescence signals can be correctly interpreted.

Research Objectives

1. **Molecular-scale modelling of dye–silica interactions**

   - Use MD simulations to investigate the adsorption of R6G on silica nanoparticles under varying conditions (pH, surface chemistry, particle size).

   - Explore R6G dimerisation with MD and DFT to quantify binding energies, electronic structure changes, and potential fluorescence quenching pathways.

2. **Photophysical characterisation of dye behaviour**

- Perform steady-state absorption and emission spectroscopy to establish baseline behaviour of R6G in solution and in the presence of silica nanoparticles.

- Employ fluorescence anisotropy to measure nanoparticle size in model systems and benchmark against SAXS.

- Use time-resolved fluorescence to distinguish bound from unbound dye populations and to probe microenvironmental effects.

3. **Development and application of FRAP methodology (core objective)**

- Establish and optimise a FRAP protocol for nanoparticle characterisation.

- Validate the method on model colloidal systems (LUDOX HS40 and AS40) to test reproducibility and sensitivity.

- Apply FRAP to sodium silicate solutions to extract diffusion coefficients and particle size distributions, with emphasis on distinguishing silicates of identical molar ratio but different preparation histories.

4. **Complementary validation approaches**

- Benchmark FRAP-derived particle sizes and diffusion coefficients against SAXS.

- Compare FRAP and NMR measurements, highlighting cases where FRAP resolves differences undetectable by NMR.

5. **Integration and evaluation**

- Correlate molecular-level insights from simulations with experimental fluorescence observables, establishing the mechanistic basis of FRAP sensitivity.

- Critically evaluate the advantages and limitations of fluorescence-based methods relative to established nanometrology techniques, positioning FRAP as a candidate method for routine silicate characterisation.

Chapter 2

Basics of Molecular Dynamics

"Today the computer is just as important a tool for chemists as the test tube. Simulations are so realistic that they predict the outcome of traditional experiments."

Nobel Prize in Chemistry 2013 Press Release

2.1 Introduction to Molecular Dynamics

The foundation of all science, including MD, lies in the use of models. In the field of physics variety of models, such as point charges, simple harmonic oscillator (HO) or planetary model of the atom are used to describe the most complex phenomena. In the case of MD, the models are used to describe the physicochemical properties of the particles, model interactions etc., therefore before discussing the principles outlined in this chapter, it is important to introduce the concept of a physical model.

A physical model is a representation of a system or concept which is used to study, explain or predict that system's behaviour in real life. They are used to visualise complex systems, test hypotheses, or communicate ideas. Good examples of physical models are a wind tunnel model for aircraft aerodynamics testing or an anatomical model of the human body for medical study. In terms of computer simulations, a model refers

to a representation that is designed to mimic the characteristics and behaviours of a real-world object or system through computational methods and is built upon physical laws and mathematical equations that approximate the actual physical properties and interactions. It is important to understand, that models use simplified representations of real-world phenomena by focusing only on the most relevant variables and interactions, making complex systems more manageable to study and understand. This simplification allows to create a computerised version of systems that capture essential behaviours without the overwhelming detail of full-scale reality, predict outcomes and test potential solutions in a controlled environment. Therefore, the rapid progress of physics over the last few centuries owes much to the reliability and validation of physical models and concepts; without them, the field as we know it might never have emerged. Moreover, without physics, the MD would certainly not exist, as in its core, it relies on those simplest physical models.

MD is a powerful computational method that allows to simulate the physical movement of atoms and molecules. The history of MD started in 1957 when Alder and Wainwright successfully used an IBM 704 computer to simulate the elastic collisions between hard spheres [72]. The simulations were based on classical equations of motion, where the evolution of the many-body system was solved numerically [73]. Typically, the interactions in MD simulations are described using force fields (FF), which contain all the needed parameters to evaluate the complex interactions of the various components studied. Furthermore, with the advances in NMR spectroscopy [74], X-ray crystallography [75] and the rise of machine learning models, such as ALPHAFOLD [76,77], more molecular structures became available, hence MD simulations became a well-established and irreplaceable tools for the investigation of biomolecules [78], lipids [79], and complex inorganic nanocomposites [80]. With the recent addition of modern graphics processing units (GPUs), such simulations became feasible on a rather long timescale at a modest cost [81,82]. As a result, MD simulations can also be used to study complex interactions of small biomolecules with inorganic structures on a large scale, providing atomic-level resolution into these systems and significantly simplifying the interpretation of real-world experiments [83]. Moreover, MD serves as a powerful tool to verify experimental

hypotheses, bridging the gap between observation and theory. In this way, it not only complements experimental work but also deepens our understanding of fundamental processes, revealing the underlying principles that govern molecular behaviour.

2.2 Fundamentals of Molecular Dynamics

Standard classical molecular dynamics models utilising large numbers of atoms rely on assumptions, such as the Born-Oppenheimer Approximation (BOA), which allows to apply Newton's equations of motion to the system of interacting particles [84,85]. BOA states that because the atomic nuclei are much heavier than the electrons surrounding them, their wave functions can be treated separately [86]. Furthermore, due to the relatively large mass of the nucleus compared with the electron mass, the coordinates of nuclei in a system are approximated as fixed. This approximation is widely used, allowing to speed up calculations by multiple orders of magnitude in both classical MD and DFT calculations. As a result, to a good approximation, atoms behave as classical particles and the dynamical simulation can be performed by solving Newton's second equation of motion:

$$-\frac{dU}{d\mathbf{r}} = m\frac{d^2\mathbf{r}}{dt^2} \tag{2.1}$$

Here U is the potential energy at a position $\mathbf{r}$, which is a vector containing the Cartesian coordinates of all particles, i.e., it is a vector of length 3N, where N is the number of atoms in the system. Having the position vector $\mathbf{r}$ and the velocity $\mathbf{v}$, the resulting acceleration a can be calculated, thus allowing to predict the position and velocity of each point particle in future time steps. This results in a trajectory which contains positions and velocities for all atoms present in the system as a function of time. The most common method of implementing this integration is the Velocity Verlet algorithm which utilises two 3rd order (forward and backwards) Taylor expansions which allow to approximate the positions and dynamic behaviour of all atoms at a time t :

$$r\left(t + \Delta t\right) = r\left(t\right) + v\left(t\right)\Delta t + \frac{1}{2}a\left(t\right)\Delta t^2 \tag{2.2}$$

The velocity is updated every $t + \frac{\Delta t}{2}$ step:

$$v\left(t + \frac{\Delta t}{2}\right) = v\left(t\right) + \frac{1}{2}a\left(t\right)\Delta t \tag{2.3}$$

The resulting acceleration at a time $t + \Delta t$:

$$a\left(t + \Delta t\right) = -\left(\frac{1}{m_i}\right) dU\left(r\left(t + \Delta t\right)\right) \tag{2.4}$$

and the velocity at time $t + \Delta t$:

$$v\left(t + \Delta t\right) = v\left(\Delta t + \frac{\Delta t}{2}\right) + \frac{1}{2}a\left(t + \Delta t\right)\Delta t \tag{2.5}$$

To obtain the final trajectory, the algorithm is repeated millions of times as directed by timestep Δt, until the position of all atoms are obtained for the desired simulation time.

2.3 Molecular Mechanics (MM) Force Fields

In a typical MD simulation, the potential energy function is associated with a set of forces, collectively called FF, which acts on the atom [87]. As a result, the potential energy depends solely on the particle's position in space and represents the most computationally demanding part of molecular dynamics simulations, primarily due to the non-bonded interaction terms. Therefore, incorporating the forces into the FF and the necessary parametrization is essential for the accurate evaluation of molecular interactions in classical MD simulations.

A range of FF are used for molecular dynamics simulations, such as CHARMM [88–91], AMBER [92], GROMOS [93], OPLS [94] etc. All of them share a common trait - they use the same method of calculating the total potential energy of the system, hence produce comparable results. From Newton's 2nd law, the force can be calculated,

which is the negative gradient of a scalar potential energy function:

$$F(r) = -\nabla U(r) \tag{2.6}$$

The expression for the total potential energy of a system comprises of a sum of bonded and non-bonded interactions:

$$U_{\text{total}}(r) = \sum U_{\text{bonded}}(r) + \sum U_{\text{nonbonded}}(r) \tag{2.7}$$

The FF used throughout presented research work is CHARMM36 FF, which was developed by Martin Karplus, earning him a Nobel prize in Chemistry in 2012. The CHARMM FF is an all-atom FF containing parameters for a wide variety of chemical groups and compounds present in biological system. Furthermore, for the simulations of inorganic structures, i.e., silica nanoparticles, INTERFACE FF is used [59, 95–97]. INTERFACE FF is the extension of the most commonly used harmonic force fields such as CHARMM, AMBER or GROMOS, and it allows the simulation of inorganic-organic and inorganic-biomolecular interfaces. This FF has been successfully used in MD studies involving organic compound interactions with various silica structures [98,99]. Both of the FFs are additive and contain parameters for both bonded and non-bonded interactions. The bonded interaction terms account for bond stretching, angle and dihedral torsions, while the non-bonded term describes van der Waals (vdW) and Coulombic interactions. As these interactions are treated differently due to their distinct physical nature and mathematical formulations, they are discussed in detail in the following sections, highlighting the specific models, equations, and parameterisation approaches used to represent each type accurately. The following sections are based on the NAMD User Guide, including the explanations, equations, and theoretical foundations presented [100].

2.3.1 Bonded Potential Energy Terms

Bonded potential terms are those which involve 2-, 3- and 4-body interactions of atoms sharing covalent bonds. Commonly, harmonic potential is used to model and describe such interactions, which are treated as springs. As a result, the atomic bonds cannot be broken or created without additional substantial computational overheads arising from more sophisticated models, such as Morse potential [101].

The first term is the 2-body spring potential term which describes the vibrational motion between a pair of covalently bound atoms. The potential energy term for the 2-body bond is as follows:

$$U_{\text{bond}} = k_b (r_{ij} - r_0)^2, \tag{2.8}$$

where r_{ij} describes the distance between two covalently bound atoms, r_0 is the equilibrium distance and k_b is the bond spring constant.

The next term is the 3-body bond potential, which describes the angular vibrational motion between three covalently bound atoms (i, j, k):

$$U_{\text{angle}} = k_\theta (\theta - \theta_0)^2 \tag{2.9}$$

Here, the first term is comprised of θ, which is the angle between vectors $\mathbf{r}_{ij}$ and $\mathbf{r}_{kj}$, θ_0 is the equilibrium angle, and k_θ is the angle constant.

The last term accounts for the 4-body torsion (dihedral) angle and describes torsional interactions between atoms which are separated by three covalent bonds, where the central one is exposed to torsional deformations. The term can be split into two components:

$$U_{\text{torsion}} = \begin{cases} k(1 + \cos(n\psi + \phi)) & \text{if } n > 0, \\ k(\psi - \phi)^2 & \text{if } n < 0. \end{cases} \tag{2.10}$$

The top term is often called the proper dihedral (often simply called dihedral), and the bottom one the improper dihedral (usually called improper). Proper dihedrals describe rotational flexibility about a bond and determine the relative orientation of

bonded groups, contributing to the molecule's conformational energy landscape. Improper dihedrals, in contrast, are used to enforce specific geometric constraints that are not captured by bonds, angles, or proper dihedrals alone. They are defined over four atoms, with one central atom typically bonded to the other three, and are usually applied as harmonic restraints around an equilibrium angle to maintain planarity of peptide bonds or aromatic rings, preserve chirality at stereocentres, and prevent unphysical out-of-plane distortions of sp^2 centres [102]. Their inclusion ensures that molecular geometries remain physically realistic during simulations, compensating for the limitations of classical force fields.

The ψ is a dihedral angle between two planes – (i, j, k) and (j, k, l), ranging between 0 and 2π. For the case when $n > 0$ (proper dihedral), ϕ is the phase shift and k is the multiplicative constant. For the $n = 0$ case (improper dihedral), ϕ acts as an equilibrium angle. This splitting of the torsional potential into two terms allows for complex variations of the potential, which is effectively a truncated Fourier series.

2.3.2 Non-bonded Potential Energy Terms

The second group of essential interactions that must be included in MM FF are the vdW and electrostatic Coulomb interactions which are especially important when studying processes such as adsorption or aggregation. The nonbonded terms involve all pairs of atoms except those separated by exactly three bonds, which are accounted for in the bonded potential term, thereby avoiding duplicate calculations. The nonbonded interactions are computed based on a neighbour list and are the most computationally demanding during each MD step evaluation.

The vdW interactions are short-range forces caused by the correlations in the fluctuating polarisations of nearby particles, which is a consequence of quantum dynamics [103], and consist of four components [104]:

- Attractive or repulsive electrostatic interactions, referred to as Keesom interactions or Keesom forces [105];

- Polarisation effects, which are the attractive interactions between a permanent

multipole on one molecule and an induced multipole on another, referred to as the Debye force [106];

- London dispersion forces, which are attractive interactions between any pair of molecules, including non-polar atoms, arising from the interactions of instantaneous multipoles [107];

- A repulsive component resulting from the Pauli exclusion principle [108, 109].

Commonly, vdW interactions are described by Lennard-Jones (LJ) potential, which accounts for the weak dipole attraction between distant atoms, and the repulsive term as the distance between the atom pair decreases:

$$
U_{\text{vdW}} = -\varepsilon_{i,j} \left[\left(\frac{R_{\text{min}}}{r_{ij}} \right)^{12} - 2 \left(\frac{R_{\text{min}}}{r_{ij}} \right)^{6} \right]
\tag{2.11}
$$

The r_{ij} defines the distance between the pair of atoms, $\varepsilon_{i,j}$ is the potential well depth, and R_{min} is the radius at which the potential is at its minimum. In the LJ potential, the first term describes the short-range repulsion, while the second term is responsible for the long-ranged attractive interactions.
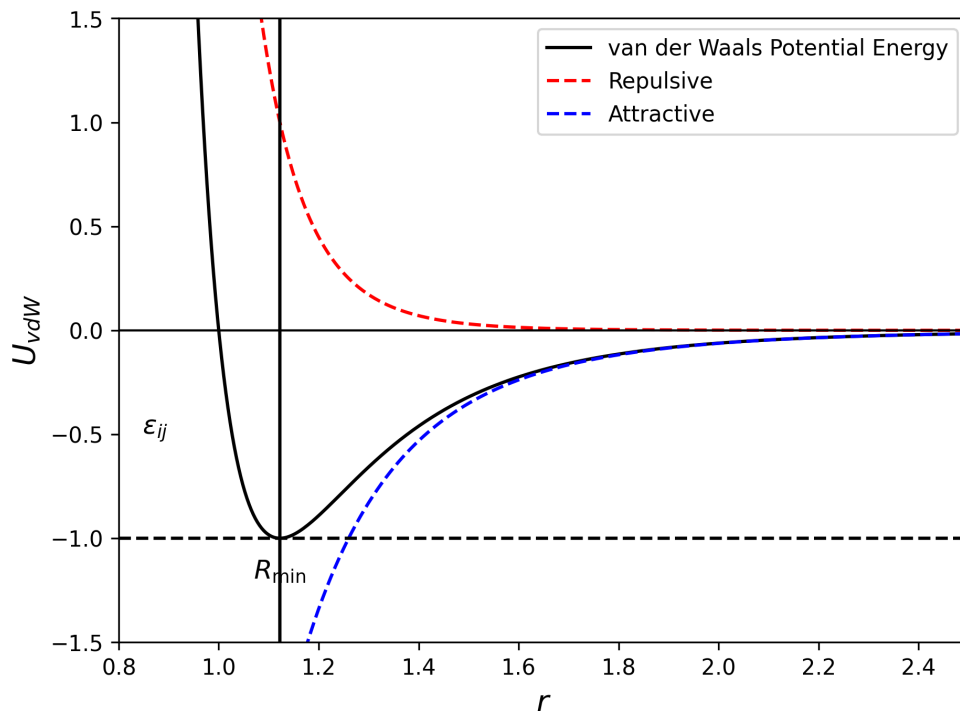
Figure 2.1: Lennard-Jones potential energy curve decomposed into repulsive and attractive components. The total potential energy is shown in black, with the repulsive ($\propto r^{-12}$) and attractive ($\propto -r^{-6}$) contributions shown as red and blue dashed lines, respectively.

The second term in the nonbonded potential energy terms is the electrostatic potential, which is repulsive for atomic charges with the same sign and attractive for those with opposite signs, and is expressed using Coulomb's law:

$$U_{\text{elec}} = \frac{1}{4\pi\varepsilon_0} \frac{q_i q_j}{\varepsilon_r r_{ij}} \tag{2.12}$$

The first fraction in the expression represents the Coulomb constant, ε_r is the dielectric constant, which is fixed for all electrostatic interactions, and r_{ij} is the separation distance of two atoms. The q_i and q_j are the atomic partial charges on the respective atoms, and while they can be assigned using empirical rules, typically they are assigned by fitting to the electrostatic potential calculated by electronic structure methods [110]. For example, as hydrogen bonding is largely caused by the attraction

between electron-deficient hydrogen and another electronegative atom, such as oxygen or nitrogen, accurate assigning of partial charges allows for modelling such interactions.

As the nonbonded interactions are very computationally demanding and calculating those between all atoms is highly inefficient, they are typically truncated at a set distance. As the vdW term falls off rapidly, generaly a cutoff radius is used to speed calculations so that atom pairs which are greater than the cutoff, have vdW interaction energies set to zero. On the other hand, the Coulomb potential falls off only as r^{-1}, hence the introduction of a cutoff introduces sharp discontinuities between the atoms inside and outside the radius. To somewhat overcome this, switching or scalling functions are introduced, which modulate the nonbonded interactions, by smoothing it at the outer and inner cutoff radii. Nowadays Particle Mesh Ewald (PME) is used to compute the full electrostatics of the system without the need for cutoff.

In general, the FF terms contribute to the total potential energy function as follows:

$$U_{\text{bonds}} > U_{\text{angles}} > U_{\text{dihedrals}} > U_{\text{impropers}} > U_{\text{non-bonded}} \tag{2.13}$$

Typically, in systems near equilibrium, the strongest contribution to the total potential energy comes from the bonded interactions, while the non-bonded electrostatic Coulomb and vdW interactions have the smallest contributions. Nonetheless, important interactions, such as π-π stacking, come from $U_{\text{non-bonded}}$, hence those terms cannot be overlooked and additional care must be taken when parametrising molecules [111]. Strictly speaking, the majority of real-life processes are centred around non-bonded interactions; therefore, those interactions cannot be simply ignored when the final goal is performing accurate simulations.

2.4   Particle Mesh Ewald and Ewald Summation

The PME is a widely used method in MD simulations, which allows to compute long-range interactions in a periodic system. In PME, the short-range interactions are evaluated in real space, while the long-range interactions are calculated in a Fourier

space by employing the Fast Fourier Transform (FFT) algorithm. Due to this, the energy converges rapidly when compared with a direct summation, and is the *de facto* standard method for calculating long-range interactions in periodic systems nowadays. Due to the use of the Fourier sum, the system under study must be infinitely periodic which is the case in MD simulations, as such simulations are normally accomplished by creating a charge-neutral unit cell that can be infinitely reproduced, thus satisfying the primary requirement of PME. A typical workflow of PME is shown in Figure 2.2.
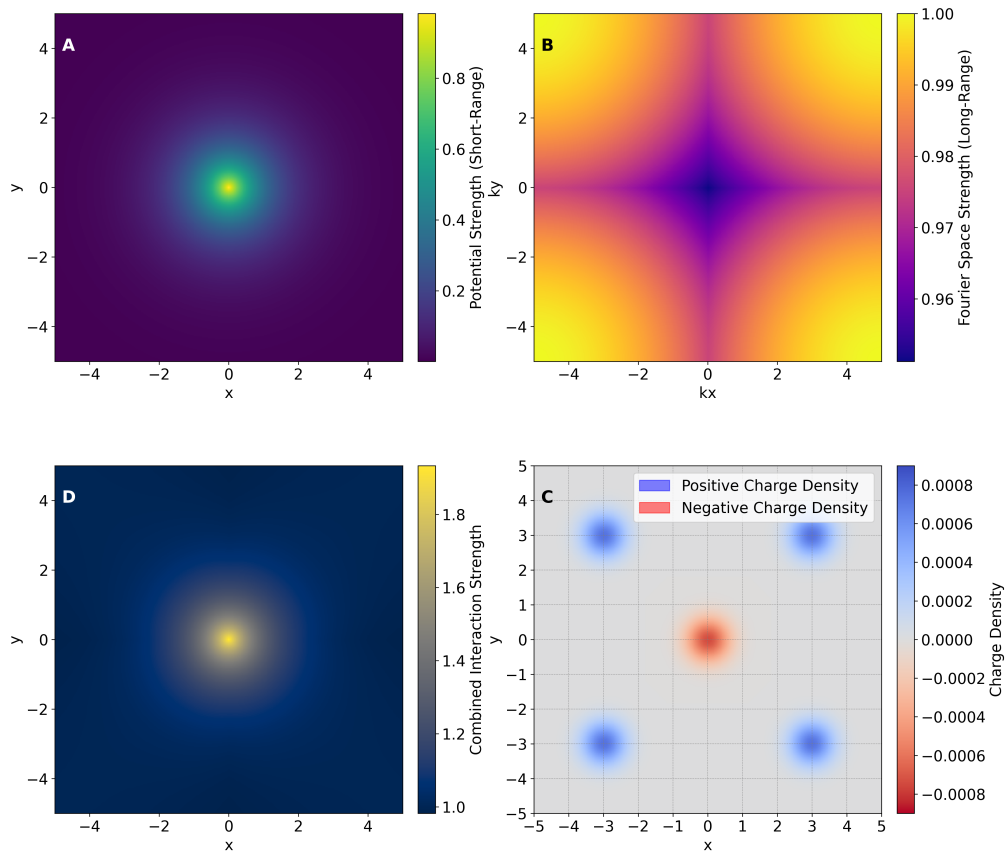
Figure 2.2: Visualisation of the PME method components for electrostatic interaction calculations. (A) Real space direct interactions capture short-range potentials with exponential decay. (B) Reciprocal space representation of long-range interactions shown in Fourier space. (C) Charge interpolation onto a mesh grid, illustrating the distribution of positive and negative charges with Gaussian spreading. (D) Combined real and reciprocal space interactions produce a balanced and accurate electrostatic potential. Colour bars indicate the scale of potentials or charge density in each panel.

In the first step, the short-range interactions between particles are calculated directly in the real space. In this case, with the increasing interparticle distance, the potential decreases rapidly, which is represented by a decaying field. Although real-space interactions are very efficient at calculating long-range forces, calculating them over long-range becomes a very computationally intensive task. As a result, long-range interactions are calculated in Fourier space, as this allows PME to compute long-range forces efficiently by smoothing interactions over a distance. This can be seen on the second plot, which shows that in a Fourier space, the long-range contributions are smooth, thus allowing to capture global interactions without extensive computational overheads. The following step involves placing particle charges on a grid for efficient FFT-based calculations. This way interpolated charges simplify the calculations as each grid point represents a localised charge density, allowing to distribute the charge information along a domain, creating a smoother representation which is more computationally manageable. Finally, in the last step both short-range real-space and the long-range Fourier-space interactions are combined to calculate the full electrostatic potential. This results in a balanced interaction field that includes both local and global effect efficiently. This allows for an accurate calculation of interactions by utilising the strengths of both real and Fourier spaces for accurate electrostatic calculations. Lastly, the whole process is repeated throughout the duration of the simulation.

2.5   Thermostats and Barostats

To successfully run MD simulations, two key parameters that directly affect the outcome of the simulation must be specified: temperature and pressure. As a result, the user selects an ensemble in which the simulation will be performed. Three common ensembles are used for MD simulations [112]:

- *Microcanonical ensemble* (NVE): the number of atoms (N), system volume (V) and total energy (E) is constant;

- *Canonical ensemble* (NVT): the number of atoms (N), system volume (V), and

temperature (T) are constant;

- *Isobaric-Isothermal ensemble* (NPT): the number of atoms (N), system pressure (P) and the temperature (T) are constant.

The choice of ensemble typically depends on the specific goals of each stage of the simulation. During the energy minimisation step, the main goal is to relax the initial structure, and since this isn't a dynamic process but rather an optimisation algorithm (typically steepest descent or conjugate gradient) and no time integration is involved, usually, there are no ensemble constraints involved. During the equilibration step, usually performed in NPT, the purpose is to reach a stable temperature, pressure and density, adjusting from potentially artificial starting configuration resulting from the energy minimisation. By performing equilibration in NPT ensemble, the system volume can fluctuate, thus allowing it to reach the correct density and ensure proper molecule packing. The production runs are typically performed in NVT ensemble to ensure that the system remains stable during production runs, resulting in more reliable and consistent results. Furthermore, NPT simulations require an additional barostat to maintain constant pressure, thus introducing additional computational overhead. On the other hand, NVT simulations are faster and cheaper since they only require a thermostat to control the temperature. There are cases when production runs are performed in different ensembles, e.g., membrane simulations; however, those are not covered in this work since they are irrelevant.

To maintain a desired constant temperature, thermostats are used in MD simulations, which adjust the velocity of the atoms, which directly affects the temperature, i.e., the higher the velocity, the higher the temperature and vice-versa. The thermostat controls the temperature by monitoring the target temperature and rescaling or adjusting the velocities when needed, thus ensuring that the desired temperature is maintained.

From the kinetic theory of gas, we know that the temperature is a function of the momenta of all atoms. In a system containing N atoms, the temperature can be

calculated from using the average kinetic energy of all atoms:

$$\left\langle \frac{1}{2} m_i v_i^2 \right\rangle = \frac{N}{2} k_B T \tag{2.14}$$

Where N is the number of degrees of freedom in a system and k_B is the Boltzmann constant. As MD simulations are dynamic and the atom velocities are changing during the simulation, the temperature becomes a function of time:

$$T(t) = \sum_{i=1}^{N} \frac{m_i v_i^2(t)}{N k_B} \tag{2.15}$$

A piston barostat must be used to maintain constant pressure in the system by allowing the simulation cell to expand and contract when performing simulations in an NPT ensemble.

Commonly used thermostats are Berendsen [113], Andersen [114], Nosé-Hoover [115, 116], Bussi [117], Heyes [118] and Langevin [119–121]. For the work presented in this thesis, the Langevin thermostat was employed to control the system temperature by adding a frictional term and a random (stochastic) force to Newton's equations of motion, representing the effect of particle collisions and thermal fluctuations.

2.6 Langevin Dynamics

Langevin dynamics allows study of the movement of the particles in a system where they interact with the surroundings. This is achieved by adding random forces to Newton's equations of motion, thus mimicking the effect of collisions with surrounding particles, similar to a viscous fluid. By combining deterministic forces with stochastic and frictional terms, Langevin dynamics provide a great balance between accuracy and computational efficiency. The main components of the Langevin equation are:

- *Deterministic force* $-\frac{dU}{dx}$ which represents the forces that arise from the interactions between particles;

- *Damping force* $-m\gamma\frac{dx}{dt}$ which simulates the resistance due to the environment,

thus slowing the particles;

- *Stochastic Force* $R(t)$ which represents the random effects of surrounding particles on a particle of interest. This random force is often sampled from a Gaussian distribution and scaled according to the system's temperature, ensuring that the particles move in a way that aligns with the desired thermodynamic properties.

Thus, the final equation of motion for Langevin dynamics is of the following form:

$$m\frac{d^2\mathbf{x}}{dt^2} = -\nabla U(\mathbf{x}) - m\gamma\frac{d\mathbf{x}}{dt} + \mathbf{R}(t) \tag{2.16}$$

2.7   Water Model

Water plays a central role in most molecular dynamics simulations, and its accurate representation is essential for reproducing structural, dynamical, and thermodynamic properties of solvated systems. Over the years, a variety of models have been developed to balance accuracy with computational efficiency. Simple rigid models such as SPC, SPC/E, and TIP3P [122] are widely used due to their efficiency, while more advanced models such as TIP4P, TIP5P, and polarizable water models aim to improve the description of hydrogen-bonding networks, dielectric properties, and diffusion behaviour [123]. Each of these models has particular strengths and limitations, and the choice is generally dictated by the system studied and the properties of interest.

In this work, the TIP3P (Transferable Intermolecular Potential with 3 Points) model was employed. TIP3P is one of the most widely adopted water models, primarily due to its computational efficiency and its compatibility with major biomolecular force fields such as AMBER and CHARMM. It represents water as a rigid three-site molecule with partial charges assigned to the oxygen and hydrogen atoms and a Lennard–Jones interaction centred on the oxygen. This simple representation allows efficient computation while reproducing key bulk properties of liquid water, including density, radial distribution functions, and diffusion coefficients under ambient conditions.

The rigidity of the TIP3P geometry is maintained during simulations using con-

straint algorithms such as SHAKE, RATTLE [124], or LINCS [125], which fix the O–H bond lengths (≈ 0.9572 Å) and the H–O–H angle ($\approx 104.5°$). By enforcing these constraints, water molecules retain their geometry throughout the simulation, enabling the use of larger integration timesteps and ensuring stable hydrogen-bonding interactions with solutes.

Despite its practical advantages, TIP3P has known limitations [126]. It lacks explicit polarizability and tends to overestimate water mobility, which can lead to discrepancies in properties such as viscosity or dielectric response. Nevertheless, its balance of speed, robustness, and force field compatibility makes TIP3P a reliable choice for large-scale simulations where computational efficiency is a priority.

2.8 Periodic Boundary Conditions

In typical MD simulations, there is a finite number of atoms within a simulation box, however in real-life systems, the environment is virtually infinite when compared with molecular dimensions. To overcome this problem, and introduce this concept of infinite system into MD simulations, Periodic Boundary Conditions (PBC) are used. PBCs are a crucial concept in MD simulations as they help to model an infinite system by repeating a finite simulation box in all directions, thus mimicking the behaviour of an infinite system. Furthermore, in simulations without PBCs, particles at the edges of the box have fewer neighbours when compared with particles further from the edge, resulting in artificial edge effects, while with PBCs in place, the box is essentially "wrapped" around itself in all directions. When a particle exits the box from one side, it re-enters the box on the opposite side with the same velocity, giving the illusion of continuity. However, care must be taken when setting up PBCs, especially when estimating the size of the primary simulation cell box. The simulation box must be large enough to avoid "self-interactions", where a particle interacts with its image due to periodicity. It should also be larger than twice the cutoff distance, which is typically used for van der Waals interactions in non-bonding calculations.
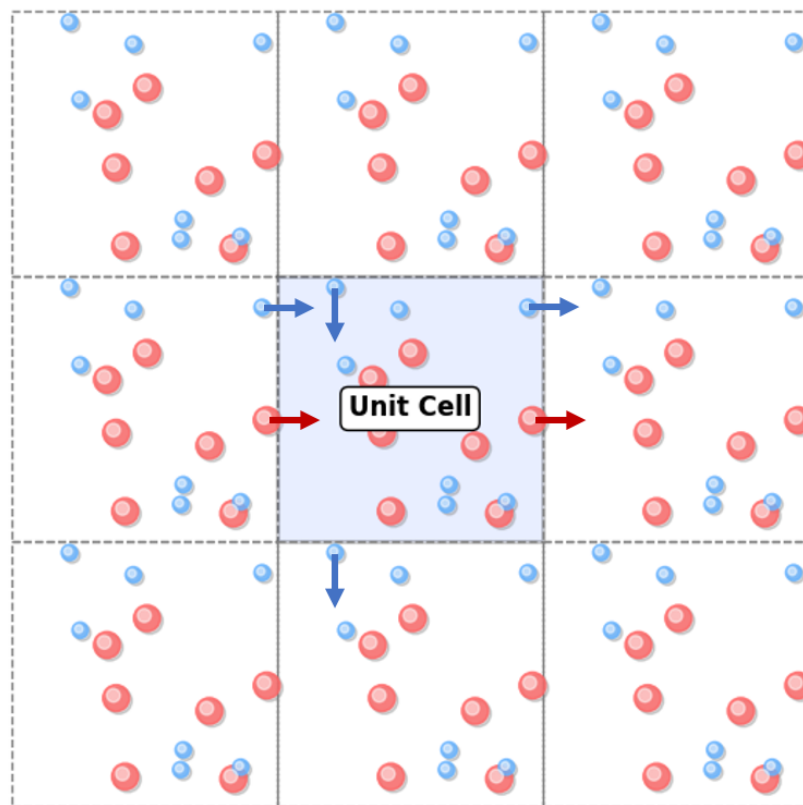
Figure 2.3: Illustration of PBC used in simulations to model infinite systems. The central simulation box (shaded in blue) is surrounded by replicated images in all directions, ensuring particles exiting one side re-enter from the opposite side. This approach minimises edge effects and mimics bulk behaviour by creating a seamless, repeating environment.

2.9   Enhanced Sampling Methods

Traditional MD is often limited by "timescale barriers" as the system gets trapped in a local energy minimum and cannot cross the energy barriers due to the slow atomic movements. Furthermore, many biomolecular processes, such as protein folding, conformational changes, adsorption and desorption of molecules etc., occur on much larger timescales that standard MD simulations can reach due to large energy barriers of the aforementioned processes. As a result, enhanced sampling methods are used to sample these slow events more frequently, achieve better convergence in energy calculations or

study complex conformational changes and transitions in macromolecules. One such method is SMD in which an external harmonic force is applied to a specific atom or group along a chosen reaction coordinate at a constant velocity or force. Thus, the external force is effectively "steering" the system in a desired direction, allowing to study protein unfolding, dimer dissociation or receptor-ligand binding. Furthermore, SMD has demonstrated excellent agreement with experimental techniques, such as MP-SPR and AFM [127–129]. In constant velocity pulling, the specified SMD atom is attached to a dummy atom through a virtual spring which acts as a handle to exert the external force. In contrast, in constant force pulling, a predefined external force is applied directly to the SMD atom, without relying on a velocity-controlled movement. However, constant force pulling is not used in this work, as the focus is on velocity-controlled perturbations.

To obtain information about the magnitude of energy at different transitions during SMD simulation, a modified equation for the potential energy of the spring can be used:

$$dE = \frac{1}{2}k\,d(x^2) \tag{2.17}$$

The force exerted by the spring is

$$dF = -k\,dx \tag{2.18}$$

Solving for $dx = -\frac{dF}{k}$ and substituting into the energy expression gives

$$dE = \frac{(dF)^2}{2k} \tag{2.19}$$

Finally, if the spring is already under an initial force F_0, the incremental energy change becomes

$$dE = \left(F_0 + \frac{dF}{2}\right)\frac{dF}{k} \tag{2.20}$$

where F_0 is the force at the end of the transition, dF is the force difference, and k is the spring constant. Typically, to estimate the binding energies, a force as a function

of the simulation time plot is created. From this plot, it is possible to estimate dF and, using the equation 2.20, calculate the interaction energies.

Other enhanced sampling methods exist such as Replica Exchange MD (REMD) [130], Umbrella sampling [131] or metadynamics [132], however, those will not be discussed here as they are not relevant to this work.

2.10 Limitations

While classical MD simulations are a widely used computational approach and have become an indispensable tool in studying molecular systems, it has several limitations that affect the accuracy and applicability of the results:

- While FFs are based on empirical data and high-level *ab initio* calculations, the latter are limited to small model compounds. As a result, the empirical parametrisation may not be accurate for all types of systems. Furthermore, as the FFs are often parametrized for specific classes of molecules, their accuracy is limited in diverse systems. Since most FFs assume fixed bond structures, it is computationally demanding to simulate chemical reactions where bond formation or breaking is essential, such as catalytic reactions.

- Since FFs do not account for quantum mechanical effects like charge transfer, and all charges defined during the system preparation cannot change, systems, where these effects are important (e.g., transition metal complexes), may be misrepresented. Additionally, traditional FFs assume that atomic charges are fixed and do not respond to changes in environment, therefore the polarization effects cannot be properly described, which might lead to inaccuracies in situations where electronic redistribution is significant, e.g., in ionic binding or in the presence of strong electric fields.

- Due to the limitation of computational resources, MD simulations typically apply a cutoff distance for non-bonded interactions. However, electrostatic interactions are long-range, and truncating them at a set distance might lead to discrepancies

34

in systems where electrostatics are important, such as electrolyte solutions or large charged biomolecules.

- Water is a crucial component of most simulations, yet traditional models such as SPC or TIP3P are far from ideal and often are limited in their ability to capture the full complexity of water behaviour. Additionally, FFs' performance varies depending on environment, hence applying the same FF for different environments (e.g., liquid, solid) may lead to inaccurate results.

Despite these limitations, FF MD simulations still remain a powerful tool which is constantly improving as new FF and other methods are being developed which allow to account for electronic and reactive behaviour. For scenarios, that exceed these limitations, other advanced methods such as QM/MM or machine-learning-based FF such as MACE [133, 134] are being explored as a potential solution.

Chapter 3

Introduction To Density Functional Theory

3.1 Introduction

DFT is a computational quantum mechanical modelling method used to investigate the electronic structure in atoms, molecules and condensed matter systems. While the roots of DFT start with the Thomas-Fermi model for the electronic structure of materials, the basis for the contemporary DFT is the proof by Walter Kohn and Pierre Hohenberg, stating that the ground state properties of a many-electron system can be determined solely from the electron density, rather than requiring detailed knowledge of the wavefunction [135]. The computational breakthrough in DFT happened in 1965 when W. Kohn and L. J. Sham introduced orbitals into the picture [136]. This transformed a very complex many-electron problem into a more manageable framework, where instead of solving for the exact wave function of a system with many interacting electrons, they suggested mapping the real system onto a virtual system of non-interacting independent electrons, which produces the same electron density as the real interacting system. Using this approach, the most complex interactions, which are a fraction of

the whole energy are condensed into an exchange-correlation functional, where even a rough approximation will provide a reasonably accurate result. Conceptually, DFT is very similar to Hartree – Fock (HF) theory, however it provides significantly better results, therefore becoming one of the most popular electronic structure methods to this day.

3.2   The Schrödinger Equation

A hundred years ago, Schrödinger formulated the fundamental equation of quantum mechanics which laid the foundation for the integral part of the field – the wave mechanics [137]. By solving it, any observable physical quantity of the system can be determined, since all the information about given systems is contained in its wave function. Therefore, the goal of an *ab initio* (first principles) study is to solve the many-particle Schrödinger equation for a system of interest, for example, a rhodamine 6G dimer. The time-independent, non-relativistic, many-particle Schrödinger equation (TISE) has to following form:

$$\mathbf{H}\Psi(\mathbf{R}, \mathbf{r}) = E\Psi(\mathbf{R}, \mathbf{r}) \tag{3.1}$$

where $\mathbf{R}$ are the nuclear and $\mathbf{r}$ the electron coordinates. The many-particle Hamiltonian consists of the following five terms:

$$\mathbf{H} = T_e + T_n + V_{en} + V_{ee} + V_{nn} \tag{3.2}$$

The first two terms describe the kinetic electronic and nuclear energies, V_{en} describes the electronic-nuclear potential energy, and the last two terms describe electron-electron and nuclear-nuclear interactions. The main problem is that the motions of electrons in atoms correlate because of the strong Coulomb repulsion between them, therefore the electron-nuclear many-particle problem is one of the most complex problems of quantum mechanics. As a result, the TISE can be solved analytically only in the simplest cases, as the computational resources required to solve it scale exponentially

with both the number of electronic coordinates $3n$ and number of nuclear coordinates $3N$ in the system. If we would assume that a single gram of any substance contains 10^{23} electrons, then solving TISE for this system using modern HPC would require approximately $1,000,000,000,000$ terabytes of computing space to represent the $3n$ coordinates of each electron [138]. Luckily, from the electronic point of view, the nuclei are stationary; therefore, to a good approximation, the movement of nuclei and electrons can be separated, which is the previously discussed BOA. Although this approximation substantially simplifies the calculations, an even more efficient approach for handling electronic structure, DFT, will be discussed in detail in the next section.

3.3 The Hartree - Fock method

Before discussing DFT, it is important to briefly mention the first practically useful method of solving many-particle problem, which is the HF, or self-consistent field (SCF) method [139, 140]. Here, the many-particle wave function is approximated by a single Slater determinant, which ensures that the wave function is antisymmetric with respect to the exchange of any two electrons, thus satisfying the Pauli exclusion principle. Furthermore, instead of treating electron-electron interactions explicitly, in HF it is assumed that each electron moves in a mean-field created by all the other electrons, effectively reducing the problem to solving one-electron equations iteratively.

Despite its foundational role, the HF method has several notable weaknesses:

1. The most critical weakness is the inability to capture electron correlation, specifically the interactions between the electrons beyond the mean-field approximation, such as the dynamic correlation which describes the instantaneous repulsion between electrons as they avoid each other in real-time. As a consequence, the total electronic energy is overestimated leading to poor accuracy for properties that depend on the electron correlation.

2. It completely fails to describe dispersion interactions, which arise from correlated fluctuations in electron density. These forces are essential for non-covalent inter-

actions (e.g., π stacking), therefore HF cannot accurately predict binding energies or molecular geometries in systems where dispersion is critical, such as aromatic dimers, e.g., R6G dimer.

3. The results are highly dependent on the basis set, with small basis sets leading to substantial errors, while larger basis sets significantly increase the computational costs. Nonetheless, even with large basis sets, it fails to predict accurate energy values due to the inherent lack of electron correlation.

To overcome these limitations, DFT, particularly through the Kohn-Sham formalism, offers a more accurate and efficient framework by incorporating electron correlation effects into the electronic structure calculations.

3.4 The Kohn-Sham Equation

The entire DFT field is based on the framework introduced by Kohn and Hohenberg, along with the set of equations derived by Kohn and Sham in 1965, which state that the ground state energy from Schrödinger's equation is a unique functional of the electron density. A crucial task is to understand the meaning of the term "functional". As the name suggests, functional is a closely related term to the familiar concept of a function. A function takes a value of a variable and defines a single number. A functional has a similar concept, but it takes a function as an input and defines a single number from it. Hence, we can say that the ground state energy E, can be written as a functional $E[n(\mathbf{r})]$, where $n(\mathbf{r})$ is the electron density. Furthermore, the electron density $n(\mathbf{r})$ can be written in terms of the individual electron wavefunctions by summing over all individual electron wavefunctions that are occupied by electrons:

$$n\left(r\right) = 2\sum_{i} \psi_i^*\left(r\right)\psi_i\left(r\right) \tag{3.3}$$

The factor of two comes from the concept of electron spin and the Pauli exclusion principle, stating that an individual electron wavefunction can be occupied by two separate electrons with opposite spins.

Now, it is useful to express the functional defined by Kohn and Hohenberg in terms of single electron wavefunctions, which as mentioned previously, define the electron density. Let's split the functional into two terms, the first $E_{\text{known}}\left[\{\psi_i\}\right]$, which can be written down in an analytical form, and $E_{\text{XC}}\left[\{\psi_i\}\right]$:

$$E\left[\{\psi_i\}\right] = E_{\text{known}}\left[\{\psi_i\}\right] + E_{\text{XC}}\left[\{\psi_i\}\right] \tag{3.4}$$

The term $E_{\text{known}}\left[\{\psi_i\}\right]$ can be written as a sum of four terms (in order): the electron kinetic energies, the Coulomb interactions between the electron and the nuclei, the Coulomb interactions between pairs of electrons, and the Coulomb interactions between pairs of nuclei:

$$E_{\text{known}}\left[\{\psi_i\}\right] = -\frac{\hbar^2}{2m} \sum_i \int \psi_i^* \nabla^2 \psi_i \, d^3r + \int V\left(r\right) n\left(r\right) \, d^3r$$
$$+ \frac{e^2}{2} \iint \frac{n\left(r\right) n\left(r'\right)}{|r - r'|} \, d^3r \, d^3r' + E_{\text{ion}} \tag{3.5}$$

The other term, needed to describe all quantum mechanical effects that are not included in the $E_{\text{known}}\left[\{\psi_i\}\right]$, is the exchange-correlation (XC) functional. Assuming that we can accurately determine the $E_{\text{XC}}\left[\{\psi_i\}\right]$, there is no guarantee that solving this expression will not be a Sisyphean task. Thankfully, this problem was solved by Kohn and Sham (KS) who showed that finding the right electron density can be as simple as solving a set of equations in which each equation only involves a single electron, each having the following form:

$$\left[-\frac{\hbar^2}{2m} \nabla^2 + V\left(r\right) + V_H\left(r\right) + V_{XC}\left(r\right)\right] \psi_i\left(r\right) = \epsilon_i \psi_i\left(r\right) \tag{3.6}$$

At a first glance, the KS equation is virtually identical to the Schrödinger equation, and this is indeed the case. This is because the solution to this equation are single-electron wavefunctions, each depending on three spatial variables $\psi_i(\mathbf{r})$. On the left-hand side, three potential energy terms appear, $V(\mathbf{r})$, $V_H(\mathbf{r})$, and $V_{\text{XC}}(\mathbf{r})$. The first term appeared in the $E_{\text{known}}\left[\{\psi_i\}\right]$ and it defines the interaction between an electron and the collection

of atomic nuclei. The next term is the Hartree potential, which is simply the classical Coulombic repulsion of an electron density with itself:

$$V_H(r) = e^2 \int \frac{n(r')}{|r - r'|} d^3 r' \tag{3.7}$$

The last term is the infamous exchange-correlation term, which can be formally defined as a "functional derivative" of the exchange-correlation energy:

$$V_{XC}(r) = \frac{\delta E_{XC}(r)}{\delta n(r)} \tag{3.8}$$

In theory, the approach of starting from a tentative set of KS orbitals using the density constructed from the initial guess and solving the KS equation to get new eigenfunctions over and over again should produce the exact ground-state energy and density. However, things are not as simple as they might seem due to the small but vital approximated contribution – the exchange-correlation energy E_{XC}. The biggest challenge of DFT is the description of this term, which is directly correlated with the accuracy and the quality of the results and will be discussed next.

3.5   The Exchange-Correlation Functionals

In all wave function-based electronic structure methods, the quality of these methods and how the electron correlation is included can be typically assessed in a very straightforward way. Commonly, this can be characterised using an ordering parameter, such as the level of excitation, e.g., CCS (Coupled Cluster Singles), CCSD (Coupled Cluster Singles and Doubles), and CCSD(T) (CCSD with perturbative Triples), or the order of perturbation, such as MP2, MP3, MP4 (Møller–Plesset perturbation theory of second, third, and fourth order, respectively). While there are no such ordering parameters for DFT, the functionals can be classified into rungs which depend on the level of approximation, commonly referred to as the Jacob's ladder [141]. The simplest of functionals being in the first rung, and dangerously close to outdated HF methods, often referred to as Hartree "hell", while on the last rung, we have very computationally demand-

ing double-hybrid functionals, that are the pinnacle of chemical accuracy (typically ± 1 kcal/mol) and approach the precision of the gold standard of quantum chemistry – CCSD(T).

3.5.1   Local Density Approximation

The simplest and the oldest approach, the mother of all DFT approximations is the local density approximation (LDA). In LDA, it is assumed that the local density can be approximated as a homogeneous electron gas, or in simple terms that the density is a slow varying function. This is a single system for which the form of exchange-correlation energy is precisely known. To generalize this approximation for an inhomogeneous system, it is assumed that the exchange-correlation energy at each point in space depends on a locally constant electron density. Although LDA is the simplest, and least accurate of the approximations, it has shown to predict accurate results for systems which resemble a uniform electron gas, such as those that exhibit strong metallic, ionic or covalent bonding, while for molecules it is far less useful [142]. Additionally, it tends to overestimate binding energies and underestimate the bond lengths.

3.5.2   Generalized Gradient Approximation

The next rung in the Jacob's ladder contains functionals from a family based on generalized gradient approximation (GGA), where in addition to the local electron density, the first derivative (∇) of the density is included [143]. The inclusion of the first derivative allows for accurate capture of the asymptotic behaviour of the energy density, thus reducing the error in exchange energy by almost two orders of magnitude when compared with the simple LDA. Due to this, GGA functionals, such as Perdew-Burke-Ernzhof (PBE) [144], have become a standard tool for plane-wave DFT involving periodic systems.

3.5.3 meta-GGA Methods

A logical extension to GGA functionals is including higher-order derivatives of the electron density, with the Laplacian ($\nabla^2 \rho$) being a second-order term, resulting in functionals that are also dependent on the kinetic energy density. In general, they are more accurate than LDA and GGA, especially when predicting properties like reaction barriers or phase transitions. Furthermore, they remain computationally less demanding than hybrid functionals discussed next, hence they remain a favourable choice for large systems. A popular functional from this family is TPSS (Tao-Perdew-Starovero-Scuseria) [145].

3.5.4 Hybrid Functionals

The fourth rung of Jacob's ladder is reserved for the hybrid functionals. Hybrid functionals are a type of exchange-correlation functionals, which incorporate a mixture of traditional DFT and exact (HF) exchange [146]. This approach helps to overcome some limitations of the pure DFT, especially for the systems where electron-electron interactions cannot be fully captured by local and semi-local approximations. To better understand the concept of hybrid functionals, it is useful to split them into their components:

- Pure DFT functionals, mentioned previously, rely on approximations that describe the exchange-correlation energy based on the electron density and sometimes its gradient.

- HF theory is capable of providing the exact exchange from the wavefunction, allowing for accurate capture of the electron repulsion effects; however, it tends to overestimate the correlation energy.

Now, by combining the two theories and including a fraction of the exact HF exchange with the DFT exchange-correlation function a vast improvement to many chemical and material properties can be achieved. In general, the exchange-correlation energy of a

hybrid functional can be represented as:

$$E_{XC}^{\text{hybrid}} = aE_X^{\text{HF}} + (1-a)E_X^{\text{DFT}} + E_C^{\text{DFT}} \tag{3.9}$$

where E_X^{HF} is the exact exchange energy obtained from the HF theory, E_X^{DFT} is the DFT exchange, and E_C^{DFT} is the DFT correlation. a is the mixing parameter obtained from fitting to the experimental data and is often between 0.2 and 0.25. Due to this empirical parametrisation, hybrid DFT calculations cannot be formally called *ab initio* as they require prior knowledge from experiments. Unfortunately, with the improved accuracy, the computational cost increases substantially as HF exchange calculations scale as N^4, where N is the measure of the system size, resulting in a significant bottleneck when running hybrid DFT calculations. Nonetheless, these functionals offer a perfect middle ground between accuracy and efficiency, especially for small to medium-sized systems, without the need for more sophisticated approaches. One of the most widely used hybrid functionals is B3LYP (Becke (3 parameter) – Lee – Yang – Parr), which includes 20% of exact HF exchange [147–149].

A sub-group of hybrid functionals are the so-called range-separated hybrid (RSH) functionals, which partition the electron-electron interaction into short-range and long-range components by applying HF exchange in one part of the range and DFT exchange in the other [150]. They offer a further increased accuracy for systems with significant charge-transfer character, predict significantly better band gaps for semiconductors and insulators, and are especially accurate for systems that are held by relatively weak vdW interactions. An example of such a functional is ωB97X-D [151, 152].

3.5.5 Double-Hybrid Functionals

On the final rung of Jacob's ladder, we have Double Hybrid functionals, which go further beyond hybrids and combine DFT exchange-correlation with exact HF exchange and a portion of second-order perturbative correlation (MP2) [153, 154]. This approach brings them close in accuracy to the wave-function-based methods; however, due to MP2 scalability as N^5, they are very computationally demanding, thus limiting their

application to medium-sized systems at most. The most widely recognised double-hybrid functional, B2PLYP, was introduced in 2007 by Stefan Grimme and Frank Neese [154].

3.6 Basis Sets

All *ab initio* methods try to solve the Schrödinger equation without fitting the parameters to experimental data. One of the approximations essential to all *ab initio* and DFT methods is the introduction of the basis set, being either plane-wave, wavelet or atomic orbital (AO) type, with the choice of basis set depending on the nature of the problem at hand. An introduction of a basis set allows to expand an unknown function, such as a molecular orbital, and obtain a tractable solution to the Schrödinger equation by limiting the calculation to a finite set of known functions. However, this method introduces its own problems as to expand an orbital in a complete basis set, one would have to use an infinite number of functions, making it a computationally impossible task. For the work presented in this Thesis, only AO basis sets were used, so the following discussion will be focused on that particular type of basis set.

There are two main types of AO, namely Slater Type Orbitals (STO) and Gaussian Type Orbitals (GTO). While STO tend to mimic the behaviour of an actual atomic orbital and exhibit the correct exponential near the nucleus, they are not commonly used in DFT due to the complexity of integrals involving STO. On the other hand, GTO fails to describe the correct behaviour near the nucleus and requires multiple functions to be used per orbital. However, as they decay quickly with the distance from the nucleus, they are very efficient for molecular calculations, making them particularly popular in molecular quantum chemistry. As a result, the increased number of GTO basis functions is easily compensated by the ease with which the required integrals can be calculated.

It is important to discuss the hierarchy of Gaussian Basis Sets, as the most important factor here is the number of basis functions to be used. The smallest possible number of functions is called a minimal basis set, with only enough functions employed

to contain all the electrons of the neutral atoms [155]. While this type of basis set is very cheap computationally, the obtained results are far from accurate, hence this type of basis set should be avoided at all costs. A set-up from a minimal basis set, is the so-called Split-Valence Basis Sets [156], which use multiple functions for valence electrons, thus increasing the flexibility and accuracy. An example is TZV [157], a valence triple-zeta basis set, which means that it contains three times as many functions as the minimum basis set. It is important to note, that with increasing basis set size, the calculation time increases drastically as well which is represented in Table 3.1.

Basis Set	Number of basis functions	SCF time [s]	Energy [E_h]
def2-SVP	246	10.974	-538.852
def2-TZVP	494	30.377	-539.429
def2-QZVP	1098	123.866	-539.464

Table 3.1: Comparison of SCF time and total energy for single-point calculations on the anthracene dimer using the B3LYP functional with different basis sets. While absolute DFT energies are not physically meaningful, differences between them can provide useful insights into basis set convergence.

However, as mentioned previously, due to the computational restraints and the finite size of the basis set, a few important limitations must be considered. First, the Basis Set Superposition Error (BSSE) must be accounted for. If the basis set is too small and the molecule of interest consists of two fragments, e.g., in a weakly interacting complex, they might use each other's basis functions, resulting in overestimated binding energies. The magnitude of the BSSE correction when using different basis sets is shown in Table 3.2. Next, as the basis set increases and more functions are added, the calculations approach "the basis set limit", where increasing the basis set size further provides minimal improvement in accuracy.

Basis Set	ΔE [kcal/mol]	ΔE_{BSSE} [kcal/mol]
def2-SVP	11.56	-3.18
def2-TZVP	10.18	-0.69
def2-QZVP	9.89	-0.23

Table 3.2: Binding energy (ΔE) and magnitude of BSSE correction (ΔE_{BSSE}) in kcal/mol for the anthracene dimer calculated with the B3LYP functional and various basis sets. The values highlight the BSSE and its reduction with increasing basis set quality.

In summary, while the basis set plays a crucial role in accuracy, efficiency and feasibility for electronic structure calculations, the choice of basis set is often determined by the computational resources;, hence achieving a balance between basis set size and computational cost is essential, especially for larger systems.

3.7   Solvent Model in DFT Calculations

In quantum-chemical calculations, it is often necessary to account for the effect of the surrounding solvent, as solvation plays a key role in stabilising polar and charged species. Solvent models can generally be divided into two categories: explicit models, where individual solvent molecules are included in the calculation, and implicit models, where the solvent is represented as a homogeneous polarizable medium. Explicit approaches provide a detailed description of solute–solvent interactions but are computationally expensive at the DFT level, since each additional water molecule contributes a large number of electrons, increasing the basis set size and the cost of self-consistent-field calculations. Moreover, adequate sampling of solvent configurations would require many snapshots, making explicit solvation practically infeasible in DFT studies.

To overcome this, continuum solvent models such as PCM (Polarizable Continuum Model) [158], COSMO (COnductor-like Screening MOdel) [159], and CPCM (Conductor-like PCM) [160] are widely used. In these models, the solute is placed inside a cavity defined by overlapping atomic spheres, and the polarisation of the surrounding dielectric medium is computed self-consistently with the electronic density of the solute. This provides a computationally efficient way to capture macroscopic

solvent effects while avoiding the need to model individual solvent molecules.

In the present work, the CPCM model was employed with water as the dielectric medium ($\varepsilon \approx 78.4$). CPCM stabilises polar and charged species and effectively reproduces the macroscopic electrostatic response of water on orbital energies, excitation energies, and binding affinities. While it does not capture explicit hydrogen bonding, ion pairing, or dynamic solvent fluctuations, it provides a physically reasonable approximation of solvation at the quantum-chemical level.

A useful parallel can be drawn between CPCM in DFT and the TIP3P model employed in MD simulations. Both approaches account for solvent polarity and stabilisation of charged or polar species, albeit at different levels of detail. TIP3P captures microscopic solute–solvent interactions, including hydrogen bonding, diffusion, and local structuring, whereas CPCM provides macroscopic dielectric screening without atomic resolution. Despite these differences, CPCM often reproduces overall stabilisation trends that are consistent with the average electrostatic environment observed in TIP3P simulations. In practice, the use of CPCM in DFT, alongside TIP3P in MD, provides a complementary picture of solvation, where the continuum model captures the bulk dielectric response and the explicit MD model resolves local, dynamic solvent interactions.

3.8 DFT and *ab initio* Calculations for Molecular Parametrisation

DFT and *ab initio* calculations are irreplaceable when parametrising new molecules for FF-based simulations. The calculations typically involve deriving parameters such as bond lengths, angles, charges and torsions, which will allow accurate description of the energetics and geometry of molecules in classical MD simulations. Typically, this involves multiple steps:

- Performing geometry optimization to obtain bond lengths, angles, and the overall structure of the molecule;

- Vibrational frequency calculation, which allows the extraction of harmonic frequencies to refine bond and angle force constants;

- Torsional potential scans to calculate energy as a function of torsion angle to derive torsion parameters;

- Charge calculations to derive atomic charges, which will allow the reproduction of the electrostatic potential of a molecule;

- Finally, the obtained data has to be validated by comparing the force field form with high-level quantum mechanical/experimental results.

Typically, DFT methods are used for all bonded interactions, while MP2 is used for non-bonded interaction energies and for systems where electron correlation is significant. Once all of the parameters are obtained, they are fitted to a specific form used by the target FF. This involves fitting bond lengths, angles and torsion energies to the functional form of the chosen FF.

3.9   Atomic Partial Charges

In quantum mechanical calculations, the predominant methods for determining atomic charges include Mulliken Population Analysis, Natural Population Analysis (NPA), and RESP (Restrained Electrostatic Potential) fitting.

Mulliken Population Analysis computes atomic charges by assessing the overlap of atomic orbitals within the molecular wavefunction [161]. Although it is simple and popular, its accuracy can be impacted by the choice of basis set, leading to inconsistent charge distributions.

NPA employs the wavefunction and natural orbitals to derive atomic charges [162]. It is typically regarded as more reliable than Mulliken analysis, offering a more accurate and physically meaningful charge distribution.

Nevertheless, RESP fitting has emerged as the most widely used method, especially for force field development and molecular simulations [163]. RESP calculates atomic charges by aligning the electrostatic potential created by the molecular system with a

set of point charges. This approach is favoured as it delivers a more precise depiction of the electrostatic environment surrounding atoms, which is essential for applications like molecular dynamics simulations that require accurate charge distributions.

3.10 DFT Problems and Limitations

While DFT is considered a robust theory, and failures in the form of completely erroneous results are relatively rare, even when applied to complex molecules or exotic systems, there are still some areas where the current functionals are known to perform poorly:

- The weak interactions, such as dispersion forces, arising from electron correlation in wavefunction methods are the biggest shortcoming of standard DFT methods [164]. The majority of the functionals display a fully repulsive interaction between rare gas atoms, and those that predict a weak stabilising interaction, underestimate the effect and fail to have the correct R^{-6} long-distance behaviour [165, 166]. S. Grimme has proposed to include dispersion by adding an empirical attraction term, which generally improves the performance, but is an *ad hoc* repair [167]. The earliest models included simply an R^{-6} energy term for each atom pair, with an atom-dependent C_6 parameter. Nowadays, the method has been refined to include higher-order terms and better describe the medium-range dispersion. Furthermore, Becke and Johnson have proposed a physics-inspired dispersion mode, where the C_6 parameter is written as a function of the atomic polarizabilities, thus introducing an explicit dependence on the actual electronic structure of the system [166]. As a result, the dispersion forces are no longer a significant weakness of the theory.

- For chemically bonded systems, similar to H_2, often results in incorrect and underestimated dissociation energies with an error of around 200 kJ/mol [168, 169]. This is usually a problem for functionals which do not include exact exchange, however, since HF theory overestimates activation barriers, hybrid methods typ-

ically give reasonable results.

- The main drawback of DFT is the fact that it is applied to a static system. To perform chemically accurate dynamic simulations, we would have to resort to *ab initio* MD simulations, where instead of FF, the interactions between system components are calculated on the fly, often using DFT [170, 171]. Consequently, the high computational cost of these simulations restricts them to timescales on the order of picoseconds (ps).

The concepts presented in this chapter were used throughout this thesis to obtain atomic-level insight into the invisible processes and interactions happening between silica nanostructures and R6G. Since the nanoparticles of interest are beyond what can be resolved using optical microscope, the only way was to resort to computer simulations. In general, MD allowed to gain insight into the R6G-NP interactions which confirmed the experimental observations. Nonetheless, since R6G is a non-standard molecule in all FFs, its parameters had to be custom-made. Therefore, DFT calculations at various levels of theory were used to cross-validate the obtained MD results. While *ab initio* MD has massive potential in this field due to much more accurate DFT calculations involved, classical force-field driven MD simulations were able to successfully identify the required dye-NP interactions.

Chapter 4

Basic Photophysics

"I am almost inclined to coin a word, and call the appearance fluorescence, from fluor-spar [i.e., fluorite], as the analogous term opalescence is derived from the name of a mineral."

By Sir George Gabriel Stokes, from the "On the Change of Refrangibility of Light" (1852)

4.1   Origins of Fluorescence

Spectroscopy is the study of the interaction between matter and electromagnetic radiation. When light or other forms of radiation are absorbed or emitted by molecules, they provide valuable information about the molecular structure and behaviour. One of the key phenomena explored in spectroscopy is fluorescence, where a molecule absorbs light at one wavelength and then, in the case of a single-photon process, re-emits it at a longer wavelength, usually after undergoing internal relaxation processes.

Fluorescence, in particular, occurs when molecules absorb photons of specific wavelengths, exciting electrons to a higher energy state. The excess energy is then released through various processes, including non-radiative and radiative pathways. A Jablon-

ski diagram commonly represents these relaxation processes, which provides a visual overview of the different states involved in fluorescence emission.
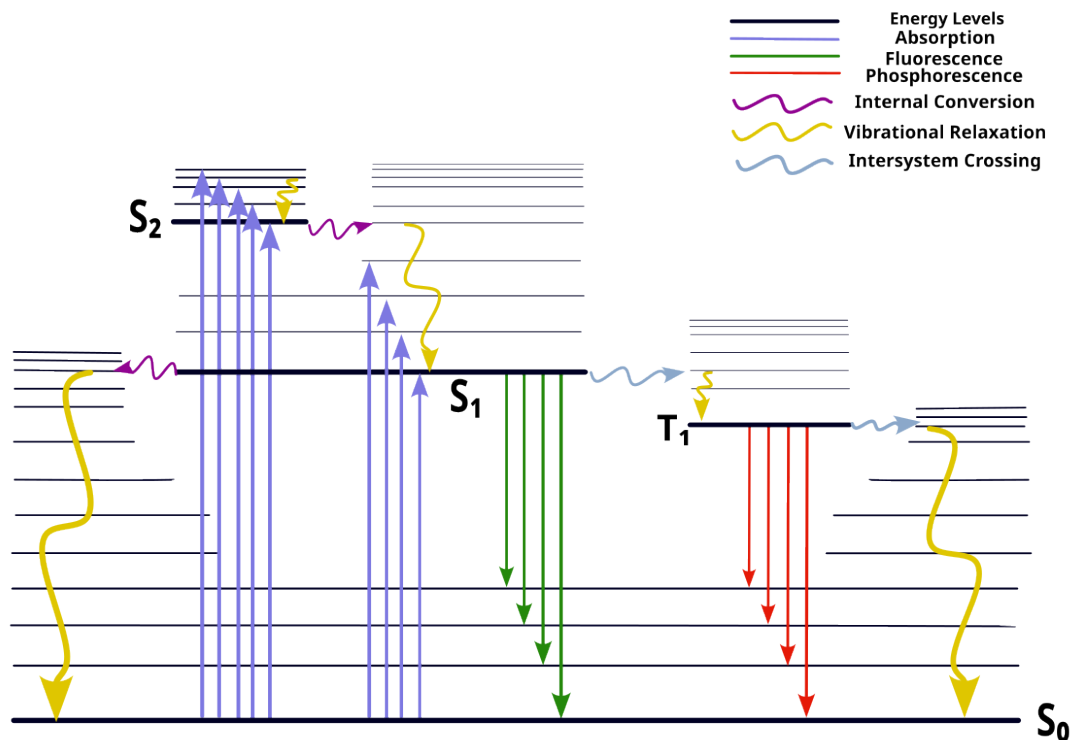
Figure 4.1: Illustration of the Jablonski diagram showing the possible radiative and non-radiative transitions.

When an electron absorbs a photon with energy matching the gap between the ground state (S_0) and an excited electronic state $(S_1$ or $S_2)$, it first relaxes vibrationally within the excited state, then undergoes internal conversion to the lowest vibrational level of the first excited state (S_1). Vibrational relaxation is a rapid non-radiative process in which the molecule loses excess energy to the surrounding solvent or medium, causing the molecule to transition to the lowest vibrational level of the excited state [172]. From this point, the electron can either emit a photon and return to the ground state, resulting in fluorescence, undergo a non-radiative internal conversion, or transition to a triplet state via intersystem crossing. From the triplet state, it may relax back to the ground state through either phosphorescence or further non-radiative decay. In contrast to fluorescence, phosphorescence involves spin-forbidden transitions, such

as from a triplet excited state to the singlet ground state, resulting in much longer-lived excited states and extended emission lifetimes. However, triplet states can also deactivate non-radiatively, through processes such as vibrational relaxation or collisional quenching, which may compete with or even suppress phosphorescence depending on the environment.

The transition from a ground state to an excited electronic state occurs on the timescale of femtoseconds (10^{-15} s), which is virtually instantaneous when compared with the motion of atomic nuclei. This rapid electronic transition is governed by the Franck–Condon principle, which describes the intensity distribution of vibrionic transitions—transitions that involve both electronic and vibrational states. According to this principle, electronic transitions are assumed to occur without a significant change in the positions of the nuclei, since the nuclei cannot respond quickly enough to the fast electronic transition.

This idea is rooted in the BOA, which separates electronic and nuclear motions due to the large difference in their masses. As a result, the electronic transition is represented as a vertical line on a potential energy diagram, with no change in nuclear coordinates during the transition. The probability of a transition between different vibrational states is determined by the Franck-Condon factor, which quantifies the overlap between the vibrational wavefunctions of the initial and final electronic states.

This factor is mathematically defined as:

$$F_{i,f} = |\langle \psi_f | \psi_i \rangle|^2 \tag{4.1}$$

where ψ_i and ψ_f are the vibrational wavefunctions of the initial and final states, respectively. A larger overlap between these wavefunctions corresponds to a higher Franck–Condon factor, resulting in a more intense transition. In practice, the most intense vibrionic transition usually occurs from the vibrational ground state of the lower electronic state to the vibrational state of the excited electronic state that is vertically above it on the potential energy surface.

After excitation, the molecule typically relaxes to the lowest vibrational level of the

excited electronic state via vibrational relaxation (a non-radiative decay process). Upon returning to the ground state through fluorescence, phosphorescence, or non-radiative decay, the transition typically follows a similar vertical path, but from the lowest vibrational state of the excited state. This results in a redshifted emission spectrum relative to the absorption spectrum, a phenomenon known as the Stokes shift. According to the Kasha rule, the radiative transition typically occurs from the lowest vibrational level of the first excited electronic state (S_1) to the ground state (S_0), regardless of the higher excited state (S_n, with $n \geq 2$) initially populated [173]. Nevertheless, there are known exceptions to this rule, referred to as anti-Kasha behaviour, where emission occurs from higher excited states rather than the lowest singlet excited state [174].

If the potential energy curves of the ground and excited states are similar in shape, the absorption and emission spectra often appear as approximate mirror images of each other, a phenomenon known as the mirror image rule [175]. This is due to the similar spacing of vibrational levels in the ground and excited states.

The redshift in emission is primarily a result of non-radiative energy loss in the excited state, leading to fluorescence photons that have lower energy than the incident excitation photons. When a fluorophore is part of a larger molecule, its dipole moment changes upon excitation to an excited electronic state. The surrounding solvent molecules, however, cannot adjust rapidly, and this adjustment happens only after vibrational relaxation because solvent molecules need to adjust to the new dipole moment of the excited molecule [175]. This reorganisation contributes not only to the Stokes shift but can also influence the fluorescence lifetime.

4.2   Quantum Yield

Fluorescence quantum yield (Q) is a quantity describing the ratio of photons emitted by the fluorophore to the number of absorbed photons and mathematically is described using the following expression:

$$Q = \frac{k_r}{k_r + k_{nr}} \tag{4.2}$$

where k_r is the radiative decay rate and k_{nr} is the non-radiative decay rate. In the case when the radiative decay rate is significantly larger than the non-radiative rate, the quantum yield Q can approach unity; however, it can never exceed one due to energy losses in the system.

4.3 Fluorescence Lifetime

The fluorescence lifetime is a parameter describing the average time the fluorophore stays in an excited energy state before emitting a photon and returning to the ground state. The average time must be taken, as the emission of a photon is a stochastic process and the time that the individual molecules stay in the excited state may vary. Mathematically, fluorescence lifetime can be described as an inverse sum of the non-radiative and radiative decay rates [176]:

$$\tau_f = \frac{1}{k_r + k_{nr}} \qquad (4.3)$$

In the system, where only the radiative decays are present and the non-radiative decay rate is 0, then the quantum yield will be equal to unity. This quantity is called the natural fluorescence lifetime and is described using the following mathematical expression:

$$\tau_n = \frac{1}{k_r} \qquad (4.4)$$

When a population of fluorophores is excited using a δ-function at $t = 0$, then some molecules $[M^*]$, will be promoted to the S_1 excited state. The decay of this population from the excited to the ground state due to the fluorescence emission is described using the following rate equation [176]:

$$\frac{d[M^*]}{dt} = -(k_r + k_{nr})[M^*] = -\frac{[M^*]}{\tau} \qquad (4.5)$$

A general solution for this differential equation is in a form of simple exponential decay

function:

$$[M^*](t) = [M^*](0) \exp\left(-\frac{t}{\tau}\right) \tag{4.6}$$

Since fluorescence intensity is proportional to the number of excited molecules, the equation can be re-written in the following form:

$$I(t) = I(0) \exp\left(-\frac{t}{\tau}\right) \tag{4.7}$$

In the case where multiple non-interacting fluorophores are present, the expression can be expanded by linearly summing over all species, where each component represents a separate excited state:

$$I(t) = \sum_{i=1}^{n} I_i(0) \exp\left(-\frac{t}{\tau_i}\right) \tag{4.8}$$

In practice, however, a δ-pulse excitation is not possible as there is a delay arising from the instrumental response time needed to detect the fluorescence decays, which is often comparable with the measured lifetimes. Consequently, the experimentally observed decay curves represent a convolution of the ideal exponential decay with the instrumental response function (IRF), encompassing contributions from the laser pulse profile, detector response, and associated electronic timing effects. A measurement of both of these and extraction of the undistorted decay function will be described in Chapter 5.

4.4 Fluorescence Quenching

Quenching is a process which reduces the fluorescence quantum yield of a fluorophore, thus reducing the overall intensity. Fluorescence quenching can be divided into two large subcategories, both involving close interactions between the fluorophore and an external molecule, referred to as quencher: static quenching and dynamic quenching. In static quenching, which does not depend on diffusion or molecular collisions, the intensity reduction is often caused due to the fluorophore in the ground state forming nonfluorescent complexes with the quencher. As the static quenching involves the

interaction of external molecules with the fluorophore in the ground state, the excited state is unaffected and so is the resulting fluorescence lifetime.

The second type of quenching is dynamic quenching, often referred to as collisional quenching, which occurs when a fluorophore in the excited state collides with a quencher. As a result of this collision, the energy carried by the fluorophore is transferred to the quencher and released as excess heat to the environment [177]. The fluorescence lifetime decreases in the presence of dynamic quenching, as the excited-state population is depleted more rapidly due to collisional encounters with quenchers.

4.5   Fluorescence Anisotropy

The principle of fluorescence anisotropy is based on a condition, which states that for light absorption, the electric component, or a vector of the electromagnetic wave, must be parallel or close to parallel to the transition moment of the molecule [175]. When in solution, the orientations of the aforementioned transition dipoles are completely random. Therefore, if such a system is excited using, for example, linearly polarised light, only the molecules whose transition dipole moments are oriented similarly to the direction of polarisation will be excited. This will result in a highly anisotropic distribution of molecules, which is often called photoselection and is the underlying principle of fluorescence anisotropy. Following this, the excited fluorophore population will fluoresce, while Brownian motion disrupts the original arrangement of these molecules. The rate of fluorophore rotation in the solution impacts the degree of polarisation of the emitted fluorescence relative to the excitation source. When rotational diffusion is slower, a greater portion of the emitted light maintains its initial polarisation. Conversely, when rotational diffusion is faster, the emitted light becomes increasingly depolarised.

In a typical anisotropy measurement, a polarizer is placed in both emission and excitation arms, and the polarization of the emitted fluorescence is recorded. Typically, the excitation light is polarized along the vertical axis, and the emission light is collected in both vertical and horizontal axes. Both decays $I_{VV}(t)$ and $I_{VH}(t)$ are then combined

to form the fluorescence anisotropy function $R(t)$, defined as:

$$R(t) = \frac{I_{VV}(t) - I_{VH}(t)}{I_{VV}(t) + 2I_{VH}(t)} \tag{4.9}$$

In the simplest case of spherical and freely rotating fluorophores, the anisotropy decay follows a simple exponential model:

$$R(t) = R_0 \exp\left(-\frac{t}{\phi_R}\right) \tag{4.10}$$

Where ϕ_R is the characteristic decay constant, usually called rotational correlation time, and R_0 is the initial anisotropy, which has a maximum theoretical value of 0.4 for a single-photon excitation. A value of 0.4 can be obtained when both excitation and emission dipoles are parallel according to the following expression:

$$R_0 = \frac{2}{5}\left(\frac{3\cos^2\beta - 1}{2}\right) \tag{4.11}$$

where β is the angle between the excitation and emission dipoles.

The rotational correlation time, ϕ_R, connects to the average molecular rotational diffusion coefficient, D. In the simplest scenario involving a spherical particle, it also relates to the hydrodynamic volume of the fluorophore, V, and the local viscosity, η. This relationship can be expressed through the following equation:

$$\phi_R = \frac{1}{6D} = \frac{V\eta}{Tk_B} \tag{4.12}$$

where T is the temperature and k_B is the Boltzmann constant. Time-resolved fluorescence anisotropy is widely utilised to study molecular rotation, offering insights into molecular size and interactions in solution. It is especially valuable for examining protein-ligand binding, membrane dynamics, and conformational changes in biomolecules [178]. Furthermore, it acts as a potent tool in nanoparticle metrology, facilitating the estimation of particle size based on rotational diffusion rates [35, 39].

4.6   Rhodamine Dyes: Monomers and Dimers

Rhodamine dyes such as R6G and RB owe their strong fluorescence to the rigid, conjugated xanthene core that dominates their electronic structure. This consists of three fused aromatic rings with alternating single and double bonds, which creates an extended π-electron system capable of efficient π–π transitions in the visible range. Because these properties underpin their use throughout this thesis as the primary fluorophores for probing interactions in silicate solutions, it is essential to consider the molecular origin of their strong fluorescence first.

4.6.1   HOMO-LUMO Transitions and Orbital Basis of Fluorescence

At the molecular orbital level, the fluorescence of R6G and RB originates from the lowest electronic transition between the highest occupied molecular orbital (HOMO) and the lowest unoccupied molecular orbital (LUMO). Both orbitals are localised on the xanthene chromophore and the amino substituents, ensuring strong orbital overlap and a large transition dipole moment [179]. This spatial arrangement explains the high intensity of the $S_0 \rightarrow S_1$ transition and the strong fluorescence efficiency observed for the monomers.
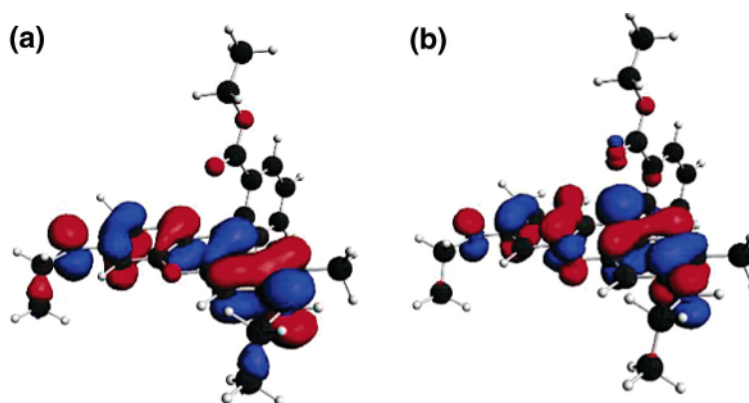
Figure 4.2: The HOMO (a) and LUMO (b) of R6G involved in the $S_0 \rightarrow S_1$ transition. Reproduced from [179] with permission from the American Chemical Society.

Theoretical studies support this picture [179]. Using the BP86 functional, the lowest

excitation energy of R6G was calculated to be $2.62\,\text{eV}$ ($474\,\text{nm}$) with an oscillator strength of 0.6, corresponding to the HOMO–LUMO transition [179]. Experimentally, R6G in aqueous solution absorbs most strongly at $530\,\text{nm}$ ($2.33\,\text{eV}$), with a vibronic shoulder around $470\,\text{nm}$. The difference between theory and experiment ($\approx 0.3\,\text{eV}$) can largely be attributed to solvent effects. When solvent screening was included via the COSMO model, the calculated excitation energy shifted to $2.44\,\text{eV}$ ($508\,\text{nm}$), in much better agreement with experiment. Importantly, the HOMO and LUMO were both found to be localised on the xanthene core and ethylamino substituents, consistent with the high fluorescence quantum yield, as the strong orbital overlap ensures a large transition dipole moment.

R6G and RB fluoresce in their monomeric forms because their structures contain a rigid, conjugated xanthene core. Optical excitation promotes an electron from a bonding π orbital (HOMO) to an antibonding π^* orbital (LUMO), i.e. a π–π^* transition, and the extended conjugation lowers the HOMO–LUMO gap into the visible region, giving the dyes their bright colours. Fluorescence is efficient because the transition carries a large dipole moment, the Franck–Condon overlap between ground- and excited-state vibrational wavefunctions is good, and spin–orbit coupling is weak in these light-atom organic molecules, minimising intersystem crossing to triplet states. Together, these factors explain why monomeric Rhodamine dyes absorb and emit strongly in the visible range.

4.6.2 Dimer Formation and Types of Aggregates

While R6G and RB fluoresce strongly in their monomeric forms due to efficient π–π^* transitions within the conjugated xanthene core, their behaviour changes when the dyes come into close contact at high concentration or under conditions that favour aggregation. In these situations, the molecules can associate into two principal geometries. H-type dimers arise from a face-to-face, parallel stacking of the chromophores, which produces a characteristic blue-shifted absorption band relative to the monomer. J-type dimers, by contrast, form through a head-to-tail alignment of transition dipoles, giving rise to red-shifted absorption and emission features. Although both configurations are

theoretically possible, J-aggregates are energetically less stable in solution and generally require stabilisation by an external potential, for example intercalation into layered hosts or confinement within ordered channels [180]. As no such conditions are present in the current system, only H-type aggregates are observed.

4.6.3 Influence of Silicate Solutions on Dimerisation

The likelihood of dimer formation also depends on the chemical form of the dye. R6G remains cationic under alkaline conditions and is repelled by the negatively charged silica surfaces. This electrostatic exclusion enhances dye–dye contacts between the hydrophobic aromatic cores, promoting π–π stacking and stabilising H-type dimers. RB, on the other hand, contains a carboxyl substituent and can adopt several protolytic forms [181]. At high pH it tends to exist in a zwitterionic lactone structure that is more neutral and hydrophilic, reducing the hydrophobic driving force for π–π stacking. Consequently, under silicate conditions at pH 11–12, R6G readily forms dimers, whereas RB remains predominantly monomeric.

4.6.4 Non-Fluorescence of H-Type Dimers

Because R6G readily forms H-type aggregates under alkaline silicate conditions, it is important to consider the photophysical consequences of such aggregation, in particular, why these dimers, despite their strong absorption, fail to fluoresce.

The absence of fluorescence from H-type dimers can be understood by considering how the excited states of two closely stacked chromophores interact. In an isolated monomer, excitation promotes the molecule from the ground state (S_0) to the first excited state (S_1), which possesses a finite transition dipole and therefore allows radiative decay. When two identical chromophores are brought into close contact, their excited states couple and the excitation becomes delocalised across both molecules. This delocalisation produces two exciton states through Davydov splitting: a symmetric (E^+) and an antisymmetric (E^-) combination of the monomer excitations [182].
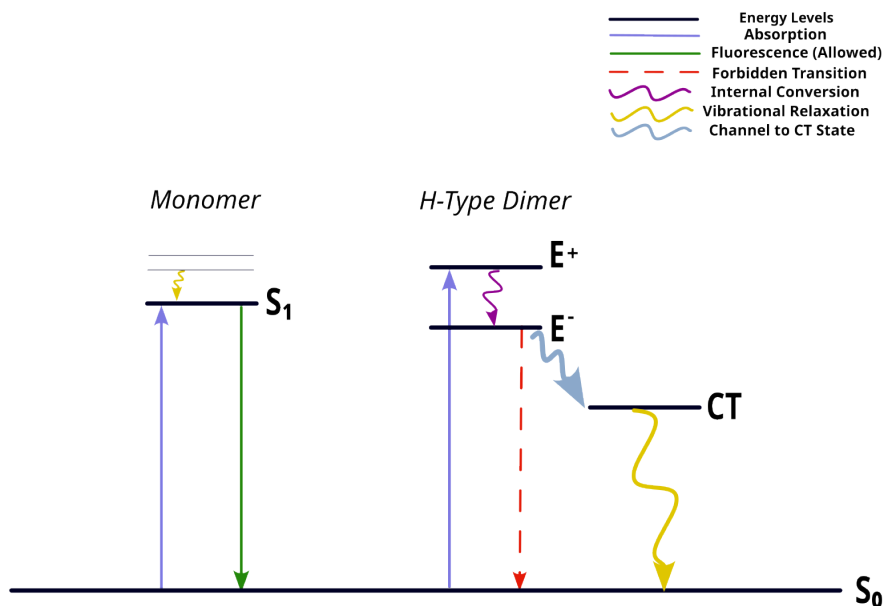
Figure 4.3: Energy-level diagram comparing radiative and non-radiative pathways in Rhodamine monomers and H-type dimers. Exciton splitting in the dimer produces allowed (E^+) and forbidden (E^-) states, with relaxation channels leading predominantly to non-fluorescent outcomes.

The E^+ state carries strong oscillator strength because the transition dipoles add constructively, giving rise to the intense blue-shifted absorption characteristic of H-aggregates. The E^- state, by contrast, has transition dipoles that cancel, making it optically forbidden. Following Kasha's rule, excitation energy absorbed into E^+ relaxes rapidly and non-radiatively into the lower-lying E^- state.

In addition, the close π–π stacking permits orbital overlap between monomers, which can generate intermolecular charge-transfer (CT) states [183]. These CT states have weak electronic dipoles due to poor orbital overlap and also unfavourable vibrational overlap with the ground state, leading to negligible Franck–Condon factors. Both the dark exciton (E^-) and CT states therefore lack efficient radiative pathways.

The combined effect is that excitation energy in H-type aggregates is funnelled into states from which radiative decay is strongly suppressed. Instead, relaxation proceeds predominantly by non-radiative channels, explaining why H-type dimers, despite their strong absorption, are essentially non-fluorescent.

Chapter 5

Experimental Procedures

Fluorescence is a multi-parameter phenomenon that can be described using several parameters, such as emission and excitation wavelengths, lifetime, polarisation, and quantum yield, among others. The objective is to recover as many of these parameters as possible. However, in practice, it is not a straightforward task, as multiple instruments are needed to measure different fluorescence parameters. In general, the measurements can be classified into two categories: steady-state and time-resolved. This Chapter discusses the basic fluorescence measurements and a variety of techniques presented in this thesis.

5.1   Absorbance

The first measurement that is performed when starting a series of fluorescence measurements is the acquisition of the absorbance spectrum. Strictly speaking, absorbance is not a fluorescence measurement, but a critical complement to any fluorescence measurements, as it allows identification of absorption bands for the most efficient excitation [184]. This can be done by comparing the intensity of light passing through the sample, with a reference sample. The ratio of the two intensities is referred to as

transmittance:

$$T(\lambda) = \frac{I(\lambda)}{I_0(\lambda)} \tag{5.1}$$

Now, the transmittance can be used to calculate the absorbance at each wavelength:

$$A(\lambda) = \log\frac{I_0(\lambda)}{I(\lambda)} = -\log T(\lambda) \tag{5.2}$$

Knowing the value for absorbance, the concentration of the measured substance can be calculated using the Beer-Lambert law:

$$A(\lambda) = \varepsilon(\lambda) \times l \times c \tag{5.3}$$

Here $\varepsilon(\lambda)$ is the molar extinction coefficient, l is the path length, and c is the concentration of the measured substance.

A schematic of a typical dual-compartment absorption spectrometer is shown in Figure 5.1. The spectrometer employed in this study is the Lambda 25 UV-Vis spectrometer manufactured by Perkin Elmer. This instrument is fitted with two lamps: a deuterium lamp (D) for UV excitation (190 – 330 nm) and a halogen lamp (H) (330 – 1100 nm), allowing for full coverage of the spectrometer's operational range. By utilising a set of mirrors (M) and a monochromator (Mono), the samples are gradually exposed to a range of wavelengths until the specified range has been fully covered. The reference signal (R) is measured alongside the sample (S) to adjust the measured signal for solvent and cuvette absorption. Finally, the resultant absorbance is determined as the difference between the signals recorded by the two detectors.
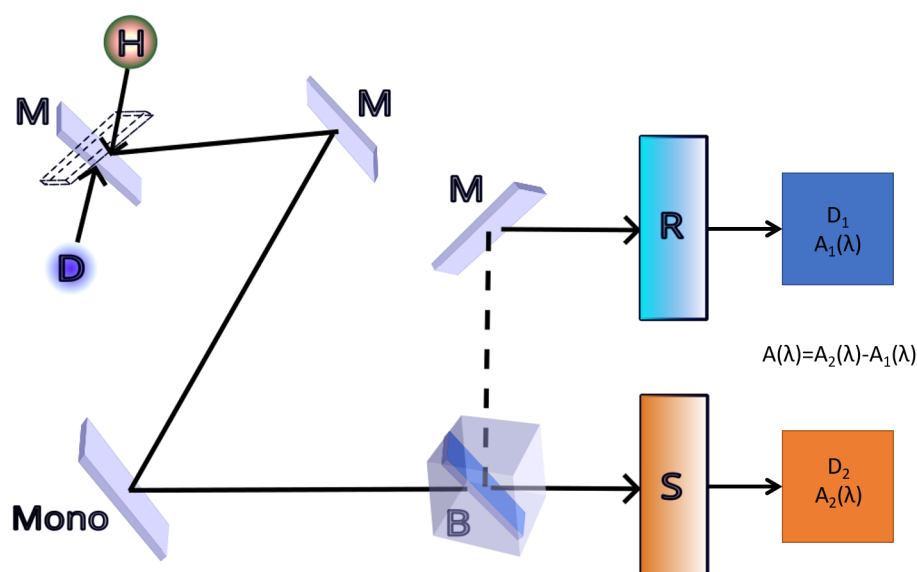
Figure 5.1: Schematic of a Perkin Elmer Lambda 25 spectrometer. The radiation generated by deuterium (D) (190 – 330 nm) and halogen (H) (330 – 1100 nm) lamps is guided by mirrors (M) to the monochromator (Mono) and then through the beam splitter (B) to reference (R) and measured (S) samples and finally to corresponding detectors (D1, D2).

5.2 Steady-State Measurements

In steady-state measurements, samples are illuminated by a continuous beam of light, thus allowing to measure the specimen's emission and excitation spectra. A spectrometer used for the work presented in this thesis is Fluorolog3 by HORIBA-IBH, with its schematic shown in Figure 5.2. Typically, a source of this continuous illumination is a Xenon arc lamp, due to its wide and almost linear spectrum ranging from ultraviolet to near-infrared [172, 175]. Next, the arc lamp-produced beam of light passes through the excitation monochromator, which allows for the filtering and selection of specific wavelengths to reach the sample.
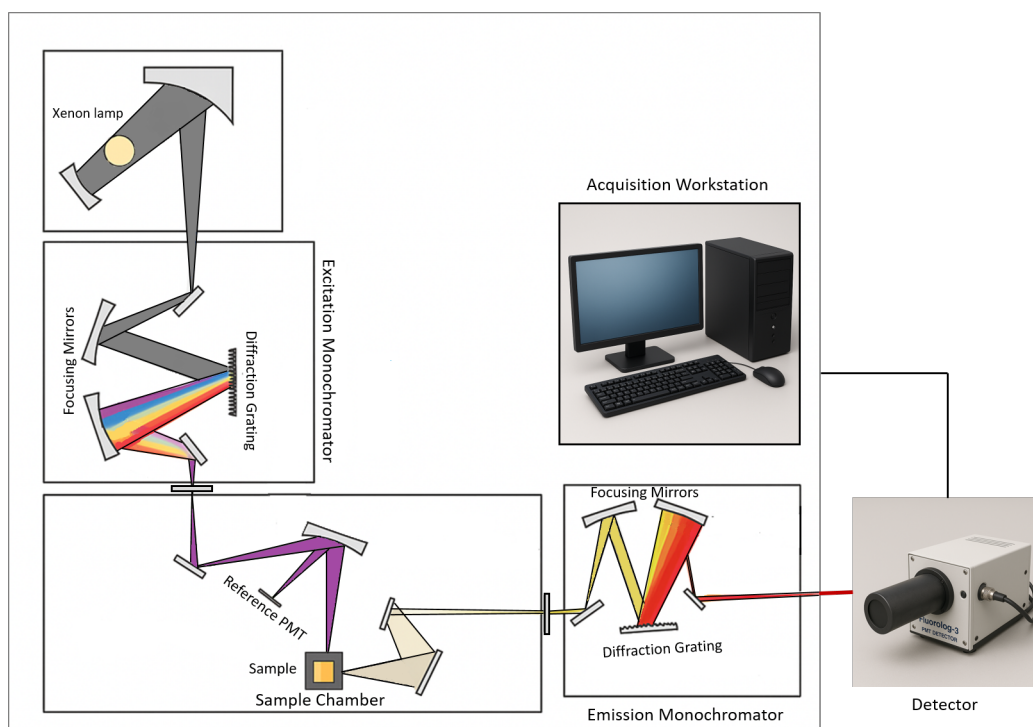
Figure 5.2: Schematic of a typical Steady-State Spectrometer.

To monitor the variations in the xenon lamp output and compensate for those if needed, a small fraction of the excitation light is diverted to the reference silicon photodiode. The emission from the sample is collected at a $90°$ angle to the excitation beam to minimize the detection of the excitation light and reflected light. Next, the emitted light passes through the second monochromator located in the emission arm, which selectively transmits the signal to the photomultiplier, which converts the photons to electrons via the principle of the photoelectric effect, which are then multiplied to provide a measurable electric current at the output.

To obtain the emission spectrum of the sample, the excitation monochromator is set to a wavelength which matches the absorption band identified during the UV-Vis measurements and using the monochromator in the emission arm, the fluorescence intensity is measured as a function of the emission wavelength. In the excitation, the emission wavelength is fixed, typically to cover the whole range of the emission wavelengths, and then the fluorescence intensity is measured as a function of the excitation wavelength.

In most cases, the excitation spectrum will be identical to the UV-Vis absorption, as long as the fluorophores obey Kasha's rule [173].

5.3   Time-Resolved Fluorescence Measurements

Time-resolved measurements allow for monitoring the emission of a sample as a function of time [175]. Broadly speaking, time-resolved techniques can be divided into two main groups: frequency-domain and time-domain. Frequency-domain, also known as phase-modulated measurements, are based on the harmonic modulation of excitation light at high frequency [175]. As this type of measurement is beyond the scope of this work, it will not be discussed further.

Time-domain measurements are performed by illuminating the sample with a pulse of light whose duration is significantly shorter than the sample's decay time. However, it is important to emphasise that the measured fluorescence decay does not represent the true decay of the sample as in practice the excitation pulse is significantly broader than the theoretical δ-function and the detector response is relatively slow. As a result, the recorded fluorescence intensity decay curve is convolved with the instrumental response function (IRF), and to recover the decay parameters a re-convolution must be performed:

$$F(t) = L(t) \otimes F_c(t) = \int_0^t L(t - t') \, F_c(t') \, dt' \tag{5.4}$$

In practice, the IRF $L(t)$ is obtained by measuring the scattering of the excitation beam. Once $L(t)$ is measured, it is re-convoluted with the assumed fluorescence impulse response $F_c(t)$ and compared with the measured decay function $F(t)$. Often the analysis of such data is performed using a nonlinear least-squares method and assessed using a statistical goodness of fit criterion, e.g. χ^2 test. The main difficulty of such analysis lies in the fact that it is highly dependent on the model used and is notoriously easy to over-parametrise the model. Typically, the simplest model satisfying the goodness of fit criterion is assumed as the correct model.

5.3.1 Time-Correlated Single Photon Counting

The commonly used technique for performing time-domain measurements is time-correlated single photon counting (TCSPC). To perform such measurements, a few components are needed:

1. A short pulse excitation source with optical pulses as short as 100 ps with a repetition rate ranging from 10 kHz to 1 MHz;

2. Typical components, found in all conventional spectrometers, such as monochromators, polarisers and focusing optics;

3. Timing electronics, such as time-to-amplitude converter (TAC);

4. A single-photon detector.

In a typical forward-mode working TCSPC spectrometer, the pulsed excitation source is used to excite the sample and simultaneously acts as a start signal in the measurement cycle. The fluorescence emission of the sample is filtered using a monochromator and detected at a 90° angle to separate it from the excitation beam. The excitation source's flash generates an electronic signal, serving as the start impulse for the TAC. When the TAC receives the start signal, it begins charging a capacitor until it gets the stop pulse from the detector or reaches the end of its cycle. The capacitor then discharges, producing an analogue output pulse whose amplitude corresponds to the time between the start and stop signals. This pulse is digitized and sent to a multichannel analyser (MCA), which records multiple signals to create a histogram of photon counts over time. A schematic of such setup is shown in Figure 5.3.
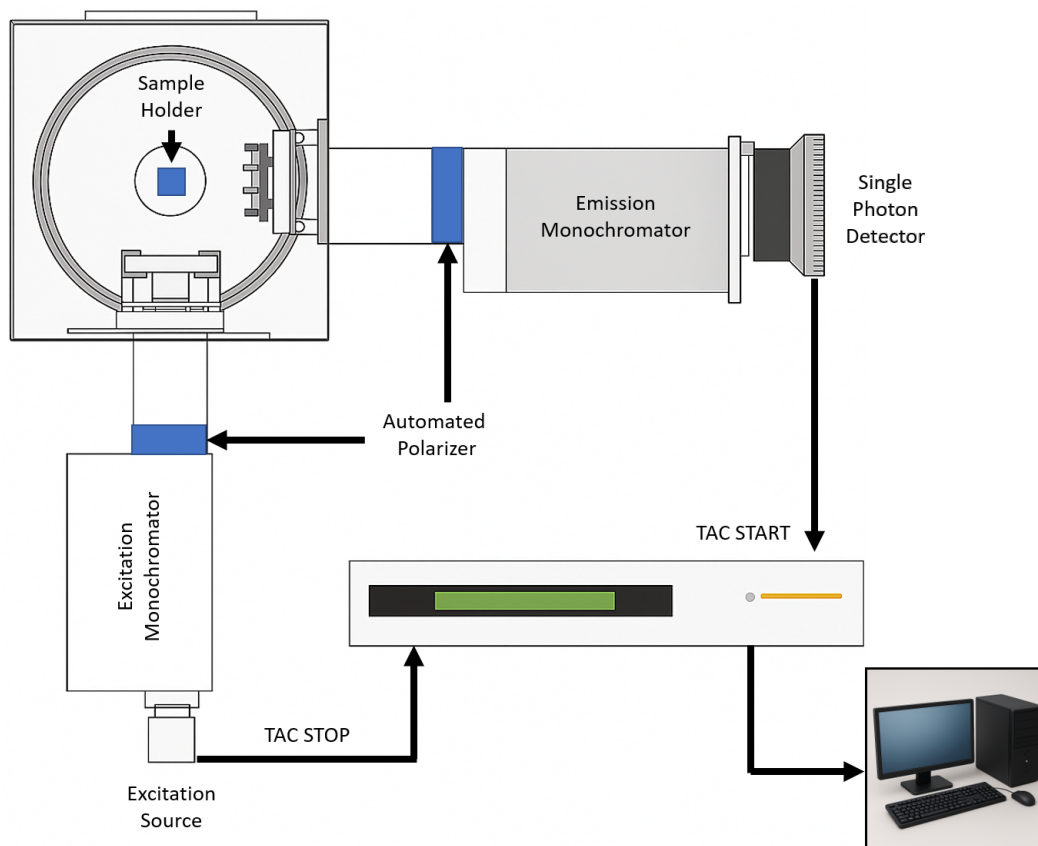
Figure 5.3: Schematic of a typical TCSPC setup working in reverse mode.

One unavoidable artefact present in all detectors, including TCSPC measurements, is photon pile-up [185, 186]. The pile-up effect occurs because a TCSPC device can detect only one photon per signal period. At high photon detection rates, only the first detected photon is recorded, while subsequent photons in the same cycle are ignored, leading to artificially shortened fluorescence lifetimes. Additionally, detectors have a "dead time" during which they recover from a previous detection, causing any photon arriving in this period to be lost. This effect distorts the histogram and shifts fluorescence decays to shorter times. To minimize pile-up, the photon count rate is typically kept below 1–2% of the laser repetition rate. Modern systems can detect multiple photons per cycle, but if the detection probability is too high, the TAC may continuously reset, leading to data loss. This issue can be mitigated by operating the

TAC in reverse mode, where the fluorescence photon generates the START signal, and the next excitation pulse serves as the STOP signal.

5.3.2   Fluorescence Decay Analysis

The TCSPC-obtained histograms, which are the measured fluorescence decays, can be used to perform reconvolution of equation 4.8. Reconvolution is an iterative process, in which the chosen exponential model is convolved with the pre-recorded IRF and compared to the experimental data. This process repeats until the model best fits the data, minimizing the difference between the measured and calculated parameters, such as lifetime and pre-exponential factors [175, 185].

Various methods exist for analysing time-resolved decays, each offering unique advantages. For instance, the maximum entropy method excels in representing decay without imposing a specific model [187]. Alternatively, the lifetime distribution approach simplifies decay analysis by reducing required parameters [188], while the maximum likelihood model effectively handles data noise through Poisson statistics [189]. In this thesis, a multi-exponential least-squares model is used, known for its simplicity and robustness, with demonstrated exceptional performance over time [190–192]. Furthermore, for fluorescent dyes exhibiting fluorescence intensity decays following a simple mono-exponential model, each recovered component corresponds to a fluorophore exposed to a different environment [193]. Strictly speaking, n-exponential decay times describes n excited states, however, even if this is not appropriate to the kinetics, multi-exponentials can still be used to describe a decay. Typically, the multi-exponential model is fitted to the measured fluorescence decays, and has the following expression:

$$F(t) = A + \sum_{i=1}^{n} B_i \exp\left(-\frac{t}{\tau_i}\right) \tag{5.5}$$

where A is the background offset, index i denotes the individual exponential components in the model, B_i are the pre-exponential factors which denote the intensity contribution of the given lifetime component, and τ_i are fluorescence lifetimes.

The nonlinear least squares method (NLLS) is the most used approach to evaluate

the quality of fit [175]. It quantifies the mismatch between the experimental data $Y(t)$ and the fitted function $F(t)$ using the chi-square (χ^2) value, which can be calculated using the following expression [194]:

$$\chi^2 = \sum_{i=1}^{N} \left(\frac{Y(i) - F(i)}{\sigma(i)} \right)^2 \tag{5.6}$$

Here N is the number of data channels selected for the analysis, $Y(i)$ is the fluorescence decay data, $F(i)$ is the fitted function, and $\sigma(i)$ is the expected deviation from statistical consideration. A key advantage of TCSPC is that the data follows a known Poisson statistical distribution, making it easy to determine the standard deviation as

$$\sigma(i) = \sqrt{Y(i)} \tag{5.7}$$

In photon counting experiments, $\sigma(i)$ represents the expected deviation based on statistical considerations and is typically estimated directly from the data. As the number of collected counts increases, σ becomes less significant, leading to improved precision. The χ^2 is minimized by adjusting the parameters of the fitting function, with the minimum reached when the actual deviation between $Y(i)$ and $F(i)$ matches the expected deviation $\sigma(i)$. For a perfect fit, the value of χ^2 should be close to 1. However, the value of the χ^2 is not the only indicator of the quality of the fit.
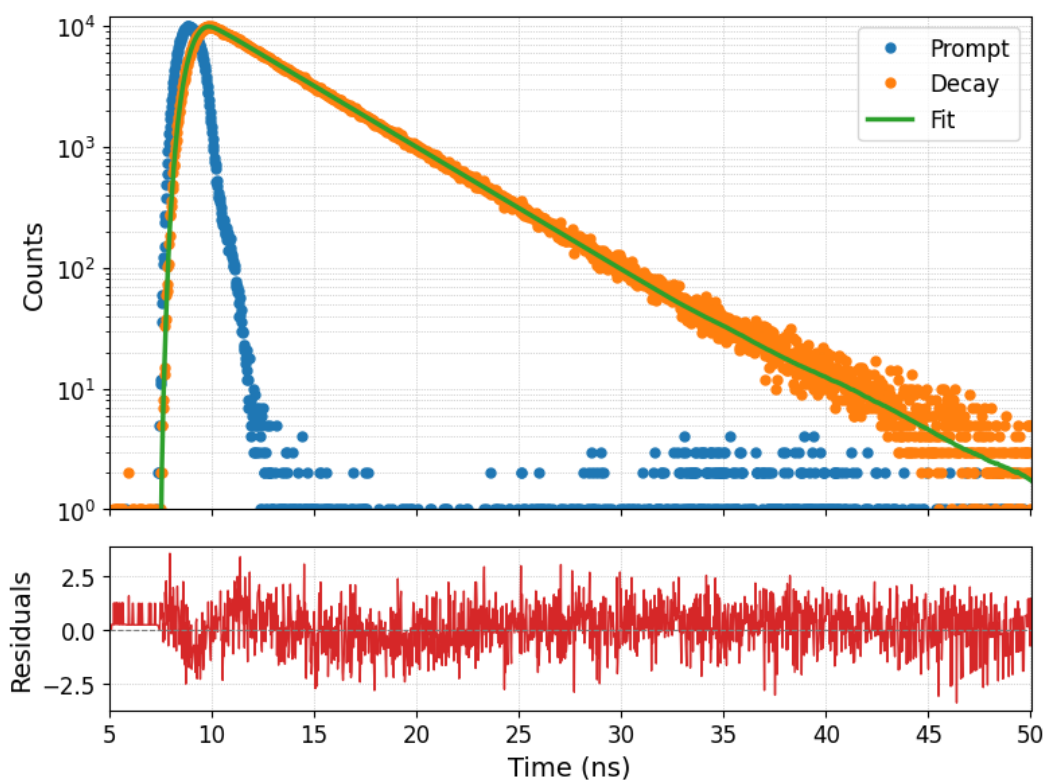
Figure 5.4: R6G decay with a corresponding mono-exponential fit, 10 μM sample, $\lambda_{\mathrm{ex}} = 494\,\mathrm{nm}$, $\lambda_{\mathrm{em}} = 548\,\mathrm{nm}$.

Another critical indicator of fit quality is the distribution of residuals, defined as the difference between the measured and fitted intensities at each time point. Ideally, residuals should fluctuate randomly around zero without any systematic patterns. Such behaviour indicates that the chosen model captures the essential decay dynamics of the system. In the case of Rhodamine 6G, shown in Figure 5.4, the fluorescence intensity decay was fitted to a mono-exponential model. The residuals appear randomly distributed and centred around zero, supporting the conclusion that a single-exponential decay function adequately describes the fluorescence decay kinetics in this case. Structured or non-random residuals, on the other hand, would suggest that a more complex model (e.g., multi-exponential) may be required.

5.4 Time-Resolved Anisotropy Decays

5.4.1 Measurements

In time-resolved fluorescence anisotropy experiments, the rotational dynamics of molecules are investigated by analysing the polarisation of the emitted light. When a sample is excited with vertically polarised light, the fluorescence emission can be detected in two polarisation directions: vertically (VV) and horizontally (VH). By measuring these two components over time, the anisotropy decay, $R(t)$, can be constructed, which provides insight into how the molecule's orientation changes as it moves or rotates. Fluorescence anisotropy experiments work because linearly polarised light preferentially excites molecules whose absorption dipoles are aligned with the excitation field, a process known as photoselection. The emitted fluorescence retains some degree of polarisation depending on the molecule's rotation during the excited-state lifetime.

However, in practical experiments, the detectors used to measure the emission light may not be perfectly balanced. The detector measuring the VV emission might have a slightly different efficiency or response compared to the one measuring the VH emission. This mismatch can distort the measured anisotropy and lead to inaccurate results.

The G-factor is a correction factor used to account for this imbalance between the detectors. It compensates for any differences in sensitivity or efficiency between the detectors, ensuring that the measurements of the vertically and horizontally polarised light are comparable. The G-factor adjusts the anisotropy data so that the true molecular dynamics are reflected rather than any systematic biases caused by the detector setup.

Mathematically, the anisotropy decay, $R(t)$, is calculated from the intensities $I_{VV}(t)$ and $I_{VH}(t)$, but the G-factor is introduced to normalise the VH measurement relative to the VV measurement. Therefore, the corrected anisotropy decay is given by:

$$R(t) = \frac{I_{VV}(t) - G \cdot I_{VH}(t)}{I_{VV}(t) + 2 \cdot G \cdot I_{VH}(t)} \tag{5.8}$$

Here, G adjusts the contribution of the VH emission to account for the detector im-

balance, ensuring that the observed decay accurately represents the molecular rotation or dynamics. Without it, the anisotropy decay data could be skewed, leading to misleading conclusions about the molecular behaviour. The factor of 2 in the denominator arises because, in an isotropic sample, the total fluorescence intensity is composed of one component parallel to the excitation and two equivalent perpendicular components, ensuring proper normalisation of the emission intensity in three-dimensional space.

Experimentally, the G-factor is obtained from the ratio of the perpendicular (HV) and parallel (HH) polarised emission components when the excitation light is horizontally polarised:

$$G = \frac{\int I_{\mathrm{HV}}(t)\, dt}{\int I_{\mathrm{HH}}(t)\, dt} \tag{5.9}$$

Since most of the excitation light is blocked due to the polariser being placed in the horizontal position, measuring the G-factor can potentially be very time-consuming. The G-factor is simply a numerical value used to correct for any imbalance between the detectors. It adjusts the relationship between the VV and horizontally VH emissions to ensure accurate anisotropy measurements. While the G-factor is crucial for correcting any detector imbalance, it is a constant value in a given experiment and does not require frequent recalibration. It can be measured once and then reused, provided that the same experimental parameters are applied to the same instrument and the optical components are not replaced. Typical values depend on the detection system: for filter-based setups, G is usually close to 1, whereas for systems using an emission monochromator, G is often around 0.5, though this can vary with wavelength and grating settings.

For the anisotropy measurements, the peak counts from the $I_{\mathrm{HV}}(t)$ and $I_{\mathrm{HH}}(t)$ signals are sufficient when they reach around 1000 counts. In practice, the $I_{\mathrm{VV}}(t)$ and $I_{\mathrm{VH}}(t)$ measurements are acquired by keeping the excitation polarizer in the vertical position throughout the experiment. Meanwhile, the emission polarizer is toggled between vertical and horizontal orientations, with each position being held for a specified dwell time, typically 60 seconds or more. This process continues until a peak difference of 10,000 counts is achieved, ensuring that the measurements are accurate and stable

before proceeding with the anisotropy decay analysis.

A subtle but important point is that photoselection is not absolute. Although linearly polarised light excites molecules aligned with the field most efficiently, the probability of excitation follows a $\cos^2 \theta$ distribution, where θ is the angle between the transition dipole and the excitation polarisation [175]. Even molecules misaligned to some degree are still excited, leading to a partially oriented ensemble of excited molecules. This incomplete orientation limits the maximum initial anisotropy $R(0)$ to 0.4 in the ideal case of one-photon absorption in an isotropic medium (See Chapter 4). In practice, measured $R(0)$ values are often lower due to ultrafast depolarisation processes such as solvent relaxation, local probe flexibility, or energy transfer [175].

5.4.2 Data Analysis

In time-resolved anisotropy experiments, the data analysis typically starts with the calculation of the sum and difference curves from the measured intensities. These curves are crucial for extracting the anisotropy decay and understanding molecular dynamics.

The sum and difference of the measured intensities in the VV and VH are calculated as follows:

$$S(t) = I_{\mathrm{VV}}(t) + 2 \cdot G \cdot I_{\mathrm{VH}}(t) \tag{5.10}$$

$$D(t) = I_{\mathrm{VV}}(t) - G \cdot I_{\mathrm{VH}}(t) \tag{5.11}$$

Here, $S(t)$ represents the total fluorescence intensity, combining both the VV and VH components, while $D(t)$ reflects the polarisation dependence of the emission, which is linked to the molecular anisotropy.

Once the sum and difference curves are obtained, a reconvolution analysis is applied to the total fluorescence intensity $S(t)$, as described in section 5.3.2. This analysis is designed to fit the experimental data to a decay model which represents the overall fluorescence dynamics, yielding parameters, such as the fluorescence lifetime or decay constants. Once a suitable fit is found for the sum data, a second reconvolution is

performed on the difference data $D(t)$, which provides the anisotropy decay, $R(t)$:

$$D(t) = S(t) \otimes R(t) \tag{5.12}$$

Here, the convolution operation accounts for the relationship between the sum and difference curves, allowing the recovery of the anisotropy decay $R(t)$.

The model used for the anisotropy decay, $R(t)$, in the reconvolution analysis software assumes that the fluorophore behaves as a simple spherical object with a maximum of two rotational correlation times. Theoretically, more exponential components could be used to describe $R(t)$; however, this is generally not beneficial because many different models and parameter combinations would fit the data equally well, making the results ambiguous. Therefore, the mathematical expression for $R(t)$ is:

$$R(t) = b_1 e^{-t/\tau_1} + b_2 e^{-t/\tau_2} + r_\infty \tag{5.13}$$

Here, b_1 and b_2 represent the fractional contributions of the two rotational correlation times τ_1 and τ_2. r_∞ is the residual anisotropy, which accounts for the small anisotropy that remains at long times, reflecting any restricted angular motion of the fluorophore. A value greater than zero suggests that the molecule is experiencing some constraints on its rotational freedom (e.g., due to interactions with its environment or surrounding macromolecules). The initial anisotropy R_0, which represents the anisotropy value at time zero, can be calculated from b_1 and b_2 as:

$$R_0 = b_1 + b_2 \tag{5.14}$$

This reflects the total anisotropy at the moment of excitation and indicates how the molecule's orientation is initially distributed.

5.5   Fluorescence Recovery After Photobleaching

FRAP, introduced by Daniel Axelrod in 1976, is a widely used technique to study the lateral mobility of fluorescently labelled molecules [60]. It involves photobleaching a defined region and monitoring fluorescence recovery as unbleached molecules diffuse back into the area, allowing extraction of parameters such as diffusion coefficients and mobile fractions. While powerful and non-invasive, FRAP relies on assumptions like homogeneous diffusion, which may not hold in complex environments. In this thesis, FRAP is applied to study the diffusion of industrial sodium silicates, supporting the development of a nanometrology method for silica-based nanoparticles.

5.5.1   Photobleaching in FRAP

In FRAP, photobleaching refers to the deliberate, localised, and irreversible loss of fluorescence caused by intense laser irradiation. Excited fluorophores, such as R6G or RB, undergo chemical changes that prevent them from emitting light. Once bleached, these molecules leave a non-fluorescent region, and the subsequent recovery of fluorescence reflects the diffusion of unbleached molecules into this area. Photobleaching is therefore not merely a limitation but the central mechanism that enables quantitative FRAP analysis of molecular diffusion and mobility.

Photobleaching can occur through several pathways. One common mechanism involves the triplet excited state of the fluorophore, which can react with molecular oxygen to form reactive species that permanently damage the fluorophore [195]. Another mechanism is photooxidation, where these reactive species modify the fluorophore or nearby molecules, leading to loss of fluorescence, although this is less significant for some dyes such as Cy5 or ATTO 647N [196]. Fluorophores can also undergo direct photochemical reactions, producing non-fluorescent products without involving the triplet state, as seen with methylene blue [197].

Understanding these mechanisms helps in selecting fluorophores and optimising experimental conditions to control photobleaching, ensuring accurate measurement of

diffusion and molecular mobility in FRAP experiments. This also naturally leads to the importance of choosing suitable fluorophores, which is discussed in the following subsection.

5.5.2 Fluorescence probes for FRAP

The fundamental property that is exploited during FRAP is, of course, fluorescence, hence, the selection of the fluorophores is the keystone of a successful FRAP experiment [198]. The decision of what type of fluorophore to use will directly depend on whether the fluorophore itself is used for the FRAP experiment or is coupled to the molecule of interest, e.g., by labelling in the case of labelled nanoparticle. In the latter, one needs to ensure that the attached fluorophore does not significantly affect the mobility of the molecules of interest. Lastly, the fluorophore should be readily bleachable during the initial photobleaching phase, yet sufficiently stable to resist significant photobleaching during the subsequent image acquisition, despite the prolonged illumination required for monitoring fluorescence recovery.

The most commonly used fluorophores for FRAP are fluorescein and green fluorescent protein (GFP) [199]. Nonetheless, both fluorophores mentioned above have significant drawbacks, with fluorescein being very prone to photobleaching, hence it might be problematic when used for prolonged experiments, while the GFP has been shown to exhibit reversible photobleaching, thus complicating the analysis of the recovery [200, 201]. In addition to fluorescein and GFP, other fluorophores may be selected depending on the specific application and system under study [202]. For example, dyes such as rhodamine or Alexa Fluor dyes are often chosen for their superior photostability and fluorescence intensity, making them ideal for experiments requiring prolonged imaging [203, 204]. Quantum dots have also gained popularity in FRAP applications, especially for studying nanoparticles or for applications in nanometrology [205–207]. These probes provide narrow tuneable emission spectra, exhibit high photostability, and feature a large surface area for functionalization [208–210]. This is especially advantageous for investigating the diffusion of particles, such as nanoparticles in suspension. Additionally, the fluorophore's spectral properties, especially its absorption and

emission wavelengths, must match the laser excitation sources and the detection filters utilised in the imaging system. Lastly, the functionalization process mustn't influence the particles' diffusion behaviour when labelling nanoparticles with fluorophores, especially in nanometrology contexts. This is essential to ensure that the measured diffusion coefficient truly reflects the particles' behaviour in solution, rather than being influenced by the labelling method.

5.5.3   Performing the Experiment

The typical FRAP experiment consists of three stages:

1. Initially, a sequence of frames is acquired to act as a reference for the initial intensity, called the *pre-bleach phase*.

2. The next step is the *bleaching phase*. During this step, a rapid and powerful laser pulse is applied to the region of interest (ROI), and the fluorophores in the ROI are irreversibly photobleached. The laser power must be high enough to cause a drop in intensity to at least approximately 75% of the pre-bleach value, but also low enough to avoid excessive photodamage that could perturb the system or cause mobile molecules to become immobile. The latter is particularly important when studying cells [211]. Additionally, the laser pulse must be short enough to minimise molecular diffusion during bleaching. Ideally, the bleaching duration should be less than one-tenth of the recovery half-time [211].

3. The final phase is the actual data acquisition phase, called the *post-bleaching phase*. During this phase, recovery images are collected using either a CLSM or a widefield microscope with a camera. This phase should typically continue until the recovery reaches a plateau, although this depends on the specific experiment. A key consideration here is the time interval between frames. For slow diffusion, a varying timestep may be used, starting with the smallest possible interval immediately after bleaching, then gradually increasing over time. For fast diffusion, a constant interval simplifies data analysis, but can result in very large datasets requiring significant computational resources to process.

When it comes to experimental settings, such as laser power, bleach duration and imaging step, a universal approach does not exist. Settings and parameters need to undergo thorough testing and refinement over several trials, as they are closely linked to the specific system being examined. Proper calibration is vital to achieving an optimal experimental setup. After identifying the best parameters, it's advisable to create pre-set configurations to ensure uniformity across various experiments. Even minor changes in the experimental conditions can greatly influence the recovered parameters of interest, highlighting the necessity for precision and consistency in the experimental design.

5.5.4   Data Analysis

Contrary to the simplicity of the experiment, the FRAP data analysis is not straightforward. A variety of models exist that can be used to analyse the experimental data, and different to e.g., TCSPC experiments, where multi-exponential model is often used for variety of systems, here the model selection depends strongly on the system that is studied. The choice of model can vary based on the characteristics of the molecules under investigation, such as whether they exhibit simple or anomalous diffusion, or if there are immobile components involved.

Despite the model that will be used to obtain the actual parameters of interest, the main workflow of FRAP data analysis will be more or less identical. An image processing software that can measure the intensity in defined regions is needed to extract the necessary parameters from the obtained image stack. A good choice is *ImageJ* [212–214], as it is freely accessible and rather intuitive in its usage. Furthermore, due to the large number of available plugins, the analysis can be easily optimised by utilising those plugins.

Multiple ROIs

Typically, the intensity of multiple ROIs must be measured to generate the final FRAP recovery curve. These ROIs are selected in such a way that they capture both the

81

bleached region (ROI_1) and areas that represent the non-bleached surrounding regions (ROI_2). The following steps are usually performed to ensure accurate intensity measurements:

1. **Pre-bleach ROI Measurement:** Before photobleaching, the fluorescence intensity of the ROI is measured over several frames to capture the baseline fluorescence level, I_0.

2. **Post-bleach ROI Measurement:** After photobleaching, the fluorescence intensity in the same ROI is monitored over time as the recovery proceeds. This is essential for capturing the temporal dynamics of fluorescence recovery.

3. **Control ROIs:** Additional ROIs, often selected from regions of the sample outside of the bleaching zone, are used to measure background fluorescence and correct for any potential fluctuations or drift in illumination over time. These control ROIs help to normalize the data and reduce errors arising from factors unrelated to molecular diffusion, such as shifts in the microscope's focus or slight variations in light intensity.

It is important that the same ROIs are consistently measured across frames to maintain uniformity in the analysis. *ImageJ* allows the user to track and select ROIs across the image stack, making it easy to monitor intensity changes in real-time.

Data Pre-Processing

Once the fluorescence intensities for each ROI have been measured, the data must be processed to correct for the residual bleaching and other potential sources of error:

1. **Background Subtraction:** This is the most important data preprocessing step, as it accounts for any inherent fluorescence or bleaching due to prolonged imaging, both of which are not related to the diffusion process. This can be simply done by dividing the bleached ROI by the control ROI (shown in Figure **5.5**).

2. **Intensity Normalisation:** To ensure that a direct comparison between different experiments or experimental conditions is possible, a standard practice is to nor-

malise the data. Typically, this is achieved by dividing the fluorescence intensity at each frame by the pre-bleach intensity I_0, resulting in a recovery curve where the maximum intensity is set to 1.

3. **Time Point Interpolation:** In some cases, due to errors in image capturing, there might be data points missing. Interpolation techniques can be used to estimate the missing values by fitting the data to a curve or by averaging neighbouring points. This can be especially helpful in experiments with irregular frame capture rates.
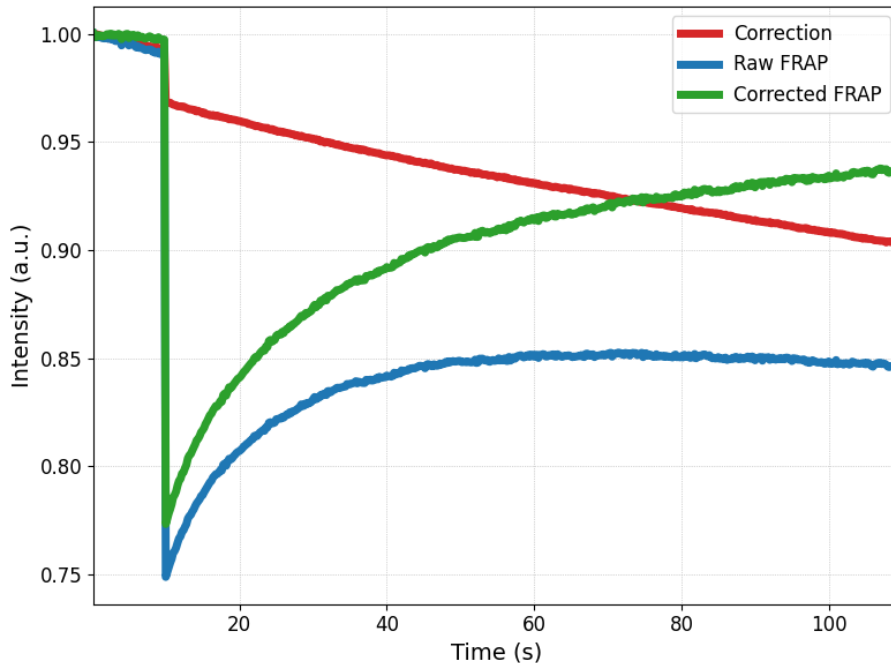
Figure 5.5: FRAP analysis showing intensity changes over time. The red curve represents the photobleaching correction signal, the blue curve shows the raw FRAP intensity in the bleached region, and the green curve displays the corrected FRAP recovery curve after normalisation. Data are normalised to pre-bleach intensity levels and corrected for acquisition bleaching.

Fitting the Recovery Curve

Once the intensity data has been obtained, corrected and normalised the next step is to fit the FRAP recovery curve to a model that best describes the diffusion of the system

under study. Several models can be used, depending on the complexity of the diffusion
and sample under study.

For systems exhibiting simple diffusion, e.g., large nanoparticles in viscous solution,
or free R6G in glycerol, a simple mono-exponential model is often used:

$$I(t) = I_\infty \left(1 - e^{-t/\tau} \right) \tag{5.15}$$

where $I(t)$ is the intensity at time t, I_∞ is the final intensity at the recovery plateau,
and τ is the recovery time constant, which is directly related to the diffusion coefficient.

When prior knowledge of their binary nature exists, the bi-exponential model can
provide an excellent balance between accuracy, simplicity, and reliability, as will be
shown in Chapter 9. Lastly, the tri-exponential model, in which each component cor-
responds to a distinct sample fraction, such as free dye and two types of nanoparticles
of varying sizes, can differentiate all three components with a single measurement,
thereby offering a size distribution. However, this model is only reliable in relatively
high-viscosity environments, as it tends to underperform at low viscosities, leading to
size overestimation and over-parameterisation; therefore, it should only be applied af-
ter careful validation. Consequently, the general form of the exponential model is the
following:

$$I(t) = A + \sum_{i=1}^{n} I_{\infty,i} \left(1 - e^{-t/\tau_i} \right) \tag{5.16}$$

This model serves as the primary focus of this thesis and is the subject of this discussion.
Models like the Two-Phase model, which includes mobile and immobile components
such as membrane-bound or aggregated molecules, and anomalous diffusion models
for systems exhibiting non-standard diffusion behaviours (e.g., confined diffusion), are
irrelevant to this thesis and will not be examined in depth [62, 215].

Extracting Key Parameters

From the fitted recovery curve, several key parameters can be extracted:

1. **Mobile fraction (M_f):** Mobile fraction represents the proportion of the

molecules in the bleached ROI, which can diffuse. This is obtained directly from the fitted model by taking the difference of I_0 and I_∞. A high M_f indicates that a large portion of molecules in the bleached ROI are mobile, while a low value indicates that a substantial portion of the molecules are immobile or bound.

2. **Recovery time constant (τ):** The time constant τ represents how quickly the fluorescence intensity recovers to its steady-state value. It is inversely proportional to the diffusion coefficient and can be used to estimate the rate of diffusion. A shorter τ corresponds to faster diffusion and vice-versa.

It is important to note, that recovery half-time ($t_{1/2}$) is usually used instead of τ. While both of those parameters are closely related, they represent different aspects of the FRAP recovery process. The recovery time constant τ defines the time it takes for the system to reach approximately 63% of its total recovery, since $1 - e^{-1} \approx 0.63$. In contrast, the recovery half-time ($t_{1/2}$) is defined as the time required for the fluorescence intensity to reach 50% of its final steady-state value. To derive the recovery half-time, we set:

$$I(t_{1/2}) = \frac{I_\infty}{2} \tag{5.17}$$

which results in:

$$\frac{1}{2} = 1 - e^{-t_{1/2}/\tau} \tag{5.18}$$

Rearranging and solving for $t_{1/2}$ gives:

$$t_{1/2} = \tau \ln 2 \approx 0.693\tau \tag{5.19}$$

Consequently, the recovery half-time is proportional to the recovery time constant, with $t_{1/2}$ approximately equal to 0.693τ. Thus, while the recovery time constant is directly related to diffusion, the recovery half-time offers a more intuitive measure, indicating the duration needed for recovery to reach its halfway

point. Additionally, it can be applied in calculating the diffusion coefficient (D), especially when considering a circular bleached region of radius w, where the diffusion coefficient can be estimated using the expression:

$$D \approx \frac{w^2}{4t_{1/2}} \tag{5.20}$$

As a result, the recovery half-time is typically preferred over the recovery time constant for estimating the diffusion coefficient because it provides a more stable and reproducible parameter in most experimental setups.

Statistical Analysis and Validation

Lastly, statistical analysis should be conducted to ensure the reliability of the results:

1. **Goodness of fit:** The fit's quality should be evaluated using metrics like R^2 or reduced chi-squared to determine how accurately the model represents the experimental data.

2. **Error Estimation:** The uncertainty in diffusion parameters must be assessed by calculating confidence intervals or standard deviations from several repetitions.

3. **Reproducibility:** To confirm that the results are consistent and not artefacts of the experiment, it is important to conduct multiple trials.

5.5.5 Experimental Setup

In this section, the custom-built FRAP widefield microscope developed and used in this thesis will be described in detail. The system combines high-resolution widefield fluorescence imaging with a dedicated FRAP scanner, allowing for precise photobleaching and recovery measurements. The setup includes a modular microscope platform, motorised sample stage, high-performance objective, advanced illumination and laser systems, and a sensitive detection unit. The following subsections will provide a comprehensive overview of each component and its role in the FRAP experiment. A schematic of the FRAP setup is shown in Figure 5.6.
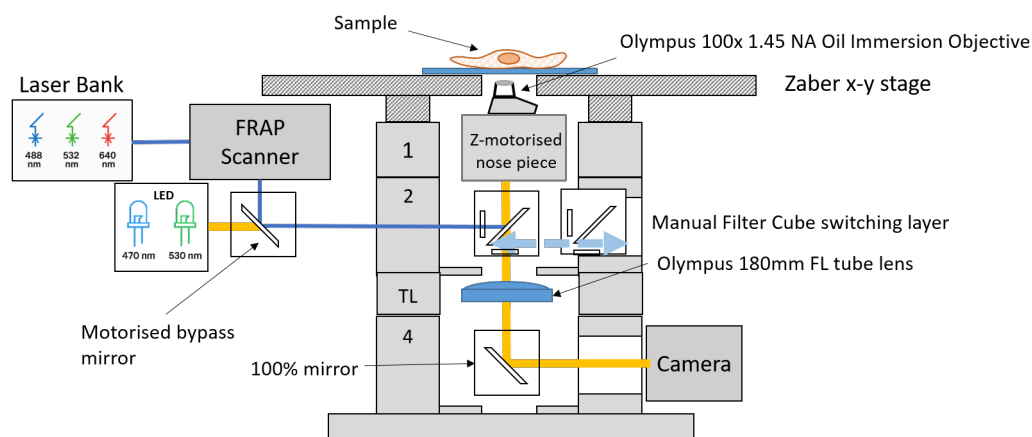
Figure 5.6: Schematic of a custom FRAP setup based on Cairn Research OpenFrame platform.

Microscope Base and Structure

The whole optical setup is based on a modular OpenFrame platform by Cairn Research, which serves as the structural foundation of the system. The platform is designed in a way, which allows it to accommodate multiple optical and mechanical components while providing stability and flexibility for future modifications due to the modular design. The OpenFrame includes a focusing/objective layer, equipped with a motorised focus, allowing for precise control of the objective position in the Z-direction, which is critical for maintaining consistent focus during both widefield imaging and FRAP experiments. An XY-stage adapter plate is integrated into the platform, allowing the addition of sample stages. A single objective holder and adapters for the Z stage are included, ensuring compatibility with different objective configurations.

Sample Stage and Positioning

The system includes a motorised XY microscope stage with a travel range of $100\,\mathrm{mm}$ $\times$ $120\,\mathrm{mm}$, providing large-scale movement, while still maintaining high positional accuracy. A universal insert allows to accommodate different sample holders, making the system adaptable for a variety of experiments. A programmable 3-axis joystick allows real-time manual control of the stage, giving the user the ability to adjust sample

positioning during the experiment.

Objective Lens

The system is equipped with an Olympus $100\times$ high-performance oil immersion objective with a numerical aperture of 1.45 and a working distance of $0.13\,\mathrm{mm}$, providing excellent resolution and light-gathering ability. The objective is optimised for fluorescence imaging, making it ideal for high-resolution FRAP experiments. Furthermore, it features a $0.17\,\mathrm{mm}$ cover glass correction, thus allowing compensation for variations in sample thickness, ensuring sharp, high-contrast imaging across the field of view.

Illumination System

The widefield illumination system includes a pair of high-stability LED light sources for fluorescence excitation. A stabilised OptoLED power supply is used to control the intensity and modulation of the two LED channels at $470\,\mathrm{nm}$ and $530\,\mathrm{nm}$. The power supply features full front panel control with feedback circuitry to maintain consistent output intensity during long imaging sessions. A TwinLED coupling unit is used to combine and direct the LED into the optical path. The light path is directed towards the sample via a direct epi-illuminator and a motorised bypass cube, allowing switching between different illumination modes.

FRAP Scanner

A dedicated ASI fibre-coupled laser FRAP scanner provides the FRAP capability. The scanner features a micro-mirror scan head with a diffraction-limited scan lens of $39\,\mathrm{mm}$ focal length and a $2.4\,\mathrm{mm}$ MEMS mirror for rapid and precise targeting of the photobleaching region.

Laser Bleaching and Control

The laser system is based on a Cairn TriLine Laser Launch configured with three continuous wave (CW) laser lines at $488\,\mathrm{nm}$, $532\,\mathrm{nm}$, and $640\,\mathrm{nm}$, which are specifically

used for photobleaching during FRAP experiments. The lasers are delivered via a high-power, single-mode, polarisation-maintaining fibre, ensuring stable and precise laser delivery. The lasers at 488 nm and 532 nm provide 150 mW of power, while the laser at 640 nm provides 100 mW of power. The laser beams are combined and directed to the sample using a set of steering mirrors and dichroics mounted in a TriLine laser mounting module. The system includes an electro-mechanical shutter for rapid switching of the laser output, which is essential for precisely controlling the bleaching phase in FRAP. The availability of multiple laser lines enables flexible targeting of different fluorophores for photobleaching, making the system highly adaptable for potential multi-channel FRAP experiments.

Emission Path and Detection

Fluorescence emission from the sample is collected through the objective and directed towards the detection system using a series of mirrors. The system includes a dual infinity slider compatible with Olympus U-MF2 cubes, allowing flexible separation of excitation and emission paths. A silver-coated right-angled mirror directs the light to the camera. The detection optics are optimised for high NA objectives, ensuring maximum signal collection and minimal distortion.

Filter Sets and Microscope Cubes

The system is equipped with Chroma sputter-coated filters for precise spectral separation of fluorescence signals. The filters include excitation filters for 470 nm and 530 nm LEDs, as well as bandpass filters for 488 nm and 532 nm lasers. The microscope is fitted with Olympus-compatible filter cubes, allowing rapid switching between fluorescence channels. The combination of high-quality filters and dichroics ensures that the system can capture clean, high-contrast fluorescence signals with minimal background noise.

Camera

The detection system includes a high-sensitivity CellCam Kikker camera manufactured by Cairn Research, with an 11.6 MP sensor and a pixel size of 4.63 × 4.63 μm, and low read noise of 1.5–1.6 electrons. It supports a frame rate of 35 fps at full resolution, using a USB 3.0 interface for fast data transfer. The camera's high sensitivity and low noise make it ideal for detecting weak fluorescence signals during FRAP recovery.

In conclusion, the custom FRAP widefield microscope outlined above is a highly integrated and multifunctional system tailored for high-resolution fluorescence imaging as well as accurate FRAP measurements. Its stable OpenFrame platform, high-performance objectives, advanced illumination and laser bleaching capabilities, coupled with a sensitive detection unit, ensure precise and reproducible analysis of molecular diffusion and dynamics. The modular design and compatibility with diverse optical components render this system exceptionally adaptable to various experimental conditions, making it an invaluable tool for exploring complex biological systems.

Chapter 6

Dynamics of Xanthene Dyes in the Presence of Silica Nanoparticles: Influence of crystal structure, size and pH

Adapted from articles published under CC-BY license in:

- *Doveiko, D., Kubiak-Ossowska, K., & Chen, Y. (2024). Impact of the crystal structure of silica nanoparticles on Rhodamine 6G adsorption: a molecular dynamics study. ACS Omega, 9(3), 4123–4136.* `https: // doi. org/ 10. 1021/ acsomega. 3c06657`

- *Doveiko D, Martin A.R.G., Vyshemirsky V, Stebbing S, Kubiak-Ossowska K, Rolinski O, Birch D.J.S., Chen Y. Nanoparticle Metrology of Silicates Using Time-Resolved Multiplexed Dye Fluorescence Anisotropy, Small Angle X-ray Scattering, and Molecular Dynamics Simulations. Materials, 2024; 17(7):1686.* `https: // doi. org/ 10. 3390/ ma17071686`

- *Doveiko, D., Asciak, L., Stebbing, S., Shu, W., Kubiak-Ossowska, K., Birch, D.*

J. S., & Chen, Y. (2025). Quantitative nanometrology of binary particle systems using fluorescence recovery after photobleaching: application to colloidal silica. Langmuir, 41(29), 19173–19182. `https://doi.org/10.1021/acs.langmuir.5c01287`

- *Doveiko D, Kubiak-Ossowska K, Chen Y. Nanoparticles as adsorbents for hydrophobic molecules: Exploring size, pH, and structural dependencies. J Chem Phys. 2025; 163(2):024708.* `https://doi.org/10.1063/5.0274630`

6.1 Introduction

The development of nanotechnology in the 21st century can be compared to 20th century breakthroughs, such as semiconductor technology or molecular biology [216]. At the nanoscale, materials exhibit unique physicochemical properties that differ from their bulk counterparts [217]. Many nanomaterials have strong size-dependent properties; e.g., gold NPs have different colours depending on their size due to quantum effects [218]. Furthermore, the size of NPs influences their interactions with biological systems, with smaller NPs penetrating cells and tissues differently, thereby affecting their safety and effectiveness [219]. This highlights the importance of accurate size measurement methods for nanoparticles such as silica, which are widely used in industrial and research settings.

In the early 2000s, a new approach for nanoparticle metrology was proposed, utilizing the relationship between particle size and its rotational diffusion rate, as measured by time-resolved fluorescence anisotropy of fluorescent dyes [33, 220–222]. One major limitation of this method lies in the fact that SNPs do not exhibit strong intrinsic fluorescence. Moreover, the origin of their weak fluorescence remains poorly understood [223]. As a result, SNPs must be externally labelled with fluorescent dyes, meaning that the measured size corresponds to the SNP-dye complex, not the nanoparticle itself. A further complication arises from the dye's unknown orientation and binding configuration on the SNP surface. Since this cannot be determined experimentally, the extent to which the dye contributes to the apparent hydrodynamic or rotational size

remains unclear [224]. This uncertainty fundamentally limits the accuracy of size determinations using fluorescence-based techniques. Therefore, understanding how dyes interact with SNPs is essential for achieving the most accurate possible estimates of nanoparticle size. Without this knowledge, the interpretation of FRAP and time-resolved anisotropy results may be skewed by unaccounted-for dye-particle interactions.

As mentioned in Chapter 1, one of the most promising dyes for labelling SNPs is R6G, a member of the xanthene dye class. Xanthene dyes are a popular class of organic dyes that can be used successfully for labelling purposes. They are widely used in biological imaging [225], fluorescence microscopy [226], dye lasers [227], and chemical sensors [228] due to their bright fluorescence, suitable lifetime, and high photostability, even at high pH [37,193].

The interaction mechanism between dyes and SNPs can be effectively investigated using computational methods, such as MD. These methods provide a detailed understanding of processes occurring at the atomic level. In this chapter, MD simulations were conducted to explore the interactions of xanthene dyes with anionic SNPs structured in α-quartz and α-cristobalite forms, focusing on nanoparticles of varying sizes. While both are crystalline polymorphs of silica (SiO$_2$), α-quartz has a trigonal crystal structure and is more densely packed, whereas α-cristobalite has a tetragonal structure, resulting in a slightly lower atomic density and distinct surface characteristics. These structural differences can influence dye adsorption behaviour and NP–dye interactions observed in the simulations.
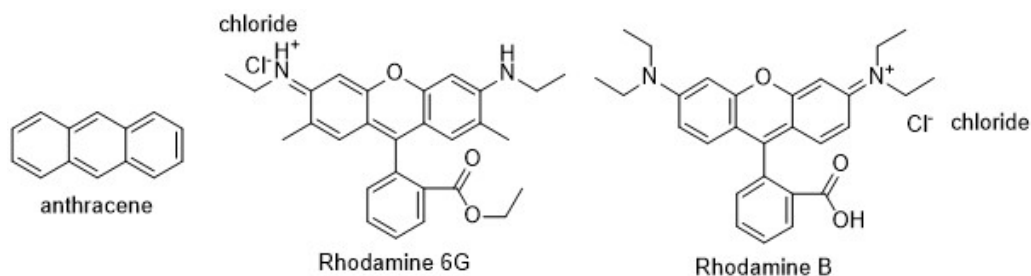
Figure 6.1: Chemical structures of aromatic molecules used in the MD simulations.

The cationic xanthene dyes, R6G and RB, were simulated to analyse their ad-

sorption behaviours within these systems (Figure 6.1). Additionally, anthracene was included as a simplified model compound due to its extended conjugated π-system and planar aromatic structure, which closely align with the key features of xanthene dyes. Although it does not possess the charged functional groups found in R6G and RB, anthracene offers an efficient means to simulate π–π stacking and surface interactions while avoiding the complexities of side chains and ionic effects. Together, these studies provide a comprehensive overview of how aromatic dyes interact with silica nanoparticles across various physicochemical conditions. Additionally, it is crucial to note that computational studies have shown that the surfaces of α-cristobalite can possess silanol group densities comparable to those of amorphous silica [229]. This similarity makes α-cristobalite a suitable model for investigating amorphous silica surfaces without requiring complex modelling techniques. Furthermore, the studies were designed to explore the effect of solute pH by ionising the surface of the SNPs and substituting Si–O–H with Si–O–Na$^+$. This deprotonation directly influences the overall charge of the nanoparticle, with more deprotonated groups leading to a greater net negative surface charge. Beyond characterising the impact of crystal structure on adsorption, the results are broadly applicable to any system involving dye–NP interactions. Additionally, the general molecular interactions observed between R6G and SNPs may be extrapolated to other dye–NP systems, making this work applicable beyond the immediate case of R6G.

6.2 Methods

For all simulations described in this chapter, the standard procedure of constructing systems using structures from the Protein Data Bank (PDB) is not applicable. This is primarily because NAMD [230, 231] is not inherently designed for simulations involving inorganic materials, and the widely used CHARMM [88,89,91] force field lacks parameters for silica-based systems. To overcome this limitation, the Interface FF was employed [96], as it is specifically developed for hybrid organic–inorganic interfaces. Additionally, both R6G and RB are non-standard molecules within the CHARMM36

force field, necessitating the generation of custom parameters for each dye.

Interface FF acts as an extension of more commonly used harmonic force fields such as CHARMM [88], AMBER [92], and GROMACS [93] and by employing the same rules, it allows to simulate inorganic–organic and inorganic–biomolecular interfaces. In this particular case, it allows the creation of silica structures from different bulk materials at different degrees of surface ionisation which correspond to different pH levels [96].

As the system contains inorganic SNPs and organic fluorescent dyes, CHARMM-GUI had to be used to set up the simulation of the systems. CHARMM-GUI is a web-based graphical user interface which allows building systems for the MD simulations interactively and, if necessary, even generates the final input files for the simulations [232]. All of the simulations in all configurations are prepared using the method, which will be discussed further.

6.2.1   Rhodamine 6G Parametrization

The initial R6G structure was taken from `2v3l.pdb` [233]. To make it compatible with the CHARMM-GUI pipeline, the structure is submitted to the "PDB Reader" extension, which converts a `.pdb` file from RCSB PDB into a CHARMM-readable format [234, 235]. Additionally, it generates topology and parameter files for R6G using CGenFF, which can be used to build the system and prepare for the simulations [88].
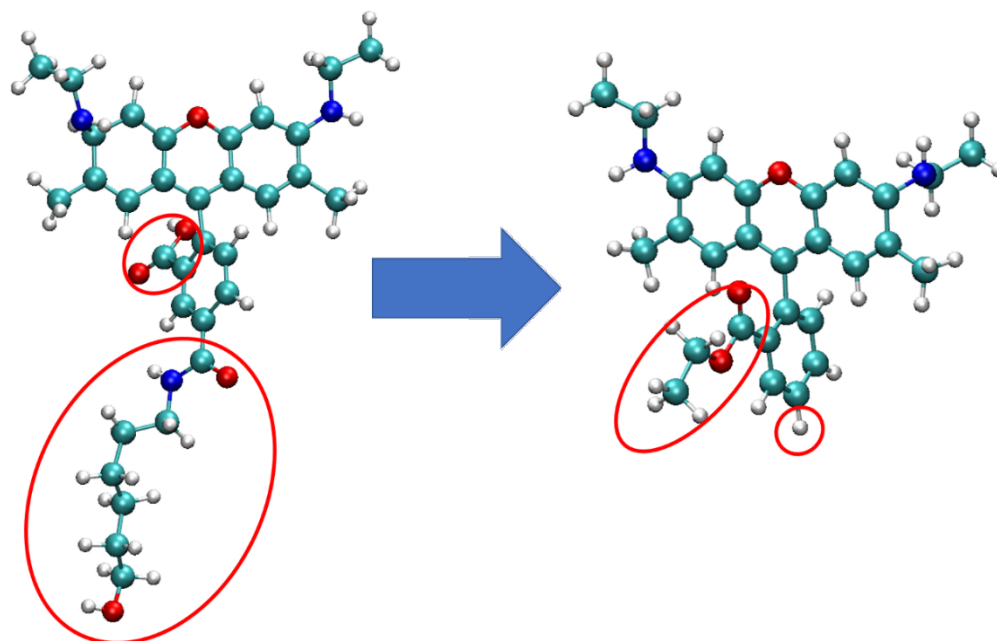
Figure 6.2: R6G structure from `2v3l.pdb` (left) and the structure after modification (right), which corresponds to the form most commonly used in experiments and is therefore used in all MD simulations. Modified parts are circled in red.

It is important to note that the PDB structure is an amino alkyl-coupled R6G and not the classical R6G structure [233]. This must be modified for these studies to ensure that it matches the structure used in experiments (see Figure 6.2). The modification must be performed using CHARMM-GUI to ensure compatibility with the rest of the system and to avoid errors during the simulation setup. This has been done in the following steps:

1. In the "Select Model/Chain" part, "hetero" needs to be ticked before moving to the "Manipulate PDB" part.

2. Under the "PDB Manipulation Options" at the "Reading HETERO Chain Residues," "CSML Search" is clicked, which will open a new pop-up window. Since the residue "R6G" does not exist in any CHARMM topology or parameter files, it must be parametrised here.

3. First, "Click if you want to customise your ligand structure using sketch pad"

needs to be selected. In a new window, the structure of the molecule will be shown and can be easily manipulated.

4. By using the "Delete" option, the unnecessary atoms and chains can be removed; in this case, the aminoalkyl functionalisation must be removed.

5. Once everything is removed, the $H^{\pm}$ icon should be double-clicked to add hydrogen atoms to the free carbons where atoms were removed.

6. The next step is to modify the organic groups to match the standard R6G structure. To do this, "Chain" should be clicked, and then the atoms that will be converted into the CH_3 group need to be selected.

7. At this stage, a final modification is required. The presence of an O–H–CH_3 configuration is incorrect, as the hydrogen atom in this arrangement would exhibit two covalent bonds. Consequently, the hydrogen atom must be replaced with a carbon atom. This is achieved by selecting the carbon atom in the right panel, followed by selecting the corresponding hydrogen atom to effect the substitution. The structure is thus adjusted to conform to the correct chemical configuration.

8. Finally, "Use PDB for ligand FF parametrization" should be clicked, followed by "Generate PDB." The `.pdb`, `.psf`, `.crd`, `.rtf`, and `.prm` files for the dye structure will be generated by CHARMM-GUI.

While CHARMM-GUI can accurately parametrise molecules in a geometrical sense, it does not perform quantum chemical calculations to determine the partial charges of the atoms. Therefore, to determine partial charges, RESP charges derived from accurate DFT B3LYP/6-31G** calculations by P. Chuichay et al. were used [236]. The theoretical background and justification for using RESP charges are discussed in detail in Chapter 2, Section 3.9. The charges in the CHARMM-GUI-generated topology files were manually corrected to match the literature charges, and the generated parameter files were then compared with the values acquired by AC Vaiana et al. using automated frequency matching for cross-validation [237].

6.2.2   Rhodamine B Parametrization

A similar approach was used to obtain RB parameters. Specifically, the initial structure was taken from the PDB entry `4glj.pdb` [238] and uploaded into the PDB Reader of CHARMM-GUI. Since the structures of both R6G and RB are virtually identical, their parameters will also be almost identical, with the main difference being the presence of a carboxyl group in the side chain. Therefore, values used for R6G can also be used here, after ensuring that the penalty values in the CHARMM-GUI generated parameters are low. In this context, a "penalty" refers to a numerical score indicating how closely the newly assigned parameters match existing parameters in the force field. Penalties lower than 10 suggest a fair analogy, penalties between 10 and 50 indicate that some basic validation is recommended, and penalties above 50 signify poor analogy, requiring extensive validation or optimization. High penalty scores often arise when the molecular structure under study differs significantly from those in the force field's training set, potentially leading to less accurate simulations. While the difference in the parameters is virtually non-existent due to small structural differences, the partial charges must be recalculated since they are not available in the literature. To do this, the RB `.pdb` file was converted to `.xyz` file using the OpenBabel online server [239]. Next, the structure was optimised using ORCA 6.0.1 in a multi-step method [240–242]. First, at the ωB97X-D4/SVP level of theory, followed by another geometry optimization run with a larger basis set (def2-TZVP) [151, 152, 167, 243, 244]. Next, the geometry optimization was re-run in a conductor-like polarizable continuum solvation model (CPCM, water) [160] since all of the MD simulations are typically performed in water. Finally, the atomic charges were calculated using a CHELPG (charges from electrostatic potentials using a grid-based method) scheme developed by Breneman and Wiberg [245]. During the DFT calculations, RB charge and multiplicity were both set to 1. R6G and RB are structurally similar cationic dyes, sharing the same core molecular framework and overall shape, with only minor differences in their side chains. This close resemblance results in similar physical and photophysical properties, such as strong fluorescence, nearly identical absorption and emission characteristics,

and a comparable charge distribution, as shown in Figure 6.3.
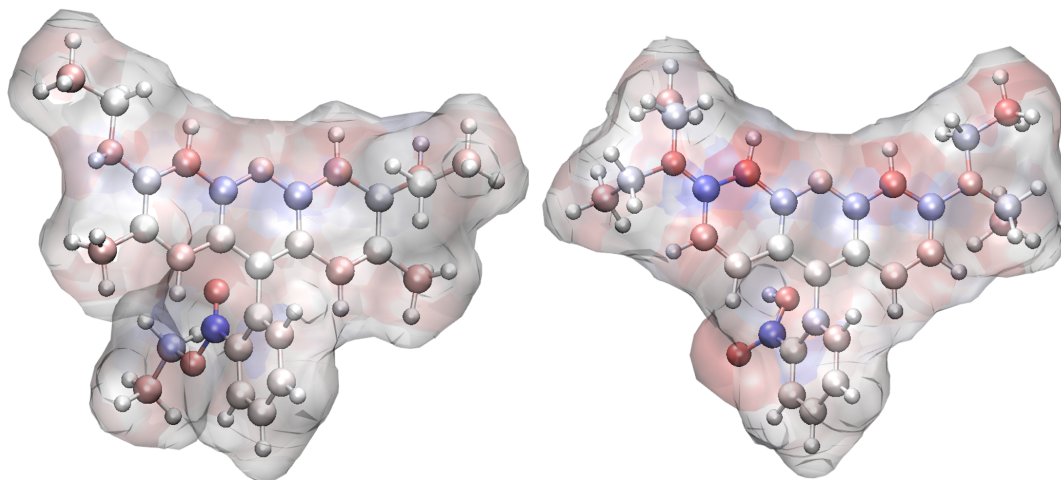
Figure 6.3: Left: R6G; Right: RB, coloured according to charges: white – neutral, red – negative, blue – positive

6.2.3   Silica Nanoparticle

To build a nanoparticle, a different extension of CHARMM-GUI called "Nanomaterial Modeler" was used [246]. For the nanomaterial type, either α-cristobalite or α-quartz in spherical shape was used. Nanoparticles of various sizes were employed, tailored to the specific objectives of the investigation, with the details of each system presented in the corresponding results section. It is important to note that due to the small size of the SNPs and the effects of crystal structure, the measured diameter between heavy atoms, such as O, or Si, might slightly differ from the nominal value.

The specific pH value is achieved by modifying the surface of the SNP by ionizing (deprotonating) a fraction of surface silanol groups. The degree of surface ionization indicates, in percentages, how many Si–OH groups are converted into Si–O^{-}–Na^{+}. For pH 3, which is the isoelectric point of the SNPs, all surface silanol groups are fully protonated, while for pH 7 the degree of surface ionisation is 13.3%, and 30.0% for pH 12.

6.2.4   System Creation in Multicomponent Assembler

Next, the dye and NP system must be assembled. To do this, the "Multicomponent Assembler" extension in CHARMM-GUI is used [247]. To be able to specify the number of components and manipulate the system parameters, one must upload the `.psf` and `.crd` files of specific structures. Additionally, if specific structures are using custom topologies and parameters, those must be uploaded as well. The uploaded files for R6G/RB (1–5) were the same in all cases, while the files for the NPs depended on the NP structure used in the specific simulation:

1. `r6g.prm`

2. `r6g.rtf` (with adjusted partial charges)

3. `step1_pdbreader.psf`

4. `step1_pdbreader.crd`

5. `step1_nanomaterial.psf`

6. `step1_nanomaterial.crd`

Independent of the pH or SNP size, the system is built in a vacuum with no ions as it will be prepared for the simulation further using VMD.

6.2.5   Preparing the System in VMD

Finally, the system building was completed using VMD, a graphical software designed for the display, analysis, and final set-up of molecular systems [248]. Typically, VMD allows full system construction from scratch, provided that all necessary parameters are included in standard topology and parameter files. In the present case, however, the initial geometries of the dye and silica components had to be prepared externally via a graphical interface, as they were not available in standard sources like the PDB. Therefore, VMD was used only for solvation, ionisation, and final system setup in this case. Solvation involves adding solvent molecules, typically water, around the system

of interest. The solvent provides a realistic environment that influences the dynamics of the system, such as stabilising electrostatic interactions [249], controlling temperature and pressure [113], and allowing for the proper exploration of conformational space [73]. It also helps in mimicking hydration effects, particularly in biological systems, where water (usually via hydrogen bonds) plays a crucial role in stabilising and influencing the function of macromolecules [250,251]. By default in NAMD, this is done using a TIP3P water model, which is a three-site model with three interaction points corresponding to the atoms of the water molecule [122]. This is accomplished using the "Add Solvation Box" extension in VMD. The important parameter here is the box padding, which is set to a value greater than 12 Å to avoid any potential interactions with the periodic image (e.g., itself). However, the actual value has to be determined empirically, since the aim is to achieve a comparable number of atoms in the system containing SNPs of comparable sizes, to ensure that the dye concentration in all simulations is approximately identical. After the solvation, two new files are created:

- `system_S.psf`

- `system_S.pdb`

Next, the system is neutralized, which is done using the "Add Ions" extension. In all systems, one chloride ion was added per xanthene dye molecule (R6G or RB) to neutralise its $+1$ charge, while all sodium ions originated from the ionisation of the silica nanoparticle surface. As a result, two new files with solvated and ionized systems were created:

- `system_SI.psf`

- `system_SI.pdb`

Lastly, the water box must be centred to obtain accurate measurements of the primary simulation cell, and non-water atoms have to be fixed in their positions for the water-only minimisation step. This is done using two scripts developed by Dr. Karina Kubiak-Ossowska:

- `ctrbox.tcl`

- `fix_protein.tcl`

After executing the scripts, the final structure files needed for the simulation are created:

- `system_SC.psf`

- `system_SC.pdb`

- `system_FIX.pdb`

Such a method of system preparation was used for all systems involving SNP-dye interaction studies. The details of each system will be discussed within the designated results section since the system setup varies depending on the studied interactions.

6.2.6 Molecular Dynamics Protocol

All simulations were performed using NAMD3 CUDA [230, 231] version with the CHARMM36 [89] force field and VMD [248] was used to visualise and analyse the simulations. Initially, each simulated system underwent a 1000-step water-only min-imisation using the steepest descent method with all non-solvent molecules restrained, followed by 100 ps equilibration at 300 K and 1 bar maintained via the Langevin baro-stat and thermostat (NPT ensemble). The obtained system was subjected to 10,000 minimisation steps with no constraints applied, followed by 30 ps of heating to 300 K and 270 ps equilibration with a 1 fs time step. The production runs were performed in the NVT ensemble, where a Langevin thermostat with a damping coefficient of 5 ps^{-1} was used to control the temperature with a 1 fs time step integrator. The 100 ns production run at 300 K was repeated four times for each system to ensure that the system was not trapped in a saddle point and to improve statistical reliability. In all cases, PME with 1.0 Å grid spacing was used for the fast evaluation of electrostatic interactions, while the cutoff for the van der Waals interactions was set to 12 Å.

6.2.7 Data Analysis

Most of the analysis has been done using VMD software and combined with results obtained from a custom TCL script (See Appendix 11.3), which allowed for the extraction of the centre of mass x, y, and z ($(COM)_{xyz}$) coordinates of the specified part of the system. The COM distance plots for each SNP–R6G pair were created using MATLAB [252] or Python.

To decide whether the particle is adsorbed or just experiences electrostatic interactions, a range of conditions had to be met:

1. The decision about whether the particle is adsorbed cannot be made solely based on the COM distance between the two entities. A crucial factor is the orientation of the dye on the nanoparticle's surface. R6G, a xanthene dye, features a xanthene core, which is composed of three interconnected aromatic rings. For the dye to adsorb, the xanthene core must lie relatively flat against the NP's surface. Therefore, each potential adsorption event is checked using VMD to ensure the correct orientation. Suppose a dye molecule approaches the NP closely, but the xanthene core does not align flat. In that case, this interaction is regarded as an electrostatic interaction and is not included in the adsorption analysis. Conversely, if the dye molecule is oriented correctly at any point, this interaction is classified as adsorption, and any subsequent movement of the dye is considered relocation. This classification applies to the entire trajectory when the dye remains near the NP.

2. It is well known that R6G tends to form aggregates, primarily due to stacking interactions and its hydrophobic nature [253]. The simulations showed that these aggregates do not adsorb easily to silica NPs; however, there is a noticeable competition between aggregation and adsorption. The aggregate can get very close to the NP until one of the dyes adsorbs and then the second component of the aggregate diffuses away, resulting in one adsorbed dye and one free dye. A detailed discussion of such interactions is presented in Chapter 7. Due to the

complexity of this mechanism, all interactions of such nature were ignored as the aggregates are non-fluorescent, and they do not affect the experiment outcome in any way.

3. As the simulations have implied PBCs, the possibility of dye interacting with the periodic image must be considered. As a result, when analysing the dye-NP interactions, all interactions due to PBCs were analysed as well.

Next, a method of analysis must be established to ensure that in all cases the trajectories are analysed objectively. As in previous cases, there were a few requirements established:

1. Each MD system is treated as a whole, regardless of the number of NP present. When multiple NPs are included, they are considered collectively as a single entity. While the overall system structure remains consistent within each specific type of simulation to ensure comparability, such as keeping the number of dye molecules fixed, some variation exists between the systems described in the individual subsections of this chapter. These differences reflect the distinct aims of each simulation set, which target specific factors influencing dye adsorption. Treating each NP separately would lead to variations in adsorption conditions, making direct comparisons between different systems less reliable.

2. If multiple dye molecules adsorb onto the same NP at the same time, only the first event is counted. The analysis tracks how long an NP remains occupied by any dye. Once adsorption occurs, the NP is considered occupied for the duration of that event, and any additional simultaneous adsorptions are ignored to avoid NP. Although such simultaneous adsorption events were not observed in the simulations, this approach was adopted as a precaution to ensure consistency in the analysis and to avoid potential ambiguity in occupancy tracking.

The classification of adsorption events (state A), R6G reorientation near the SNP surface (state R), and transient electrostatic interactions resembling adsorption (state T) was determined based on the COM distance and molecular orientation. Specifically, an

adsorption event (state A) was identified when the COM distance between R6G and the SNP was ≤ 5 Å, with the xanthene core of R6G aligned parallel to the surface. If R6G approached the SNP but never achieved parallel orientation, the interaction was attributed to strong electrostatic forces temporarily trapping the molecule in an "adsorption-like" state (state T). Such events were typically short-lived, rarely exceeding 2 ns, with the majority lasting under 1 ns. Finally, if the R6G xanthene core was parallel but undergoing repositioning on the SNP surface, this process was classified as reorientation and simultaneously considered part of state A, hereafter referred to as R/A.

To distinguish between systems easily, a simplified naming scheme was introduced, where the first number gives the particle diameter in Å, symbol c or q stands for α-quartz or α-cristobalite, and the last number 3, 7 or 12 indicates the pH.

6.3 Results and Discussion

6.3.1 Structural Differences of α-Quartz and α-Cristobalite SNPs

To be able to fully understand the impact of the crystal structure on the simulation outcome and R6G interactions with SNPs in particular, it is crucial to understand the structural differences between qSNPs and cSNPs and how those might affect the adsorption. The composition of the SNP surface was analysed using 20 Å and 40 Å diameter SNPs to investigate how the concentration of ionised silanol groups influences solute ion dynamics and, consequently, the system's electric field. The number of surface silanol groups was estimated by first generating SNP structures with different degrees of ionisation using CHARMM-GUI. The volume of each SNP was then calculated, and the number of silanol groups per unit area (Å^2) was obtained. Finally, the values were normalised to 20 Å and 40 Å diameters to allow direct comparison between different SNP sizes and crystal structures.
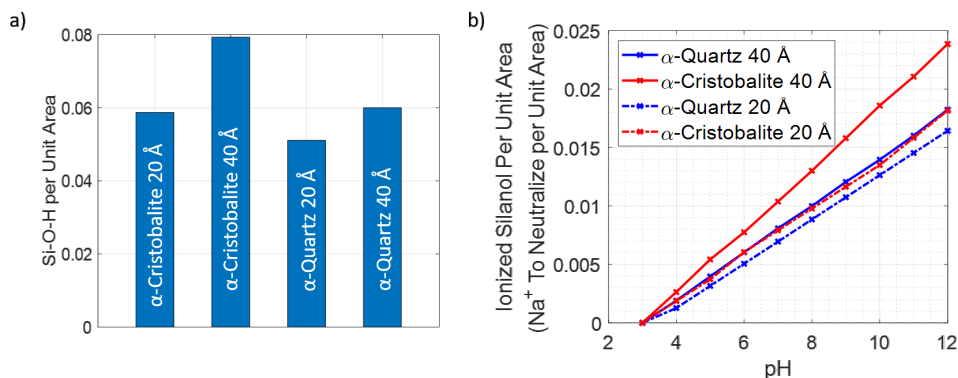
Figure 6.4: Silanol groups on SNP surface. (a) Estimated number of surface silanol groups per unit area (Å^2); (b) Number of ionized silanol groups per Å^2 at different pH values.

Figure 6.4 indicates that the number of ionized groups per Å^2 is always much higher in the case of α-cristobalite, which has more surface silanol groups per Å^2 when compared with α-quartz of the same size. This comes from the fact that α-cristobalite has a lower atomic packing fraction in the unit cell and molar density, hence, there are more silanol groups on the NP surface, which undergo ionisation with growing pH [254]. A higher number of silanol groups with negative partial charges might indicate that there are more candidates to interact via electrostatic forces with the potential adsorbate; nevertheless, as is shown below, the entire picture is not as simple as it may seem at first glance.

At pH 3, which corresponds to the isoelectric point of silica NPs, the situation is fundamentally different. With no net surface charge, the system's electrostatics are greatly simplified. As a result, adsorption is driven primarily by vdW interactions. While this leads to more stable binding once the dye is adsorbed, the initial adsorption is delayed due to the absence of electrostatic attraction pulling the dye towards the nanoparticle. Due to these simplifications, systems at pH 3 cannot be effectively used to model real-life conditions, where electrostatic interactions play a crucial role in the adsorption process. Therefore, a detailed comparison of both structures is based on simulations performed at pH 7 and pH 12.

Results presented in Figure 6.4 suggest that the strongest and most stable R6G

adsorption occurs on 40cSNP, while the weakest adsorption is observed on 20qSNP at both pH values, with this effect being more pronounced at pH 7. Adsorption stability appears to be comparable for 40qSNP and 20cSNP at both pH values. However, this simple analysis does not entirely align with the simulations, which account for a more complex interplay of factors beyond just the number of ionised groups on the SNP surface. The simulation system must be (i) neutral and (ii) exist in a buffer to reflect the experimental conditions; therefore, Na^+ and Cl^- ions were added to the simulation cell. As Figure 6.4b indicates, the number of Na^+ ions per $Å^2$ required to neutralize the SNPs strongly depends on pH, while the dependence on SNP diameter is substantial in the case of α-Cristobalite but relatively minor in the case of α-Quartz structure. The 40cSNP, which is characterised by the largest number of silanol groups, requires the most Na^+ to be introduced; the 20qSNP is on the opposite end, while 40qSNP and 20cSNP are in the middle and very similar. The presence of Na^+ ions influences the accessibility of silanol groups to the adsorbate as well as the electrostatic field created by SNPs. These counterions form a labile layer around the negatively charged silanol groups, partially screening the SNP dipole and moderating the electric field experienced by R6G. This layer is dynamic, allowing ions to move and redistribute in response to the adsorbate approach, and therefore plays a critical role in determining adsorption behaviour.

Dipole moments were measured using the built-in VMD "Dipole Moment Watcher" tool; however, due to precise measurement between well-defined moieties, it might not be possible to directly compare the obtained values with the experimental ones. The measured dipole moments are very large for molecular systems, on the order of hundreds of Debye, which might seem unusual at first glance. Although the absolute values reported by VMD are significantly overestimated compared to experimental expectations, the relative differences between nanoparticles are preserved, allowing meaningful comparison of trends across systems. This is physically reasonable because the nanoparticles contain many thousands of atoms and hundreds of ionised surface silanol groups whose vector sum produces a large net dipole. The magnitude also scales with nanoparticle size and surface asymmetry, especially at high pH, where more silanol groups are

deprotonated. Expressing these values in e·Å units (1 D $\approx$ 0.208 e·Å) provides an intuitive measure of the dipole: for example, 925 D corresponds to approximately 193 e·Å.

At pH 7, the dipole moment for 20cSNP is 625 D ($\approx$ 130 e·Å) while for 40qSNP, it is 925 D ($\approx$ 193 e·Å, approximately 50% difference). Similarly, at pH 12, it is 500 D ($\approx$ 104 e·Å) and 900 D ($\approx$ 187 e·Å, approximately 80% difference). For the 20qSNP, the dipole moment is 125 D ($\approx$ 26 e·Å) at pH 7 versus 250 D ($\approx$ 52 e·Å) at pH 12 (100% difference), while for the 20cSNPs, it is 100 D ($\approx$ 21 e·Å) versus 200 D ($\approx$ 42 e·Å) (also 100% difference). The discrepancy in the dipole moment values explains the difference in adsorption observed at pH 7, where its affinity and stability are significantly higher in the case of qSNPs (as described in detail in the next section). It is important to note that these dipoles are measured for the nanoparticle alone, without the counterion layer. The counterion layer forms around the negatively charged silanol groups and partially shields the nanoparticle's electric field. Charged species such as Na^+ and Cl^- interact dynamically with the SNP surface, moderating the electrostatic environment and influencing how R6G molecules experience attractive or repulsive forces. This dynamic screening means that while the intrinsic SNP dipole is large, the effective field acting on an adsorbate is smaller and modulated by the surrounding ions, which is essential for interpreting adsorption behaviour.

However, at pH 12, the adsorption follows a different pattern, as the dipole moments do not reflect the impact of the crystal structure of the SNP. As already mentioned, α-cristobalite has a lower molar density, and as a result, cSNPs have more silanol groups on the surface. Therefore, at high pH, more of those groups will be ionized (deprotonated), with more Na^+ introduced to the system. The counterions will comprise a labile layer on the SNP surface as shown in Figure 6.5, and reduce the R6G adsorption affinity by exhibiting a repulsive force on the cationic dye [255]. In other words, the dipole moment has to be measured for the SNP only, without the counter ion layer, as the interacting ions moderate the electric field created by the SNP, resulting in the observed discrepancy.
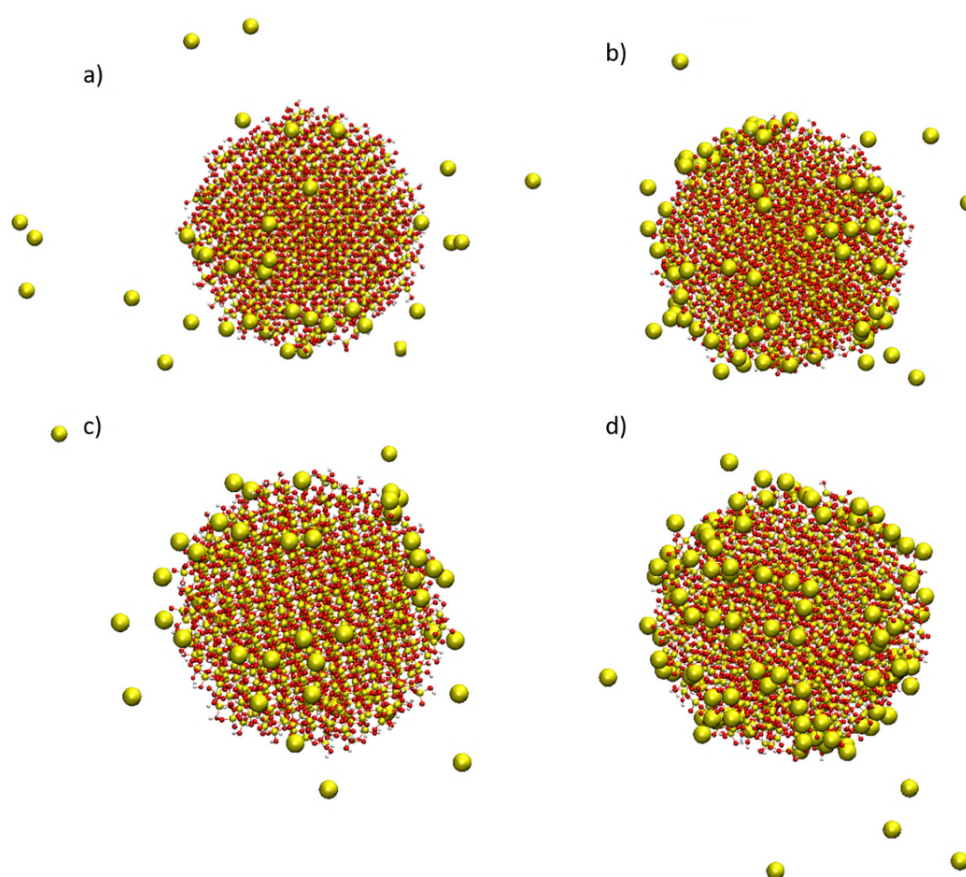
Figure 6.5: 40 Å SNP structures with ion layer: a) 40qSNP7; b) 40qSNP12; c) 40cSNP7; d) 40cSNP12.

An additional important factor is the effect of SNP size on the generated electric field. With decreasing SNP diameter, the size factor becomes less important as there are multiple SNPs in the system, each with its electric field. Therefore, R6G experiences a superimposed electric field created by multiple SNPs and R6G molecules present in the system. It is worth noticing that R6G molecules have a higher probability of adsorbing to cSNPs as the dye molecules favour binding to unionised silanol groups via hydrogen bonds [255, 256]; nevertheless, the adsorption on qSNPs tends to be more stable and longer.

6.3.2 Size and pH Effect

Protocol

To have a detailed representation of the size and pH effect on the rate of adsorption, a wide variety of systems was prepared. Namely, nanoparticles of 36 Å, 50 Å, and 100 Å diameter at pH 3, 7, and 12 were built, and systems containing one or two SNPs with three adsorbates each were prepared. This resulted in the following systems:

1. For α-cristobalite, simulations were performed using three particle diameters (36, 50, and 100 Å) at three pH levels (3, 7, and 12) with R6G, resulting in nine systems. Additionally, nine systems were created using two particles at the same radii and pH levels. Next, three systems were simulated using a slab geometry at the three pH levels. Finally, simulations with the 100 Å single SNP and slab geometry were repeated using RB and Anthracene, yielding six systems for each solute (12 systems total). In total, this resulted in 33 unique systems for the α-cristobalite structure.

2. For α-quartz, the same set of simulations as for α-cristobalite was performed, including three particle radii at three pH levels with R6G, as well as systems with two particles and slab geometries. Additionally, the 100 Å single SNP and slab geometry simulations were repeated with RB and Anthracene. As a result, 33 distinct systems were prepared for the α-quartz structure.

In total, 66 individual systems were generated, and each production run was repeated four times from the same starting point to improve statistical reliability and capture a broader range of possible interactions. This resulted in 264 molecular dynamics trajectories in total, each 100 ns long. All trajectories were carefully analysed, and the most representative events or trajectories are described.
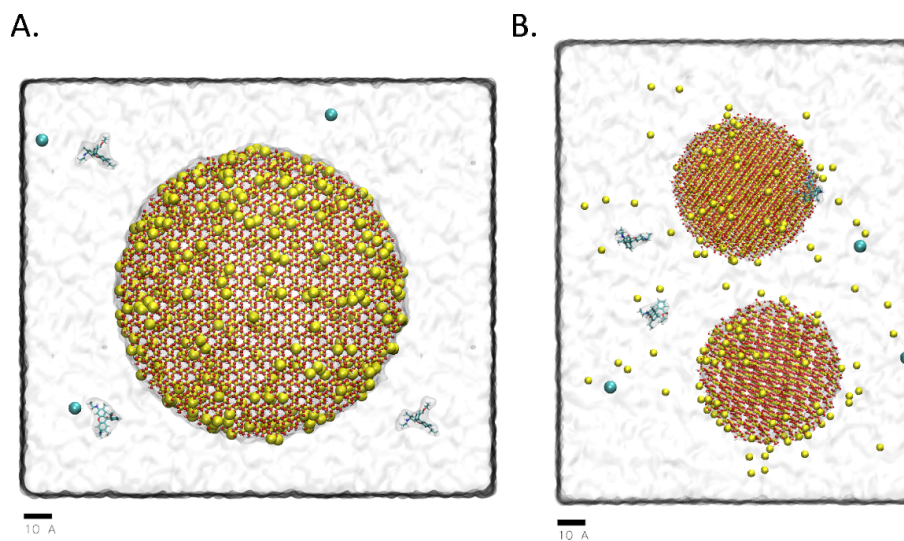
Figure 6.6: Exemplar Initial Nanoparticle System Setups. (A) 100 Å Silica NP simulation; (B) Two 50 Å Silica NP simulation.

Size Effect

Since xanthene dyes adsorb onto silica surfaces via hydrogen bonding with silanol groups, and the pH influences this interaction through deprotonation, the size effect was examined at pH 3. This pH corresponds to the isoelectric point of silica NPs, minimising electrostatic effects that could otherwise enhance or suppress adsorption.

Results for the hydrophilic α-quartz and α-cristobalite, shown in Figures 6.7A and 6.7B, indicate a significant increase in adsorption affinity with growing NP size.
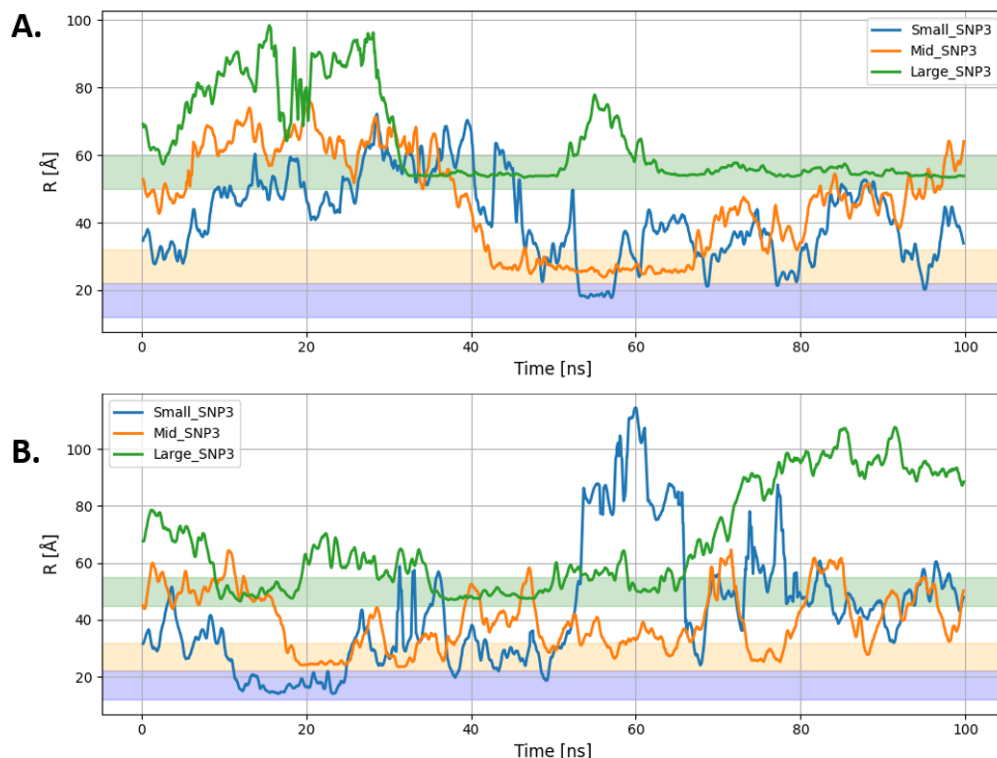
Figure 6.7: R6G adsorption to NPs represented as COM distance plots between the adsorbate and the adsorbent: (A) α-Quartz, (B) α-Cristobalite. A flat line within the shaded box indicates adsorption; a smaller fluctuation amplitude implies greater adsorption stability. "Small" denotes 36 Å diameter SNPs, "Mid" denotes 50 Å, and "Large" denotes 100 Å.

Adsorption time on α-quartz increased from around 5 ns for the 36 Å NP to over 70 ns for the 100 Å NP, a 14-fold increase in adsorption duration corresponding to an $\sim$ 8.5-fold increase in surface area (assuming that particles are perfectly spherical). This is a manifestation of three phenomena:

1. R6G with its flat xanthene core can marginally adjust its shape to match the curvature of the NPs (discussed in detail in Section 6.3.3), therefore smaller curvature and, so larger size will result in more stable adsorption.

2. Larger NPs diffuse more slowly, which aids in adsorption, while smaller NPs, due to their faster diffusion combined with rapid adsorbate movement, reduce the probability of achieving a favourable configuration and successful adsorption.

3. In the case of charged NPs, a higher net negative charge can help guide the positively charged R6G molecule towards the SNP through long-range electrostatic attraction. However, as discussed previously, excessive surface charge can lead to counter-ion layering and screening effects, which in turn suppress adsorption by preventing close contact between the dye and the surface.

A similar trend of increasing adsorption probability with nanoparticle size is observed for cSNPs. However, in this case, adsorption is less stable, as evidenced by fluctuations in the COM plots (Fig. 6.7B), suggesting that adsorbates can move on the surface, desorb, and re-adsorb. This instability is likely due to the lower density of α-cristobalite compared to α-quartz, which results in a higher number of exposed silanol groups on the surface, as discussed in Section 6.3.1. As a result, the adsorbed R6G molecule can form new hydrogen bonds with neighbouring silanol groups, leading to a dynamic adsorption state where movement across the nanoparticle surface is facilitated by the abundance of hydrogen bonding sites.

At other pH values, the overall trend remains consistent. However, the complexity of electrostatic interactions at varying pH levels makes detailed analysis more challenging, as isolating these effects becomes necessary. The comprehensive discussion of pH influence on adsorption is presented in the next section.

In general, it was found that the rate and stability of adsorption increase with NP size. For silica nanoparticles, a threefold increase in diameter, corresponding to an 8.5-fold increase in surface area, leads to a 14-fold increase in the stable adsorption period.

pH Effect

Since NPs are often used in a variety of environments at different pH levels, it is essential to understand the impact of pH on the rate of adsorption. The discussion presented in this section is focused on the 100 Å diameter SNPs because they (1) diffuse slowly, allowing for faster and more effective adsorption, and (2) have relatively low curvature, enabling adsorbates to better adjust their shape, leading to more stable

113

adsorption. Both factors have already been identified as important contributors to the size effect. In this analysis, particular attention is given to α-cristobalite, which offers several advantages: it serves as a useful structural analogue for modelling amorphous silica due to its disorder at the surface, it has been extensively studied and validated in force field development, and its relatively open surface structure facilitates dye-surface interaction studies. To examine the full range of pH values, from acidic to alkaline, three pH values were selected: pH 3 (the isoelectric point of silica NPs), pH 7 (with a 13.3% protonation level), and pH 12 (with 30% protonation). The results of adsorbate interactions with 100 Å α-cristobalite NP at these pH values are shown in Figure 6.8.

In general, with increasing pH, adsorption is gradually suppressed, a direct consequence of surface deprotonation. The adsorbates primarily interact with silica structures via Si-O-H groups through hydrogen bonding [255, 256]. Moreover, the strong affinity of xanthene dyes for SNPs at pH 3 suggests that the adsorption is not primarily driven by electrostatic interactions, as commonly assumed [35, 257], but rather by vdW forces. While experiments and MD simulations conducted at alkaline pH accurately reflect adsorption under those conditions, they can be misleading when interpreting general trends [35, 39, 223]. This is because two effects overlap, making electrostatic interactions more apparent and easier to analyse, potentially overshadowing the underlying contributions of vdW forces, which are dominant at short distances.

The minimal variation in xanthene dye adsorption across acidic to neutral pH values are expected, as the dye structures and charge distributions are very similar, as shown in Figure 6.3. The results in the alkaline range should be treated with caution, since in this regime, the carboxyl group in the RB sidechain becomes deprotonated, and the dye transforms from a cation to a zwitterion, which would result in suppressed adsorption due to electrostatic repulsion from the carboxylic group [258, 259]. Since classical MD cannot model charge transfer, such effects cannot be accounted for in those simulations. Although *ab initio* MD can model charge transfer, it is computationally expensive and cannot easily be performed over the long timescales required to study adsorption dynamics.
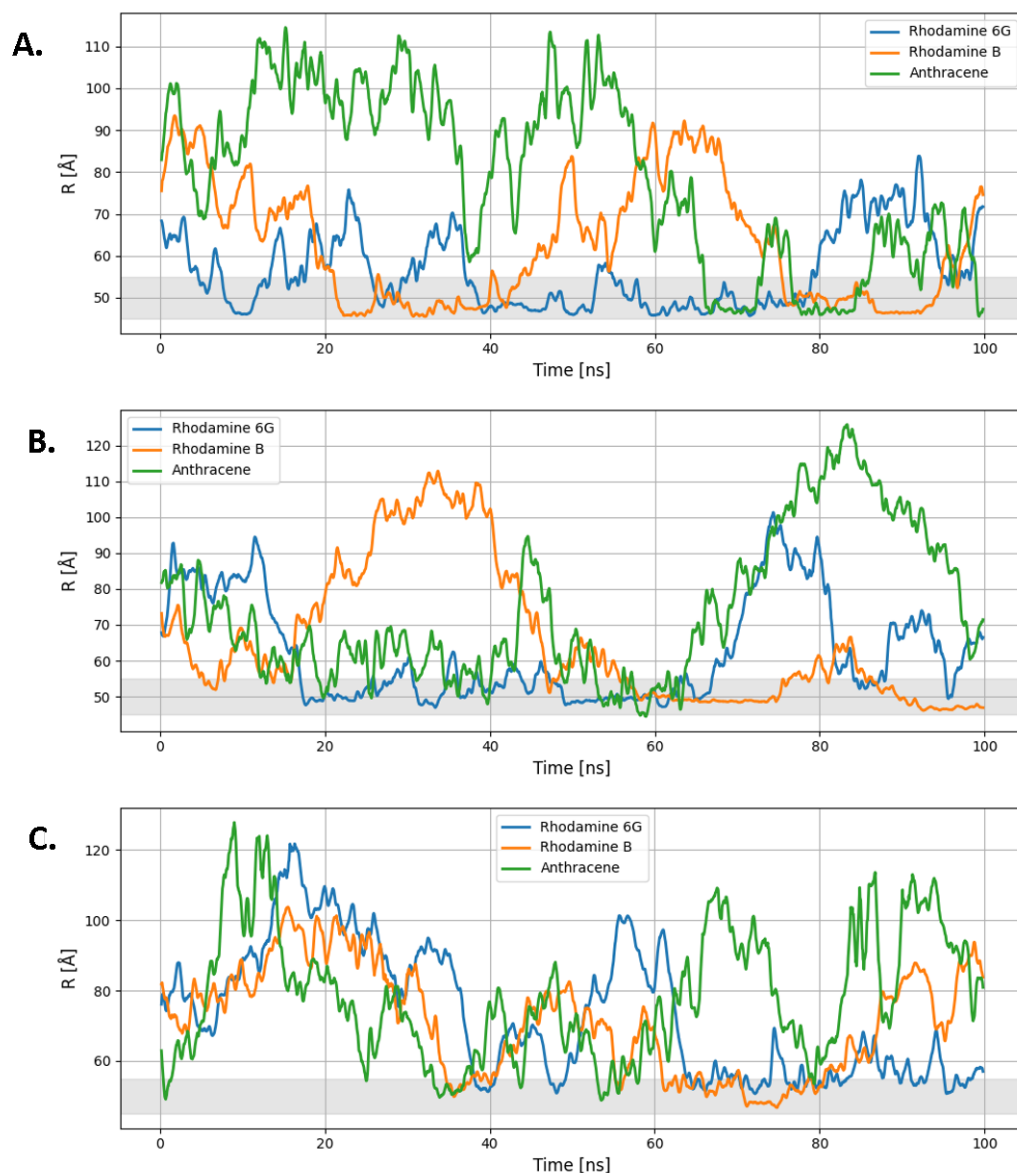
Figure 6.8: COM distance plots of various adsorbates during adsorption to a 100 Å α-cristobalite nanoparticle at different pH levels: (A) pH 3, (B) pH 7, and (C) pH 12. Adsorption is indicated when the COM distance plots remain stable within the shaded region for a certain period of time.

Finally, it is important to consider the effect of polarity on adsorption. Simplified molecular analogues, such as anthracene, which closely resemble the xanthene core, can be used to model more complex dye structures, providing a clearer understanding of

adsorption mechanisms across different systems explored in this thesis. A closer inspection of the COM plots shown in Figure 6.8 reveals that the polarity of the adsorbent significantly affects adsorption. Specifically, anthracene adsorbs less effectively than both xanthene dyes, which can be attributed to its highly hydrophobic nature. This hydrophobicity prevents it from adsorbing to the highly hydrophilic silica, especially at high pH, where 30% of the surface hydrogens are replaced with sodium ions. This reduces the number of available hydrogen bonding sites and suppresses adsorption. Additionally, the hydrophobic nature of the xanthene dyes contributes to the dimer formation, as individual monomers seek to minimise the area exposed to water. A detailed discussion of this dimerisation phenomenon can be found in Chapter 7.

The increase in pH suppresses the adsorption through two main mechanisms:

1. **Deprotonation of silanol groups:** As pH rises, silanol groups are deprotonated, reducing the number of available hydrogen bonding sites for adsorption.

2. **Formation of a counter-ion layer:** Deprotonation creates a positive counter-ion layer on the nanoparticle surface to neutralize the effect of deprotonation. This layer generates a repulsive force against positively charged dye, such as R6G or RB. For adsorption to occur, at least one of these counter-ions must be displaced, which significantly hinders the adsorption process.

For smaller nanoparticles, the overall trends are generally the same. However, the analysis becomes more complicated due to the increased mobility of these particles, which introduces additional noise into the results.

6.3.3 R6G Adsorption Mechanics and its Effect on the Complex Size

With the general R6G–SNP dynamics clearly understood, the next step is to examine the R6G adsorption mechanism in more detail. Since adsorption is highly pH-dependent, the analysis of R6G adsorption and its orientation on SNP mainly focuses on results obtained at pH 7. While this pH is not ideal due to the presence of sodium ions complicating the analysis, their inclusion is essential for accurately assessing adsorption

dynamics under realistic experimental conditions. This ensures a more representative observation of adsorption behaviour and the role of sodium ions in the system.

Protocol

A separate set of simulations was conducted to examine the impact of R6G size on the experimentally measurable size of the R6G–SNP complex. Specifically, eight systems were prepared, each containing six R6G molecules, one 40 Å α-quartz or α-cristobalite NP (both at pH 7 and pH 12), or three 20 Å α-quartz/α-cristobalite NPs at both pH values. The initial system setup for 40 Å and 20 Å SNPs is visualised in Figure 6.9, and the total number of atoms per system was around 85,000. For detailed comparison, refer to Table 1. Since R6G serves as the label dye throughout this thesis, the analysis focuses exclusively on its behaviour, excluding other potential adsorbates. Simulations at pH 3 were not performed for this part of the study, as this acidic regime does not reflect the experimental conditions used in FRAP or anisotropy measurements, which are typically carried out under alkaline conditions with sodium counterions present.
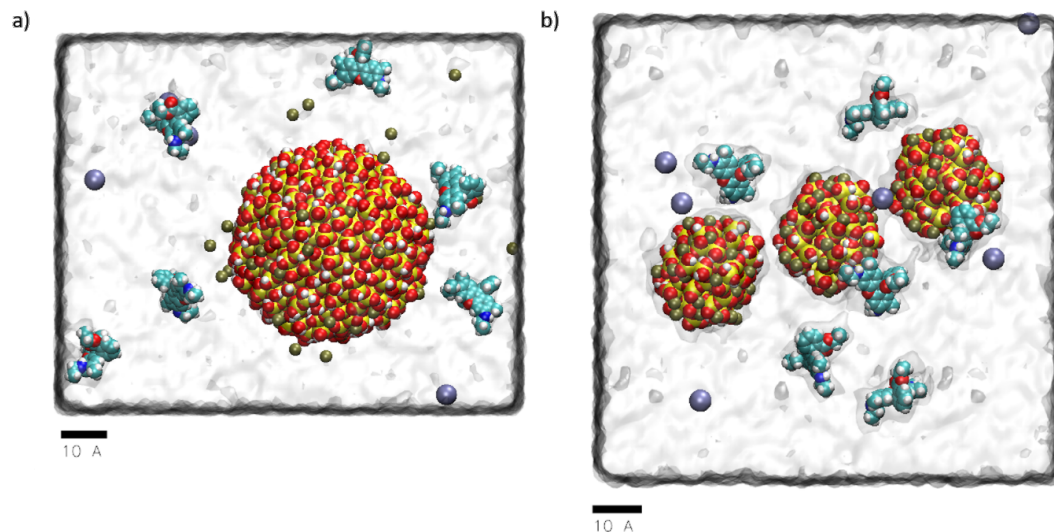
Figure 6.9: Initial system setup. (a) Example of 40 Å SNP system, containing one SNP and six R6G molecules; (b) Example of 20 Å system, containing three SNPs and six R6G. Water is indicated by the transparent film while oxygen (red), silica (yellow), hydrogen (white), carbon (cyan), chlorine (ice blue), and sodium ions (tan) are indicated by VdW spheres. Note the scale of each system.

R6G Adsorption Mechanics

The simplified dye–NP COM distance plot as a function of simulation time for the two best-adsorbing R6G molecules at pH 7 is shown in Figure 6.10a. Initially, both R6G molecules are approximately 15 Å away from the SNP surface, which ensures that the molecules are not subject to vdW forces, which might bias the system into adsorption. After initial free diffusion, they form a dimer at around 15 ns, which dissociates around 40 ns. For a detailed dimerization study refer to Chapter 7. At around 63 ns, the R6G represented by the red line adsorbs to the SNP surface and stays adsorbed until the end of the trajectory, which corresponds to state A.
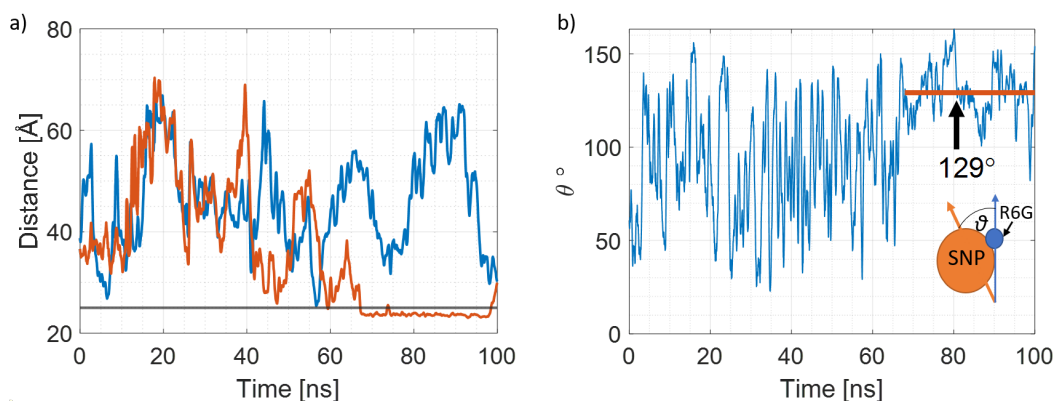
Figure 6.10: R6G adsorption process. (a) Simplified COM distance plot for two best adsorbing R6G molecules, R6G_4 (blue) and R6G_5 (red). The grey line marks the 5 Å distance from the SNP surface; (b) Angle (θ) between SNP and R6G_5 dipole moments. The red line represents the average θ when the R6G_5 is adsorbed. The inset on 6.10b shows how the θ angle was measured.

Notably, multiple monomeric R6G adsorption was not observed, which can be attributed to the requirement for antiparallel dipole moment orientation in this asymmetrical molecule (relative to the xanthene core plane; see Figure 6.12b). This behaviour was consistently observed across all independent trajectories—eight systems featuring SNPs of various sizes and pH values, with four independent runs per system. Specifically, adsorption on opposite sides of the SNP would require either (i) interaction through the tail side of the xanthene core with an antiparallel dipole orientation or (ii) interaction via the flat side of the xanthene core but with parallel dipole orientation.

However, results show that effective adsorption requires the R6G dipole to be antiparallel to the SNP's dipole, with the xanthene core oriented flat against the SNP surface. This is consistent with previous studies on R6G dimerization, where interactions occurred via the flat surfaces of the molecule, with the side chains projecting outward from the dimer [236, 260]. As a result, only a single R6G monomer can adsorb per SNP, regardless of nanoparticle size, making the formation of an R6G monolayer on the surface energetically or geometrically unfavourable. It is important to note that these observations pertain specifically to pH 7 conditions, where adsorption is primarily driven by electrostatic interactions. At lower pH values (e.g., pH 3), adsorption behaviour differs due to the increased influence of van der Waals forces, as discussed previously.

An alternative method of identifying the R6G state is monitoring the orientation of R6G and SNP dipole moments, which in the case of adsorption should be anti-parallel (the angle θ between them should be 180°). It is important to note that a 180° angle might be achieved only in the ideal case of two isolated dipoles. In this specific case of a system containing six R6G molecules, the dipoles of interest are not isolated, as each R6G molecule has its own dipole moment. The electric field in the system is further shaped by the presence of ions, creating a highly complex electrostatic environment. Every component remains dynamic, freely diffusing and rotating, adding to the intricacy of local interactions. Therefore, the R6G of interest needs to constantly adjust its orientation to the fluctuations of the electric field around it. For this reason, expected θ values are in the range of 90° to 180°, and achievement of a stable angle of 180° is unlikely. As illustrated in Figure 6.10b, the angle θ fluctuates between approximately 25° and 150°, which is a result of the SNP being almost stationary due to its large size and a free R6G that is moving freely. At around 63 ns, the system settles down, θ begins to change more slowly and within a narrower range. From 63 ns to 100 ns, it fluctuates around a mean of 129°, suggesting that a stabilising interaction has been established. This observation, combined with Figure 6.10a and visual analysis, indicates that R6G adsorbed onto the SNP, or in other words, state A (stable adsorption) was achieved. It is important to note that fluctuations of the θ angle value at state A are a reflection of

the complicated electric interactions in the simulation system.
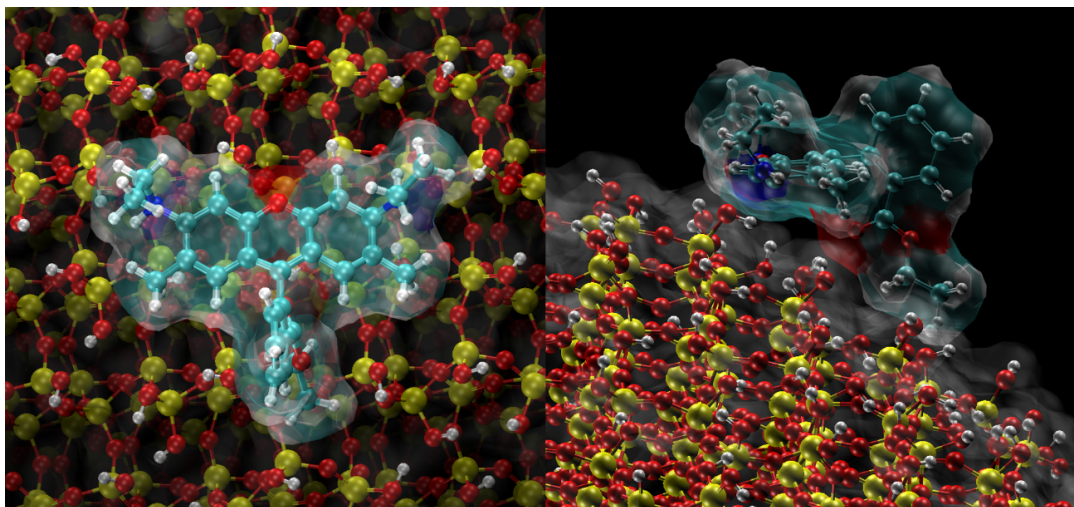
Figure 6.11: R6G adsorption on SNP. Left: Top view of the adsorbed R6G; Right: Side view of the adsorbed R6G. Atoms are represented as ball-and-stick.

The above analysis indicates that R6G adsorption onto SNP might be identified by:

1. visual analysis of the trajectory,

2. monitoring the R6G–SNP COM distance,

3. monitoring the angle between the dipole moment of each R6G molecule and the SNP.

Figure 6.12a shows the COM distance as a function of simulation time for the two best-adsorbing R6G molecules at pH 7 for the 40cSNP7 system. Similarly to 40qSNP7, in the case of 40cSNP7 systems, the dye molecules were initially more than 12 Å away from the SNP surface, which indicates there are no non-bonded interactions that would bias the system and/or drive R6G molecules towards adsorption. After a short ~ 3 ns period of free diffusion in the electrostatic field sourced by 40cSNP and modified by solute ions, R6G_3 adsorbs onto the SNP surface, where it stays for 16 ns (until the 19th ns). The next adsorption event happens at around the 39th ns when, after long free diffusion, R6G_4 adsorbs to the surface of the SNP and stays adsorbed until the 43rd ns, when it experiences interactions with R6G_3, forms a dimer at 50 ns, and

desorbs at 80 ns. It is important to note that both adsorption events are not very
stable and, therefore, are identified as states R/A, but not state A as in the case of
40qSNPs. That is because, on the COM distance plot, the reported adsorption events
are represented as multiple and relatively short interactions. A closer look at the
plots indicates that during the events observed in the periods 3–19 ns and 39–43 ns,
there are notable distance fluctuations that contradict the definition of state A (stable
adsorption). Nevertheless, the plots and visualization of R6G behaviour suggest that
this is state R/A, when, according to the definition, the R6G molecule is near the SNP
surface (so it might seem to be weakly adsorbed), but the orientation of the xanthene
core is being changed. Although the adsorption is not as stable as in the case of
40qSNP7, the R6G_4 xanthene core is still oriented parallel between 39 ns and 43 ns.
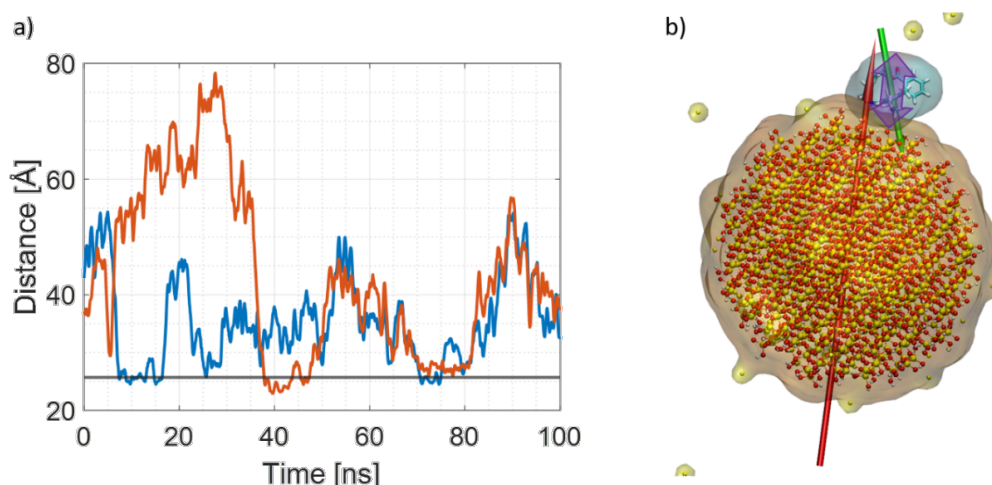
Figure 6.12: R6G adsorption on 40cSNP7. (a) Simplified COM distance plot for two
best adsorbing R6G molecules, R6G_3 (blue) and R6G_4 (red); the grey line marks the
5 Å distance from the SNP surface. (b) 40cSNP7–R6G complex with visualised dipole
moments.

The events observed from the 50th ns until the end of the trajectory are related to
R6G dimer interactions rather than a monomer. During this period, R6G_3 and R6G_4
are dimerised (details regarding R6G–R6G interactions are presented in Chapter 7),
hence, the interaction with SNP observed between 70 and 80 ns cannot be classified
as monomer adsorption. During this time, the R6G dimer approaches the SNP at

a distance, suggesting possible adsorption of monomeric R6G. Nevertheless, due to the competition between the forces governing adsorption and those holding the dimer together, neither of the R6G molecules can orient its xanthene core parallel to the SNP surface. Dimer adsorption on the SNPs is not observed due to geometric restraints, as the flat parts of the core face the other R6G molecule rather than the SNP, and successful adsorption requires the xanthene core to align parallel to the surface. Hence, although the R6G dimer may spend some time near the SNP, stable adsorption is not possible because the optimal geometry and electrostatics cannot be achieved. Moreover, the R6G–R6G vdW forces are weaker than the SNP–R6G electrostatic attraction, and as a result, dimer dissociation and adsorption of monomeric R6G to the SNP, as well as dimer–SNP interaction and desorption, are observed. This section is included to clarify the interpretation of the distance plots; a full analysis of dimer behaviour is presented separately in Chapter 7.

In the case of 20qSNP7, adsorption is represented as a series of multiple short interactions with R6G repositioning spontaneously, which corresponds to state R/A. As shown in Figure 6.13a, the R6G–20 Å SNPs COM distance never goes beyond the "stable adsorption" distance of 5 Å to the SNP surface. At pH 12, neither the adsorption state A nor R/A is detected; the COM distances are not stabilising in any case (Figure 6.13b). For a detailed discussion of the pH impact on adsorption behaviour, refer to Section 6.3.2. Furthermore, R6G molecules stay far away from any SNP for a longer time than was observed in the case of 40 Å SNPs. It might be a result of the more complicated electrostatic field with more sources. The electrostatic field exerted on particular R6G molecules is now a superposition of electric fields created by all three NPs, other R6G molecules and solute ions. To adsorb/interact with any SNP, R6G needs to be well-oriented with respect to all three SNPs while prioritising one of them; hence the lag time is longer so the entire process slows down significantly. Furthermore, 20 Å SNPs diffuse faster than 40 Å ones; therefore, the field fluctuations are larger which additionally impacts the adsorption speed. Lastly, the charge of 20 Å SNP is significantly lower than 40 Å ones, resulting in a lower electrostatic attraction to that specific SNP (see Table 1 for system details) and the dipole moment values

discussed in subsection 6.3.1.
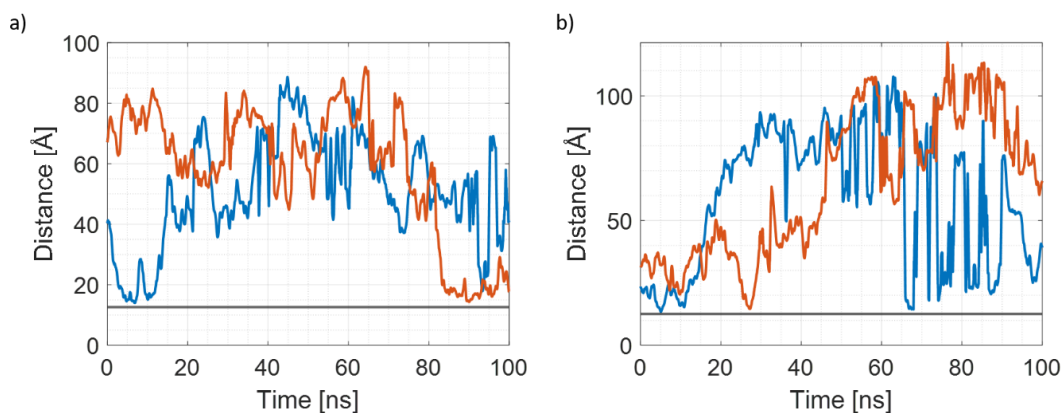
Figure 6.13: COM distance plots for 20qSNPs. a) Simplified COM distance plot for two best adsorbing R6G molecules, R6G_1 (blue) and R6G_2 (red) for 20qSNP7; b) Simplified COM distance plot for two best adsorbing R6G molecules, R6G_1 (blue) and R6G_2 (red) for 20qSNP12. The grey line marks the 5 Å distance from the SNP surface.

In summary, at acidic to neutral pH values, adsorption is primarily driven by vdW interactions due to the low or absent surface charge of the SNPs, whereas at high pH, increased SNP negative charge leads to adsorption dominated by electrostatic interactions, as discussed in subsection 6.3.2.

6.3.4 Selective Adsorption

To assess whether dye adsorption to the SNP is size- and charge-dependent, MD simulations were performed on a system consisting of one large SNP and three small SNPs with varying dye amounts. Given that silicates are polydisperse, it is essential to investigate how adsorption occurs in systems with multiple SNPs of different sizes. This approach helps to understand the influence of size variation on the adsorption dynamics in a more realistic, diverse nanoparticle environment.

Protocol

To match the experimental conditions and mimic the prepared binary LUDOX samples discussed in Chapter 9, the pH of the system was set to 9 through the deprotonation of

the surface silanol groups of the SNPs. As simulating SNPs at their real sizes (12 nm and 22 nm diameter) would be computationally expensive, the system was rescaled to reduce the computational cost. Based on linear scaling, simulating a 100 ns trajectory of a system consisting of 300,000 atoms took approximately 72 hours, so a system of 3 million atoms was estimated to take around 720 hours (30 days). However, considering PME overhead and GPU communication, a more realistic estimate for 3 million atoms would range between 800 and 1000 hours (33–42 days). Namely, the 12 nm diameter HS40 SNP was modelled as 51.4 Å, while the 22 nm AS40 was modelled as 102.6 Å diameter SNP. This allowed maintaining the SNP size ratio of around 2, while significantly reducing the computational costs. However, it is essential to point out that the system rescaling artificially suppresses the dye-to-SNP adsorption arising from the increased SNP diffusivity, larger curvature, and reduced total net negative charge of the SNP when compared with their full-sized counterpart. As a result, the observed simulation mechanics should act as a guide by indicating the trends rather than exactly replicating the experimental conditions. Each system had one large SNP and three small SNPs in all cases, with the dye molecule number ranging from one to four. Moreover, in the obtained MD systems, R6G exhibits a threefold higher probability of adsorbing to the smaller SNPs compared to larger ones, primarily due to their threefold greater abundance. Due to varying R6G concentrations, the above resulted in four simulation systems, each containing a single 102.6 Å diameter SNP surrounded by three 51.4 Å SNPs and 1, 2, 3 or 4 dye molecules. The R6G molecules were positioned to ensure equal probability of adsorption onto any SNP, avoiding bias toward a specific one with the minimal distance between each of the system components being no less than 15 Å. The total number of atoms per system was around 450,000. The initial system setup is shown in Figure 6.14.
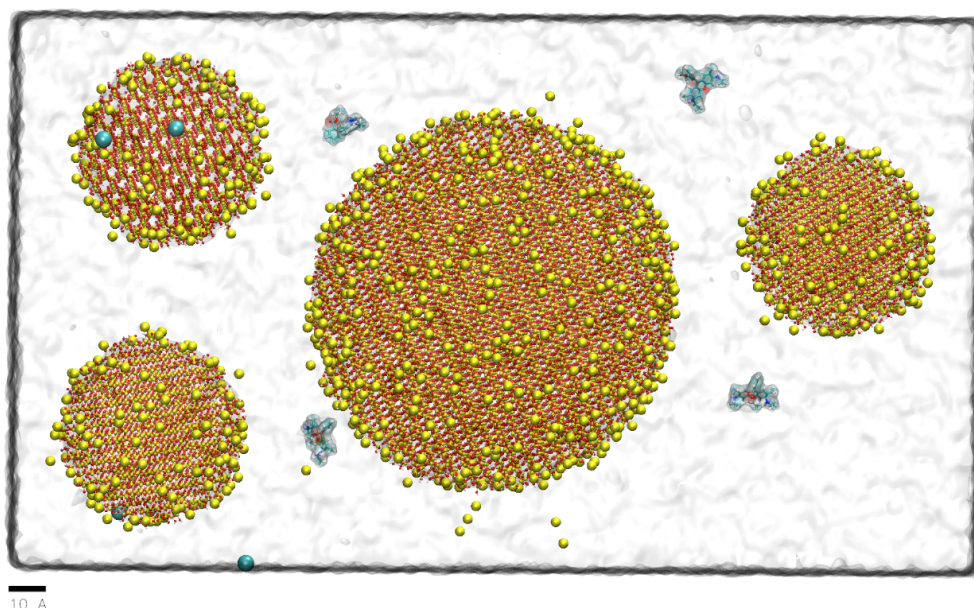
Figure 6.14: Initial system setup. Water is indicated by the transparent film, the SNPs are represented using CPK representation, ions as vdW spheres, and R6G molecules as liquorice, with the following colour coding: oxygen-red, silica-yellow, hydrogen-white, carbon-cyan, chlorine-ice blue, sodium-large yellow spheres.

Size-Dependent Adsorption

Figure 6.15 presents the COM distance plots as a function of simulation time for each dye–SNP pair in a system containing four dye molecules.
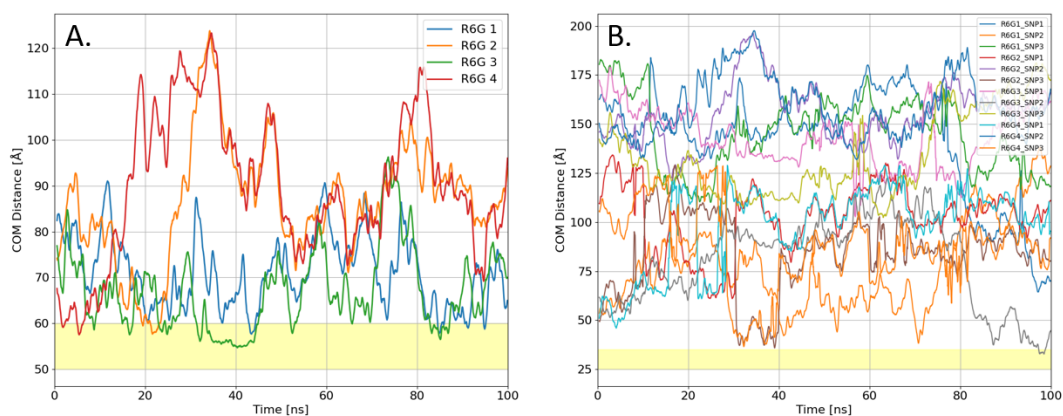
Figure 6.15: COM distance plots. **A.** Each of the four R6G molecules to the 102.6 Å diameter SNP; **B.** Each R6G–51.4 Å SNP pair. The shaded yellow area marks the range of successful adsorption.

Simulation results indicate that dye adsorption probability and stability are strongly influenced by the radius of the target SNP. It is likely due to the higher net negative charge of the large SNP, which facilitates the localisation of favourable adsorption sites for the free R6G molecules. Furthermore, the smaller curvature of larger SNPs allows for better shape adjustment for the adsorbing dye, resulting in more stable binding. This is evident in the prolonged period of unchanged COM distance (~ 32 ns to ~ 45 ns) for the large SNP, compared to the much shorter adsorption duration (~ 100 ns) for smaller SNPs.

The presence of R6G dimers in the system is also notable and can be identified in the COM distance plots, where overlapping curves of different dyes suggest that two R6G molecules move together. However, as previously discussed, these dimers do not adsorb onto SNPs and are non-fluorescent, meaning they have no impact on FRAP measurements [38,39]. This preferential adsorption of R6G to larger SNP is consistently observed in other systems with fewer dye molecules (data omitted for clarity). Furthermore, in a polydispersed system, the complexity of electrostatic interactions among SNPs of different sizes and dye molecules significantly suppresses adsorption compared to an isolated, monodispersed system [38]. Despite this suppression, the overall trends remain consistent. In such a system, successful adsorption requires R6G molecules to adjust their orientation and conformation in response to the system's superimposed electric field while maintaining close proximity to an SNP to enable short-range vdW interactions to stabilise the SNP–R6G complex.

In summary, MD simulations demonstrate that R6G adsorption rates are highly dependent on SNP size, with larger SNPs promoting stronger binding. This is largely attributed to their greater net negative charge and smaller curvature, which facilitate dye conformation adjustment during adsorption. A similar trend was observed in FRAP experiments on binary particle systems, presented in Chapter 9, where lower dye concentrations allowed for more precise measurement of larger SNPs, even when the concentration of those was significantly lower than that of smaller SNPs.

6.3.5   Effect of R6G Adsorption on the Dye-SNP Complex Size

Now that the effects of crystal structure, SNP size, pH, and adsorption mechanics have been systematically investigated, the final and arguably most important question remains: What is the actual contribution of the dye to the overall size of the SNP–dye complex? Both time-resolved fluorescence anisotropy and FRAP rely on diffusion-based readouts, meaning that they don't measure the nanoparticle itself but the entire fluorescent complex. Understanding how much the presence and orientation of R6G alters the apparent size is, therefore, critical for making accurate measurements and meaningful comparisons across experimental conditions.

The VMD-measured diameter of the SNP alongside the diameter of the nanoparticle–R6G complex as a function of the simulation time is shown in Figure 6.16. In the case of the 40 Å diameter particle, even when the biggest possible distance between the furthest R6G and a silicate oxygen atom on the other side is taken into consideration, the dye contribution to the measured complex size is in the range of 10% (yellow line). However, by looking at the size of the R6G on its own and adding it to the SNP size, it is evident that the obtained value is significantly larger than the actual, measured size of the R6G–SNP complex (purple line). This suggests that the shape of the SNP plays a crucial role when measuring the size. Moreover, the dye may not lie entirely flat on the surface, but marginally adjusts its shape to match that of the NP, as shown in Figures 6.16 and 6.11. The complex size is, therefore, smaller (yellow line) than the added sizes of separated counterparts (purple line).
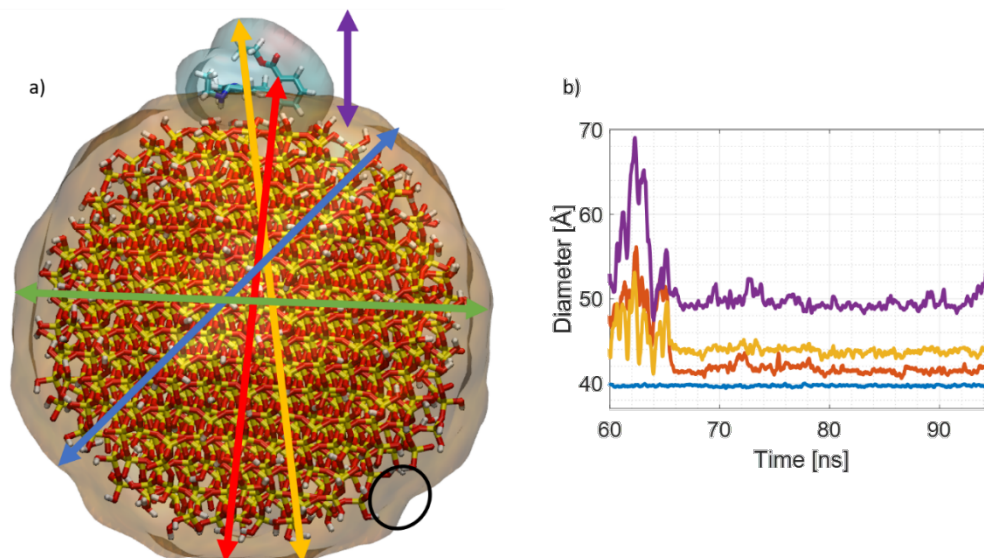
Figure 6.16: 40 Å diameter SNP size measurements. a) SNP–R6G complex. The black circle indicates local SNP surface irregularity, while the arrows represent the directions of distance measurements. The colour code consists of green and blue, which denote the SNP diameter measured in two different directions, red indicates the distance between the R6G xanthene core atom and the SNP atom on its opposite side, yellow signifies the largest distance between any R6G and SNP atom, and purple illustrates the maximal thickness of adsorbed R6G molecules. All atoms are depicted by thick sticks coloured according to atom type: oxygen is red, silica is yellow, hydrogen is white, carbon is cyan, and nitrogen is blue. To illustrate the size of the complex, the dye's surface is represented transparently. b) Measured diameter of the SNP–R6G complex as a function of simulation time; the colour code corresponds to the arrows code, while the purple line simply sums the R6G thickness and SNP diameter.

The situation is somewhat different in the case of smaller SNPs. The size contribution of R6G is significantly larger in these examples and can be up to 50% of the measured size. The main reason is that 20 Å SNPs are significantly more curved when compared with 40 Å diameter SNPs. R6G, which is relatively rigid at its xanthene core plane, therefore cannot bend enough to match precisely 20 Å SNPs curvature (Figure 6.17).
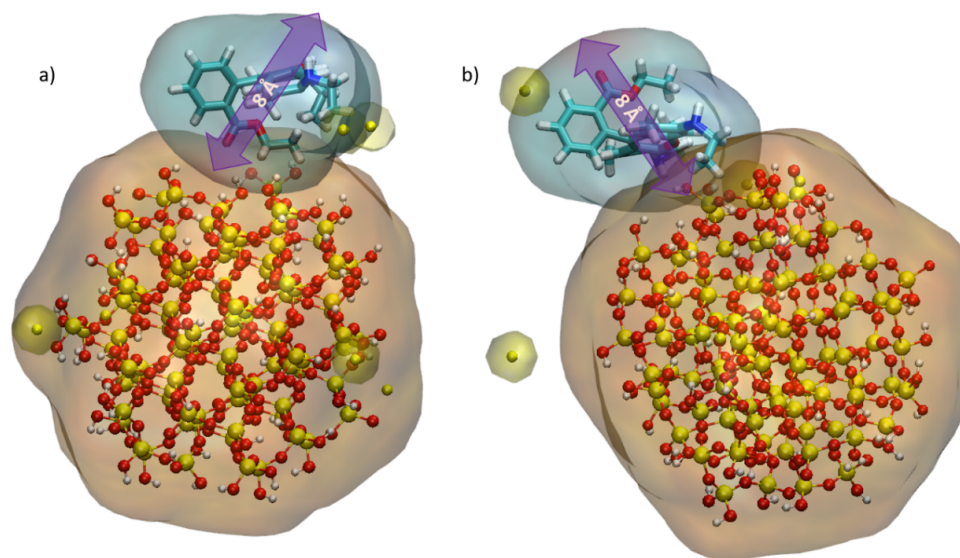
Figure 6.17: SNP-R6G structure. (a) 20qSNP7-R6G complex; (b) 20cSNP7-R6G complex

Finally, it is important to address the assumption of the SNP shape. In all simulations, the NPs were modelled as perfectly spherical- a common and practical simplification in molecular dynamics, given its symmetry and straightforward implementation. However, this may not reflect real-life systems, where particle shape can vary due to synthesis conditions or surface effects. While the spherical model provides a consistent baseline for comparing adsorption and diffusion behaviour, it may underestimate the complexity of real diffusion dynamics, particularly in techniques like FRAP or anisotropy, where shape plays a direct role. Although beyond the scope of this work, incorporating more realistic geometries, such as ellipsoids, could offer further insights into the influence of particle shape on the observed dynamics.

A recent study by G. Hu et al. using SAXS demonstrated that silicates with a ratio below 4.2 tend to form ellipsoidal primary particles, suggesting that the spherical MD model may not fully capture the actual particle morphology [261]. This shape anisotropy also means that, in the case of an ellipsoidal particle, the dye could preferentially adsorb onto the larger, flatter surface area. The lower curvature of this region

allows R6G to better align with the surface, potentially reducing its contribution to the apparent hydrodynamic size. As a result, the dye's impact may fall within the typical experimental uncertainty, often in the range of 20–30%, effectively masking its presence. A more detailed analysis of this effect is presented in Chapter 8.

6.3.6   Estimation of Dye–SNP Dissociation Barriers from Residence Times

Having established how the presence of R6G affects the apparent size of the SNP–dye complex, it is also important to consider the strength and timescale of the dye's interaction with the nanoparticle surface, which can be estimated from residence times observed in the simulations.

The connection between residence times and binding free energies can be framed through Eyring transition state theory, which describes how a system crosses an energy barrier separating bound and unbound states. In this formalism, the rate constant (k, the probability per unit time of desorption) for dissociation is given by

$$k = \frac{k_B T}{h} \exp\left(-\frac{\Delta G^{\ddagger}}{RT}\right), \tag{6.1}$$

where $\Delta G^{\ddagger}$ is the activation free energy barrier for dissociation, k_B is the Boltzmann constant, T is the absolute temperature, h is Planck's constant, and R is the gas constant. Since simulations provide residence times, τ, these can be inverted to rates ($k = 1/\tau$) and used to estimate $\Delta G^{\ddagger}$. The microscopic attempt frequency—the rate at which the system "tries" to cross the barrier—appears naturally in the Eyring prefactor, with

$$\tau_0 = \frac{h}{k_B T} \approx 1.6 \times 10^{-13} \text{ s} \tag{6.2}$$

at room temperature. This τ_0 reflects the vibrational timescale of molecular bond fluctuations and is not an adjustable parameter.

Applying this to the present system, residence times ranging from 1 to 100 ns correspond to activation free energies of roughly 5–8 kcal·mol^{-1}. The conversion comes

from rearranging the Eyring equation:

$$\Delta G^{\ddagger} = -RT \ln \left(\frac{kh}{k_B T} \right) = RT \ln \left(\frac{\tau}{\tau_0} \right) \tag{6.3}$$

Each order-of-magnitude increase in τ raises the barrier by ~ 1.36 kcal·mol^{-1} at 300 K. These values indicate interactions stronger than simple van der Waals contacts ($\sim$ 1–2 $k_B T$), but weaker than covalent bonds (> 50 kcal·mol^{-1}), placing them in the range characteristic of hydrogen bonding (3–7 kcal·mol^{-1}) and weak electrostatic interactions [262]. This aligns with the expected chemistry of the SNP surface, which features silanol groups interacting with the cationic R6G molecules.

It is important to note that this approach estimates activation free energies for dissociation ($\Delta G^{\ddagger}$), not the total binding free energy (ΔG_{bind}), which also includes entropic contributions and the equilibrium constant of association. Accurate ΔG_{bind} values would require knowledge of both association and dissociation rates ($K_d = k_{\text{off}}/k_{\text{on}}$), or extensive free-energy calculations such as umbrella sampling, metadynamics, or potential of mean force methods. Nevertheless, the present approach provides a consistent way to interpret simulation observables: residence times on the order of tens of nanoseconds indicate moderately strong, reversible interactions, in line with chemical intuition for dye–silicate interactions.

While these activation free energies cannot be directly equated to rupture forces from steered molecular dynamics simulations, a qualitative correlation can be expected: higher $\Delta G^{\ddagger}$ values should correspond to stronger mechanical resistance to dye desorption. For context, barriers in the 5–8 kcal·mol^{-1} range are in line with typical hydrogen bonds (3–7 kcal·mol^{-1}), stronger than transient hydrophobic contacts (<3 kcal·mol^{-1}), and comparable to interactions seen in dye–lipid binding ($\sim$5–10 kcal·mol^{-1}) [262,263]. This aligns with the planar, cationic nature of R6G, which favours electrostatic and hydrogen-bonding interactions with the silicate surface while allowing dynamic exchange.

To obtain directly comparable thermodynamic binding energies, future work could combine equilibrium free-energy methods, such as umbrella sampling, PMF calcula-

tions, or metadynamics, with experimental adsorption constants. This would place the kinetic barriers derived here on the same scale as ΔG_{bind} for dye–DNA or dye–lipid interactions, providing a rigorous cross-system comparison.

Comparisons with other systems further contextualise these values. For example, R6G binding to DNA has reported equilibrium free energies of -9.5 to -8.1 kcal·mol^{-1} [264]. While these describe thermodynamic stability (ΔG_{bind}) rather than kinetic barriers ($\Delta G^{\ddagger}$), the similar energetic range supports the chemical plausibility of the present estimates. Overall, the 5–8 kcal·mol^{-1} barriers correspond to interactions strong enough to stabilise adsorption on nanosecond timescales, yet weak enough to allow dynamic exchange–a hallmark of reversible surface labelling rather than permanent adsorption.

6.4   Conclusions

This chapter provides a detailed molecular-level view of xanthene dye interactions with SNPs, focusing on how surface structure, particle size and pH influence adsorption mechanics and, ultimately, the measured size of the SNP-R6G complex, as obtained in the experiments. Across a broad simulation set, several consistent trends were identified.

Increasing the pH led to progressively weaker dye adsorption. At pH 3, which is the isoelectric point of the SNPs, at which the surface is neutral, a strong vdW-driven binding was observed. However, the whole process was rather slow due to the lack of long-range electrostatic interactions, which would promote the adsorption by guiding the cationic dye towards an anionic SNP. At pH 7, where 13.3% of surface silanol groups are deprotonated, a moderate repulsion is introduced; however, the adsorption is still stable and happens relatively fast due to the Coulombic attractive forces between the dye and SNP. However, at pH 12, where the ionisation degree is 30%, a highly charged surface is created, which, when screened by counter-ions, forms a diffuse electric double layer that significantly suppresses the adsorption. These electrostatic effects not only control whether the dye adsorbs or not but also how it orients and diffuses near the surface. Furthermore, it controls the dimerisation process, which is discussed in detail

in the next Chapter.

Larger NPs (e.g., 100 Å diameter), due to their lower surface curvature and, in the case of charged surface, higher net negative charge, showed significantly more stable adsorption. The flatter SNP surface allows better alignment of the dye's planar xanthene core, resulting in longer residence times and less rotational freedom. In contrast, smaller SNPs with higher curvature disrupt optimal binding geometry and, when combined with their increased diffusion rates, lead to weaker and less persistent adsorption. Moreover, the dye consistently showed preferential adsorption to larger SNPs, where the lower curvature and broader surface area offered more favourable binding configurations and longer surface residence times.

Lastly, the most important question was investigated, which is the impact of the dye size on the apparent hydrodynamic size of the SNP-dye complex. Simulations revealed that when the dye is strongly adsorbed and the xanthene core is aligned perfectly parallel to the SNP surface, especially on large, low-curvature SNPs, its contribution to the complex size is minimal and often under 15%, therefore it falls within the experimental error margin, which can be 20–30%. Therefore, in such cases, the dye contribution is negligible, and the measured size is, within the error margin, equal to the SNP size. However, when the dye is loosely bound, or fluctuates in orientation, which is the case in the small radius SNPs, its spatial footprint becomes more significant, approaching 50%, potentially skewing diffusion-based measurements such as FRAP or time-resolved anisotropy. In spherical models, this effect is more pronounced, as shown in this chapter, whereas flatter ellipsoidal geometries help bury the dye's influence, as further discussed in Chapter 8.

Together, these findings not only highlight the key factors governing dye–SNP interactions but also clarify how structural and environmental variables influence the diffusion measurements and the resulting particle size estimate. This provides a crucial foundation for improving the accuracy of fluorescence-based nanometrology and interpreting experimental data in complex colloidal systems.

Chapter 7

Dynamics of Xanthene Dyes in the Presence of Silica Nanoparticles: Rhodamine 6G Dimerisation

7.1   Introduction

One important feature that directly affects the usability of R6G is its tendency to form dimers at high concentrations. The H-type aggregates that are formed are not fluorescent, so obtaining the accurate values of the dimer binding energies is important for optimising constructs based on R6G's fluorescent properties, such as labelled NPs. Measurements of dimerisation energies, especially in solutions, are experimentally very demanding, or even currently impossible, so computational estimates of the stability of dimers in solutions are irreplaceable. Therefore, in this Chapter, the possibility of R6G dimerisation in the presence and absence of SNPs was explored, which was previously studied by Dare-Doyen et al. and Chuichay et al [236, 260]. However, a more complex approach was taken here, compared to their work, by examining larger systems containing six R6G molecules in the presence of SNP and solute ions.

R6G is a cationic dye with a $+1e$ charge, and, from an electrostatic perspective, its molecules should repel each other. However, regardless of the number of R6G molecules present in the system, free R6G consistently tends to form dimers without any interaction with solute ions, as observed in previous studies [260, 265, 266]. Understanding the driving forces behind this dimerisation, whether through π-π stacking, dispersion forces, or other non-covalent interactions requires accurate computational modelling. To achieve this, advanced electronic structure methods must be employed to account for the intricate interplay of these forces.

In recent decades, Kohn-Sham DFT [136] has become a primary tool to probe the electronic structure of molecules and address many-electron problems, which are crucial for advancing our understanding of modern physics, chemistry and biology [267, 268].

The popularity of DFT stems from its excellent balance between its reliability and computational cost, offering significantly greater accuracy than modern semi-empirical methods while being much less computationally demanding than the gold standard of the field: the CCSD(T) approach [269, 270]. However, the CCSD(T) model [271] scales as N^7 (where N is a measure of the system size), requiring a substantial amount of computational resources. Other sophisticated post-HF methods, such as second-order

many-body perturbation theory with the Møller–Plesset partitioning of the Hamiltonian (MP2), scale as N^5 [272]. While more feasible than CCSD(T), MP2 is still a rather demanding approach. Efforts to speed up those methods, such as the domain-based local pair-natural orbital (DLPNO) methods, resulting in DLPNO-CCSD(T) with nearly linear scaling, or the RIJCOSX-MP2 method, have been developed [273]. However, the requirement for a large basis set in post-HF methods, needed to minimise the BSSE, limits the system size that can be effectively calculated using those approaches [274, 275].

On the other hand, the theoretical details and caveats of DFT are very well understood, with ongoing improvements addressing its weakness, such as the addition of dispersion correction, which mitigates known significant drawbacks of DFT [167, 276, 277]. Furthermore, DFT is considered a robust theory, and failures in the form of completely erroneous results are relatively rare, even when applied to complex molecules or exotic systems. This reliability has made DFT a black-box-like method that non-experts can successfully apply to various problems without needing to delve deeply into the complex underlying theory [278]. However, accurately interpreting DFT results still requires specialist knowledge.

Nonetheless, calculations of large systems are still very demanding, even with the additions mentioned above and different approximations such as "Resolution of the Identity" (RI) [279] and "Chains of Sphere" (COSX) [280] as implemented in ORCA [240, 241] or SENEX [281] in TURBOMOLE [282], and the help of state-of-the-art HPCs. A method that provides faster, yet comparable, results is essential for accelerating scientific progress. To address this, an SMD-based approach is introduced to measure the binding energies of aromatic dimers, with its validity demonstrated through comparison with DFT calculations. This study systematically investigates H-type dimers of R6G and anthracene, incorporating functionals of increasing complexity. Calculations are performed on a wide range of dimers, each with different conformations for both optimised and unoptimised structures, to explore the effect of diverse geometries on the measured binding energies. The results presented in this chapter demonstrate that SMD enables faster binding energy assessments for large

molecules, thus complementing DFT. The presented method is not intended to replace QM/DFT entirely but to complement them by addressing specific computational challenges. While DFT remains a powerful and widely used tool in modern computational chemistry, the presented SMD method enables significantly faster binding energy assessments of large molecules without compromising the overall framework of DFT in broader applications.

Typically, in systems near equilibrium, the strongest contribution to the total potential energy function comes from the bonded interactions, while the non-bonded electrostatic Coulomb and vdW interactions have minor contributions, as described in detail in Chapter 2. The $\pi - \pi$ stacking comes from the $U_{\text{non-bonded}}$, and it is included via vdW interactions, which, as described in Chapter 2, include Keesom, Debye and London forces as well as the Pauli exclusion principle. Those complicated interactions are included in CHARMM36 FF via two simple parameters ε and $R_{\min}/2$ (required for the LJ potential) specified for each atom.

Atom name	ε (kcal/mol)	$R_{\min}/2$ (Å)	Chemical Group
C	-0.110	2.0000	Pure NMA*
CA	-0.070	1.9924	Benzene
CC	-0.070	2.0000	Acetic Acid
CE1	-0.068	2.0900	Propene
CE2	-0.064	2.0800	Ethene
C3	-0.020	2.2750	Cyclopropane
H	-0.046	0.2245	TIP3P**
HA	-0.022	1.3200	Methane/Ethane
OB	-0.120	1.7000	Acetic Acid Carbonyl
OH1	-0.152	1.7700	TIP3P**

*NMA – N-Methylaniline

**TIP3P – 3-site rigid water molecule commonly used in molecular dynamics simulations.

Table 7.1: Exemplar vdW parameters from CHARMM36 FF.

Table 7.1 indicates that each atom type has multiple parameters with marginally different ε and radii, each of them representing atoms from different chemical groups, e.g., in CHARMM FF atoms CA describe sp^2 carbons in the aromatic rings [237], so the ε and radius are unique to this specific type of carbon hybridization in this unique configuration. The same applies to all other atoms, such as hydrogens, oxygens etc., and indirectly reflects the electronic structure of the atom. It is worth mentioning that a

simple, protein-only FF consists of over ten types of hydrogen and nitrogen atoms, and over twenty carbon atoms [88]. Due to those small, and therefore frequently overlooked differences in ε and radii, force-field-driven MD simulations allow reproduction of some quantum effects, such as π-π stacking.

In this chapter, the applicability of SMD in calculating binding energies of dimers will be addressed and the proposed method described in detail, alongside the broader study of R6G dimerisation in solution and in the presence of SNPs. Furthermore, the approach is validated using DFT calculations by employing functionals from various rungs of Perdew's "Jacob's ladder," which classifies functionals based on their accuracy in predicting exchange-correlation energy [141]. While there are more sophisticated *ab initio* and force field methods that can potentially provide even more reliable binding energies, the drawback of such methods, as mentioned previously, lies in their computational cost and complexity. By combining MD, SMD, and DFT, this chapter provides insight into aromatic dimer interactions in the presence and absence of SNPs and highlights how force-field-driven approaches can complement quantum mechanical methods in studying non-covalent interactions.

7.2 Methods

7.2.1 Dimer Generation Using MD

For the detailed description of the simulations used in the analysis of dimerization in the presence of SNPs, refer to Chapter 6, Section 6.3.3. The detailed description of the R6G parametrisation is presented in Section 6.2.1.

For the MD simulations used to generate the initial dimer structures, two anthracene or R6G molecules were placed in a water box and allowed to diffuse freely. To ensure that the individual monomers were not biased toward dimerization, the initial distance between them was approximately 20 Å, with a water box padding of 20 Å to exclude interactions with periodic images. The rectangular periodic simulation cell size was 67 Å × 70 Å × 65 Å and contained 27,442 atoms for R6G simulations, while for the

anthracene simulations, the cell size was 72 Å × 50 Å × 46 Å (14,781 atoms). As in all previous simulations, the system underwent a 1000-step water-only minimization using the steepest descent method with all non-solvent molecules restrained, followed by 100 ps equilibration at 300 K and 1 bar, maintained via the Langevin barostat and thermostat (NPT ensemble). The obtained system was subjected to 10,000 minimization steps with no constraints applied, followed by 30 ps of heating to 300 K and 270 ps equilibration with a 1 fs time step. The production runs were performed in the NVT ensemble, where a Langevin thermostat with 5 ps^{-1} damping was used to control the temperature, also using a 1 fs time step integrator. The 100 ns production run at 300 K was repeated four times to ensure that the system was not trapped in a saddle point and to generate four unique dimers independently. A custom TCL script was used to measure the COM distance between the two dye molecules. This, combined with visual analysis, allowed the identification and selection of four unique dimers, one from each simulation, that were used as starting structures for both the SMD simulations and DFT calculations. In all cases, PME with 1.0 Å grid spacing was used for efficient evaluation of electrostatic interactions, while the cutoff for vdW interactions was set to 12 Å.

7.2.2 Density Functional Theory Calculations and Geometry Optimisation Methods

DFT calculations were performed using four different dimer configurations for both anthracene and R6G. All calculations were performed using ORCA 5.0.4 [240–242]. To get a valid comparison between the estimated energies using SMD and the conventional DFT, binding energies were calculated at multiple levels of theory:

1. **Generalised Gradient Approximation (GGA)** functional: **BP86**, which combines Becke's exchange functional (B88) and Perdew's correlation functional (P86), and improves on the Local Density Approximation by incorporating the gradient of the electron density [283, 284].

2. **Hybrid GGA**: **B3LYP** (Becke 3-parameter-Lee-Yang-Parr) functional [147–

149], which is one of the most widely used functionals and includes a portion of exact HF exchange, thus further improving the accuracy of the calculated electronic properties.

3. **Hybrid-meta-GGA**: **M06-2X**, a global hybrid functional with high nonlocality, which includes both gradient and kinetic energy density terms [285].

4. **Range-separated hybrid**: ω**B97X-D**, which separates the exchange interaction into short-range and long-range components by applying different treatments to each [151, 152].

For BP86, B3LYP and ωB97X-D functionals, Grimme's atom-pairwise dispersion correction based on tight binding partial charges (D4) was used [243, 286, 287], while for the M06-2X functional, D3 dispersion correction with a zero-damping scheme was used [167] due to a lack of available parameters for the D4 correction. At each step, starting from the lowest (BP86) to the highest level of theory (ωB97X-D), the dimer and two individual monomers were optimised in a conductor-like polarizable continuum solvation model (CPCM, water), followed by harmonic frequency calculations to confirm that the obtained stationary point is a minimum. The zero-point energy (ZPE) and thermal corrections were applied to the obtained energies, while BSSE correction was applied according to Boys and Bernardi procedure [288], to account for the basis set incompleteness effect. Triple ζ valence def2-TZVPP basis set [244] with auxiliary def2/J [289] were used for all optimization and frequency calculation tasks for computational efficiency, without significant decrease in accuracy. For fast evaluation of the Coulomb and exchange integrals a RIJCOSX algorithm [279, 290] which significantly accelerates the calculations and maintains high numerical precision was used. The final energies were refined at the ωB97X-D4/def2-QZVPP [244] level of theory to ensure the highest possible accuracy for the computed binding energies and act as a final reference point for the DFT calculated binding energies. Single point energies (SPE) of unoptimized dimers were also calculated using the aforementioned methods without the ZPE and thermal corrections but with BSSE correction to provide a direct comparison of the energy differences and act as a direct validation of the SMD-obtained energies. This

comprehensive approach ensured that the energy differences were not artefacts of the optimization process. An increased grid (defgrid3) was used to reduce the numerical noise and increase the accuracy of the results. Through this approach, a robust comparison across different levels of theory was possible. The binding energies (ΔE) were calculated using the supramolecular approach:

$$\Delta E = E_{\text{Monomer 1}} + E_{\text{Monomer 2}} - E_{\text{Dimer}} \tag{7.1}$$

where $E_{\text{Monomer 1}}$ and $E_{\text{Monomer 2}}$ are the energies of individual monomers (optimized with ZPE, thermal, and BSSE corrections or unoptimized only with BSSE correction), and E_{Dimer} is the energy of the dimer. The same method of calculating ΔE was applied to both optimized geometries and unoptimized ones, i.e., directly taken from MD simulations with no additional steps.

7.2.3 Steered Molecular Dynamics

The selected MD-generated dimer was solvated with TIP3P [122] and neutralized using NaCl, with water box padding set to 15 Å. The cut-off for the vdW interactions was set to 12 Å, while the electrostatic interactions were evaluated using the PME method. The obtained rectangular periodic simulation cell size was 44 Å × 44 Å × 45 Å with approximately 6,800 atoms for R6G simulations and 41 Å × 35 Å × 38 Å and around 4,500 atoms for the anthracene simulations. The differences in atom numbers between systems arose from the fact that each dimer had a slightly different conformation and size, which in turn affected the final box size. The system minimization was performed in the same two-step manner as described in the MD section. Throughout the minimization process, all dimer atoms were constrained and fixed in place to prevent them from being pulled apart by the conjugate gradient and line search algorithm. The above ensured that each of the used dimers is unique and has a slightly different conformation than the others. To estimate the binding energy of the dimers using force field methods, a constant velocity (0.01 Å/ps) SMD pulling with a harmonic force constant of 4 kcal/(molÅ), equivalent to 278 pN/Å, and an integration step of 1 fs, total

SMD trajectory length was 2 ns. Due to the constant velocity pulling protocol, the force is directly available in the simulation output, which makes it easy to generate force-extension plots and analyze the pulling process. At lower pulling velocities, the simulation timescale became inefficient, whereas altering the force constant introduced significant noise into the trajectories, which dominated over the local unbinding potential. Furthermore, high velocity and spring constant values could lead to structural alterations of the pulled molecule. However, as shown in the Results section, the RMSD data indicate that the structures remained well-preserved throughout the simulation and were consistent with MD simulations.

The SMD simulations for DFT-optimized anthracene and R6G Dimers #1 were repeated 10 times, to assess the method's precision. Given that the obtained values did not differ significantly in the case of ten and four repetitions, i.e., (18.44±2.46) kcal/mol for R6G dimer from 10 repetitions vs. (18.98 ± 2.05) kcal/mol from four repetitions and (7.36 ± 1.66) kcal/mol vs. (7.23 ± 1.92) kcal/mol for the anthracene dimer, the remaining SMD simulations were repeated four times from the same starting point. To minimize the noise arising from the friction between the pulled R6G and the fixed dye molecule, one of the dimer components was fixed, and the other was pulled away in the direction perpendicular to the aromatic planes by applying the external force to all heavy atoms of that plane. To further minimize the noise, constant temperature control was disabled to ensure that the disturbance caused by the molecular movement was minimal. Despite the temperature control being switched off, the temperature remained close to the set value of 300 K and fluctuated from around 296 K to 302 K. The force and displacement plots as a function of simulation time, combined with visual analysis, were used to calculate the binding energies. The energy calculation method has been previously used for estimating the desorption energies of proteins with success [127, 129, 291, 292].
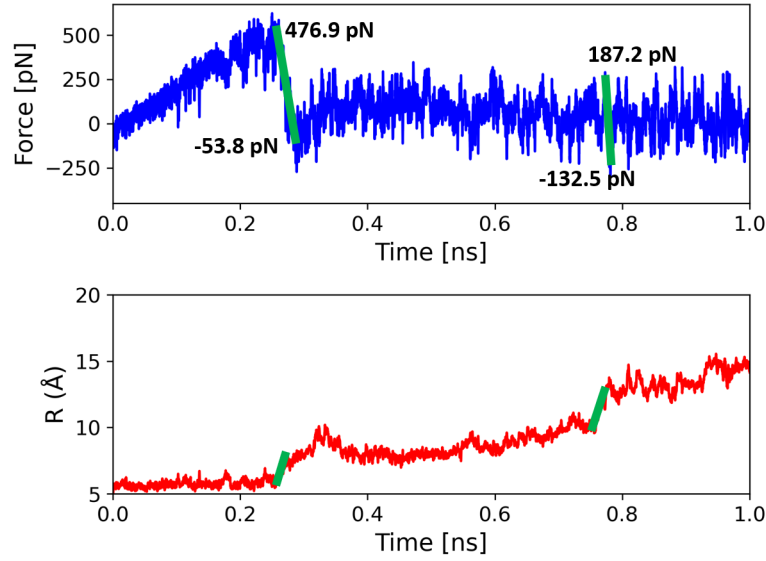
Figure 7.1: Exemplar SMD plot for the R6G dimer optimized at ωB97X-D4/def2-TZVPP, with the dimer dissociation steps marked.

The calculation of the ΔE using SMD begins by plotting the force and displacement as functions of simulation time. Next, software capable of interactive plot analysis is used to identify the dissociation steps, which are characterised by sharp drops in the force plots and corresponding increases in the displacement plots, as indicated by the green bars in Figure 7.1. The identified steps are then confirmed through visual analysis of the trajectories using software such as VMD. After verification, the binding energy is calculated using the equation provided below (Eq. 7.2). If the dissociation occurs in two steps (as in the presented case), the calculation (Eq.7.2) is performed for each step, and the final energy barrier is obtained as the sum of the two. Here, the final energy barrier, ΔE, is calculated to be 18.69 kcal/mol. It is important to note that any dissociation steps involving the breaking of a bond-like interaction followed by the formation of a new one should be disregarded; hence, visual inspection of the trajectories is essential. The formula is a simple potential energy of a spring formula but written in terms of the SMD measurable quantities:

$$dE = \left(F_0 + \frac{dF}{2} \right) \left(\frac{dF}{k} \right) \tag{7.2}$$

For a detailed derivation, refer to Chapter 2, Section 2.9. All MD and SMD simulations were performed using NAMD3 CUDA [230, 231] version with CHARMM36 FF [89] and VMD [248] was used to visualise and analyse the simulations.

7.3   Results and Discussion

7.3.1   Dimerisation in the Presence of Silica Nanoparticles

It is well known that when used in high concentrations or the presence of silica films, R6G tends to form dimers [253, 293, 294]. To study R6G dimerisation in the presence of silica nanostructures, the simulations from the previous chapter were utilised, specifically those involving various R6G–SNP systems. These simulations included a total of eight systems, with each 100 ns simulation repeated four times for better statistics. Each system contained six R6G molecules and either a single 40 Å α-quartz or α-cristobalite NP (at pH 7 and 12) or three 20 Å α-quartz/α-cristobalite NPs at both pH values. To distinguish the systems, they were labelled as 40qSNP7, 40qSNP12, 40cSNP7, 40cSNP12, 20qSNP7, 20qSNP12, 20cSNP7, and 20cSNP12. The structure of the H-type dimer is shown in Figure 7.2.
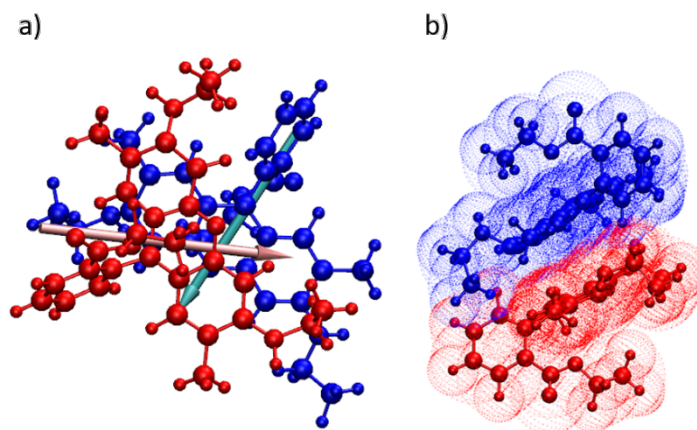
Figure 7.2: R6G Dimer a) Top view of the dimer with visualized dipole moments.; b) Side view of the dimer.

The detailed simulation analysis revealed, that R6G adsorption on SNPs and R6G

dimerisation are competing processes. R6G monomers tend to adsorb on SNPs while dimers do not. Interestingly, adsorbed R6G monomer might be approached by other R6G monomers, leading to dimerisation and desorption. Alternatively, a competition between dimer and monomer can be seen, where a monomer can approach a dimer, temporarily creating a trimer and replacing one of the dimer components. Usually, such trimers did not exist for more than 8 ns. Another possibility is the dimer interaction with the SNP, which is followed by dimer dissociation and resulting in one adsorbed R6G and one free R6G molecule. Both desorption and dissociation were observed for 40qSNP7, 20qSNP7 and 20qSNP12 systems, while desorption only in the 40cSNP7 system and a single event of dimer dissociation (breakage) only in 20cSNP7 system. In other words, the obtained trajectories confirm that R6G can form dimers both in solution and on the SNP matrix, whereas trimers appear to be transient states, reflecting the dynamic exchange of molecules. Summarising, R6G may exist in three stable forms: (1) as a free monomer, (2) as a monomer adsorbed on SNP, and (3) as a free dimer. In contrast, larger conglomerates, such as adsorbed dimers and both free and adsorbed trimers, are unstable and represent only transient intermediate states. Both the trimer and adsorbed dimer are unstable due to geometric constraints, i.e., for the stable adsorption/dimerisation to occur, the xanthene core of R6G must be oriented parallel to the SNP/other R6G molecule, which is a dimer component. Obtained trajectories confirmed the existence of a mixture of the above moieties at any time.

It is worth emphasising that there is no apparent reason why the last would not apply to larger than 40 Å SNP and silica surfaces. Furthermore, in the case of high R6G concentration, dimerisation in solution is favoured over dimerisation on the SNP matrix, independent of the crystal structure of the SNP in the system.

The dimerisation process was monitored across all systems described in Chapter 6, Section 6.3.3, in each iteration, and the number of dimers in the solute and on the SNP matrix was calculated, as shown in Tables 7.2 and 7.3. Due to the transient nature of trimers, they are not included in the analysis.

	40qSNP7	40qSNP12	40cSNP7	40cSNP12
\<Dimer\>	4.75	3.25	5.00	3.25
\<T\>	82.22 ns	81.65 ns	106.13 ns	90.18 ns
\<TPerDimer\>	18.69 ns	26.38 ns	23.68 ns	27.42 ns

Table 7.2: Dimer statistics for 40 Å SNP systems averaged over four independent runs of each trajectory. \<Dimer\> indicates the average number of dimers in the system, \<T\> indicates the sum of the time the dimers existed in the system, and \<TPerDimer\> indicates the average time the given dimer existed in the system before dissociating.

	20qSNP7	20qSNP12	20cSNP7	20cSNP12
\<Dimer\>	4.75	5.75	3.75	3.50
\<T\>	80.95 ns	115.6 ns	77.22 ns	94.53 ns
\<TPerDimer\>	20.97 ns	21.17 ns	29.31 ns	25.04 ns

Table 7.3: Dimer statistics for 20 Å SNP systems. Symbols as in Table 7.2.

For the 40SNP systems, sixty dimers formed in the solute, and five dimers formed on the SNP matrix, all at pH 7. Of those five dimers, three were formed in the 40qSNP7 system, with one dissociating while two desorbed. In the 40cSNP7 system, two additional dimers were formed, both desorbing before dissociating. In the 20SNP systems, sixty-four dimers formed in the solute, and seven were formed on the SNP matrix. The latter was present in all systems, except for the 20cSNP7, with two in 20qSNP7, one of which dissociated, four in 20qSNP12, two of which dissociated, and a single dimer in the 20cSNP7 system that also dissociated. Furthermore, it was observed that for the 40SNPs, irrespective of the crystal structure, the average number of dimers in the system decreases at pH 12 compared to pH 7; for instance, 4.75 in 40qSNP7 drops to 3.25 in the 40qSNP12 system (see Tables 7.2 and 7.3). It is important to note that although the number of dimers declines with increasing pH, dimer stability rises, with the average time a dimer exists in the 40qSNP system increasing from 18.69 ns at pH 7 to 26.38 ns at pH 12. The same trend is observed for the 40cSNP systems in terms of both the number of dimers and their existence time. When the 20qSNP case is examined, it is observed that the trend is somewhat different. For smaller SNPs, the average number of dimers rises from 4.75 at pH 7 to 5.75 at pH 12, and the time of existence also increases from 20.97 ns to 21.17 ns. This suggests that, in addition to

pH, SNP size also impacts the dimerisation process. It may be speculated that as the diffusion speed of SNPs increases, it becomes more challenging for R6G molecules to achieve the orientation favourable for adsorption; hence, they become more susceptible to other potential processes, namely dimerisation. Another factor that contributes to enhanced dimerisation is the counterion layer density at high pH. It should also be emphasised that the lifetimes of individual dimers were highly irregular, with some persisting for only around 5 ns while others remained intact for up to 40 ns. These fluctuations indicate that the stability of a given dimer is strongly dependent on its instantaneous conformation. In agreement with the binding energy calculations discussed in the next sections, different conformations of the R6G H-type dimer exhibit different energetic stabilities, which translates directly into variable lifetimes in the MD trajectories. Dimers adopting geometries corresponding to higher binding energies tend to persist for longer, whereas less favourable orientations dissociate more rapidly. Thus, the apparent irregularity in the lifetimes is not unexpected, but rather a dynamic manifestation of the conformational dependence already established in the binding energy analysis presented in detail in the next sections.

Close examination of the dimer behaviour in all of the systems indicated that for 40qSNP7 systems, the dimer dissociation tends to happen faster than the whole dimer desorption (7.76 ns vs 12.7 ns), while for the 20qSNP7 and 20cSNP12 systems, the dissociation is significantly slower when compared with desorption (3.4 ns vs 18.8 ns and 9.6 ns vs 13 ns). Looking at the results mentioned above, it can be concluded that the time of desorption/dissociation is strongly affected by the size and/or the number of SNPs in the system. It was found that with bigger SNPs, the adsorption is more stable, and we are more likely to reach state A; therefore, one of the dyes forming a dimer is more likely to adsorb to the surface. As the binding energy for the R6G–qSNP is higher than that of R6G–R6G, the dimer dissociates, leaving behind an adsorbed R6G. On the other hand, when the system contains multiple small SNPs, the R6G molecule can't reach state A, even in its monomeric form. As a result, it takes significantly longer for one of the components of the dimer to reach an optimal orientation, which would result in dimer dissociation and adsorption.

147

7.3.2   Binding Energy Calculations of Anthracene and Rhodamine 6G Dimers

With a clearer understanding of the dimerisation process in the presence of SNPs, the next step is to further explore the properties of these dimers, particularly their binding energies. This is crucial for understanding their absorption behaviour and interactions with SNPs, which can influence their stability and overall performance. To address this, DFT calculations were performed and compared with SMD-obtained energies.

As mentioned in the Methods section, to obtain a set of four independent dimers for both anthracene and R6G, classical MD simulations were performed using CHARMM36 FF. Each 100 ns long simulation (without any additional constraints) generated distinct molecular conformations, providing a diverse set of dimer geometries. Such an approach ensured that the chosen dimers were not biased towards a particular conformation, thereby providing a robust starting point for subsequent DFT calculations and SMD simulations. The following section presents the results of these analyses, offering deeper insights into the stability and interactions governing dimer formation. Exemplar structures of anthracene and R6G dimers are shown in Figure 7.3.
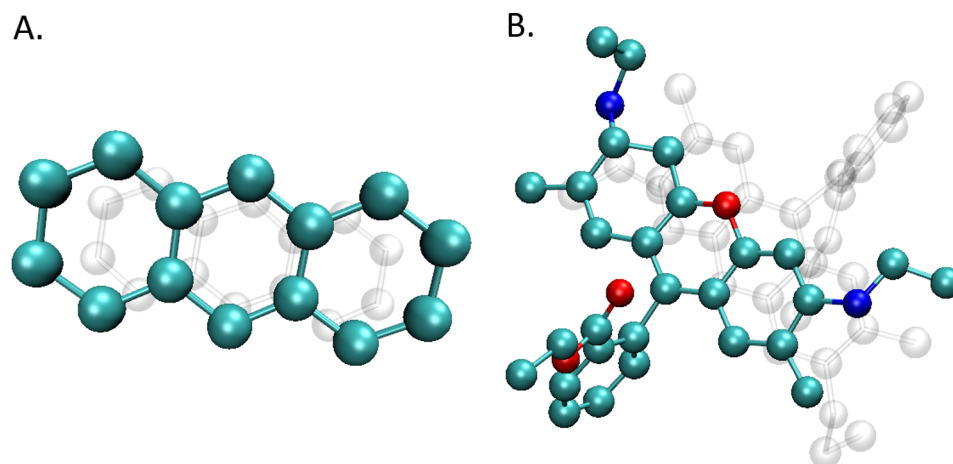
Figure 7.3: Starting Dimer Structures: A. Anthracene Dimer, B. R6G Dimer. Structures are shown by ball and stick representation, coloured by name: C, O and N are shown in cyan, red and blue, respectively while hydrogens are omitted for clarity. Shadow (depth cueing) is used to distinguish separate monomers in a dimer structure.

Density Functional Theory

A range of DFT calculations were performed to get a full insight into the magnitude of the binding energies of the dimers studied. These calculations aimed to provide a valid comparison with SMD simulations and ensure that the energy differences observed are intrinsic to the molecular interactions rather than artefacts of the optimization process. Initially, the electronic energies of each structure were calculated at multiple levels of theory, including GGA, hybrid GGA, hybrid-meta-GGA, and range-separated hybrid functionals. The specific functionals used were BP86, B3LYP, M06-2X, and ωB97X-D. This range of functionals allowed for a detailed comparison of how each level of theory captures electron correlation and exchange interactions, particularly the non-local components of HF exchange.

Next, the structures were optimized at each level of theory to account for quantum mechanical effects such as Pauli repulsion, which are not explicitly defined in MD force fields. This step was crucial because MD force fields might fail to account for detailed electron-electron repulsions, as they lack explicit terms to describe the interactions. This can result in the potential overbinding of molecules. By optimizing the structures, it was ensured that the geometries obtained were close to the minimum on the potential energy surface for each dimer.

For the DFT part, the main part of the analysis was centred around optimised structures as typically done in the field, however, calculations for the unoptimized geometries were also added. Although such calculations are uncommon and often lack significance due to the abundance of unoptimized structures, in this specific instance, they served as a valid basis for comparison with the SMD simulations.

Anthracene   Binding energies obtained for optimized and unoptimized anthracene dimers are shown in Figure 7.4.
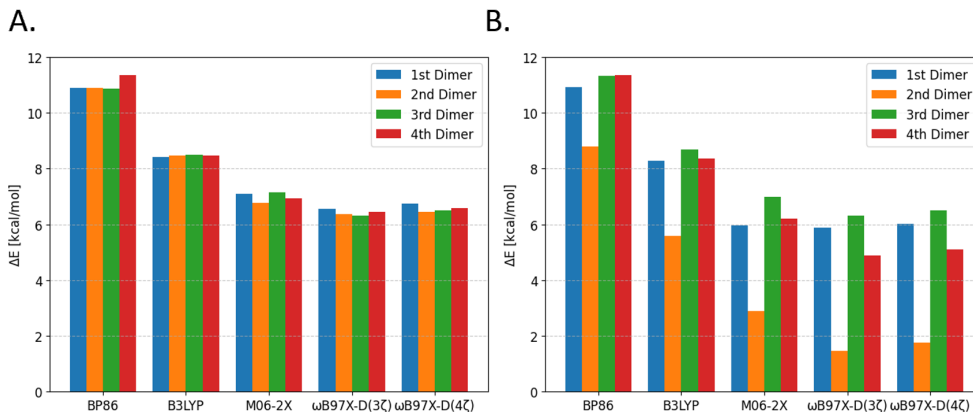
Figure 7.4: Binding Energies of anthracene dimers at different levels of theory; A. Optimized structures; B. Unoptimized Structures.

For the optimized structures (Fig. 7.4A), the energies of four independent dimers are virtually identical among all the functionals used, suggesting that the obtained geometries are likely near the same local minimum. The most significant difference in the binding energies is observed for the transition from BP86 to a B3LYP global hybrid, with ΔE decreasing on average from 11 kcal/mol to 8.5 kcal/mol. BP86 belongs to the family of GGA functionals, and while it does offer some improvement over LDA functionals, it does not involve an exact (non-local) component of HF exchange but rather accounts for electron repulsion by considering density gradients. As a result, it fails to capture the electron repulsion fully, hence overbinding the molecules, highlighting a common limitation of GGA functionals [144, 295]. This is well reflected by a significantly higher ΔE at BP86-D4/def2-TZVPP when compared with other functionals, arising from the fact that the rest of the presented methods are hybrid and include a part of HF exchange.

The energy decreases further when moving from B3LYP ($\Delta E = 8.5$ kcal/mol) to M06-2X ($\Delta E = 7$ kcal/mol), which can be attributed to a high non-locality of M06-2X, which includes 54% of HF exchange and offers a better treatment of dispersion interactions. The difference between M06-2X and range-separated hybrid ωB97X-D is relatively low, with ΔE decreasing from 7 kcal/mol to 6.4 kcal/mol, suggesting that there is not much improvement in the electron-electron correlations, thus indicating

that once a certain level of HF exchange and non-local treatment is included, additional improvements in electron correlation might yield diminishing returns in the form of increased computational costs at a marginal improvement in accuracy. Therefore, careful consideration is required when selecting the appropriate functional, as in some cases, a more cost-effective global hybrid may yield results comparable to range-separated hybrids. A comparison of optimized vs. unoptimized geometries is presented in Fig. 7.5A.
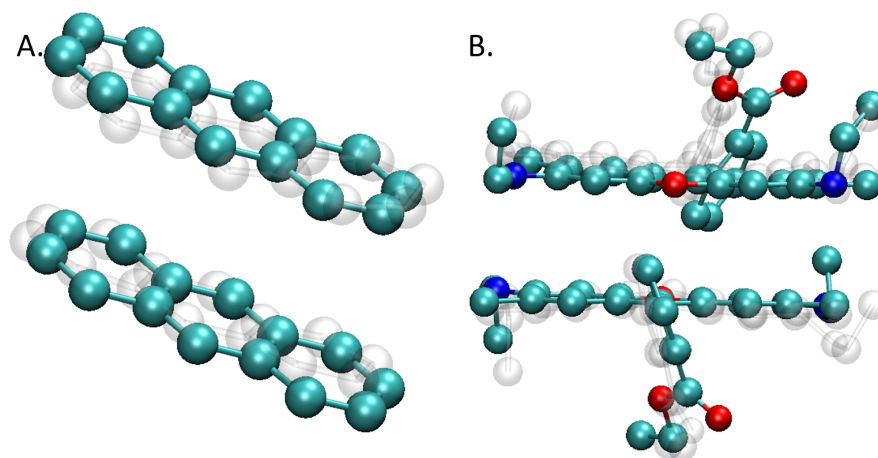
Figure 7.5: Overlap of optimized (coloured, opaque) at ωB97X-D4/def2-TZVPP and starting (shadow/ghost) dimer structures. (A) Anthracene dimer, and (B) R6G dimer. Colour scheme is the same as in Figure 7.3.

As expected, despite the general similarity in decreasing energies with the increasing level of theory, the situation for the unoptimized dimers (Fig.7.4B) is less consistent with visible differences of ΔE between the particular structures, as each of the dimers has a different conformation. This further underscores the sensitivity of the binding energy to conformation, reflecting the realistic scenario where molecular flexibility and varied intermolecular interactions play a crucial role. The most interesting case is noted for Dimer #2, where the decrease in the binding energy is the most significant with the increase of the functional capability to describe exchange-correlation energy. This discrepancy implies that the geometry of Dimer #2 was relatively far from optimal, therefore, DFT reported low ΔE (weak dimer binding). For the BP86, which has no

HF exchange and has limited capabilities, the relatively high binding energy of 8.8 kcal/mol is a result of the overbinding, mentioned previously. The decrease in ΔE at higher levels of theory arises from the fact that electron repulsion starts to dominate, hence, the binding energy is very low and equal to 1.45 kcal/mol at ωB97X-D. This is the drawback of the proposed MD method, as FF methods do not include electrons explicitly, hence, estimation of the repulsive term is impossible. This can potentially result in an overestimated stability of certain dimers as is the case of anthracene Dimer #2. As a result, the formed dimer will be stable (and indeed was) as observed during the MD trajectory, while the DFT calculations suggest that the ΔE is almost negligible.

Rhodamine 6G Binding energies obtained for optimised and unoptimised R6G H-type dimers are shown in Figure 7.6. In general, the trends observed for the anthracene dimers were also observed in the case of R6G dimers. However, given that R6G is more complex than the anthracene molecule, with a greater number of atoms and numerous side chains, the generated set of dimers represents a wider set of possible conformations than observed for anthracene. This variation may result in distinct local minima on the potential energy surface (PES).
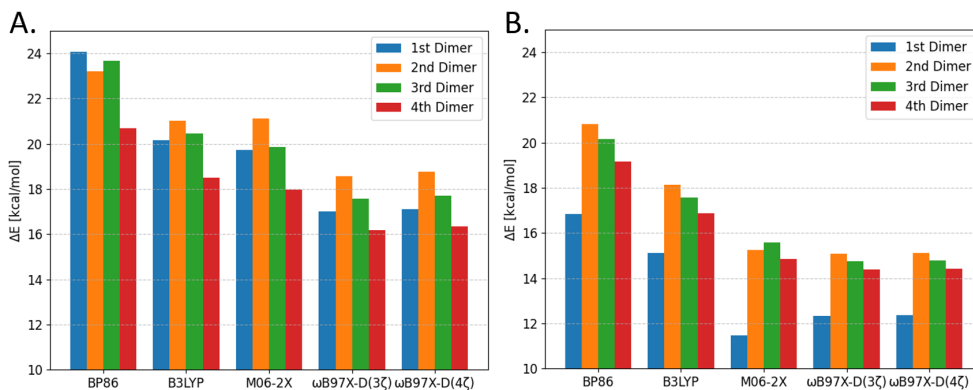
Figure 7.6: Binding Energies of R6G dimers at different levels of theory; A. Optimized structures; B. Unoptimized Structures.

H-type R6G dimers are formed via vdW interactions (π–π stacking) and not by an explicit bond; therefore, a precise estimation of dispersion forces and correct treatment

of electron–electron interactions is vital. When examining the binding energies of optimised dimers (Figure 7.6A), it is again evident that more sophisticated functionals provide a better treatment of dispersion forces and electron–electron interactions. For example, the transition from the BP86 functional to B3LYP shows an average decrease in ΔE equal to 2.9 kcal/mol, indicating that the inclusion of exact HF exchange in B3LYP and other hybrid functionals leads to more accurate energy calculations. When looking at B3LYP and M06-2X, it is evident that the differences between the energies of optimised dimers are around only 0.5 kcal/mol, suggesting that the geometry does not change significantly between the two, which was indeed the case; however, caution must be taken when using M06-2X. Both B3LYP and M06-2X are global hybrid functionals that mix a portion of exact HF exchange with DFT exchange–correlation, providing a more accurate description of electron–electron interactions. Specifically, B3LYP includes around 20% HF exchange, while M06-2X includes 54%, which accounts for its slightly lower ΔE values due to better dispersion treatment. Furthermore, the results from M06-2X Dimer #1 do not seem to follow the general trend, where the binding energy decreases with increasing levels of theory. This can be attributed to its heavy parametrisation based on empirical data [296]. Due to this high empiricism, this functional might be less predictive outside the types of systems and reactions that it was trained on, thus raising concerns about its generalizability to novel systems or conditions not represented in the training data [297]. Furthermore, it seems M06-2X tends to overestimate the binding energies and leads to other errors, such as overfitting, especially in cases where a delicate balance of forces is critical [298]. As a result, the predicted binding energies using M06-2X are closer to that of B3LYP, while the computational cost of M06-2X is comparable with ωB97X-D due to its high numerical noise and a need for a finer DFT integration grid when performing the calculations [299,300]. Lastly, a second steep decrease of around 2.3 kcal/mol is observed when transitioning from regular hybrid functionals to a range-separated ωB97X-D functional. Range-separated hybrids use different portions of HF exchange to treat long-range and short-range interactions, leading to an improved correlation treatment compared to global hybrids. This results in more precise binding energies, albeit at a significantly increased

computational cost. The final refined energies at ωB97X-D4/def2-QZVPP, which involve a highly accurate and computationally demanding basis set, suggest that the estimated energies with triple-ζ basis sets were already close to the complete basis set limit for the system studied.

The results for the unoptimized structures shown in Figure 7.6B generally report similar trends. Moreover, Dimer #1 seems to show similar traits to anthracene Dimer #2, as it does not follow the trend of other dimers and its ΔE value is lower overall than other R6G dimers. The overall binding energies at each level of theory are lower for the unoptimized structures when compared with optimized structures, e.g., 17.11 kcal/mol for the optimized vs. 12.34 kcal/mol for the unoptimized at ωB97X-D4/def2-QZVPP, which is mainly caused by the change in position of all side groups. Furthermore, there are no steep decreases when transitioning from GGA to hybrid functionals and from hybrid to range-separated hybrid as in the case of optimised geometries. Here, the energy decreases continuously with the increasing complexity of the functional, which directly corresponds to the functional capabilities of accounting for exchange–correlation and describing electron repulsion, with BP86 being the simplest and the fastest method of all and ωB97X-D being the most precise but also the most computationally demanding. Lastly, it is important to note that due to the complex structure of R6G and the flexibility of its side group, the DFT binding energies are significantly influenced by the position of these side groups, as that is the source of the largest difference between optimized and unoptimized structures as visualised in Figure 7.5B.

The generally consistent trends observed across both anthracene and R6G dimers highlight the robustness of the computational methods used. For H-type dimers, which rely heavily on vdW interactions, the choice of functional is crucial. By including these detailed analyses, the importance of selecting appropriate computational methods for accurately modelling molecular interactions is emphasised, as heavily parametrised functionals, such as those from the Minnesota family, can lead to potential errors, such as overbinding. These findings are particularly relevant for systems where vdW forces dominate, and precise dispersion corrections are necessary to avoid this. As discussed below, additional care must be taken when estimating the binding energies when using

the proposed method, as SMD tends to overbind dimers, leading to increased binding
energies.

Steered Molecular Dynamics

To ensure a valid comparison of DFT-calculated binding energies with those obtained
using SMD, simulations were performed for both optimised and unoptimized geome-
tries. The main focus of the analysis was the unoptimized geometries, as this is the
typical approach for SMD simulations. In SMD simulations, geometries are typically
not optimised because the method involves applying external forces to induce molecular
motion along a predefined reaction coordinate. Unlike energy minimisation approaches,
SMD captures the system's non-equilibrium response in real-time, often passing through
high-energy conformations. Optimising the geometries beforehand could alter these
dynamic interactions and hinder a realistic representation of the system's behaviour
under force. Nonetheless, to ensure a valid comparison with DFT calculations, SMD
simulations were also performed on optimised structures (at ωB97X-D4/def2-TZVPP
level). This allowed assessing whether FF methods can distinguish between different
geometries successfully. In both cases, one of the dimer components was fully con-
strained by fixing the coordinates of all atoms (including hydrogens), while the other
one was pulled away at a constant velocity. To ensure that all bond-like interactions
(including π-stacking) are broken simultaneously, the target molecule was pulled per-
pendicular to the aromatic planes, with the force being applied to all heavy atoms of
those planes. By combining visual analysis with force and displacement plots, dimer
binding energies were estimated using methods from previous work, as fully described
in Section 7.2.3 [38, 111]. Exemplar SMD plots are shown in Figure 7.7. In all cases,
the dimer dissociation was a multistep process, typically involving two transitions be-
fore full dissociation. Namely, for anthracene (Figure 7.7A), the first event occurred
at around 0.15 ns and the second at approximately 0.45 ns, whereas for R6G (Fig-
ure 7.7B), they appeared later, at around 0.23 ns and 0.60 ns. In all cases the dimer
was fully dissociated at 10 Å separation; therefore any interactions past that mark are
not taken into consideration. Furthermore, to obtain precise values of binding ener-

gies, any event which results in the breaking of a bond-like interaction and subsequent creation of a new one must be excluded from the analysis. Finally, it is important to address the potential effect of hydrodynamic drag in SMD simulations. As the target molecule is pulled through the aqueous environment, the spontaneous formation and breaking of hydrogen bonds reproduce a phenomenon which might correspond to friction as understood in macroscopic terms. Due to the short simulation time, and small separation distance (the full dissociation happens at 10 Å distance), the magnitude of the resulting drag force is too small to be quantifiable, and it is already included in the SMD force reported by the software.
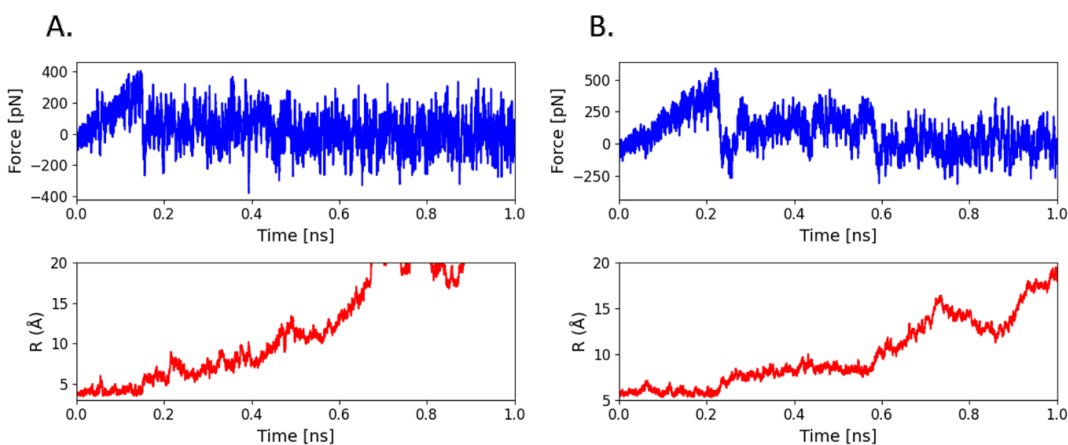
Figure 7.7: Exemplar SMD plots for the unoptimized geometries: **A.** Anthracene; **B.** R6G. Top plots in blue represent the force change as a function of simulation time, while the bottom plots in red show the displacement as a function of simulation time measured between centres of mass of the two monomers. As the dimer is fully dissociated at $R = 10$ Å, the displacement plots are created to enhance the visibility of interactions before that point.

Anthracene   The RMSD plot of the pulled anthracene molecule for one of the dimers is shown in Figure 7.8. The stability of the RMSD values indicates that the pulled anthracene molecule did not experience any extraordinary strain that would cause unnatural deformations. This was expected, as all heavy atoms of anthracene were pulled simultaneously during the SMD simulation. Additionally, the RMSD values remained consistently low (0.10–0.15 Å), further confirming the absence of significant

structural distortion.
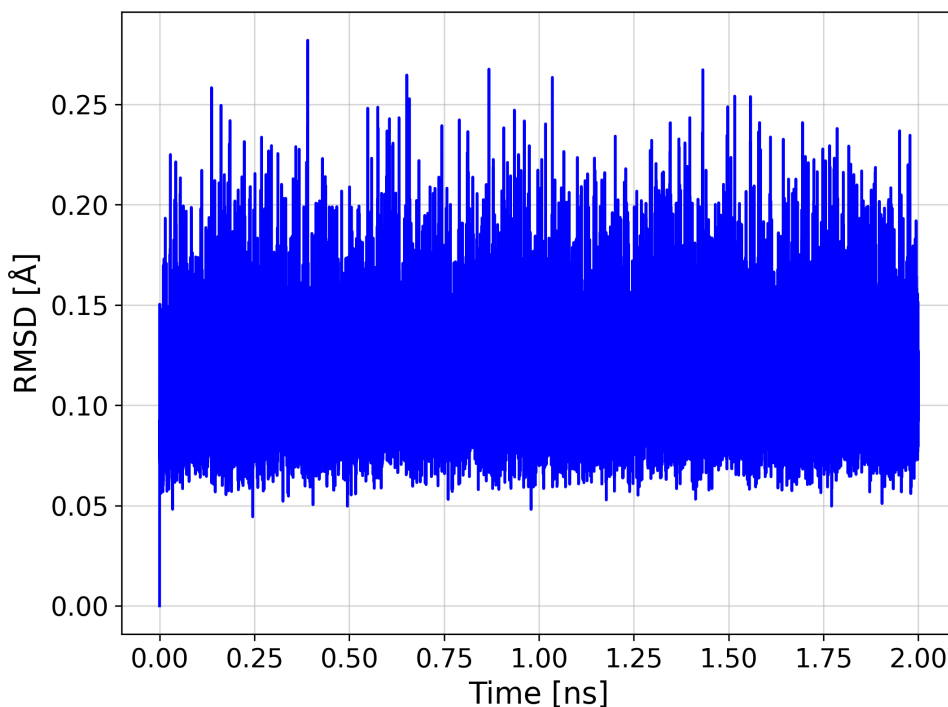
Figure 7.8: RMSD plot of pulled Anthracene molecule during the SMD simulation –
The starting structure of the pulled molecule (Frame 1) was used as a reference.

The obtained results from SMD simulations for anthracene dimers are listed in
Table 7.4. When looking at the results for the unoptimized dimers it is evident that,
in the case of anthracene dimer, SMD is capable of predicting comparable binding
energies of a dimer at a precision to that of hybrid DFT, e.g., 5.98 ± 1.49 kcal/mol from
SMD vs 5.97 kcal/mol using M06-2X for Dimer #1. The obtained ΔE values seem to
be more accurate than those obtained using pure DFT with a BP86 functional, which
contains no HF exchange, thus having limited capabilities in describing the exchange-
correlation energy. Nonetheless, the SMD approach is not ideal, since due to the lack
of explicit terms to account for electron interactions in CHARMM36 FF and lack of
explicit evaluation of the hydrodynamic drag, the method tends to overbind dimers in
some cases as observed for Dimers #2 (evident effect) and #4 (relatively minor effect).

In the first case, as already found in DFT calculations, the dimer was virtually unstable with almost negligible binding energy while the SMD obtained a value indicating that the dimer was stable. For Dimer #4, no significant differences were observed in the SMD trajectories. Both visual inspection of the trajectory via VMD and COM plot analysis confirmed the stability of both of those dimers in MD. As a result of this overbinding, there were no statistically significant differences between all four dimer binding energies obtained from SMD results, while DFT indicated notably different ΔE for each of the dimers.

Method	Dimer #1		Dimer #2		Dimer #3		Dimer #4	
	Unoptimized	Optimized	Unoptimized	Optimized	Unoptimized	Optimized	Unoptimized	Optimized
BP86-D4/(3ζ)	10.92	10.91	8.79	10.88	11.34	10.86	11.34	11.35
B3LYP-D4/(3ζ)	8.27	8.42	5.60	8.46	8.70	8.51	8.36	8.48
M06-2X-D3/(3ζ)	5.97	7.10	2.89	6.78	7.00	7.16	6.21	6.94
ωB97X-D4/(3ζ)	5.88	6.54	1.48	6.36	6.30	6.32	4.88	6.44
ωB97X-D4/(4ζ)	6.03	6.75	1.77	6.44	6.52	6.50	5.11	6.57
SMD	5.98 ± 1.49	7.36 ± 1.66	5.96 ± 1.09	7.93 ± 1.57	6.04 ± 1.14	7.99 ± 1.37	6.04 ± 1.35	7.41 ± 1.59

Table 7.4: Binding energies of anthracene dimers. All values are provided in kcal/mol, while errors for the SMD are taken to be equal to three standard deviations plus an estimated error of 0.58 kcal/mol arising from reading off the force values from the SMD plots.

It is important to highlight that performing SMD on DFT-optimized structures is not a standard practice. Due to the dynamic nature of MD simulations, where the system evolves continuously over time, molecules often do not have sufficient time to fully relax into a local minimum. However, in this study, SMD simulations were applied to the optimised dimer geometries to validate the DFT results for these structures. The results demonstrate that after geometry optimization, all dimers had very similar geometries as indicated by almost identical binding energies. As observed with unoptimized dimers, SMD successfully predicted binding energies comparable to hybrid DFT, with values such as 7.23 ± 1.92 kcal/mol from SMD vs 7.10 kcal/mol using M06-2X metaGGA functional. Furthermore, the overbinding effect, previously observed in the case of Dimer #2 and Dimer #4, is prominent here through all dimers, with the predicted energies averaging around 1 kcal/mol higher than those predicted using a range-separated hybrid functional with a highly accurate 4ζ basis. In general, the SMD-observed energy difference between starting and optimized geometries was around

21%, while the DFT-observed difference was around 11%, excluding the outliers. Nevertheless, this study, and particularly the data listed in Table 7.4, demonstrates that SMD reliably predicts binding energies of simple anthracene dimers, yielding results consistent with hybrid DFT. Therefore, we can anticipate that this method can be applied to more complex polycyclic aromatic hydrocarbons (PAH) dimers; however, it should be used with caution.

It is important to note that the binding energies obtained from SMD correspond to the non-equilibrium work performed during the pulling process, rather than a rigorous equilibrium free energy. In statistical mechanics, the Jarzynski equality establishes a formal connection between these two quantities, expressing the binding free energy as

$$\Delta G = -k_\mathrm{B} T \ln \left\langle e^{-W/k_\mathrm{B}T} \right\rangle, \tag{7.3}$$

where W is the work performed along individual pulling trajectories. A direct consequence of this relation is the Jarzynski inequality, which states that

$$\Delta G \leq \langle W \rangle. \tag{7.4}$$

It should also be emphasised that the DFT calculations reported here correspond to electronic binding energies (ΔE) rather than Gibbs free energies (ΔG), which makes the comparison with SMD work values consistent in terms of energetic trends, even though both methods do not explicitly include entropic contributions. Thus, when the average work is used as an approximation of the free energy, as in the present study, the resulting values are expected to be higher than the true equilibrium binding energies. This theoretical expectation is consistent with the systematic overbinding observed in some dimers, reflecting both the limitations of the force field and the non-equilibrium nature of SMD. Nevertheless, because the same protocol was applied uniformly across all systems, the method provides reliable comparative estimates of binding energies and a meaningful benchmark against DFT calculations. Looking forward, this limitation could be mitigated by increasing the number of independent pulling trajectories

to improve sampling of low-work pathways, thereby converging more closely to the exponential average prescribed by the Jarzynski equality. Alternatively, coupling SMD with enhanced sampling techniques such as umbrella sampling or metadynamics could yield more rigorous free energy estimates, reduce systematic overestimation, and further strengthen comparisons with DFT.

Rhodamine 6G   To further validate the method and get more insight into the accuracy and capabilities of SMD in predicting binding energies, an analogous analysis was carried out on the R6G H-type dimer. RMSD analysis was performed, to ensure that the pulled molecule does not experience any structural alterations due to pulling, with the results shown in Figure 7.9.
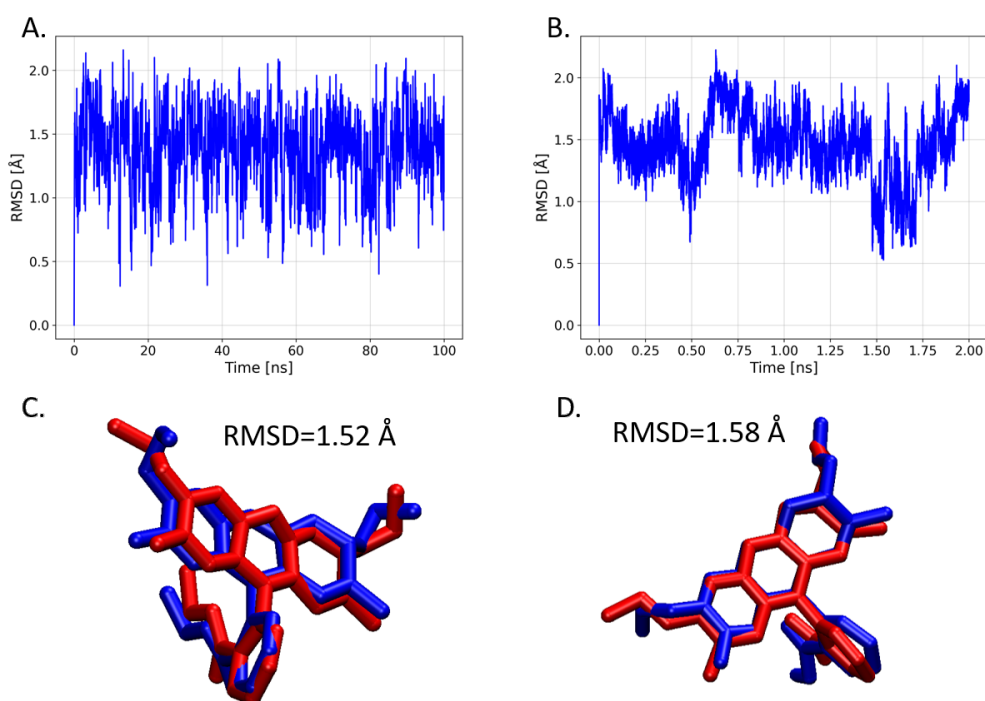
Figure 7.9: RMSD plot of pulled R6G molecule during the MD simulation. B. RMSD plot of pulled R6G molecule during the SMD simulation. Starting MD structure used as a reference structure for the plot; C and D: Overlaps of R6G structures during SMD (red) and MD (blue) trajectories.

Since all the heavy atoms of the xanthene core are pulled simultaneously during the

SMD simulation, the pulled R6G does not experience any excess stress, as evident from the comparison of Figures 7.9A and 7.9B. The RMSD values during the SMD trajectory remain within the range observed during free diffusion, further confirming the absence of significant structural strain. Notably, the RMSD values during free diffusion are also consistent with those observed in the SMD simulation, with both fluctuating around 1.5 Å.

The results for the R6G dimer SMD simulations are shown in Table 7.5.

Method	Dimer #1		Dimer #2		Dimer #3		Dimer #4	
	Unoptimized	Optimized	Unoptimized	Optimized	Unoptimized	Optimized	Unoptimized	Optimized
BP86-D4/(3ζ)	16.84	24.09	20.81	23.20	20.15	23.66	19.18	20.69
B3LYP-D4/(3ζ)	15.13	20.15	18.12	21.01	17.56	20.46	16.87	18.49
M06-2X-D3/(3ζ)	11.45	19.74	15.24	21.13	15.59	19.87	14.86	17.98
ωB97X-D4/(3ζ)	12.35	17.00	15.09	18.58	14.75	17.57	14.40	16.19
ωB97X-D4/(4ζ)	12.35	17.11	15.13	18.75	14.79	17.71	14.44	16.34
SMD	10.46±1.89	18.44±2.46	14.76±1.81	19.43±2.38	15.17±1.23	19.78±1.89	15.05±2.08	17.89±2.59

Table 7.5: Binding energies of R6G dimers. All values are provided in kcal/mol, while errors for the SMD are taken to be equal to three standard deviations plus an estimated error of 0.58 kcal/mol arising from reading off the force values from the SMD plots.

For the case of unoptimized structures, a similar trend was observed as with the anthracene dimer. One of the selected dimers (Dimer #1) was found to be less stable than the other three, which aligns with the DFT calculations. However, the difference was not as significant as it was found in the case of anthracene Dimer #2. In general, both SMD and DFT showed comparable capabilities in detecting the dimers in less stable configurations; however, this was more prominent in DFT and slightly less noticeable in SMD simulations, as expected. These results demonstrate that the proposed SMD approach allows the differentiation of variations in dimer geometries as the obtained ΔE values are different for unoptimized and optimised dimer geometries, e.g., 10.46 ± 1.89 kcal/mol vs 18.98 ± 2.05 for Dimer #1. Observation of this difference was not surprising as after optimisation, both monomers were oriented more favourably than in MD-generated structures, hence the higher binding energy. The differences between the unoptimized and optimised geometries were 27% on average; however, in the case of Dimer #1 it was over 44%. The main reason for this difference is the presence of the side groups in R6G which are very flexible and thus their orientation significantly

affects the final binding energy. Furthermore, the feature of overbinding observed in anthracene dimers is also prominent here, with typically obtained ΔE being on average 1.5–2 kcal/mol higher than those obtained using ωB97X-D4/(4ζ). It is worth noting that the weakness of M06-2X, particularly its tendency for overbinding, is more pronounced here with the functional reporting energies closer to B3LYP while containing a notably higher fraction of HF exchange (20% in B3LYP vs 54% in M06-2X) and significantly increased computational costs approaching those of ωB97X-D. This further suggests that the use of highly parametrised functionals, such as Minnesota functionals, which are often used for systems stabilised by vdW interactions, might potentially lead to overfitting.

Additionally, it is worth mentioning previously obtained results [111] predicted slightly different binding energies of dimers to the values reported here, with SMD-predicted ΔE for R6G being equal to 8.52 ± 2.80 kcal/mol and 13.45 ± 3.18 kcal/mol using DFT and 10.23 ± 1.36 kcal/mol with 9.41 ± 0.64 for anthracene, respectively [301]. Although the current results are slightly different, it is important to note that previously reported results were obtained for unoptimized structures using a single DFT functional with no corrections applied (such as BSSE or vibrational corrections). Furthermore, the impact of the outliers and the MD overbinding feature was not considered either. Therefore, those earlier findings should be considered preliminary, serving as an introduction to the method, while the current work should be perceived as a full validation of the method. Despite these differences, a good agreement between the two methods is evident in both cases.

7.4   Conclusions

In this chapter, the process of R6G dimerisation in both solution and the presence of SNPs was studied through visual analysis, and the binding energies of R6G dimers were measured. It was observed that dimers formed both in solute and on the SNP surface, with dimerisation in solute being favoured. In 40SNP systems at pH 7, 60 dimers were found in solute and five on the SNP matrix, while in 20SNP systems,

64 dimers formed in solute and seven on the SNP matrix. For 40SNPs, regardless of crystal structure, a reduction in the average number of dimers at pH 12 compared to pH 7 was noted. Both adsorption and dimerisation imposed geometric constraints on R6G due to its asymmetry in the xanthene core plane. In dimers, the xanthene cores were oriented antiparallel, facing each other, whereas adsorbed R6G required its core to be parallel to the SNP surface for stable adsorption. These geometric constraints explained the competition between R6G adsorption and dimerisation, the stability of monomeric R6G with SNPs, and the instability of R6G trimers and higher oligomers. In the case of 20qSNPs, the average number of dimers increased from 4.75 at pH 7 to 5.75 at pH 12, with an increase in dimer lifetime from 20.97 to 21.17 ns, suggesting that both pH and SNP size influenced dimerisation.

To further investigate these interactions, a DFT validation of an SMD method for estimating the binding energies of aromatic dimers was performed. Since obtaining experimental binding energy values is notoriously difficult due to the nature of dimerisation, two computational methods were employed: force field-based SMD simulations, which are highly efficient for aromatic molecules while still providing accurate binding energy values, and the more computationally demanding DFT calculations using functionals from various rungs of Jacob's ladder. Additionally, by analyzing independent dimers from multiple MD simulation runs, it was demonstrated that different monomer orientations within a dimer significantly impact the final binding energy. This effect was successfully captured in both SMD and DFT calculations. Since both types of calculation were performed on optimized and unoptimized dimer geometries, this allowed assessing the sensitivity of the SMD method and further understanding of the impact of the dimer geometry on the binding energy values. This work shows a novel example of CHARMM36 FF validation and also shows that this particular FF can capture the non-covalent interactions of the aromatic system with high accuracy. The obtained average binding energies for optimized anthracene dimers obtained using ωB97X-D4/(4ζ) were 6.46 kcal/mol vs. 7.64 $\pm$ 1.61 kcal/mol using SMD, 17.48 kcal/mol and 19.02 $\pm$ 2.22 kcal/mol for R6G H-type dimer. Furthermore, it was found that SMD can differentiate minor variations in the geometries, as the binding energies obtained

for each dimer differed accordingly and consistently fell within the uncertainty range of the hybrid DFT-calculated values. In general, it was found that global hybrids such as B3LYP or HSE [302] provide the best balance between accuracy and computational cost. The use of more complex functionals results in somewhat improved accuracy; however, due to increased computational costs, they might be too expensive for larger molecules. Caution is advised when using highly parametrised functionals like M06-2X, as they tend to overbind, exhibit limited accuracy outside their training datasets, and require a larger DFT integration grid, significantly increasing computational costs.

It is important to acknowledge the limitations of the proposed method. Due to the absence of explicit electron-electron interactions in MD force fields and the presence of unavoidable hydrodynamic drag in SMD simulations, the presented method tends to overestimate binding energies, often producing results closer to the global hybrids rather than range-separated hybrids. In some cases, such as anthracene Dimer #2, SMD even predicted stable dimers when DFT indicated otherwise. However, despite these discrepancies, the overall trends and general agreement between SMD and DFT suggest that the method can be used effectively to estimate the binding energies of larger complexes with significantly reduced computational cost compared to high-level DFT calculations.

Importantly, the proposed method is not intended to replace conventional DFT or *ab initio* calculations entirely but to serve as a complementary technique that can provide preliminary binding energy estimates at a significantly reduced computational cost. Furthermore, this work reinforces the quality of the CHARMM36 FF. Given that other popular force fields such as GROMOS [303] and AMBER [304, 305] are based on similar parametrisation principles, comparable results could be obtained using those FF as well.

Chapter 8

Nanoparticle Metrology of Silicates Using Time-Resolved Multiplexed Dye Fluorescence Anisotropy and Small Angle X-ray Scattering

8.1   Introduction

Sodium silicates are versatile inorganic chemicals manufactured on an industrial scale by combining silica sand and soda ash (sodium carbonate) under high temperatures [306]. They are often used in coating and bonding applications when in aqueous solution [307].

Additionally, they exhibit various attractive characteristics, such as being odourless, non-toxic, possessing high strength and rigidity, are resistant to high temperatures, and having an overall low cost [308]. Furthermore, they are a primary source for colloidal silica [309] and sol-gel production [310, 311] and are commercially used as binders [312, 313], adsorbents [314], and slurry for polishing silicon wafers [315]. Given their versatility and growing demand, it is crucial to understand their chemistry and have an accurate way of estimating their size.

An important characteristic of silicates is that the ratio of silica to soda concentrations directly influences the particle size distribution, and it determines the overall size of the silicate species formed [23]. As discussed in Chapter 1, there remains a significant gap in nanometrology techniques capable of quantitatively assessing the size of silicate species without extensive sample preparation or alteration. While methods such as ^{29}Si NMR spectroscopy, SAXS/SANS, and DLS offer some insights, they each present major limitations in terms of accessibility, resolution, cost, or complexity [22, 30, 31, 261, 316, 317]. This underscores the urgent need for a simple, reliable, and non-invasive approach that can be applied effectively at both research and industrial scales.

The alternative approach discussed here, originally developed in our laboratory, is based on the measurement of time-resolved fluorescence anisotropy of fluorescent probes [221]. This method utilises the relationship between silica particle size and the rate of a probe's rotational diffusion when bound to a silica particle. Fluorescence anisotropy offers several advantages: it provides high sensitivity, operates on a suitable timescale (picoseconds to nanoseconds), and can be tailored to specific experimental conditions (e.g., pH, temperature) due to the wide variety of available fluorescent probes. Moreover, the required fluorescence time-resolved instrumentation is relatively inexpensive and user-friendly, making this method accessible for a broad range of applications. In this work, the method is further expanded to enable characterisation of sodium silicates.

Despite these strengths, the method does have some limitations. The structural complexity of sodium silicates restricts the technique to measuring only the average

particle size, without resolving different species within the silicate matrix. Additionally, previous anisotropy studies have highlighted challenges such as depolarisation effects caused by probe diffusion on the particle surface and molecular wobbling, which require careful interpretation of the data. However, with proper controls and analysis, these challenges can be addressed, making fluorescence anisotropy a valuable and versatile tool for investigating silica particle size in various environments. Furthermore, unlike conventional techniques such as SAXS or TEM, this method does not require extensive sample preparation, works *in situ*, and provides dynamic information about particle behaviour in real-time.

In this chapter, the fact that R6G physically binds to silica particles is explored, while RB weakly interacts due to additional electrostatic repulsion from the carboxylic acid group [35, 38, 39, 318]. This allows using the rotational time of the weakly-interacting RB to independently determine the microviscosity, which can then be used with the rotational time of R6G to estimate the size of the particle as previously applied by D. Tleugabulova *et al.* using R6G (excitation 495 nm) and pyranine (excitation 404 nm) to study Sol-to-Gel transitions in sodium silicate [33]. In this case, both R6G and RB can also be excited with a single light source at around 500 nm if necessary, which was successfully shown. The use of a multiplexed dye approach prevents the decline in free probe concentration over time, thereby reducing the associated increase in measurement error for viscosity that was observed in previous studies employing a single dye probe [220, 222]. To ensure a more precise determination of the silica particle size, two methods of modifying microviscosity in the samples were used: dilution of the original sample in water and a change of temperature.

The findings presented in this chapter further support the interpretation of time-resolved fluorescence anisotropy in terms of silica particle size and provide insight as to its measurement limits in this application. Furthermore, they offer an alternative method for industrial applications to get a fast and accurate average size estimate of the particle size in sodium silicates. In this work, sodium silicate solution at various stages of dilution was labelled with 10 μM of R6G for the hydrodynamic radius measurements and 10 μM of RB for microviscosity measurements. Next, a range of

fluorescence measurements was performed on each sample, allowing us to understand the impact of the bound silica particle on R6G fluorescence. From steady-state measurements, it was found that when in the presence of silica structures, R6G tends to form non-fluorescent dimers, which although they decrease the efficiency of the experiment, they do not affect the measured size as they do not interact with the silica nanostructures, as reported in computational studies [38]. Since there is a significant lack of literature involving quantitative studies of particle sizes in sodium silicates, SAXS measurements were performed to validate the anisotropy results. It was found that the average hydrodynamic radius of the particle in sodium silicates obtained from anisotropy measurements is 7.0 ± 1.2 Å, which is further validated using SAXS results which reported 6.50 ± 0.08 Å. Additionally, this discrepancy in the particle sizes suggests that the particles are not perfectly spherical, which agrees with recent SAXS and TEM results obtained by G. Hu *et al.* and is further validated using molecular dynamics simulations as discussed in Chapter 6 [261].

It is hoped that this work demonstrates that the time-resolved fluorescence anisotropy method can quickly and precisely measure the average particle size in sodium silicate solutions. Moreover, this study establishes fluorescence anisotropy, supported by molecular dynamics simulations, as a novel and powerful method for characterizing sodium silicates, providing unprecedented molecular-level insights into their structure and dynamics.

8.2 Methods

8.2.1 Reagents and Sample Preparation

The sodium silicate solution used in this work was purchased from Sigma-Aldrich as a product of Millipore. According to the product description, the solution in its undiluted form has a pH of 11–11.5 at 50 g/L at 20 °C and dynamic viscosity of 130 mPa·s. It contains 25.5–28.5% SiO_2 and 7.5–8.5% Na_2O (3.7 silica to soda ratio) and has a density of 1.296–1.396 g/mL at room temperature. The content of Fe and other heavy metals

(such as Pb) is $\leq$ 50 ppm.

R6G (Bioregent, Suitable for Fluorescence), Sodium Silicate Extra Pure, and NaOH
1 N volumetric standard solution were purchased from Sigma-Aldrich, and RB (99%,
Laser Grade) was purchased from Fisher Scientific. The diluted sodium silicate samples
were prepared by mixing them with distilled water, starting from nine parts stock
silicate/NaOH and one part water (90%) until nine parts water and one part stock
silicate solution (10%) had been reached. The dye was added after the dilution at
10 μM concentration. Samples in plastic cuvettes, 1 cm $\times$ 1 cm $\times$ 4 cm, with relevant
solutions were prepared immediately before the measurements. The sodium silicate
solution is quite stable in the sealed container, but continuous exposure to CO_2 present
in the atmosphere tends to lower the pH due to the formation of carbonic acid in the
silicate, which, combined with sample evaporation, leads to gelation [312]. Therefore,
the cuvettes were covered with parafilm to minimize the exposure of the samples to
CO_2 to prevent gel formation.

8.2.2 Experimental Protocol

Temperature-Controlled Fluorescence Measurements

The samples were prepared by taking 3 mL of stock sodium silicate and adding 10 μM
of the probe directly into the sample without prior dilution. The temperature in the
chamber was controlled using NestLab RTE-111 Bath circulator connected to the sam-
ple holder, while the temperature was monitored using an Omega HH804 probe, which
was kept in the cuvette at all times during the experiment. The sample chamber was
purged at a low temperature with nitrogen to prevent condensation.

Steady-State Fluorescence Measurements

The UV-Vis absorption spectra were measured using a PerkinElmer Lambda 25 spec-
trometer with distilled water as a reference sample. Corrected fluorescence excitation
and emission spectra were obtained using a HORIBA-IBH Fluorolog3 spectrometer.
The excitation and emission spectra were collected in steps of 1 nm and the slit widths

on the excitation and emission monochromators were set to 5 nm. For the emission spectra, R6G samples were excited at 494 nm, while RB at 509 nm. For the R6G excitation spectra, the emission wavelength was set to 590 nm and the excitation wavelength was varied between 350 nm and 580 nm in 1 nm increments.

Time-Resolved Fluorescence Measurements

Fluorescence intensity decay measurements to obtain both the lifetime and anisotropy data were based on the TCSPC [319, 320] technique and performed using a HORIBA-IBH DeltaFlex system with both excitation and emission Seya-Namioka monochromators, which incorporate holographic diffraction gratings to minimise the detection of the scattered light. The R6G-labelled samples were excited using a HORIBA-IBH NanoLED [321] with a centre wavelength of 494 nm, a pulse duration of 1.5 ns and a repetition rate of 1 MHz. The emission was collected at 548 nm. RB samples were excited using a NanoLED laser diode with a peak wavelength of 509 nm, pulse duration of 200 ps, and repetition rate of 1 MHz, with the fluorescence being collected at 570 nm. Fluorescent decay data were collected using FluoroHub-A electronics containing a TAC converter operated in reverse mode with the start-to-stop rate kept below 1% to minimise data pile-up. The individual fluorescence decays were measured at a magic angle of 54.7° to eliminate orientational effects.

As the time-resolved anisotropy theory was covered in detail in Chapter 5, only a short summary that is of relevance to nanoparticle rotation is provided here.

The anisotropy decay curve is obtained by analysing vertically $I_V(t)$ and horizontally $I_H(t)$ polarised fluorescence intensity decay curves. After applying necessary corrections and fittings, the rotational correlation time, Φ_R, can be extracted.

Assuming spherical particles, the hydrodynamic radius R_H is calculated using:

$$R_H = \sqrt[3]{\frac{3kT\Phi_R}{4\pi\eta}} \tag{8.1}$$

where k is the Boltzmann constant, T is the temperature, and η is the microviscosity of the medium.

If the hydrodynamic radius R_H is known, the microviscosity η can be determined
from the rotational correlation time as:

$$\eta = \frac{3kT\Phi_R}{4\pi R_H^3} \tag{8.2}$$

In this model, the microviscosity of the sample is estimated using the rotational
time of RB in Equation (8.2). This value is then combined with Equation (8.1) and
the rotational time measured for R6G to determine the hydrodynamic radius of the
silicate-dye complex.

8.2.3   Small Angle X-Ray Scattering

Theoretical Background

SAXS is a widely used technique for probing the size, shape, and internal structure of
nanoparticles, macromolecules, and colloidal systems in the range of approximately 1–
100 nm [322–324]. In SAXS, a monochromatic, highly collimated X-ray beam is directed
at a sample, and the elastically scattered X-rays are measured at small angles (0.1° to
5° in 2θ) relative to the incident beam. The scattering process is elastic, meaning that
the energy, and therefore the wavelength, of the X-rays remains unchanged; only the
direction is altered.

X-rays interact primarily with the electron clouds of atoms, and scattering arises
from local variations in electron density within the sample. Regions of higher electron
density, such as nanoparticles suspended in a solvent, act as scattering centres against
the lower-density background. The scattering intensity $I(q)$ is recorded as a function
of the scattering vector q, defined by:

$$q = \frac{4\pi}{\lambda}\sin(\theta) \tag{8.3}$$

where λ is the wavelength of the incident X-ray beam and θ is half of the scattering
angle. The scattering angle is inversely related to the real-space feature size: larger
structural features scatter predominantly at smaller angles (low q), while smaller fea-

tures scatter at larger angles (high q). This behaviour can initially seem counterintuitive compared to optical diffraction, but it reflects the fact that sharper variations in electron density created by small structures require higher spatial frequencies (high q) to be resolved in reciprocal space.

A typical SAXS scattering profile can be divided into different regions, each carrying distinct structural information. At very low q values, the Guinier region is observed, where the intensity follows an approximately exponential decay. In this regime, the radius of gyration R_g of the scattering particles can be extracted using the Guinier approximation:

$$I(q) = I(0) \exp\left(-\frac{q^2 R_g^2}{3}\right) \tag{8.4}$$

This approximation assumes isotropic, monodisperse particles and provides a reliable measure of the overall particle size in dilute systems. At higher concentrations, particle-particle interactions can distort the low-q region, and for highly anisotropic shapes (e.g., rods or plates), the derived R_g may not represent a true spherical equivalent size. In such cases, model-based fitting or complementary techniques may be required for accurate interpretation.

8.2.4 Experimental SAXS Protocol

The SAXS data were collected with a Xenocs Xeuss 2.0 SAXS/WAXS using Cu Kα_1 radiation from a Genix3D microfocus source with a wavelength of 1.5406 Å, operating at 50 kV and 0.6 mA. Single-reflection multilayer optics with 2D collimation were employed, and the scattered beam was collimated through two sets of motorised slits with variable apertures. A DECTRIS Pilatus 1M detector was used to collect the SAXS data, with the sample-to-detector distance calibrated at 2507.35 mm and a pixel size of 172 μm. Five 30-minute images were recorded and accumulated by measuring the scattering intensity as a function of the scattering vector. Samples at their original concentration were prepared in stainless steel sample holders sealed with Kapton dots to limit air exposure. The sample-detector distance was maintained in vacuum to avoid scattering and absorption from air. The scattering curves of the samples were

corrected for background scattering from the instrument, Kapton dots, and residual atmosphere [325]. The data were analysed using BioXTAS RAW software [326].

8.3 Results and Discussion

8.3.1 Steady-State Fluorescence Measurements

The results of steady-state measurements of R6G samples in water at various concentrations of NaOH and sodium silicate and RB samples in sodium silicate are shown in Figure 8.1. In the case of R6G in sodium silicate (Figure 8.1b) there is the emergence of a new peak at around 470 nm in the absorption spectrum, which grows with increasing concentration of sodium silicate and pH in the sample. This effect is widely known, as R6G tends to form non-fluorescent dimers, also known as H-type dimers [293, 327].

To gain a more detailed understanding of this phenomenon, MD simulations were performed as described in Chapters 6 and 7. The results from these simulations strongly suggest that the dye molecules exist in a dynamic equilibrium, influenced by vdW and Coulombic interactions that govern adsorption, while hydrophobic and π-π interactions control dimerisation [111]. Specifically, the hydrophobic nature of the dye molecules drives them to minimise their exposure to water, promoting aggregation into dimers. Experimental techniques are unable to probe these detailed interactions, which is why computational methods were employed to investigate this behaviour further. For more details on the dimerisation mechanisms, please refer to Chapter 7. The aggregation of the dye molecules induced by the presence of the polar surface of the silica structures is very clearly represented in the emergence of the higher energy peak in the absorption spectra. R6G dimers have a strong absorption band at a shorter wavelength when compared with monomers; however, they do not fluoresce, which is visible in the excitation spectra shown in Figure 8.1e and f, and are mainly responsible for quenching the fluorescence. Additionally, as demonstrated in the MD simulations and discussed in detail in Chapter 6, geometric constraints prevent dimer interactions with the silica nanoparticles [38]. Notably, a similar process is not observed at the same dye concentration

in the absence of silica particles (Figure 8.1a), indicating that R6G aggregation due
to high dye concentration can be excluded. Both sets of plots exhibit a dominant ab-
sorption peak at 530 nm, characteristic of R6G, along with a vibronic shoulder around
500 nm, which overlaps with the H-type dimer absorption band. The acquired spec-
tra indicate that the emission intensity significantly depends on the sample's sodium
hydroxide content. Specifically, with an increasing concentration of NaOH, the inten-
sity of the R6G emission decreases, suggesting that the rising pH associated with the
addition of NaOH quenches the R6G fluorescence. Conversely, when examining the
absorption and emission spectra of RB in sodium silicate, one might observe that the
trend of decreased intensity in both the absorption and emission spectra with pH is
much less pronounced, as further illustrated in Figure 8.1d. It appears evident that in
cases where R6G is used, the emission intensity diminishes when the sample is less di-
luted, which corresponds to a rising concentration of NaOH and an increasing pH. The
reduction in R6G intensity in the basic regime is attributed to the quenching of R6G
excited states due to the high concentration of OH^- ions, which occurs in a multi-step
manner. Initially, at moderately basic conditions (pH 10–12), the triplet excited state
(T_1) of the dye is selectively affected, promoting non-radiative pathways such as inter-
system crossing or collisional quenching, which reduces the population of the T_1 state
and decreases overall fluorescence intensity. As the pH increases further, exceeding
12, the singlet excited state (S_1) is additionally depopulated via non-radiative decay
mechanisms, such as electron transfer or deprotonation, leading to further quenching
of fluorescence [328].

Based on the steady-state measurements, it can be concluded that R6G forms non-
fluorescent aggregates when exposed to silica particles, but the dominant factor con-
trolling its fluorescence intensity is the concentration of sodium hydroxide, or in other
words, the pH of the sample. As the pH increases, more dimers form because the sur-
face silanol groups on the nanoparticles become deprotonated. This reduces the number
of potential sites for hydrogen bonding, which influences the aggregation behaviour of
R6G. A more detailed discussion of this effect can be found in Chapter 6.
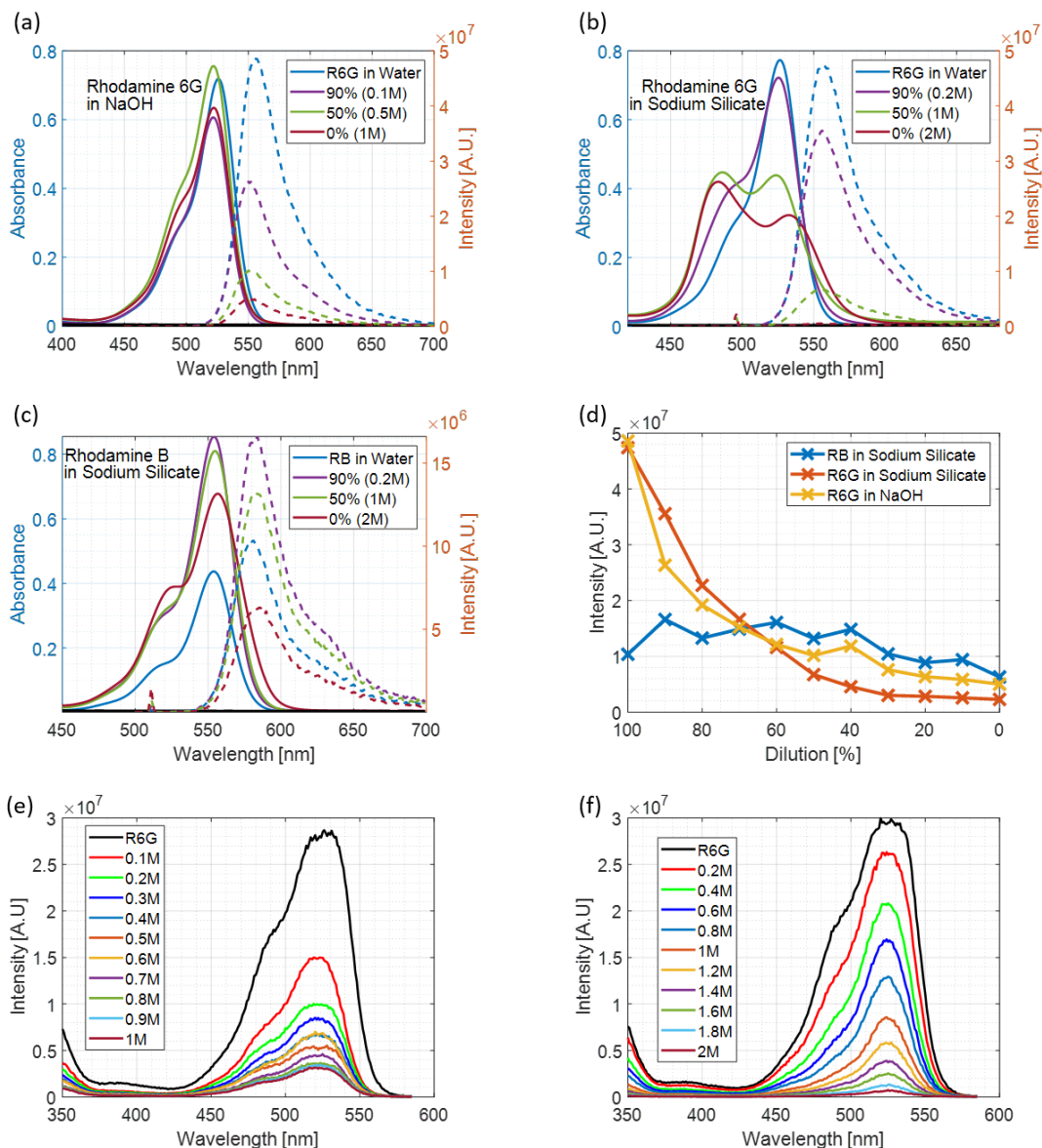
Figure 8.1: Steady-State results where percentages represent the level of dilution and
the molarity represents the concentration of NaOH in the sample. The solid line represents the absorption spectra while the dashed line represents emission spectra. (a)
R6G absorption and emission spectra in water at various concentrations of NaOH; (b)
R6G absorption and emission spectra in sodium silicate; (c) RB absorption and emission spectra in sodium silicate; (d) RB emission intensity as a function of dilution; (e)
R6G excitation spectra in water at various concentrations of NaOH; (f) R6G excitation
spectra in sodium silicate. Samples in water were prepared by diluting stock solution
in distilled water to 10 µM dye concentration.

175

8.3.2   Fluorescence Decays of Diluted Samples

Fluorescence lifetime measurements were performed and fitted to several exponential
decay models. The mono-exponential model (R6G in water) and bi-exponential model
(R6G in silicate and RB in silicate) were found to be the simplest functions that result
in acceptable values for the goodness of fit of $\chi^2 < 1.2$ (see Table 2 for R6G and Table 3
for RB). The changes in fluorescence decay components and their contributions when
the concentration of NaOH and sodium silicate is changing are shown in Figure 8.2.
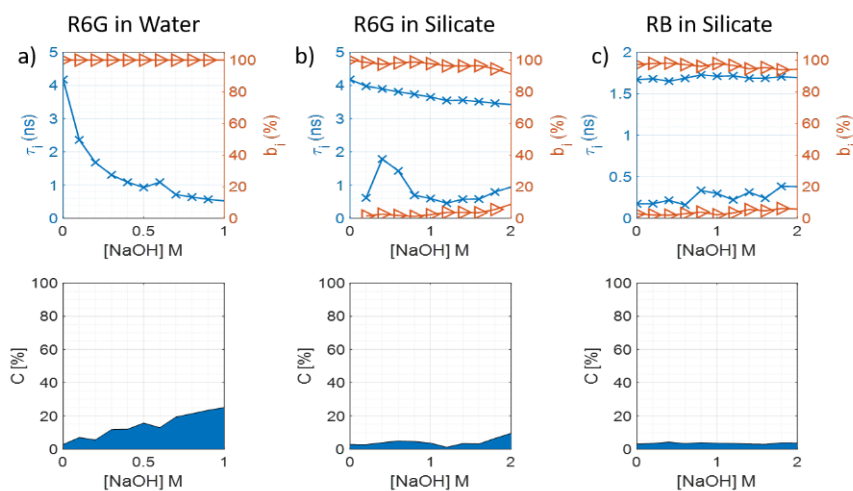
Figure 8.2: Fluorescence lifetimes (τ_i), their contributions (b_i) and scattered excitation
light contribution (c) depending on the NaOH concentration for each sample group
where the blue area represents the scatter while the white area represents the fluores-
cence.

The pure NaOH samples show the biggest decrease in R6G lifetime at higher pH
(Figure 8.2a). In the case of R6G in sodium silicate samples, the τ_1 component is also
getting shorter as the sodium silicate concentration grows, which corresponds to the
increasing amount of NaOH in the sample that is present in the manufactured sodium
silicates (Figure 8.2b). It is worth noting that when silicate particles are present in
the system, the drop in τ_1 component is not as significant as for pure NaOH samples,
which suggests that the presence of silica particles in the samples helps to maintain
the lifetime of R6G. On the other hand, RB lifetime (Figure 8.2c) stays constant in

all the samples and is only slightly affected by the presence of sodium hydroxide or silica particles. Additionally, the scattering increases with the growing concentration of NaOH, suggesting an increase in nanoscale particulates. It is also important to discuss the emergence of the second lifetime component in the sodium silicate samples. As illustrated in Figure 8.2b, in the presence of sodium silicates, there is a second lifetime component with a fluorescence lifetime shorter than 1 ns. It might be that this component corresponds to free dye in the sample, as its decay component at 1 M of NaOH closely matches the value of R6G in NaOH at 1 M concentration. The slight increase in its contribution at the 2 M concentration might also suggest that most of the dye has adsorbed to the silica particle surface; therefore, any additional dye added to the sample would not adsorb but would stay in its free form instead. Furthermore, RB also exhibits a bi-exponential behaviour, suggesting that there is an additional excited state present. The origin of this second component is not entirely clear; nevertheless, it might be suspected that a fraction of RB could potentially adsorb on some of the silicate oligomers, as was the case with Ludox colloids described by T. A. Smith et al. Given that this short component is a small fraction of the total emission, its presence does not seem to impact the particle size measurements, as will be shown in the following sections [329].

8.3.3   Time-Resolved Fluorescence Anisotropy in Diluted Samples

To precisely determine the hydrodynamic radii of both R6G and RB, two aqueous dye solutions of 10 µM concentration each were prepared and time-resolved anisotropy measurements were performed. Data were collected until a specified count difference was reached, and measurements were repeated in steps of 5,000 counts until six decays were recorded, starting at 5,000 counts and increasing up to 30,000 (Figure 8.3). Next, the data were fitted, the corresponding hydrodynamic radii were obtained, and the average dye size was calculated, as described in the Methods section. The resulting anisotropy measurements of both dyes in water gave the hydrodynamic radius of 5.9 ± 0.6 Å for R6G and 5.7 ± 0.2 Å for RB (assuming viscosity of water at 20 °C, 1 cP, and the temperature 293.15 K), which agree well with values obtained previously

by picosecond polarization grating technique and multi-colour dual-focus fluorescence correlation spectroscopy experiments [330, 331].
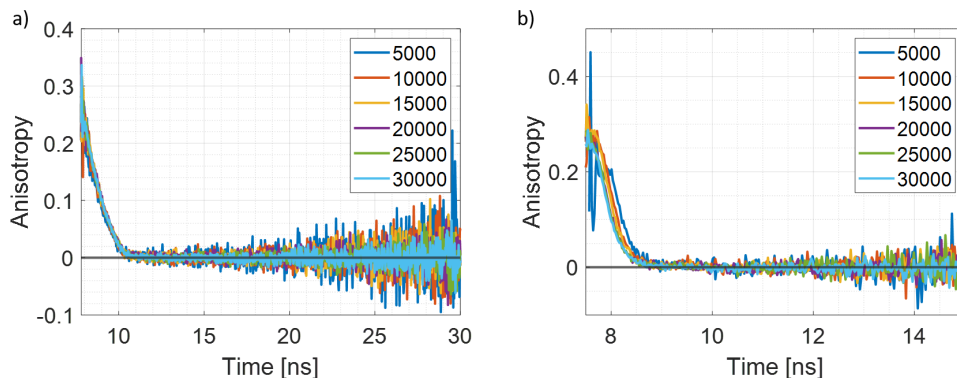
Figure 8.3: Time-resolved fluorescence anisotropy decays of used dyes at various count differences. a) R6G in water; b) RB in water.

The time-resolved fluorescence anisotropy decays of R6G–silicate complexes and RB in silicate, the latter being used to determine the microviscosity of the samples, as described in the Methods section, are presented in Figure 8.4. Both dyes are almost identical in size, and the only major difference comes from the presence of the negatively charged carboxylic acid group in RB, which will contribute to suppressing the adsorption at high pH [318]. The obtained plots are consistent with this, indicating that the decay of anisotropy is notably longer in the R6G–silicate complex when compared with the RB decays. Furthermore, it is important to discuss the discrepancy of the R_0 values from the theoretical value of 0.4. Typically, in time-resolved anisotropy measurements, the R_0 value starts at 0.4. In this case, as indicated by Figure 8.4a, this is correct only for the 2 M, 1.8 M and 1.6 M R6G samples, while for RB (Figure 8.4b), the initial anisotropy in all cases is lower than 0.4. These lower values are well known to often result from rapid intramolecular reorientation between the absorption and emission dipoles. As both dyes are comparable in size, the slower anisotropy decays of the R6G samples suggest that R6G is indeed attached to silica particles. Having the hydrodynamic radius of RB, the microviscosity of each sample was determined. Using the obtained microviscosities and the rotational correlation time of R6G-labeled particles, the size of the labelled silica particles was then calculated [318].

178

(a)

(b)
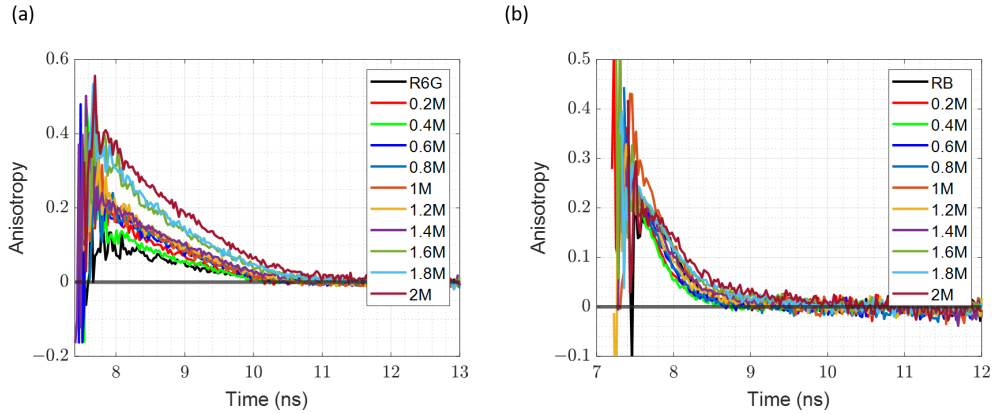
Figure 8.4: Time-Resolved Fluorescence Anisotropy Decays a) R6G-Silicate complex;
b) RB in sodium silicate samples, as a function of sodium hydroxide concentration.

The results of anisotropy decay fittings to Equation 5.13 are shown in Tables 4
and 5. Given that the χ^2 values are acceptable in most cases, it was deemed that
the mono-exponential model of anisotropy decay is appropriate. Measurements were
performed for pairs of samples with the same silicate content: one with R6G attached
to the silicates and the other with RB freely rotating in the solution. By combining
these two measurements and assuming that the microviscosity in each pair is identical,
the particle size in the sodium silicate solutions can be determined using the method
described earlier.

SiO_2 (%) (Estimated)	[NaOH] (M) (Estimated)	Rotational Time of Non-Binding Probe (RB) (ns)	Microviscosity (mPa·s)	Rotational Time of Binding Probe (R6G) (ns)	Silica Particle Size (Å)
27.0	2.0	0.54 ± 0.04	2.47 ± 0.19	1.16 ± 0.03	7.7 ± 0.8
24.3	1.8	0.46 ± 0.03	1.99 ± 0.12	0.84 ± 0.02	7.4 ± 0.7
21.6	1.6	0.41 ± 0.03	1.92 ± 0.12	0.40 ± 0.01	5.9 ± 0.5
18.9	1.4	0.35 ± 0.02	1.56 ± 0.11	0.44 ± 0.02	6.5 ± 0.7
16.2	1.2	0.32 ± 0.03	1.42 ± 0.13	0.27 ± 0.01	5.7 ± 0.8
13.5	1.0	0.40 ± 0.03	1.69 ± 0.14	0.19 ± 0.02	4.8 ± 0.8
10.8	0.8	0.30 ± 0.03	1.15 ± 0.14	0.24 ± 0.01	5.8 ± 1.0
8.1	0.6	0.25 ± 0.03	1.02 ± 0.12	0.17 ± 0.02	5.4 ± 1.2
5.4	0.4	0.26 ± 0.02	1.04 ± 0.16	0.19 ± 0.003	5.6 ± 1.4
2.7	0.2	0.22 ± 0.04	1.25 ± 0.11	0.14 ± 0.02	4.7 ± 1.2

Table 8.1: Estimated Parameters for SiO_2, NaOH Concentration, and Related Proper-
ties

Based on calculated microviscosities using RB rotational times and the estimated
particle sizes using the R6G rotational times, as listed in Table 8.1, it is evident that
the measured sizes are significantly smaller in the samples diluted to 1.6 M NaOH and

lower when compared with the undiluted and 1.8 M samples. From the MD simulations discussed in Chapter 6, it was observed that R6G orients its xanthene core parallel to the particle surface, resulting in an almost flat orientation. As a result, the impact of the dye size on the measured complex radius is expected to be negligible.

Figure 8.5 illustrates the changes in microviscosity and particle size upon sample dilution. As anticipated, the microviscosity decreases with dilution; however, the particle size also diminishes. Notably, beginning at 1.6 M [NaOH], the particle size aligns with that of free R6G. This can be attributed to dilution reducing the number of silicate particles in the sample, while the dye concentration remains constant at 10 µM, increasing the amount of free dye. Consequently, the anisotropy decay becomes dominated by the free dye. To address this issue, a stock silicate solution was prepared and labelled with 10 µM of R6G, then diluted to 50% and 20% of the original stock concentration to ensure that the ratio of the dye to silicate is maintained, independent of silicate concentration. The obtained R_H for the 50% sample was 5.73 ± 2.0 Å, and for the 20% sample, it was 6.00 ± 2.30 Å, further suggesting that the dilution of the samples yields unsatisfactory results due to the variability of different sample parameters that cannot be controlled.
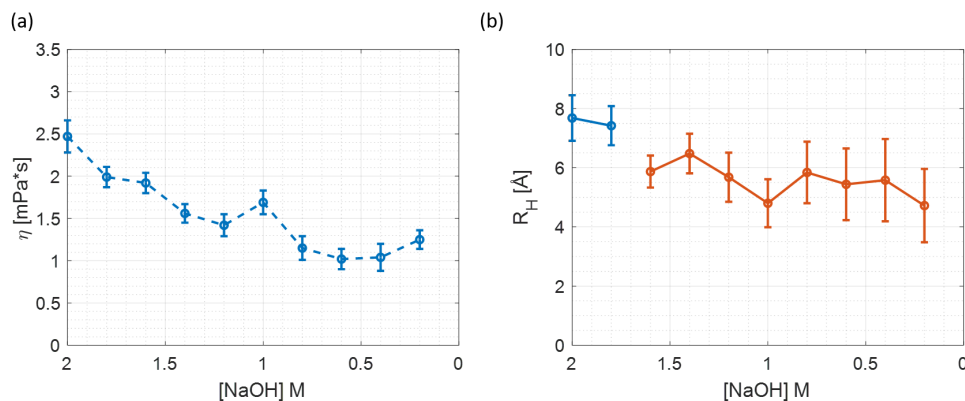
Figure 8.5: The microviscosity and particle size in dependence of sample dilution. a) Microviscosity; b) Particle size.

The formation of non-fluorescent H-type dimers seems to have no effect on particle size measurements. UV-Vis absorption spectra of 8.1b indicate the presence of

H-type dimers across all samples, ranging from 2 M to 0.6 M NaOH; however, nei-
ther the anisotropy decays presented in Figure 8.4 nor the particle sizes detailed in
Table 8.1 show any significant variations. This further supports the notion that only
R6G monomers contribute to fluorescence during particle size measurements, with the
dimers having no noticeable impact on the experimental results.

8.3.4 Fluorescence Intensity Decays at Different Temperatures

As in the case of dilution experiments, fluorescence decay measurements were performed
and fitted to several models. The two-exponential model was the simplest to generate
acceptable values of the goodness of fit parameter χ^2 (Table 8 and Table 9). Figure 8.6
shows the changes in fluorescence decay components and their relative contributions
when the temperature is changed. It is noted that both dyes behave in a very different
way. R6G (Figure 8.6a) lifetimes stay almost the same over the whole range of tem-
peratures, suggesting that the complexation with silica particles protects it from the
effects of collisional quenching at high temperatures. Moreover, the scatter goes down
at higher temperatures.
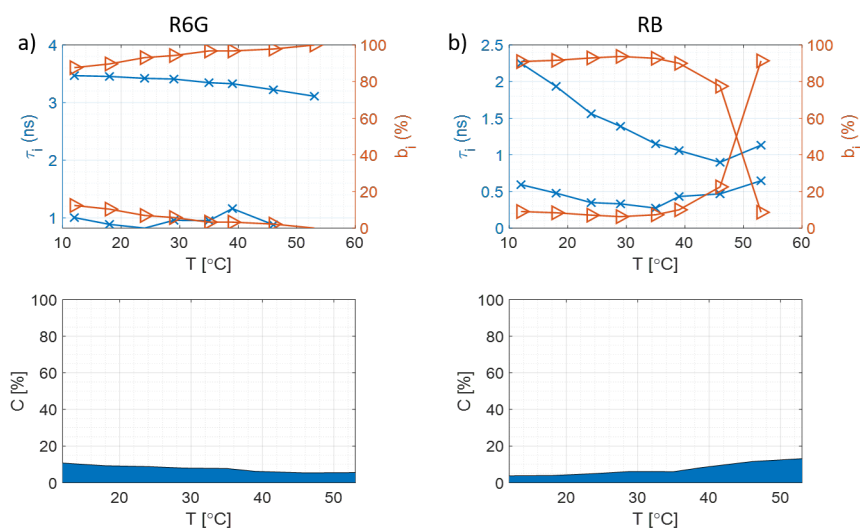
Figure 8.6: Fluorescence decay components (τ_i), their contributions (b_i), and scattered
excitation light contribution (c) depending on the temperature for each sample group
at pH 11, where the blue area represents the scatter and the white area represents the
fluorescence. (a) R6G in sodium silicate; (b) RB in sodium silicate.

In the case of RB molecules (Figure 8.6b), the lifetime drops sharply with the increase in temperature, as a result of faster molecular movement, more frequent collisions, and hence stronger dynamic quenching. Furthermore, the amount of scattered light grows with the growing temperature, which is a result of short lifetime at high temperatures, suggesting that at higher temperatures the anisotropy decay measurement may not be so accurate. Lastly, as it was the case in subsection 8.3.2 with diluted sodium silicate samples, here there are also two lifetime components present, which suggests that at all times there is a fraction of the dye which is free (shorter component), while the adsorbed dye lifetime component is dominating in the sample (longer component).

8.3.5   Time-Resolved Fluorescence Anisotropy at Different Temperatures

The fluorescence anisotropy decay of R6G-silicate complexes and RB in silicate at different temperatures are shown in Figure 8.7. In both cases, the decay follows a very clear trend: at lower temperatures, the decay is longer while at higher temperatures, the decay is faster. This is directly correlated with the microviscosity, which is higher at low temperatures and lower at high temperatures, as shown in Table 8.2. As a result, here the experiment is much more controlled, and the only factors that are changing are the temperature and viscosity, with sample composition staying the same during the whole duration of the experiment.
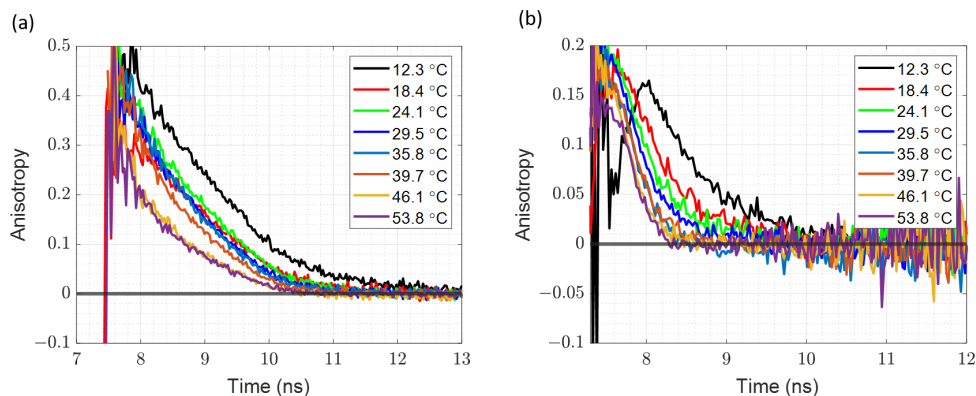
Figure 8.7: Time resolved fluorescence anisotropy decay at different temperatures of a) R6G-sodium silicate complex; b) RB in sodium silicate solution.

Tables 10 and 11 provide the details of the fitting results for both samples at different temperatures. As was the case in the dilution experiment, given that the χ^2 values are acceptable, it was deemed that a mono-exponential model is again appropriate. Similar to the dilution experiment, the rotational time of RB reported on the microviscosity at different temperatures, and the rotational time of the R6G-silicate complex combined with microviscosity allowed determination of the size of the complex. Table 8.2 lists the calculated microviscosities using RB rotational time and Equation (8.2) and the particle sizes determined using R6G rotational times and Equation (8.1). It is important to note that the size is more or less constant over a wide range of temperatures when compared with the dilution experiment.

T (°C)	Rotational Time of Non-Binding Probe (RB) (ns)	Microviscosity (mPa·s)	Rotational Time of Binding Probe (R6G) (ns)	Silica Particle Size (Å)
12 ± 1	0.72 ± 0.03	3.04 ± 0.12	1.17 ± 0.03	7.1 ± 1.1
18 ± 1	0.53 ± 0.03	2.28 ± 0.13	0.76 ± 0.03	6.8 ± 1.1
24 ± 1	0.54 ± 0.03	2.36 ± 0.13	0.82 ± 0.06	7.0 ± 1.4
29 ± 1	0.37 ± 0.03	1.66 ± 0.13	0.51 ± 0.03	6.7 ± 1.3
35 ± 1	0.23 ± 0.03	1.05 ± 0.13	0.44 ± 0.03	7.5 ± 1.5
39 ± 1	0.29 ± 0.02	1.37 ± 0.09	0.32 ± 0.03	6.2 ± 1.2
46 ± 1	0.19 ± 0.02	0.90 ± 0.09	0.18 ± 0.03	5.8 ± 1.5
53 ± 1	0.14 ± 0.02	0.69 ± 0.10	0.22 ± 0.03	7.0 ± 1.6

Table 8.2: Calculated microviscosities using RB rotational time and the estimated upper limit of the particle sizes using R6G rotational time.

The temperature dependence of microviscosity and particle radius is shown in Fig-

ure 8.8. The microviscosity (Figure 8.8a) drops with growing temperature; comparison
with Figure 8.5a indicates that the microviscosity at 2M of NaOH matches the micro-
viscosities at 18 °C and 24 °C (Figure 8.5a).
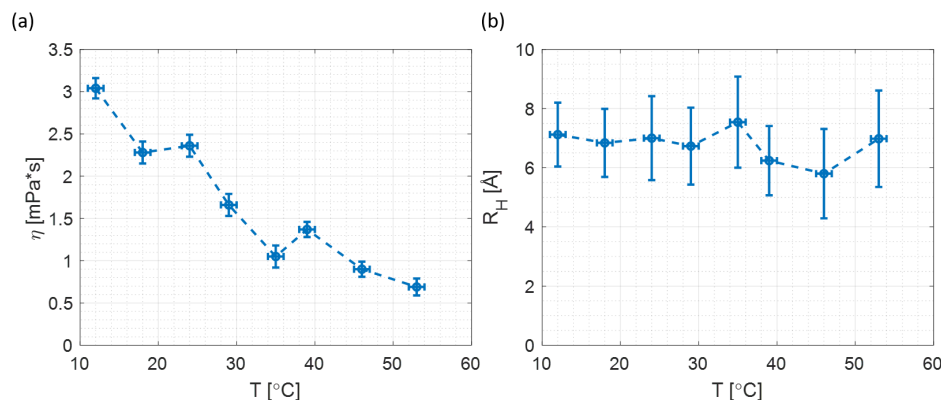
Figure 8.8: The microviscosity and particle size dependence on temperature a) Micro-
viscosity; b) Particle Size

Furthermore, a comparison of Figure 8.5b and Figure 8.8b suggests that in the
case of changing temperature, the detected particle size remains constant over a wide
range of temperatures. Additionally, the measured particle size at various temperatures
matches the results obtained for the 2M and 1.8M samples in the dilution experiment.
All the above suggests that for measuring silicate particle size, changing the tempera-
ture is a better method for altering viscosity than diluting the sample, as the sample
composition does not change with temperature.

The subsequent step is to determine the size of the silica particle (without the R6G
label dye). The determined hydrodynamic radius of R6G is 5.9 ± 0.6 Å, and the size
of the silicate-R6G complex is 7.0 ± 1.2 Å. If it is assumed that the dye attaches to
the surface of the particle without any alterations to its shape, then the silica particle
size would be 1.1 Å, which is less than the size of a water molecule (approximately
2.8 Å) [332]. It is worth mentioning that the S–O bond length is longer than that of
O–H; therefore, this simplest estimation leads to impossible results [333]. This, in turn,
strongly suggests that the dye must adjust its orientation and shape upon binding to
the silica particles. This issue will be addressed in Section 8.3.8.

8.3.6   Mutiplexed Time-Resolved Measurements

In order to simplify the method of multiplexing two dyes even further, a sample of pure sodium silicate containing 10 μM of both R6G and RB was prepared. Using $\lambda_{Ex} = 494$ nm, both fluorescence intensity decays and anisotropy decays were measured, starting from $\lambda_{Em} = 525$ nm and measured in 5 nm increments until $\lambda_{Em} = 595$ nm. The measured fluorescence intensity decays and time-resolved anisotropy decays are shown in Figures 3 and 4.

The results of fitting fluorescence intensity decays to a bi-exponential function and anisotropy decays to a mono-exponential function are shown in Figure 8.9.
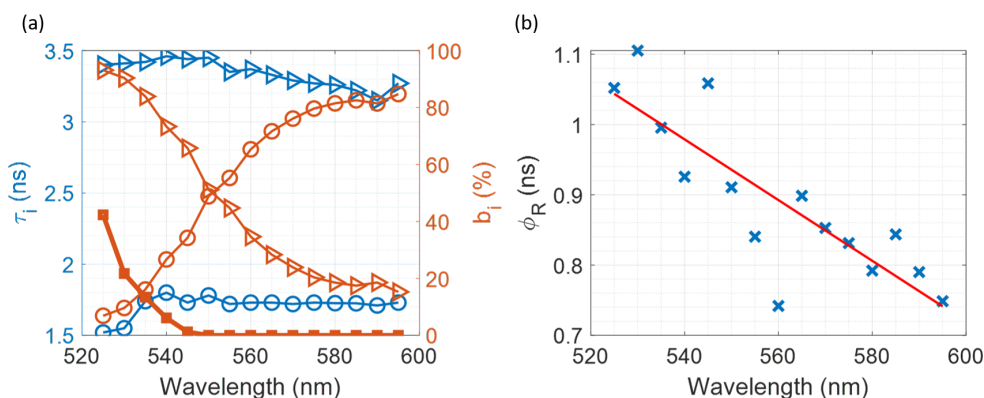
Figure 8.9: Fitting results for the Multiplexed Time-Resolved Measurements. a) Fluorescence decay components (τ_i), their contributions (bi) as a function of λ_{Em}, while the thick line with squares shows the contribution of the scattered excitation light; b) Recovered rotational times as a function of λ_{Em}. Triangles represent recovered R6G parameters, while circles represent the recovered RB parameters.

The wavelength-dependent lifetime component contribution is shown in Figure 8.9a, where at $\lambda_{Em} = 525$ nm the R6G contribution to the overall decay is over 90%, while RB is below 10%. The opposite is observed when the λ_{Em} is set to 595 nm, where the decay is dominated by the RB fluorescence with its contribution being over 80% and the R6G contribution drops below 20%. Between these two points, the contribution of the R6G gradually decreases and RB increases as the emission wavelength moves towards longer wavelengths, which is expected since the emission wavelength at 595 nm is far from the peak emission of R6G at 548 nm, and vice versa for the shorter

wavelengths.

The rotational times acquired from the anisotropy decay fitting to a mono-exponential model are shown in Figure 8.9b. The recovered rotational times exhibit a clear wavelength dependence and can be separated into three groups. The first group corresponds to emission between 525 and 545 nm, where the decays are dominated by R6G, hence the recovered rotational times reflect the R6G-silicate complex. The second group corresponds to the emission range of 580 nm to 595 nm, where the decay is dominated by RB, which is freely rotating in solution and reports the microviscosity of the medium. The third group consists of decays between these two ranges, where comparable contributions from both dyes are observed. The recovered rotational time in this region represents a mixture of the two dyes: one adsorbed to the particle surface and the other free in solution. This results from simultaneous fluorescence of both dyes due to significant overlap between their absorption and emission spectra.

Upon closer analysis, it can be observed that the precision in measuring the rotational time of the R6G-silica complex is limited by scattered excitation light (see Figure 8.9a). At shorter wavelengths, the contribution from scattered light increases exponentially, causing the initial anisotropy to exceed the theoretical limit of 0.4 (Figure 4). On the other hand, as the scattering drops to zero at longer wavelengths and the initial anisotropy decreases below the theoretical limit of 0.4 [175] (Figure 4), the only factor limiting the precision of RB rotational time measurement is the excitation source power and repetition rate. As a result, by moving to even longer wavelengths it is possible to minimize the R6G contribution further and obtain more precise readings of the microviscosity. Finally, using the average value from the second group of the rotational times (free RB in solution) and Eqn. (8.2), the microviscosity of the sample $\eta = (3.0 \pm 0.5)$ mPa·s was determined, while using the average value from the first group (R6G-silica complex) and Eqn. (8.1), the hydrodynamic radius of the particle $R_H = (7.1 \pm 0.9)$ Å was recovered. Both of these results agree with the obtained values for η and R_H discussed in sections 8.3.3 and 8.3.5.

It is important to mention that, although two measurements were needed here to successfully determine particle size because both dyes can be excited using a single

excitation wavelength, this measurement could also be performed using a T-format spectrometer, where it is possible to monitor two emission wavelengths simultaneously [334–336], or across the whole fluorescence spectrum using a linear SPAD array combined with a spectrograph [335, 337]. The choice of binding and non-binding dyes with overlapping but not identical absorption and fluorescence spectra, as demonstrated here, offers significant flexibility in optimizing precision measurements when measuring microviscosity and particle hydrodynamic radius.

8.3.7 Estimation of Dye-to-Particle Ratio and Effective Particle Concentration

To estimate the dye/particle ratio, the simplest assumption is that SNPs are monodisperse spheres of 7.1 Å, as indicated by time-resolved fluorescence anisotropy, and to calculate how many such spheres could be present at the given silicate concentration. However, this naive approach quickly reveals limitations and leads to significant overestimates of the particle number.

If the volume of the particle is calculated using the sphere volume formula and a bulk silica density of $2.2 \, \mathrm{g \, cm^{-3}}$, this results in a particle mass on the order of 10^{-21} g. Dividing the total silica mass in the solution (approximately $250 \, \mathrm{g \, L^{-1}}$ at 25% SiO_2) by this value yields an apparent particle concentration of $\sim 10^{20} \, \mathrm{L^{-1}}$. In contrast, the dye concentration at 10 µM corresponds to only 6×10^{15} molecules per litre (via Avogadro's number). This naive model, therefore, gives an average of less than 10^{-5} R6G molecules per particle.

However, this outcome is almost certainly an artefact of the crude assumptions, particularly given the strong anisotropy signals observed. In reality, sodium silicate systems are strongly polydisperse, with species ranging from dissolved monomers and oligomers (Q^0–Q^2) up to condensed clusters (Q^3–Q^4) [15, 21]. Treating all these species as "spherical nanoparticles" artificially inflates the particle count by including species that do not contribute—or have only minor contribution—to fluorescence labelling, thus lowering the apparent dye/particle ratio.

Moreover, real particles are neither dense nor perfectly spherical, but form hy-

drated, porous, and often anisotropic (ellipsoidal) structures as reported here and in the literature [261]. Fluorescence anisotropy is relatively insensitive to such deviations from sphericity, so assuming perfectly spherical particles is another oversimplification, leading to errors.

Taken together, the true population of fluorescently detectable particles is much lower than the naive model suggests. Small dissolved silicates (monomers/short chains) artificially inflate the apparent particle count but are unlikely to bind dye in a way that contributes to anisotropy, while very large colloidal aggregates rotate too slowly to be captured within the 4 ns fluorescence lifetime of R6G. In addition, hydrated silica nanoparticles have lower effective densities and packing fractions than bulk silica, meaning that treating them as solid spheres overestimates their number further.

For example, if only 1–10% of the silicate species form clusters of sufficient size to contribute to anisotropy, the effective particle count decreases by one to two orders of magnitude. Therefore, even a simple correction for polydispersity already improves the ratio from the naive $< 10^{-5}$ estimate to around 10^{-3}. When hydration, porosity, and anisotropy detection biases are also accounted for, the effective particle number is reduced by additional orders of magnitude, making ratios in the range of 0.01–1 plausible. This supports the idea that only a subset of dye molecules can potentially label particles in a way that is detected by anisotropy measurements, and under such conditions, it is reasonable to expect that several dye molecules could be associated with a single detectable particle.

From the current dataset, it is not possible to estimate the distribution accurately enough to derive a precise dye-to-particle ratio. Future work could combine anisotropy with SAXS coupled to pair distance distribution function modelling, FCS, or single-particle fluorescence imaging to provide quantitative benchmarks for particle size distributions and labelling efficiency. At the same time, it is important to maintain dye concentrations high enough to ensure good signal-to-noise ratios but sufficiently low to avoid the signal being dominated by freely diffusing dye molecules, which would otherwise overwhelm the anisotropy recovery.

To independently verify the effective size of these fluorescently detectable particles,

SAXS measurements were performed on the stock solution, as described in the following section.

8.3.8 Small Angle X-Ray Scattering and Comparison with Time-Resolved Anisotropy Measurements

To cross-validate the anisotropy results and independently determine the average particle size in the sodium silicate solution, SAXS measurements on the undiluted stock solution were performed. The summed data over five 30 min images, and the corrected SAXS data are shown in Figure 8.10. Using this reduced SAXS data, the gyration radius (R_g) was calculated by fitting the obtained corrected scattering profile to the Guinier model:

$$\ln I(q) \approx -\frac{R_g^2}{3} q^2 \tag{8.5}$$

$I(q)$ is the scattering intensity and q is the scattering vector. Due to the exponential behavior of the Guinier approximation, the radius of gyration R_g values can be determined by plotting $\ln(I)$ as a function of q^2, as shown in Figure 8.10b. The obtained value for R_g was $6.50 \pm 0.08\,\text{Å}$ with an R^2 equal to 0.95. This agrees well with the results obtained by J. Nordström et al. for the 3.3 silica-to-soda ratio silicate, which exhibits a very close composition to the silicate used in the research presented in this chapter [22]. Furthermore, a characteristic turn can be observed in the residuals plot, attributed to the polydispersity of the silicate species present in the sample.

As expected, the gyration radius is lower than the hydrodynamics radius, an artefact caused by the inclusion of the hydration shell in the case of R_H, equal to 7.0 ± 1.2 Å. Notably, the ratio R_g/R_H is between 0.75–0.87, which is close to the reference value of 0.77 for a solid sphere [338]. Nevertheless, the obtained ratio is not centred around the 0.77 value but slightly displaced towards 1.0, which suggests slightly elongated particles.
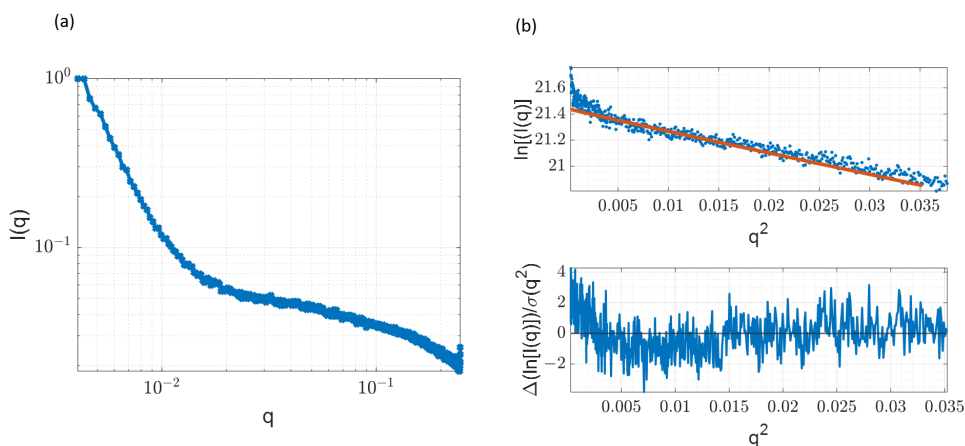
Figure 8.10: SAXS Results. (a) Corrected sample scattering profile. (b) Guinier fit
of the sample with corresponding residuals plot. Blue dots represent the experimental
data and the orange line represents the Guinier fit.

A recent study by G. Hu et al. using SAXS demonstrated that for silicates with a
ratio below 4.2, the primary particles exhibit an ellipsoidal shape [261]. This supports
the findings presented in this chapter and helps explain why the presence of dye has
minimal impact on size measurements in anisotropy experiments. Unlike in the MD
results discussed in Chapter 6, where shape-dependent effects are more pronounced,
ellipsoidal particles tend to adsorb dye on their flatter regions, this reducing the dye's
influence on the apparent particle size. However, in fluorescence anisotropy decay
measurements, it is of course the hydrodynamic radius which determines the kinetics
and this effectively can take no account of a structure being non-spherical unless much
higher statistical precision is obtained than that required for the metrology objective
described here.

8.4 Conclusions

In this chapter, two approaches, based on time-resolved fluorescence anisotropy were
presented, both of which allow the determination of particle size in sodium silicate
oligomers. In the first method, where two individual samples were used, one, labelled
with RB for microviscosity measurements and the other with R6G for radius measure-

ments, the viscosity of the original sodium silicate stock solution was altered in two ways: by sample dilution, and by changing the temperature of the sample, the latter offering advantages. In the second approach, it has been shown that the particle size can be successfully measured using a single excitation wavelength when both dyes are present in the sample simultaneously. The measured hydrodynamic radius for R6G agrees with the previously reported values, which leads to confidence that the measured sodium silicate particle sizes are not greater than reported here [339]. Additionally, SAXS measurements were performed on the undiluted sample to cross-validate the anisotropy results. Guinier analysis of the SAXS data allowed to determine the gyration radius, which was equal to 6.50 ± 0.08 Å. This result agrees well with the previous results obtained for sodium silicates of similar silica-to-soda ratio, and it simultaneously confirms the results and conclusions obtained from the anisotropy measurements. Finally, the presented results confirm the findings from MD simulations presented in Chapter 6, which showed that R6G can marginally adjust its shape to match the curvature of the nanoparticle. This implies that in the case of bigger and less curved particles, the impact of the dye on the measured complex size is up to 10%, while for the more curved smaller particles, the size contribution grows substantially and can potentially be up to 50%. Considering all the results above, it can be speculated that the particles of interest are likely not perfectly spherical. This conclusion is supported by the agreement between the anisotropy and SAXS results, as well as the shape adjustments observed in the MD simulations, which align with findings from a previous study [261].

In summary, provided that the pH and dye are compatible, i.e., the dye is stable at highly alkaline pH and maintains a sufficiently long lifetime in that environment, the simple methods described in this chapter allow efficient determination of average silicate oligomer particle sizes. Furthermore, a simple multiexponential model can be utilized to describe the fluorescence decay kinetics, as the use of fluorescence anisotropy decay does not require an understanding of complex kinetics; the fluorescence just provides a marker in time, related to particle rotation. A major benefit of the presented method lies in the labelling simplicity without the need for silicate modification which could

potentially alter the oligomer speciation, thus providing a simple method of monitoring silicates. Furthermore, the methods presented in this chapter can be easily adapted to other systems involving labelled nanoparticles to determine the average size more simply and cost-effectively. It is important to note that due to the complexity of sodium silicates and the variety of structures present, the method is limited to measuring the average size and cannot distinguish between different species within the silicate or determine size distributions.

Chapter 9

Quantitative Nanometrology of Binary Particle Systems Using Fluorescence Recovery After Photobleaching: Application to Colloidal Silica

9.1   Introduction

In Chapter 8, it was shown that time-resolved fluorescence anisotropy can be used successfully as a nanometrology tool by providing accurate size estimates of colloidal SNPs and sodium silicates [39, 221, 340]. While time-resolved fluorescence anisotropy

excels at providing precise average radii for well-defined, spherical nanoparticles in homogeneous solutions, its reliance on rotational diffusion limits insights into sample heterogeneity and complex environments. Multi-exponential fitting can, in principle, distinguish sub-populations, but overlapping correlation times and fitting ambiguities often obscure true distribution widths. Moreover, because time-resolved fluorescence anisotropy inherently assumes spherical geometry, it can break down or require complex modelling when applied to aspherical particles, leading to inaccurate or non-unique size estimates.

An alternative fluorescence-based method for measuring particle sizes is FRAP. FRAP leverages translational diffusion and spatially resolved recovery profiles to interrogate not only mean sizes but also the breadth of distributions and localised viscosity variations. Its applicability to gel-encapsulated particles, cellular contexts, and polydisperse suspensions makes it a versatile complement to time-resolved fluorescence anisotropy [341]. However, FRAP measurements can be influenced by bleaching artefacts, out-of-plane diffusion, and deviations from ideal geometry, which necessitate careful experimental design and data modelling. Additionally, FRAP does not suffer from the same breakdown with aspherical particles, since translational diffusion averages over all orientations, so even rods or plates yield a single effective diffusion coefficient that can be translated into a hydrodynamic size without forcing a spherical-only model. Nonetheless, over the last few decades, FRAP has established itself as one of the most widely used methods to study mass transport and diffusion in biological molecules. With the rise of commercially available CLSMs in the second half of the 1990s and the introduction of GFP, FRAP has become an indispensable tool in biochemical laboratories around the globe [71, 342, 343]. An important advantage of FRAP over other techniques such as diffusion NMR is its capability to probe diffusion at the micrometre scale, which introduces spatial resolution to the measurements [344, 345]. However, the main application fields of FRAP are still centred around biophysics and biochemistry involving proteins and cells, and its usage in nanometrology is limited [64, 346–349]. This is because it's common for multiple equally well-fitting models to report conflicting kinetics [350, 351]. For instance, a recovery curve may be fit equally well by a

single-component diffusion model, a two-component (fast and slow) model, or even an anomalous diffusion framework, each yielding different diffusion coefficients and thus different inferred particle sizes. Such model ambiguity can lead to substantial variation in the extracted kinetics and hydrodynamic radii unless additional constraints or independent measurements are applied. Recently, there has been some development in the field of FRAP in colloidal science, involving emulsions, gels or liquid crystals [352–355]. M. Pihl et al. developed FRAP-responsive probes using fluorescent silica nanoparticles as diffusion probes for mass transport measurement [356]. However, these strategies have been confined to either large-particle/high-viscosity systems or bespoke, synthesised fluorescent particles, leaving a notable gap in applying FRAP to unmodified, commercially available colloids and stock silicate solutions.

This chapter aims to establish FRAP as an accessible, accurate method for measuring and distinguishing SNP sizes in colloidal mixtures, and to develop a model system that enables the extension of this approach to more complex sodium silicate matrices. FRAP was successfully applied to LUDOX colloids without any additional modification by simply mixing them with R6G. The LUDOX grades studied were the 6 nm radius HS40 and 11 nm radius AS40. It was demonstrated that individual colloidal particle sizes could be effectively measured using FRAP with a straightforward multi-exponential model and, more importantly, that different nanoparticle sizes in a mixture could be distinguished. This approach provides a valuable alternative to more complex and less accessible techniques like SAXS or TEM. Furthermore, the integration of fluorescence measurements with MD simulations, as discussed in Chapter 6, reinforces the experimental findings. The MD simulations confirmed that labelling SNPs with R6G has minimal impact on the measured size [38, 39]. The simulations also demonstrated that R6G preferentially adsorbs strongly to larger SNPs, which exhibit a higher net negative charge and lower curvature.

9.2 Methods

9.2.1 Chemicals and Reagents

The LUDOX colloids and R6G (Bioreagent, suitable for fluorescence) used in this work
were purchased from Sigma Aldrich. According to the product description, LUDOX
HS-40 contains amorphous particles with a nominal radius of 6 nm, 45 cP viscosity
at 25°C, pH of 9.5 and is stabilised with a sodium counterion, while LUDOX AS-40
contains amorphous particles with a 11 nm radius, viscosity of 20 cP at 25°C, pH of
9.2 and is stabilised with ammonium hydroxide.

9.2.2 FRAP Measurements

As the nanoparticles present in the colloids are non-fluorescent, they were labelled
with R6G with the label concentration ranging from 5 µM to 20 µM. To perform the
measurements, 7 µL of labelled colloid were placed on a microscope slide with a 0.12 mm
spacer and covered with a coverslip. After that, 50 pre-bleach frames were taken at
0.2 s time step followed by 3 s bleach at full laser power over a 10 µm radius ROI and
another 500 frames with 0.2 s step during the post-bleach phase. Ten measurements
were taken at different locations on the sample, ensuring sufficient distance between
them to prevent interference from bleached molecules in previous experiments. The
FRAP analysis involved a total of 440 individual image stacks, each containing 50
pre-bleach and 500 post-bleach frames. The dataset included:

1. Ten measurements of the HS40 colloid (6 nm radius) at R6G concentrations of 5,
   10, 15, and 20 µM, resulting in 40 FRAP image stacks;

2. Ten measurements of the AS40 colloid (11 nm radius) at the same R6G concen-
   trations, producing another 40 FRAP image stacks;

3. Ten measurements for each prepared binary mixture, starting with a 9:1
   HS40:AS40 ratio and progressing to a 1:9 ratio, at 5, 10, 15, and 20 µM of

R6G. This covered nine distinct mixtures, generating a total of 360 FRAP image
stacks.

All stacks were carefully analysed, and the observed trends are summarised in this
chapter. In each case, the extracted intensity data across the bleached spot was cor-
rected for the residual bleaching from the LEDs during the imaging by monitoring
the intensity as a function of time in an ROI located further from the bleaching area.
All measurements were performed on a custom FRAP setup, based on the Cairn Re-
search Open Frame microscope, utilizing 530 nm LEDs for imaging (Cairn Research)
and 150 mW CW 532 nm laser for bleaching (Coherent) and imaged using CellCam
Kikker camera (Cairn Research), through an Olympus UPLXAPO 100X Oil Immer-
sion Objective with a numerical aperture of 1.45. The preliminary image analysis was
performed using ImageJ [212–214], while the extracted data was analysed and fitted
using MATLAB and Python [357, 358].

9.2.3   FRAP Data Analysis

The optimal parameters for the fitting of the data obtained for the pure colloids were re-
covered by deploying a two-step logarithmic search grid. Initially, a search over a larger
range of parameters was performed using a coarse grid to identify the approximate re-
gion where the optimal values were likely to lie. Once this region was determined, a
finer logarithmic grid was applied to focus the search and precisely pinpoint the opti-
mal parameters. The use of a logarithmic grid, rather than a linear one, is particularly
advantageous because it allows for a more efficient search across parameters that span
several orders of magnitude. This is important in FRAP experiments where the recov-
ery times can vary widely. The logarithmic grid search reduces the likelihood of missing
key parameter values by concentrating sampling in areas with greater relevance, ensur-
ing both computational efficiency and accuracy. As is typical in FRAP experiments,
the data were fitted to mono- and bi-exponential models, with the latter one proving
to be more suitable.

For the binary particle systems, requiring a tri-exponential fitting, the two-step

197

logarithmic grid search method was found to be no longer efficient due to its relatively high computational cost and the direct fitting was not reporting satisfying results. Therefore, a custom fitting routine based on machine learning (ML), namely the Gradient Boosting Machine (GBM) algorithm was used [359,360]. The algorithm builds an ensemble of weak prediction models by using the experimental data and sequentially adds models that correct errors made by previous ones with the key idea being the minimisation of a loss function by iteratively training models to fit the residuals of the combined model at each step. Since GBM builds models iteratively and focuses on improving predictions for challenging cases rather than being overly influenced by extreme values, outliers have less impact on the overall model performance than many traditional methods. GBM progressively adjusts to reduce the effect of these outliers, allowing for more reliable and stable predictions even in noisy data.

The two-step logarithmic grid search, while effective, requires searching across a very large parameter space to fit the tri-exponential FRAP model required for the binary system consisting of HS40, AS40 nanoparticles as well as a fraction of free dye. This search involves testing a broad range of values for the model parameters, which becomes computationally expensive, particularly when dealing with a tri-exponential model that introduces many possible combinations for the system components. The sheer scale of the grid, with its multiple parameters and the need for a very fine resolution to capture all the potential solutions, makes this approach extremely slow and resource-intensive.

In contrast, the GBM-based pre-processing step simplifies and accelerates the process. GBM does not require a large grid search; instead, it builds an ensemble of decision trees that iteratively correct the errors of the previous ones. This process is much faster than grid searching across a massive parameter space, as GBM directly learns the underlying data patterns. Once the GBM model is trained, it focuses on minimizing the residuals and reduces the effect of noise and outliers, providing a much more efficient and stable fit. As a result, the fitting process for the tri-exponential model becomes significantly faster because the initial parameter space is already refined and adjusted, allowing the tri-exponential model to be fitted with more accurate starting points.

As a result, the obtained data were first pre-processed using the ML algorithm, followed by fitting it to a tri-exponential model where each component corresponds to different system components. Specifically, the shortest recovery half-time corresponds to the free R6G, the middle component corresponds to the HS-40 with a nominal radius of 6 nm and the longest component is attributed to the AS-40 particle with a radius of 11 nm.

The resulting method proved to be significantly faster than a two-step logarithmic grid search over a large range and allows for future development in improving the fitting precision by incorporating larger data sets. The algorithm used the full ten repetitions for each sample, plus another five synthetic curves generated using bootstrapping to smooth out the data. Bootstrapping, in this context, refers to resampling the original data with replacement to generate additional training curves for the GBM, effectively increasing the dataset size and improving the model's ability to capture consistent recovery trends. In all cases, the corrected FRAP recovery curves were fitted to a multi-exponential model:

$$I(t) = b + \sum_{i=1}^{n} A_i \left(1 - \exp\left(-\frac{t}{\tau_i} \right) \right) \tag{9.1}$$

where τ_i are the recovery half-times and A_i are the corresponding pre-exponential factors. To calculate the diffusion coefficient, the following relation was used:

$$D = \frac{\Gamma \omega^2}{4\tau} \tag{9.2}$$

where Γ is the correction factor for the Gaussian beam shape, equal to 0.88, ω is the radius of the bleaching spot, and τ is the recovery half-time. Next, the particle hydrodynamic radius R_H was calculated using the Stokes-Einstein relation:

$$R_H = \frac{k_B T}{6\pi\eta D} \tag{9.3}$$

where k_B is the Boltzmann constant, T is the temperature equal to 293.15 K, and η is the sample viscosity measured using the rotational rheometer.

All data were analysed using a custom-developed data analysis pipeline created in
Python.

9.2.4 Rheological Measurements

Rheological measurements were performed on a Kinexus Prime pro+ (Netzsch) rota-
tional rheometer using a 40 mm diameter cone with a 4° cone angle. For the measure-
ment, 1.19 mL of sample was deposited between the plate and the cone, followed by
cooling the sample until a temperature of 20 °C was reached and a 5-minute equilibra-
tion at the designated temperature. Next, viscosity measurements were performed over
a shear rate range of 0.1 s^{-1} to 100 s^{-1}, with 10 points per decade and a ramp time of
30 seconds. In all cases, steady state was reached, indicating that the precise viscosity
value was obtained.

9.3 Results and Discussion

9.3.1 Viscosity Measurements

Figure 9.1A shows shear stress as a function of shear rate for each of the samples used.
All samples displayed Newtonian behaviour over the whole range of measured shear
rates. The viscosities measured between 1 s^{-1} and 100 s^{-1} shear rates were averaged
to obtain the viscosity values used for the size calculations. The error bars were taken
as three standard deviations of those values. The resulting viscosities are shown in
Figure 9.1B. The measured viscosities were found to be lower than the values specified
by the manufacturer for both HS40 and AS40. The measured viscosity of HS40 was
34 cP at 20 °C compared to the manufacturer's reported 45 cP at 25 °C and 9.6 cP
compared to 20 cP for AS40. Only the measured viscosities were used to calculate
particle sizes to ensure the consistency of the results between all samples.
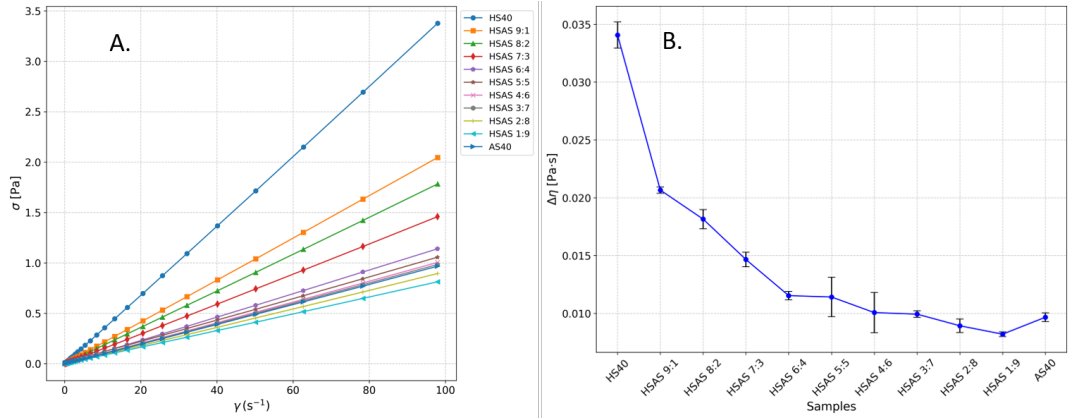
Figure 9.1: Viscosity Results. A. Shear stress as a function of shear rate for the used samples; B. Average viscosity used for the size calculations.

9.3.2 Theoretical Recovery Times

The next step was to assess whether the diffusion of each system component occurred on a timescale that could be resolvable by the assembled experimental setup. The theoretical recovery half-times for each sample component—free R6G, AS40 particles, and HS40 particles—are calculated by equating equations 9.2 and 9.3:

$$\frac{k_B T}{6\pi\eta R_H} = \frac{\Gamma\omega^2}{4\tau} \tag{9.4}$$

and solving it for τ:

$$\tau = \Gamma\frac{6\pi\omega^2\eta R_H}{4k_B T} \tag{9.5}$$

To obtain theoretical recovery times, the radii used were 0.6 nm for R6G, 6 nm for HS40 and 11 nm for AS40, while for the viscosity, the measured values shown in Figure 9.1B were used. The obtained theoretical recovery half-times are plotted in Figures 9.2A and B.
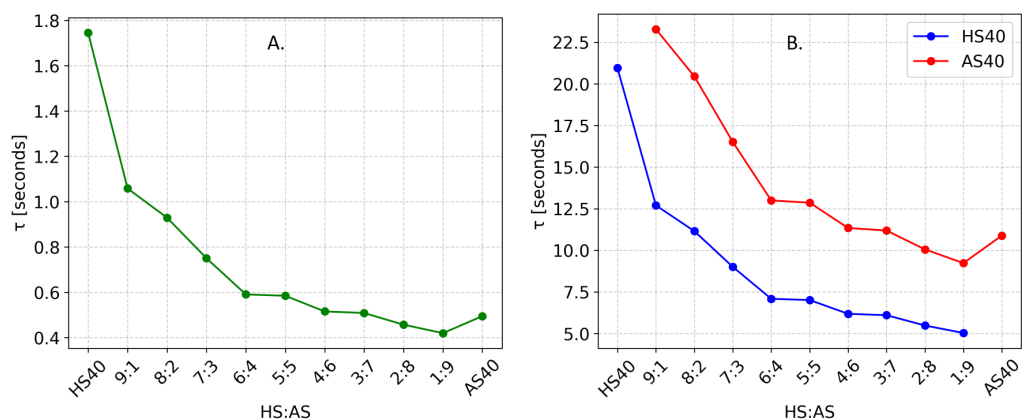
Figure 9.2: Theoretical recovery half-times for all samples. A. Free R6G in each sample;
B. HS40 and AS40 colloids

The R6G recovery half-times shown in Figure 9.2A indicate that, in most cases, free
dye diffuses faster than the measurement limit. However, as shown later, in samples
with ratios from 9:1 to 7:3 a model component can still be successfully attributed to free
dye, improving radius accuracy when using the more complex tri-exponential model. In
all other samples, adding a third component to describe the kinetics of free R6G would
lead to over-parametrisation and size overestimation. Both colloids are distinguishable
across most of the range, but accuracy improves at higher viscosities, where slower
overall diffusion allows for a more detailed representation.

9.3.3   Validation of the FRAP Data Collection

To validate the instrumental setup and data analysis, FRAP measurements were con-
ducted on a 10 µM solution of R6G in 100% glycerol, with a viscosity of 1412 cP. The
obtained average FRAP curve is shown in Figure 9.3. The FRAP curve in Figure 9.3
exhibits a typical recovery profile, characterised by a rapid initial rise in normalised
intensity followed by a slower approach to a plateau near 1, indicating full recovery
over time. The recovery follows an exponential trend, consistent with the expected
behaviour for small molecule diffusion in a high-viscosity solvent.
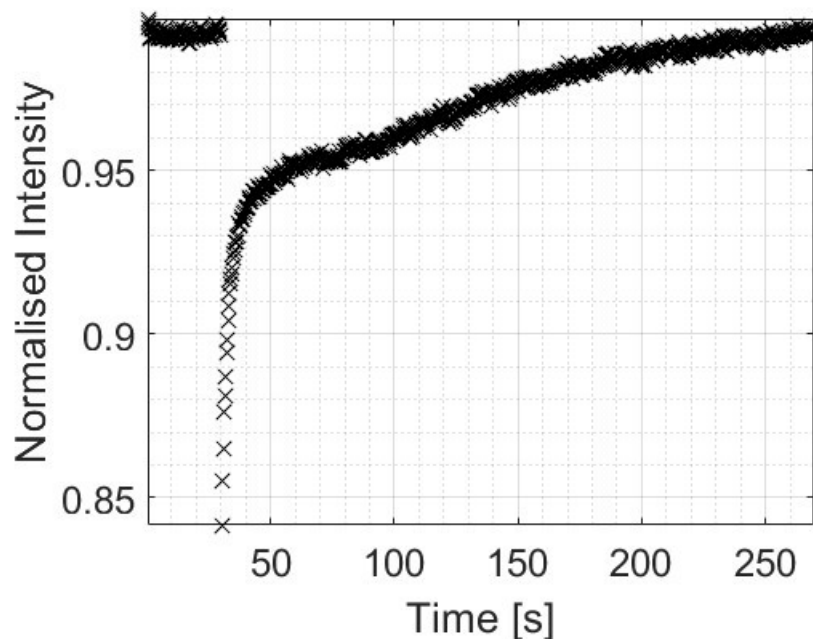
Figure 9.3: Recovery time of 10 μM of R6G in in 100% glycerol solution.

The tightly clustered data points and low scatter suggest that the measurements are highly reproducible and the instrumental setup is well-calibrated. The observed average recovery half-time of (60.73 ± 11.43) s corresponds to an average hydrodynamic radius of (5.96 ± 0.75) Å, as calculated using Equation 9.3. This agrees closely with the value obtained from time-resolved anisotropy decays (5.9 ± 0.6) Åpresented in Chapter 8 and other independent techniques such as picosecond polarization grating technique and multi-colour dual-focus fluorescence correlation spectroscopy experiments [330, 331]. This consistency reinforces the reliability of FRAP for accurately measuring the size of small molecules in viscous media and validates the effectiveness of the experimental setup and data analysis.

9.3.4 Pure Colloids

After successfully demonstrating that the assembled FRAP setup can accurately measure the hydrodynamic radius of free R6G in glycerol, the next step was to apply the approach to a well-studied system with physicochemical properties similar to those of

sodium silicates, which remained the final goal of this thesis. However, due to the complexity of sodium silicates, it was necessary to begin with a simpler system. An ideal candidate for this test is LUDOX colloidal silica. Unlike the time-resolved anisotropy discussed in Chapter 8, which focuses on rotational diffusion, FRAP utilises translational diffusion. As a result, the viscosities suitable for this type of setup must be relatively large.

Measurements on individual colloids were performed to assess whether the proposed FRAP method can overall be used to measure the size of nanoparticles in a simple monodisperse system. In both cases of 6 nm HS40 and 11 nm HS40, the dye was added directly to the sample, at concentrations ranging from 5 µM to 20 µM and the experiment was conducted according to the protocol described in the Methods section. The resulting particle sizes obtained by directly fitting the FRAP recovery curves to both mono and bi-exponential models are shown in Figure 9.4.
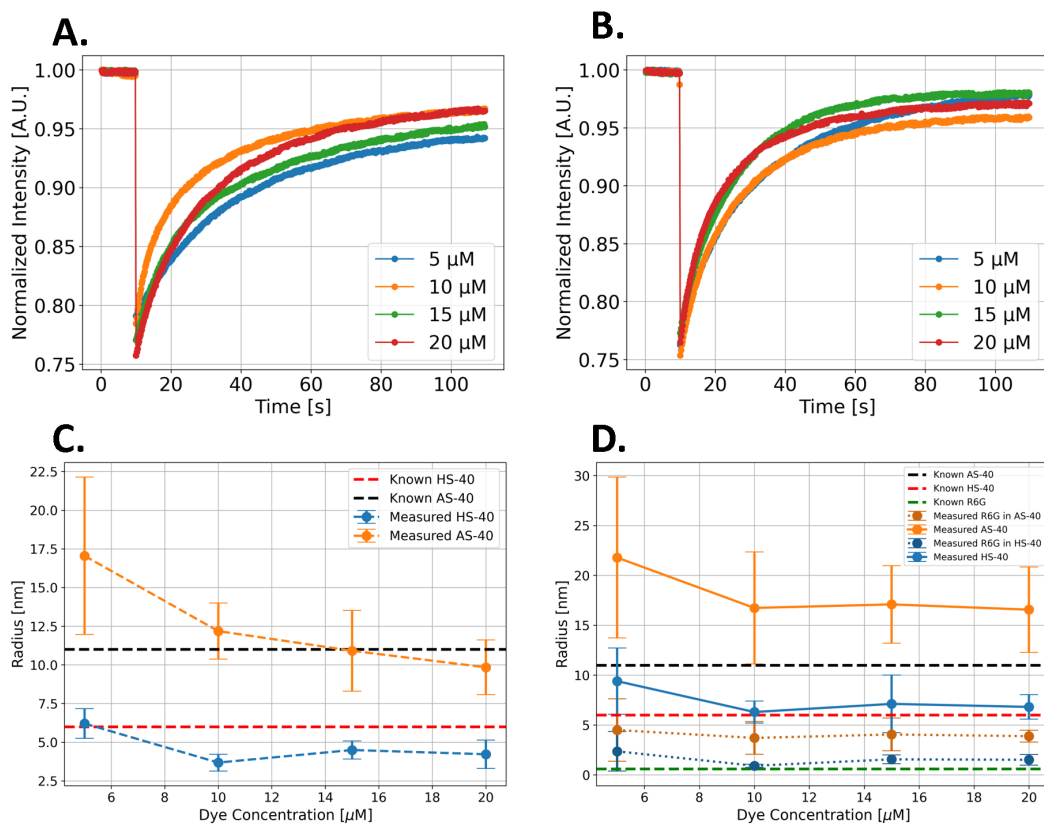
Figure 9.4: Results for the monodisperse systems: A. FRAP recovery curves for LU-
DOX HS-40 at different R6G concentrations; B. FRAP recovery curve for LUDOX
AS-40 at different R6G concentrations C. Recovered hydrodynamic radii for LUDOX
HS-40 and AS-40 when fitted to a mono-exponential model; D. Recovered hydrody-
namic radii for LUDOX HS-40 and AS-40 when fitted to a bi-exponential model. All
errors are quoted to three standard deviations. The actual sizes for the R6G (0.6 nm)
and SNPs (6 nm for HS-40 and 11 nm for AS-40) are marked with dashed lines.

The FRAP recovery curves for the individual colloids, HS-40 and AS-40, shown in
Figure 9.4A and 9.4B, reveal some interesting differences in how they behave during
diffusion, influenced by their size and viscosity. Notably, HS-40 tends to recover more
slowly at higher dye concentrations. This suggests that as dye levels increase, it might
lead to more significant interactions between the colloids or even crowding effects that
make diffusion more challenging. On the other hand, AS-40's recovery curves change
very little with varying dye concentrations, indicating that these larger particles face
less hindrance from the dye molecules. The faster recovery of AS-40 compared to HS-

205

40 can be linked to its lower viscosity, which makes diffusion more efficient. These differences show how FRAP is effective at capturing the unique diffusion behaviours tied to particle size and viscosity, with HS-40 being more sensitive to changes in dye concentration than AS-40.

The results indicate that precise size estimation strongly depends on selecting an appropriate theoretical model based on sample viscosity. The mono-exponential model in Figure 9.4C effectively captures the kinetics of the AS40 colloids and retrieves particle sizes with high precision, particularly at higher dye concentrations. This accuracy can be attributed to the short recovery half-time (0.5 s) of free R6G in AS40 (Figure 9.2A), which the current experimental setup cannot resolve. Consequently, fully assessing the free dye's impact on the measured AS40 radius remains challenging. However, the high precision of the recovered sizes suggests that this effect is minimal at the tested concentrations. Nevertheless, the influence of free dye is evident, as shown by the decrease in the average recovered size with increasing dye concentrations in AS40.

In contrast, the mono-exponential model fails to accurately recover the radius of HS40, underestimating its size and further emphasising the dependence of model selection on viscosity. This underestimation arises from free R6G diffusion, which occurs at a partially detectable rate with a recovery half-time of around 2 s. As a result, the oversimplified mono-exponential model does not adequately describe free dye diffusion, resulting in a smaller-than-expected size estimate. This effect is evident when comparing the HS40 size at 5 µM and 20 µM dye concentrations. At 5 µM, where free dye is minimal, the recovered HS40 size matches the reference value of 6 nm. However, at 20 µM, with a substantially higher free dye concentration, the size is underestimated. These findings suggest that in more viscous samples, where both dye and SNP diffusion are observable, a more complex model is necessary.

The recovered R_H of both colloids using a bi-exponential model are shown in Figure 9.4D. The bi-exponential model is unsuitable for AS40 because it over-parametrises the experimental data, resulting in significantly overestimated radii for both free R6G and SNP. However, the bi-exponential model provides a more detailed description of recovery curves in HS40 samples, yielding more accurate hydrodynamic radii. Notably,

206

at higher dye concentrations, the HS40 SNP radius is no longer underestimated, and the recovered R6G radius closely matches the expected value of 0.6 nm.

All of the above suggest that a universal model cannot accurately recover colloidal particle radii. Instead, model selection must be tailored to sample viscosity. Moreover, accounting for free dye is crucial, as oversimplified models tend to underestimate recovered sizes.

9.3.5   Binary Particle Systems

In the previous section, it was demonstrated that FRAP can precisely measure the sizes of individual colloids in a monodisperse system. The next step is to determine whether the method can also distinguish individual particle sizes in a binary particle system. To create such a system, LUDOX HS40 and AS40 colloids were mixed at ratios starting from 9:1 (HS40:AS40) to 1:9 ratio, immediately before measurements. The mixtures were added with R6G at concentrations of 5, 10, 15 and 20 µM. FRAP measurements were conducted. The average, raw FRAP curves for each mixture and R6G concentration are shown in Figure 9.5.
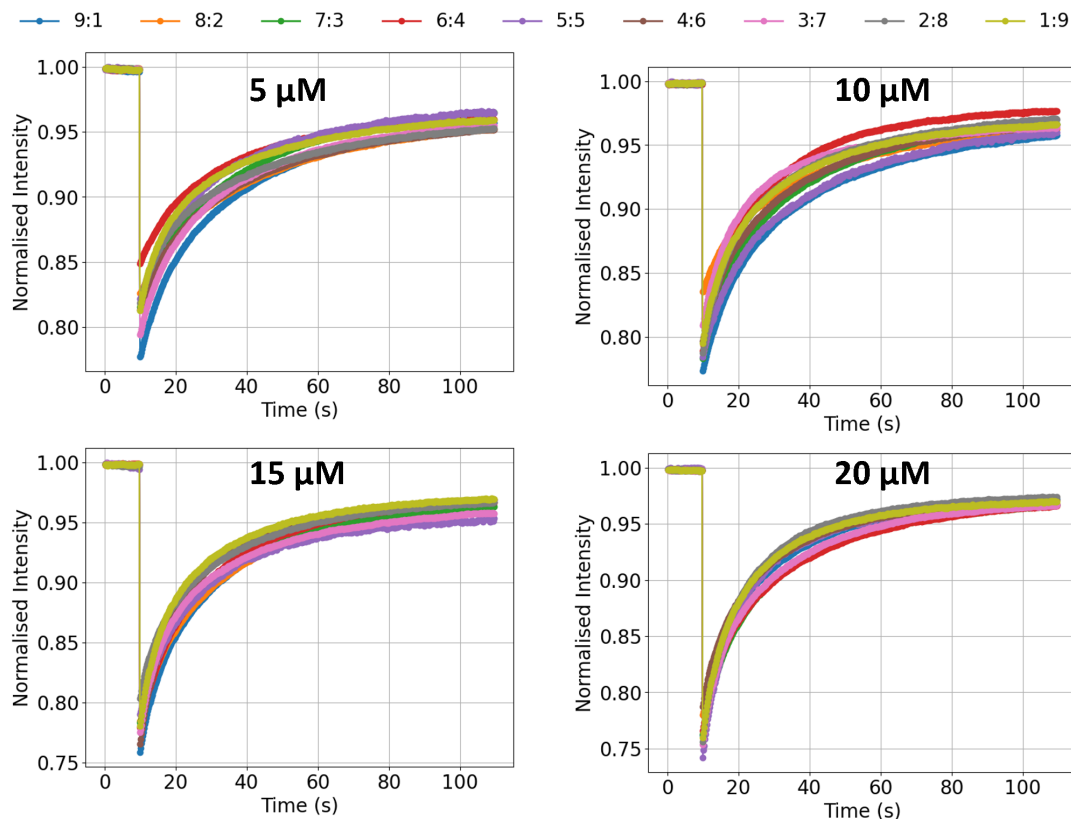
Figure 9.5: Average FRAP Recovery Curves for prepared binary systems in various concentrations and mixtures.

The FRAP curves indicate that as the proportion of AS40 (larger particles, lower viscosity) increases, recovery occurs more quickly, while greater proportions of HS40 (smaller particles, higher viscosity) lead to slower recovery. The 1:9 mixture, which has the most AS40, demonstrates the quickest recovery, whereas the 9:1 mixture, rich in HS40, displays the slowest recovery rate. This suggests that AS40, with its greater size, lower viscosity, and weaker binding interactions, promotes molecular mobility. Conversely, HS40 appears to hinder diffusion, likely due to stronger binding or increased viscosity. Recovery also shows slight improvement with higher dye concentrations (15–20 µM), implying that greater concentrations could facilitate molecular exchange or lower diffusion barriers by increasing the number of mobile particles or enhancing labelling efficiency. Nonetheless, the primary factor influencing recovery is the

mixture composition, as evidenced by the consistent pattern of recovery across vary-
ing concentrations, highlighting that the interaction between HS40 and AS40 mainly
governs diffusion dynamics.

Next, the obtained recovery curves were fitted to multi-exponential models as de-
scribed in the Methods section. It was found that 10 µM to 15 µM concentration
provided the best balance between the S/N ratio and the measurement precision.

The Mono-Exponential Model

The recovered hydrodynamic radii obtained by fitting the recovery curves to a mono-
exponential model are shown in Figure 9.6. These results demonstrated that even the
simplest models can provide some insight into sample composition. In samples with
high HS40 content, the recovered hydrodynamic radius is close to that of HS40, likely
because the 6 nm particles dominate the composition, making them easily identifiable.
In contrast, as HS40 content decreases and AS40 concentration increases, the recovered
radius shifts closer to the 11 nm AS40 SNPs.
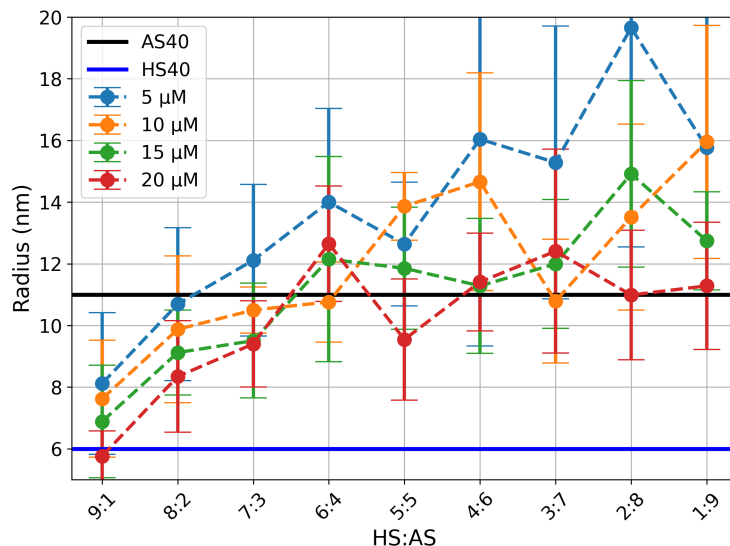
Figure 9.6: Recovered hydrodynamic radii from fitting the datasets to a mono-
exponential model for varying dye concentrations and various HS:AS ratios.

However, it is essential to highlight that this trend holds only at high dye concentra-

tions. To ensure accurate measurements and reliable recovery of individual component sizes, dye concentration must remain relatively high, around 15–20 µM. Higher dye concentrations improve labelling efficiency, enhance the S/N ratio (as indicated by reduced error bars), and enable accurate size estimation. Additionally, the observed increase in measured radius at lower dye concentrations may result from preferential adsorption of the dye to larger SNPs due to their higher net negative charge and smaller surface curvature. Furthermore, the consistent increase in the measured radius at lower dye concentrations supports the observation that dye preferentially adsorbs to larger AS40 particles due to their greater net negative charge and reduced surface curvature [361] as discussed in Chapter 6. This is further demonstrated by the rising variability and larger error bars at low dye concentrations, which reflect heightened measurement uncertainty and lower labelling efficiency. The uniform radii and reduced error bars observed at higher dye concentrations (15 µM and 20 µM) confirm that higher dye concentrations improve the S/N ratio, enhancing measurement accuracy.

The variations in radius at intermediate HS:AS ratios (approximately 5:5 to 4:6) imply that sample heterogeneity or inconsistencies in dye binding efficiency might be responsible for the noted measurement noise. These patterns highlight the necessity of optimising dye concentration to ensure precise size recovery, especially within complex mixtures. The above findings suggest that a simple mixture of two unknown colloids at different ratios can provide sufficient information to estimate particle sizes. However, this approach is suboptimal as accurately determining multiple NP sizes requires varying their concentrations and conducting at least two measurements. This is impractical, especially for polydisperse, metastable systems such as sodium silicates [13, 22, 261]. Therefore, multi-exponential models were tested.

The Bi-Exponential Model

Figure 9.7 presents the results of fitting the recovery curves to a bi-exponential model. These results largely mirror the trends observed with the mono-exponential model. Specifically, measurement precision for AS40 SNPs improves with increasing dye concentration due to an enhanced S/N ratio, expanding the range of ratios where the

size of 11 nm SNP can be accurately measured. However, at higher dye concentra-
tions, the recovered size of the 6 nm HS40 SNP is gradually underestimated more,
with free dye increasingly contributing to the average measured size of the HS40 and
R6G. Despite these limitations, the bi-exponential model significantly outperforms the
mono-exponential model by successfully identifying the presence of SNPs of different
sizes with a single measurement, which the simpler model could not achieve. However,
one should note that the bi-exponential model consistently overestimates the size of the
AS40 at all R6G concentrations in samples where the HS40 ratio is 6:4 or lower. Even
when AS40 is the dominant component, the recovered size remains overestimated. This
reinforces the trend observed in the pure colloid AS40 sample, highlighting viscosity
as the key factor limiting measurement precision. Additionally, the detection of 11
nm particles even at very low AS40 concentrations suggests that R6G exhibits size-
dependent adsorption, with a greater tendency to bind to larger SNPs, a phenomenon
observed in the MD simulations discussed in Chapter 6.
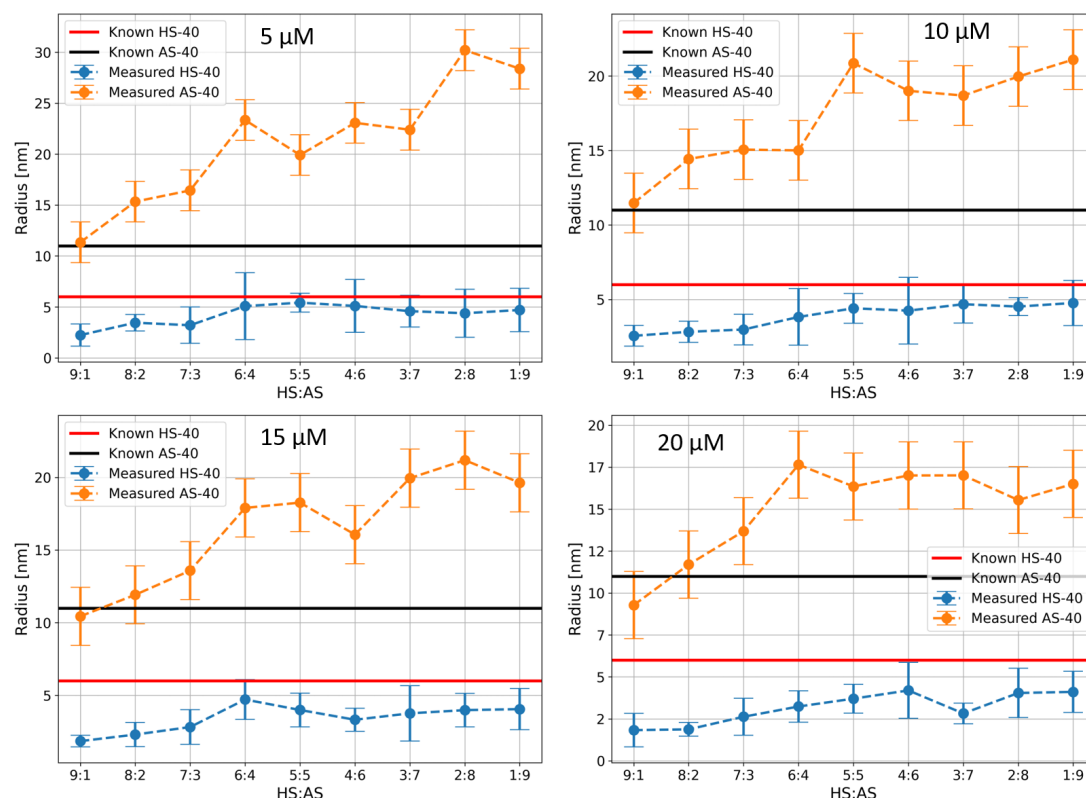
Figure 9.7: Recovered hydrodynamic radii from fitting the datasets to a bi-exponential model as a function of dye concentration.

The recovered size of HS40 is consistently underestimated across all dye concentrations and HS:AS ratios, even when HS40 is the dominant component (e.g., at 9:1 and 8:2 ratios), likely due to the contribution of free dye molecules affecting the apparent diffusion coefficient. Increased variability in HS40 size at low HS40 content suggests greater noise from free dye or challenges in resolving the smaller particle size in complex mixtures. In contrast, the recovered size of AS40 is consistently overestimated, especially at lower HS:AS ratios, which may reflect stronger dye adsorption to larger SNPs or increased solution viscosity at higher AS40 content. Sensitivity to dye concentration is evident, with greater measurement variability at 5 µM due to a poorS/N ratio, whereas at 20 µM, the AS40 size measurement stabilises, but HS40 size remains underestimated. The model shows greater sensitivity for AS40 at high dye concentrations, likely due to stronger signals from larger SNPs, as suggested by MD simulations

discussed in Chapter 6. Notably, the recovered sizes for both HS40 and AS40 are closest to their expected values around a 5:5 HS:AS ratio, suggesting that the bi-exponential model performs best when both SNPs contribute equally to the diffusion profile. These findings highlight the improved sensitivity and accuracy of the bi-exponential model compared to the mono-exponential model, particularly for resolving larger SNPs in mixed systems.

For HS40 SNPs in the mixtures, the recovered size is underestimated in all samples, even when HS40 is the dominant component (as in the 9:1 and 8:2 samples). This likely results from the oversimplified model struggling to accurately describe the diffusion of a three-component system. Consequently, the recovered HS40 radius represents a mixture of HS40 and free R6G radii.

Nonetheless, the bi-exponential model offers the best balance between accuracy and precision, enabling the identification of both larger and smaller SNPs without excessive parameterisation while maintaining reasonable accuracy and relatively small error bars. Furthermore, the accuracy of the bi-exponential model can be improved by performing FRAP measurements based on fluorescence lifetimes rather than intensity, as lifetime-based measurements would allow for complete separation of free and bound dye to their distinct lifetimes [39, 362].

The Tri-Exponential Model

To capture all system components within a single measurement, a tri-exponential model was used for fitting GBM pre-processed data, with results shown in Figure 9.8. As expected, the trends observed in simpler models are also present here. Notably, measurement accuracy improves with increasing dye concentration, as indicated by the significant reduction in error bars when comparing the 9:1 and 8:2 samples at 15 µM versus 5 µM dye concentrations.
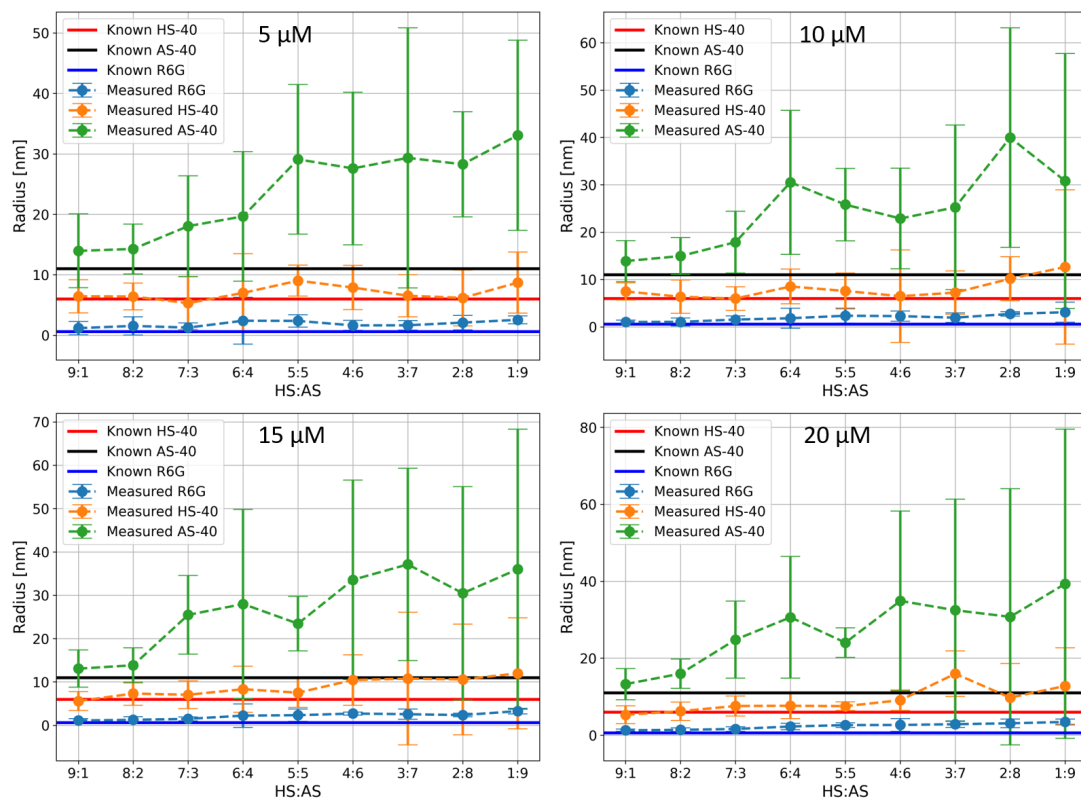
Figure 9.8: Recovered hydrodynamic radii from fitting the datasets to a tri-exponential model.

The tri-exponential model is sufficiently complex to describe the full kinetics of the sample and its components, enabling the recovery of all three sizes in a single measurement at HS40:AS40 ratios of 9:1 and 8:2. A slight overestimation of the AS40 SNP radius in the 9:1 and 8:2 samples is likely due to its relatively low concentration in the mixture. HS40, in contrast, can be accurately measured across a broader range of sample ratios due to its higher concentration in the mixture. As the AS40 concentration increases, the overall viscosity rapidly decreases (as shown in Figure 9.1), leading to faster diffusion. This results in increased variation between FRAP measurement repetitions, larger error bars, and an overestimation of size, an effect also observed in pure AS40 samples (Figure 9.4D). This is evident in all three components; the recovered size gradually increases with decreasing viscosity, reinforcing the conclusion that optimal model selection strongly depends on sample viscosity and remains a non-trivial process.

Nonetheless, at high viscosities, the tri-exponential model provides a significant advantage over simpler models. It enables useful determination of particle sizes at sufficient accuracy and precision in a binary particle system with a single measurement, even when one colloid is present at low concentrations.

9.4 Molecular Simulation Insights into FRAP

The interpretation of FRAP data in the studied SNP systems benefits from comparison with simulations presented in Chapter 6 and 7. MD results indicate that adsorption of R6G monomers onto SNP surfaces is a dynamic process, characterised by frequent adsorption–desorption cycles occurring on nanosecond timescales. Analysis of residence times discussed in Chapter 6 yields $\Delta G^{\ddagger}$ in the range of 5–8 kcal·mol^{-1}, consistent with moderately strong but reversible binding to silanol groups. This dynamic behaviour contrasts with the FRAP assumption that once dyes are adsorbed, they remain bound for the duration of the experiment. In practice, however, the desorption timescale (nanoseconds) is several orders of magnitude faster than the diffusion window probed by FRAP (seconds). As a result, the recovery curves effectively represent an ensemble average over many adsorption–desorption events, rather than static dye binding, and thus still yield reliable hydrodynamic radii. Nevertheless, the assumption of stable adsorption likely underestimates the contribution of free dye to the recovery signal, particularly at higher dye concentrations where rapid exchange between bound and unbound states may bias size estimates.

Dimer formation in solution, as observed in MD simulations, is highly conformation-dependent and transient. Lifetimes of R6G dimers are generally short (roughly 5–40 ns), with stability strongly influenced by molecular geometry as indicated by SMD and DFT results discussed in Chapter 7. On SNP surfaces, steric constraints prevent long-lived dimer adsorption, meaning that monomers dominate the adsorbed population. This observation aligns with FRAP data: the diffusion behaviour primarily reflects monomer-bound particles. Importantly, these dimers are non-fluorescent and therefore do not contribute directly to FRAP recovery. Their role is indirect: at high dye concen-

trations, transient dimerisation reduces the pool of fluorescently active monomers available for adsorption, which can manifest as slight deviations in the recovered nanoparticle sizes.

These molecular insights clarify several trends observed in FRAP experiments. In AS40-rich mixtures, faster recovery arises primarily from lower viscosity, while stronger preferential adsorption to larger, low-curvature particles ensures that AS40 dominates the recovered sizes, consistent with simulations showing stabilised adsorption on AS40 compared to HS40. Conversely, HS40-rich mixtures show slower recovery dominated primarily by viscosity, while their weaker adsorption reduces their contribution to the recovered radii. Apparent size overestimations or underestimations in binary mixtures can thus be rationalised as the combined outcome of viscosity effects, reversible adsorption with $\Delta G^{\ddagger} \sim 5$–$8$ kcal·mol^{-1}, and competition between fluorescent monomers and non-fluorescent dimers.

Future improvements could come from combining FRAP with equilibrium free-energy calculations such as potential of mean force (PMF) profiles, which would allow direct conversion of simulated residence times into thermodynamic binding free energies (ΔG_{bind}). This would bridge molecular-scale adsorption energetics with experimentally accessible diffusion coefficients, yielding a more quantitative basis for interpreting size distributions in binary and polydisperse systems. In particular, linking ΔG_{bind} with the concentration-dependent recovery trends observed in FRAP would help distinguish whether apparent size deviations arise primarily from viscosity effects, reversible adsorption, or transient non-fluorescent dimer formation. Furthermore, applying such calculations across different SNP sizes and surface chemistries would enable a direct comparison of curvature- and charge-dependent binding affinities, providing mechanistic insight into why larger particles disproportionately dominate recovery in binary systems.

9.5 Conclusions

In this work, the use of FRAP as a nanometrology tool in binary nanoparticle systems was assessed for the first time. Unlike previous studies using time-resolved anisotropy measurements, which only provide an average particle size for a two-particle system, FRAP enabled the recovery of individual particle sizes. However, data analysis is non-trivial, as model selection is highly dependent on the sample viscosity. The obtained results indicate that highly viscous samples, containing slowly diffusing particles, benefit from more complex models, whereas simpler models are more suitable for less viscous systems to avoid over-parametrization and size overestimation. This suggests a general trend: multi-exponential models are preferable for high-viscosity samples with slow diffusion, while simpler models are more effective for thinner fluids where diffusion occurs rapidly. Furthermore, optimal dye concentration was found to be around 15 µM, ensuring a strong S/N ratio. However, high dye concentrations introduce significant amounts of free dye, which can lead to underestimated sizes due to size mixing between nanoparticles and unbound dye. This issue could be mitigated by using a fluorescent dye that forms a covalent siloxane bond, reducing free dye presence and improving measurement precision [34, 224]. Alternatively, FRAP measurements based on fluorescence lifetime rather than intensity could completely separate signals from free and bound dye, as the results in Chapter 8 demonstrated distinct lifetimes for each [39].

Regardless of the model used, findings confirm that FRAP is a viable nanometrology tool for measuring SNP sizes. Even the simplest mono-exponential model provides size estimates with just two measurements. The most precise size estimate was achieved using the tri-exponential model, where each component corresponds to a distinct sample fraction. However, this model is only reliable in relatively high-viscosity environments, as it tends to underperform at low viscosities, leading to size overestimation and over-parametrisation. Finally, MD simulations, discussed in Chapter 6, revealed that dye adsorption is size-dependent, with larger SNPs serving as more suitable targets. This is largely due to their greater net negative charge and smaller curvature, which facilitates more stable dye adsorption. These observations align with trends observed in

FRAP experiments, reinforcing the potential of combining both methods to enhance the understanding of binary nanoparticle systems.

When prior knowledge of their binary nature exists, the bi-exponential model offers the best balance between accuracy, simplicity, and reliability for binary particle systems. While it slightly underestimates the size of smaller nanoparticles, its advantages outweigh its drawbacks. The combination of covalently bound dye at lower concentrations with lifetime-based FRAP should potentially further enhance measurement accuracy, enabling precise size determination for both nanoparticle species in the system.

Chapter 10

Nanometrology of Sodium Silicates using Fluorescence Recovery After Photobleaching and ^{29}Si NMR Spectroscopy

10.1 Introduction

This chapter of the thesis focuses on the application of FRAP as a nanometrology tool for industrial sodium silicates. Having revealed the mechanisms governing dye–SNP interactions through MD simulations (Chapter 6) and demonstrated the feasibility of FRAP on binary LUDOX systems (Chapter 9), the next logical step is to extend this FRAP approach to chemically more complex systems, such as sodium silicates.

As discussed in Chapter 1, sodium silicates are widely used in industrial and scientific applications due to their unique structural and chemical properties. However, their characterisation remains challenging because of their polydispersity, chemical reactivity, and tendency to evolve structurally under different environmental conditions. Traditional methods such as DLS and TEM struggle with these systems, mainly due

to small particle sizes and complications arising from sample preparation protocols. NMR, although considered the gold standard for characterising the chemical structure of silicates, does not provide direct quantitative information on particle size. Moreover, NMR is inherently blind to particle morphology or aggregation behaviour differences when samples have identical molar ratios, even if their physicochemical characteristics differ significantly. This limitation arises because NMR primarily probes the local chemical environment, such as the connectivity of silicon and oxygen atoms, rather than the spatial arrangement or size of the resulting structures. While size and connectivity can be correlated, particularly at the nanoscale where smaller particles exhibit a higher proportion of interfacial atoms and potentially altered connectivity, such distinctions may remain unresolved in typical NMR experiments due to limited resolution and experimental uncertainty. As a result, two samples with identical $SiO_2 : Na_2O$ ratios, but differing in particle size or aggregation state, as will be shown later, can produce nearly indistinguishable NMR spectra.

In contrast, FRAP is sensitive to the diffusion behaviour of fluorescently labelled particles, directly reflecting their hydrodynamic size. Differences in diffusion coefficients allow FRAP to detect variations in particle size and aggregation that are invisible to NMR, making it a complementary tool for nanoparticle characterisation.

In this chapter, FRAP is applied to sodium silicate samples to evaluate its potential as a nanometrology tool for complex polydisperse systems. Particular attention is given to how the dye concentration and sample dilution influence the measured diffusion behaviour and, ultimately, the extracted particle sizes. Importantly, by measuring diffusion-based size, rather than local chemical structure, FRAP serves as a valuable complement to NMR. For comparative purposes, ^{29}Si NMR data, kindly provided in private correspondence by Gavin Armitt from PQ Silicas UK, are also included in this chapter. These data, originally collected for internal quality control purposes, are used here to assess the correlation and the limitations between structural and diffusion-based characterisation.

10.2 Methods

10.2.1 Sodium Silicates

The sodium silicates used for the measurements presented in this chapter consisted of three different samples, each with a similar molar ratio, and have codenames SD6521, SD6522, and SD6524. The details of the samples in their native and 50% diluted forms are described in Table 10.1. All sample properties, such as viscosity, turbidity, molar ratios, and contamination data, were provided by PQ Silicas UK in private correspondence.

Name	Viscosity (cP)	Turbidity (NTU)	Na$_2$O (%)	SiO$_2$ (%)	Mol Ratio
SD6521	48	8.8	8.33	27.39	3.40
SD6522	46	5.8	8.29	26.89	3.36
SD6524	304	14	8.76	28.99	3.41
SD6521 (50%)	19	—	4.23	13.02	3.18
SD6522 (50%)	15	—	4.15	13.08	3.26
SD6524 (50%)	14	—	4.42	14.19	3.32

Table 10.1: Physicochemical properties of the samples used for FRAP measurements. Data was provided by PQ Silicas UK in private correspondence. Turbidity data for diluted samples was not provided.

As summarised in Table 10.1, the three samples, SD6521, SD6522, and SD6524, exhibit molar ratios in the narrow range of 3.36 to 3.41, characteristic of typical alkaline silicates used in commercial formulations. Despite the similar ratios, the samples vary significantly in viscosity and turbidity, reflecting potential differences in polymerisation state and aggregate content. It is important to note that silicate viscosity is primarily influenced by solids concentration, which can affect these observed variations [363]. Notably, SD6524 exhibits a much higher viscosity (304 cP) and turbidity (14 NTU) compared to the other two samples, suggesting the presence of larger or more complex silicate species and an overall higher concentration of the silicate.

In order to investigate concentration-dependent behaviour, each sample was also measured in a diluted state, prepared by halving the original silicate content. Dilution

is often employed to reduce viscosity and turbidity, which can otherwise interfere with optical measurements such as FRAP. High viscosity can slow down diffusion to the point where recovery times exceed practical imaging windows, while elevated turbidity scatters light and lowers signal quality, making it difficult to accurately monitor fluorescence changes. By diluting the sample, the goal is to improve imaging clarity and enable more precise recovery curve fitting, particularly in systems where particle interactions and optical density may obscure underlying diffusion dynamics. It is important to mention that dilution may affect speciation and particle size, which is a potential concern that must be carefully considered in the analysis.

Sample dilution resulted in notable changes in both viscosity and molar ratio. The pronounced drop in viscosity upon 50% dilution primarily reflects the reduced solids concentration, consistent with classical models where viscosity decreases significantly as particle concentration decreases [364]. The inclusion of both undiluted and diluted samples enables the assessment of structural dynamics and dye-particle interactions under different crowding and ionic strength conditions, which is critical for interpreting FRAP results in the context of colloidal stability and diffusion. NMR data were also obtained for both concentration states, supporting the interpretation of network reorganisation and providing molecular-level evidence of silicate speciation and structural transitions upon dilution.

10.2.2   FRAP Protocol

FRAP experiments were performed to evaluate the diffusion behaviour of R6G-labelled sodium silicates under varying conditions. As the sodium silicates are non-fluorescent, they were labelled electrostatically with R6G at concentrations of 5, 10, 15 and 20 µM by adding the dye directly to the sample.

For each measurement, 7 µL of the labelled sample was pipetted onto a microscope slide fitted with a 0.12 mm spacer and sealed with a coverslip. The imaging protocol consisted of 50 pre-bleach frames acquired at 0.2 s intervals, followed by a 3-second 532 nm bleaching pulse applied at full laser power over a circular ROI with a 10 µm radius. After bleaching, fluorescence recovery was monitored for 500 frames, also at

0.2 s intervals. Ten FRAP measurements were recorded at spatially separated locations on the slide for each condition and dye concentration to avoid overlap with previously bleached regions. This resulted in 40 measurements per sample (10 measurements $\times$ 4 concentrations) per dilution state. With three samples and two concentration regimes (undiluted and 50% dilution), a total of 240 FRAP image stacks were acquired and analysed.

All FRAP measurements were performed on a custom-built setup based on the Cairn Research Open Frame microscope platform described in detail in Chapter 5, Subsection 5.5.5. Imaging was carried out using a 530 nm LED (Cairn Research), and bleaching was performed using a 150 mW continuous-wave 532 nm laser (Coherent). Fluorescence was recorded using a CellCam Kikkor camera (Cairn Research) through an Olympus UPLXAPO 100X oil immersion objective (NA 1.45). Photobleaching during the imaging phase was corrected by tracking a secondary ROI located away from the bleach zone and applying normalization accordingly as described in Section 5.5.4 of Chapter 5. Preliminary image processing was performed using ImageJ, and quantitative analysis, curve fitting, and modelling were conducted using a custom Python routine.

This protocol was adapted from earlier FRAP experiments on LUDOX colloidal silica systems (Chapter 9), and applied here without modification to enable consistent comparison between model systems and chemically more complex sodium silicates.

10.3   Results and Discussion

10.3.1 ^{29}Si NMR Spectroscopy

To investigate structural differences in the sodium silicate samples, ^{29}Si NMR spectroscopy data provided by PQ Silicas UK was analysed, and is shown in Figure 10.1. The analysis aimed to assess whether the degree of silicate polymerisation and the distribution of Q-species vary across samples with similar molar ratios or following dilution. This comparison was intended to determine whether chemical structure variations correlate with the particle sizes and diffusion trends observed in the FRAP

datasets.

All NMR measurements were carried out using a high-sensitivity 64k scan protocol at 40 °C, over a 72-hour acquisition period, using a benchtop X-Pulse NMR spectrometer (Oxford Instruments) which uses a 60 MHz (1.4 T) permanent magnet. Despite the relatively low magnetic field strength of the system used for these measurements, the resulting spectra shown in Figure 10.1 show remarkably well-resolved silicon environments. Specifically, distinct resonances corresponding to Q^1, Q^2, Q^3, and Q^4 species were observed in all samples, indicating the presence of a range of silicate oligomers and network fragments. For the diluted samples, the spectra were collected after a four-week equilibration period to ensure that any slow structural rearrangements could be detected.
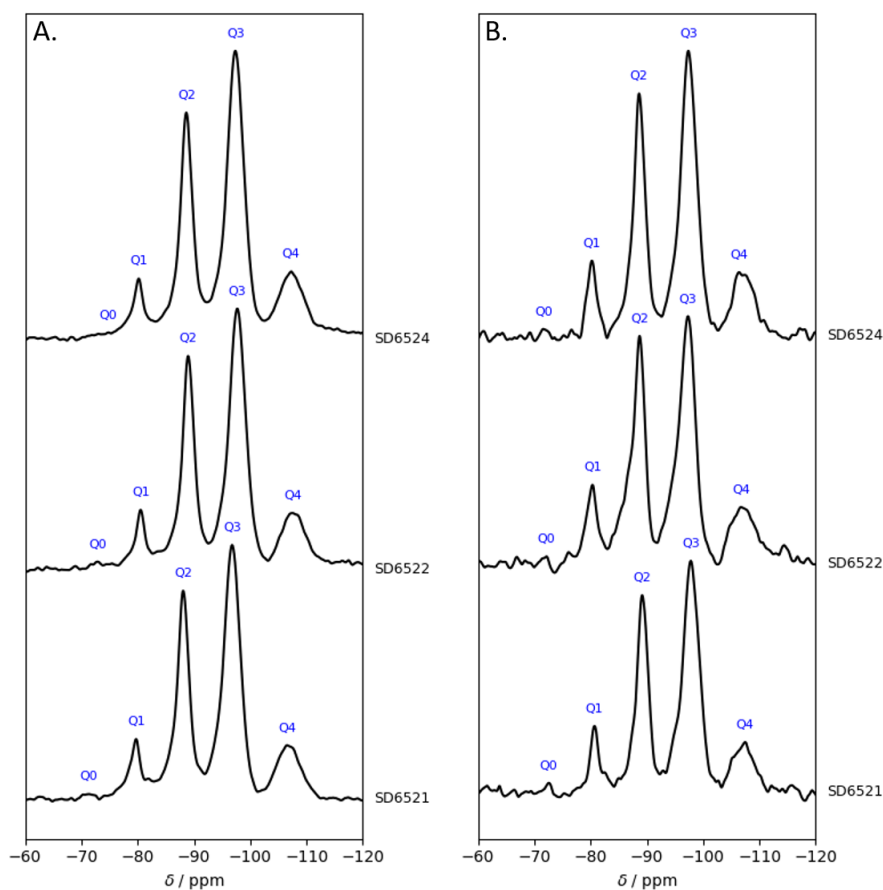
Figure 10.1: ^{29}Si NMR spectra of the silicate samples. (A) Sodium silicate samples in their undiluted form. (B) Same silicates diluted to 50% of the original concentration.

Undiluted Samples

Across the three samples, the spectra are essentially identical in terms of both chemical shift positions (Table 10.2) and relative peak intensities (Figure 10.1A and Table 10.3). The dominant signals arise from Q^1, Q^2, Q^3, and Q^4 species, consistent with silicates of intermediate polymerisation and SiO_2/Na_2O molar ratios near 3.3–3.4 [22]. Minor contributions from Q^0 species are also visible, suggesting the presence of smaller chain fragments or end groups. No significant chemical shift deviations or changes in Q-species distribution were detected among the samples, indicating a high degree of structural similarity at the molecular level.

Sample	Q^0	Q^1	Q^2	Q^3	Q^4
SD6521	—	-79.73	-88.09	-96.78	-106.55
SD6522	—	-80.53	-88.97	-97.70	-107.54
SD6524	—	-80.19	-88.65	-97.35	-107.29

Table 10.2: Peak positions (in ppm) for the Q^n species in each sample. Values for Q^0 are omitted due to lack of a clearly defined peak.

Sample	Q^0	Q^1	Q^2	Q^3	Q^4
SD6521	0.78	8.80	32.25	45.12	13.05
SD6522	0.83	7.17	30.86	45.85	15.29
SD6524	0.65	7.36	30.20	45.43	16.35

Table 10.3: Normalised NMR signal intensities (total = 100) for Q^n silicate species. Note that the Q^0 "peak" is more of a blip on the baseline.

Furthermore, the strong spectral resemblance between the samples implies that their silicate frameworks are comparably organised, despite differences in bulk properties, such as viscosity (Table 10.1). This is particularly notable given that SD6524 exhibits a much higher viscosity than SD6521 and SD6522. Additionally, the absence of detectable structural differences at this level of resolution suggests that the factors contributing to the rheological variation cannot be captured using NMR, or that such differences lie in mesoscale or dynamic properties, rather than static molecular speciation.

Diluted Samples

Following the initial characterisation of the undiluted sodium silicates, the measurements were performed on the same samples diluted to 50% of their original concentration, and the obtained spectra are shown in Figure 10.1B. The aim was to assess whether significant structural rearrangements occur upon dilution, given the expected reduction in interparticle interactions and network connectivity at lower concentrations. Despite the decreased sample concentrations, all spectra remained well resolved, with clear Q^1 to Q^4 peaks observable across all samples.

The chemical shift positions for each Q^n species remained effectively unchanged (Table 10.4) compared to the undiluted samples, indicating no changes in the silicon coordination environments detectable at the molecular level. This suggests that the fundamental silicate speciation remains stable upon dilution. Among the three samples, SD6522 showed a modest increase in the Q^2/Q^3 intensity ratio, alongside a slightly elevated Q^1 signal (Table 10.5). These subtle changes could suggest a shift toward shorter chain fragments or less polymerised species.

Sample	Q^1	Q^2	Q^3	Q^4
SD6521	-80.68	-89.15	-97.78	-107.45
SD6522	-80.37	-88.75	-97.37	-106.80
SD6524	-80.23	-88.62	-97.37	-106.39

Table 10.4: Chemical shift positions (in ppm) of each Q-species in the diluted (50%) sodium silicate samples, as determined by ^{29}Si NMR. No resolved signal was detected for Q^0.

Sample	Q^0	Q^1	Q^2	Q^3	Q^4
SD6521	-0.07	7.45	31.45	48.39	12.64
SD6522	0.17	9.70	33.81	40.94	15.38
SD6524	-0.16	7.05	31.84	47.17	13.78

Table 10.5: Normalised Q-species distribution (*total = 100*) in the diluted (50%) sodium silicate samples based on ^{29}Si NMR integration. Negative values for Q^0 reflect low-intensity signals close to the noise baseline.

However, these apparent differences are minor and fall within the known sensitivity limits of low-field benchtop NMR instrumentation [365]. As such, they cannot be confidently interpreted as definitive evidence of structural reorganisation. Rather, they underscore the difficulty of resolving subtle dynamic or supramolecular changes in silicate systems using ^{29}Si NMR alone at this field strength.

The lack of significant variation across the three samples supports the interpretation that any differences observed in subsequent measurements, such as FRAP, are unlikely to arise from major differences in silicate speciation, but rather from physical or supramolecular aspects of network organisation not directly observable using ^{29}Si NMR. While this method provides valuable information about the local chemical environments of silicon atoms, it is inherently limited in its sensitivity to supramolecular organisation, particle interactions, or network-level dynamics. As such, it appears largely blind to the differences among the three silicate samples, which are otherwise distinguishable by their macroscopic properties, such as viscosity or turbidity (Table 10.1). This highlights that, although chemically similar at the molecular scale, the samples may differ in ways that are not captured by NMR, underscoring the need for complementary techniques sensitive to mesoscale structure and dynamics.

10.3.2   FRAP Results

Following the validation of the FRAP methodology on model colloidal systems presented in Chapter 9, the method was applied to a set of industrial sodium silicate solutions provided by PQ Silicas. Despite having nearly identical molar ratios, the silicate samples studied here exhibit different viscosities, ranging from 46 cP to over 300 cP. While differences in concentration can largely account for the observed viscosity variation, other factors such as the origin of the raw materials and manufacturing conditions may also contribute. Moreover, variations in turbidity observed among the samples require careful interpretation, as turbidity depends on multiple parameters, including particle refractive index, size, and concentration, which are not fully characterised here. While ^{29}Si NMR analysis confirmed that the samples are chemically similar at the molecular level, it did not indicate structural or dynamic differences.

This highlights the need for a technique capable of probing microstructural properties beyond the local chemical environment. The primary goal of this FRAP investigation was therefore to determine whether fluorescence recovery dynamics can sensitively distinguish between samples that are chemically indistinguishable by NMR, based on their diffusive characteristics and underlying supramolecular organisation.

Each sample was labelled with R6G at 5, 10, 15, and 20 μM concentrations, and FRAP experiments were conducted using a standardised protocol to ensure consistency across measurements. Recovery curves were fitted to a multi-exponential model using a custom-fitting routine described in Chapter 9. Importantly, the samples were studied both in their native (undiluted) form and after dilution to 50% of their original concentration. This allowed exploring how this affects the dye-silicate interactions and the resulting recovered particle size. All samples were freshly prepared before measurement to avoid aggregation or pH-induced artefacts that might arise from extended storage, particularly after dilution. Ten FRAP curves were recorded for each sample, ensuring statistical robustness in the extracted parameters. The results are presented in the following sections, starting with the undiluted samples before turning to the diluted series.

Stock Silicate Samples

Mono-Exponential Model   Figure 10.2 presents the hydrodynamic radii recovered from the mono-exponential fitting of FRAP recovery curves, for three undiluted sodium silicate samples: SD6521, SD6522, and SD6524, across a range of dye concentrations (5, 10, 15, and 20 μM). The radii were calculated from recovery curves using a single-component diffusion model, assuming a uniform mobile fluorescent species. Although simplistic, this model allows for comparative analysis between samples and conditions, especially when the relative differences in recovery kinetics are of primary interest. A detailed discussion of analysis methods is presented in Chapter 9.

While this model enables comparative analysis between samples and conditions, it does not capture the inherent polydispersity of the system. Previous SAXS measurements and compositional analyses indicate that the silicate particles span a distribution

of sizes and possibly aggregation states, meaning that the diffusion measured in FRAP reflects a convolution of these species [22,39,261]. As such, the recovered sizes should be treated as apparent or effective values rather than true modal particle sizes. Nonetheless, the mono-exponential model, as discussed in Chapter 9, offers a practical means of assessing trends in dye–particle interaction strength and diffusion behaviour across different silicate systems.

Across all dye concentrations, SD6522 exhibits the largest recovered radii, followed by SD6521, while SD6524 shows the smallest sizes. An interesting trend is observed across all samples, with the hydrodynamic radius mostly decreasing as dye concentration increases; this effect is least pronounced in the SD6522 dataset, where the particle size stays in the range of 10 nm independent of the dye concentration used. The reason for this is potentially the preferential R6G adsorption discussed in detail in Chapter 6. Namely, R6G preferentially adsorbs to larger particles due to their lower curvature, reduced mobility, and higher net negative charge. However, as the dye concentration increases, smaller particles are labelled and the average measured radius decreases. This behaviour is indicative of a broad size distribution within the sample, where both small and large particles coexist. At low dye concentrations, larger particles are more likely to be labelled due to their greater surface area and binding capacity, while at higher dye concentrations, smaller particles become increasingly represented in the labelled population, leading to a reduction in the average measured size. Furthermore, with increased dye concentration, the fraction of free dye also rises, further contributing to the average size decrease. In addition, it should be noted that R6G dimers do not fluoresce, meaning that at higher dye concentrations, fluorescence from larger particles may be diminished due to dimer formation. This quenching effect likely has a comparable influence to the saturation of less accessible binding sites on smaller particles, further affecting the observed fluorescence and size measurements. Moreover, MD results presented in Chapter 6 suggest that R6G dimers do not interact significantly with silica nanoparticles due to geometrical constraints. However, since these classical MD simulations employ force field methods, their accuracy is limited, and the true nature of dimer–nanoparticle interactions can only be conclusively determined through *ab initio*

calculations.
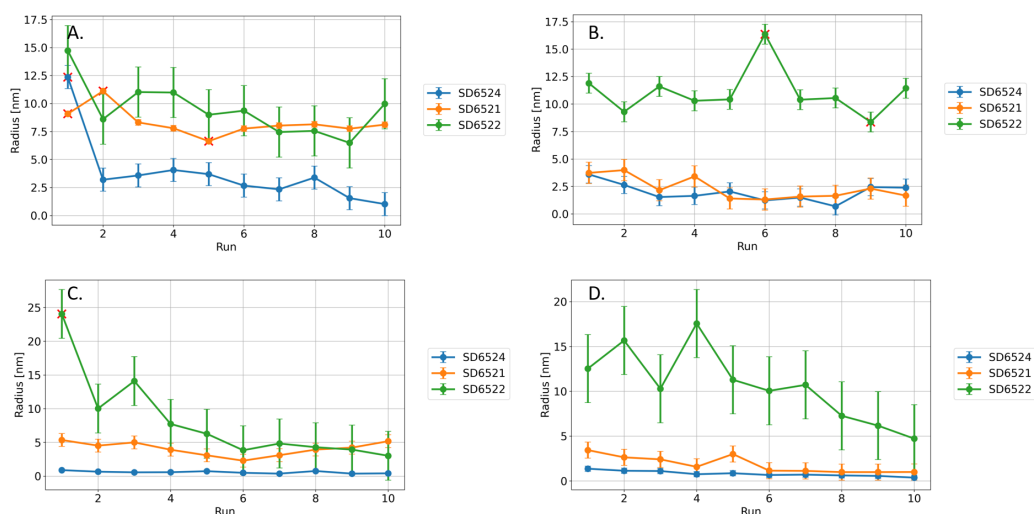
Figure 10.2: Hydrodynamic radius recovered from mono-exponential fits of FRAP recovery curves for undiluted sodium silicate samples (SD6521, SD6522, SD6524/C79) at four dye concentrations: 5 µM (A), 10 µM (B), 15 µM (C), and 20 µM (D). Recovered values from 10 replicate runs are shown, with three standard deviations as error bars. Outliers (red crosses) were excluded from error analysis.

Sodium Silicate	$R_{5\,\mu M}$ (nm)	$R_{10\,\mu M}$ (nm)	$R_{15\,\mu M}$ (nm)	$R_{20\,\mu M}$ (nm)
SD6524	2.83 ± 1.03	1.97 ± 0.78	0.57 ± 0.17	0.80 ± 0.29
SD6521	7.98 ± 0.25	2.32 ± 0.96	4.05 ± 0.95	1.82 ± 0.89
SD6522	9.51 ± 2.24	10.73 ± 0.90	6.45 ± 3.62	10.62 ± 3.79

Table 10.6: Recovered average hydrodynamic radii for undiluted sodium silicate samples at different R6G concentrations.

At low concentrations, most of the dye may be adsorbed to particles, meaning that the dominant fluorescent species during recovery is the slower-diffusing complex. In the neat state, particle sizes follow the trend SD6524 < SD6521 < SD6522 observed across all concentrations. SD6524 stands out as the most concentrated formulation, with significantly higher viscosity and turbidity than the other two silicates, which likely leads to dense nucleation and a larger number of smaller particles. As a result, in this case, R6G may accentuate those particles more than in the case of less concentrated SD6521 and SD6522, despite the preferential adsorption, contributing to the observed smaller

sizes. R6G generally prefers larger particles in systems with a wide size range, where its adsorption leans towards higher surface area or stronger binding sites. However, if most particles are already small, as could be the case in SD6524, the tendency for preferential adsorption diminishes, and the dye distributes more evenly across the particle population. This leads to a more accurate sampling of smaller species, supporting the trend of reduced apparent sizes.

In contrast, SD6522 and SD6521 have similar base formulations, as reflected by their comparable viscosity and turbidity; however, SD6522 consistently shows larger sizes, likely due to its higher impurity content promoting aggregation (Table 12). These impurities may facilitate interparticle bridging or alter surface charge interactions, leading to the formation of larger, more stable clusters even under dilution. Furthermore, some metals may even react with the silicate to form new, insoluble species. As a result, the presence of trace components appears to have a significant impact on mesoscale organisation, despite the samples being chemically similar at the molecular level. Additionally, the lower viscosity in both SD6521 and SD6522 may hinder the detection of smaller particles, potentially causing an upward shift in the apparent particle size. Since the mono-exponential model assumes only a single population of diffusing species, this unmodelled heterogeneity results in faster overall kinetics and consequently underestimated sizes.

The use of a mono-exponential model to extract characteristic diffusion times is a significant simplification. In reality, the recovery curves in these systems may reflect at least two populations: free dye, and dye adsorbed to silica particles. A detailed discussion of the applicability of different models is presented in Chapter 9.

It is important to note that FRAP analysis assumes that the photobleaching itself does not perturb the physical system. However, at higher dye concentrations or prolonged laser exposure, photothermal effects or dye-induced changes may transiently modify the local microstructure of aggregation behaviour, particularly in metastable systems, such as silicates. An example of such an effect is described later in the chapter. It is also important to highlight a key experimental limitation arising from the turbidity of the undiluted samples. High turbidity disrupts the spatial integrity of the

laser beam during the bleaching phase, resulting in a diffuse and poorly structured bleach spot, which contributes to measurement uncertainty and the magnitude of the errors. A well-defined bleaching geometry is essential for accurate modelling and fitting of the FRAP recovery, especially when relying on models that assume a spatially uniform and circular bleach profile. To mitigate this, relatively high laser powers and longer bleaching durations were necessary to ensure sufficient bleaching contrast across the detection plane. While this introduces risks of laser-induced artefacts such as local heating or photochemical aggregation, the trade-off was considered acceptable to preserve the reliability of the bleach geometry.

Bi-Exponential Model To assess the potential presence of multiple diffusing species, a bi-exponential model was applied to the FRAP recovery curves. This model was based on a slightly simplified GBM fitting routine, as described in Chapter 9. The analysis was performed on the same experimental runs that were previously evaluated using a mono-exponential model, as shown in Figure 10.3.
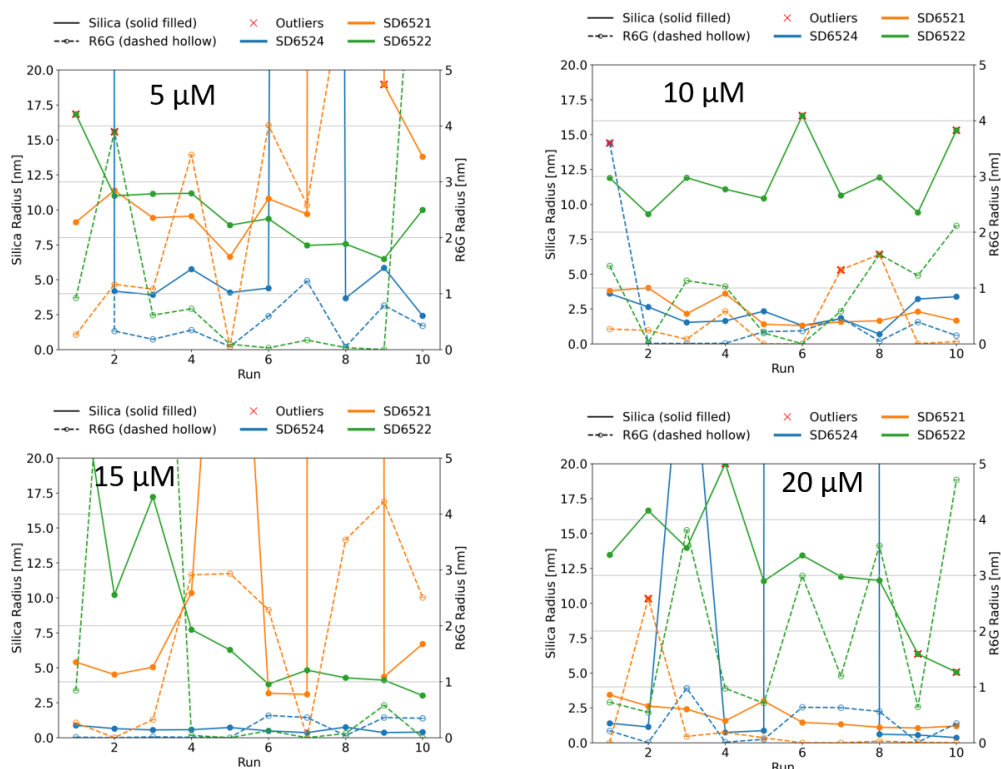
Figure 10.3: Hydrodynamic radii recovered from bi-exponential fits of FRAP recovery curves for undiluted sodium silicate samples (SD6521, SD6522, SD6524) across dye concentrations of 5, 10, 15, and 20 µM. Solid lines denote the slow component (attributed to dye bound to silicate particles), and dashed lines represent the fast component (presumed to correspond to free R6G dye). Each data point reflects one of ten replicate runs.

Unlike the mono-exponential results, which offered relatively consistent trends (e.g., decreasing radius with the increasing dye concentration for SD6522), the bi-exponential fits frequently failed to converge on physically meaningful values. Many fits yield implausibly small radii for the fast component, well below known diffusion-limited values for R6G in aqueous media, and sometimes much larger than what is expected for R6G; or unrealistically large values for the slow component, in some cases exceeding expected particle dimensions by multiple orders of magnitude. Furthermore, the recovered values oscillate significantly, suggesting that the model cannot converge properly. This instability is particularly pronounced for SD6521 and SD6522 at 15 and 20 µM, where the

relatively small particle sizes, combined with system complexity and elevated turbidity, likely degrade the S/N ratio essential for stable multi-parameter fitting.

Moreover, the assignment of fast and slow species is frequently ambiguous. For example, several runs appear to swap the expected magnitude components (especially noticeable in 15 and 20 µM results), suggesting that the model fitting process struggles to distinguish between overlapping kinetics based only on the fluorescence intensity data. This reinforces the concern raised earlier in Chapter 9: while a multi-exponential model is conceptually better suited to describe heterogeneous systems, its successful implementation hinges on clean recovery profiles and high-quality data. In the current dataset, the elevated turbidity, photobleaching artefacts, and complex and dynamic dye–silica interactions likely undermine the model's reliability.

In contrast, the mono-exponential fits, despite their simplifying assumptions, yield smoother, more interpretable trends across runs and concentrations. The decrease in apparent radius with increasing dye concentration, clearly visible in all samples, aligns qualitatively with expectations of dye saturation and increased free dye fraction, even if these values do not capture the full variety of the diffusing silicate species.

In conclusion, although the bi-exponential model approach offers an appealing framework for separating free and bound dye populations, its practical application here is hindered by experimental limitations and model sensitivity. The mono-exponential fits, while less descriptive, offer a more robust and consistent means of tracking diffusion trends across different silicates and dye concentrations.

Diluted Samples

Mono-Exponential Model   The panels in Figure 10.4 present the hydrodynamic radii extracted from FRAP recovery curves for three silicate samples, measured at multiple dye concentrations, and diluted to 50% of the original concentration. In contrast to the undiluted results (see Figure 10.2), where recovered radii for the silicates were relatively consistent between the runs, but showed signs of reduction in size at higher dye concentrations due to free dye concentrations, the diluted samples offer a less consistent view of diffusion behaviour across the concentration range.
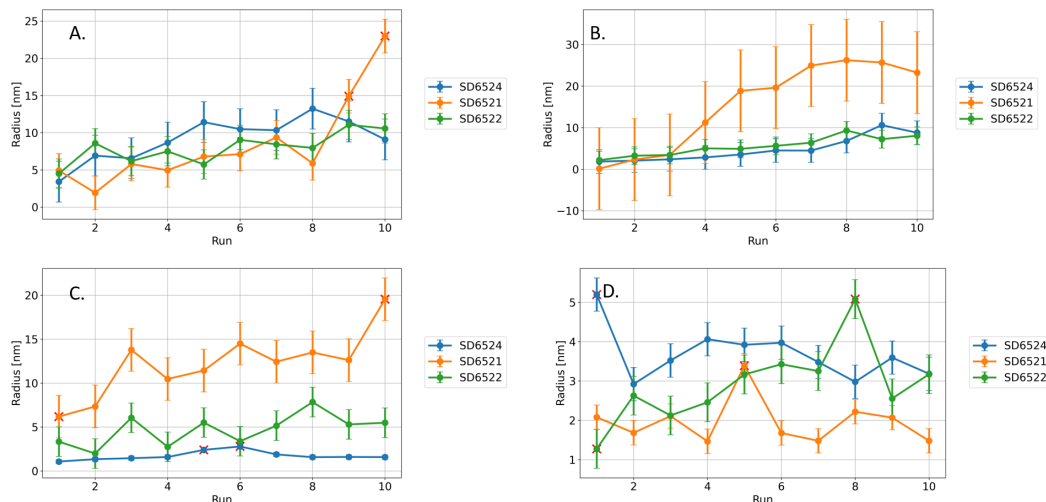
Figure 10.4: Hydrodynamic radius recovered from mono-exponential fits of FRAP recovery curves for sodium silicate samples diluted to 50% (SD6521, SD6522, SD6524/C79) at four dye concentrations: 5 µM (A), 10 µM (B), 15 µM (C), and 20 µM (D). Recovered values from 10 replicate runs are shown, with three standard deviations as error bars. Outliers (red crosses) were excluded from error analysis.

Sodium Silicate	$R_{5\,\mu M}$ (nm)	$R_{10\,\mu M}$ (nm)	$R_{15\,\mu M}$ (nm)	$R_{20\,\mu M}$ (nm)
SD6524	9.16 ± 2.74	4.77 ± 2.85	1.50 ± 0.25	3.51 ± 0.42
SD6521	5.84 ± 2.26	15.56 ± 9.85	12.00 ± 2.42	1.80 ± 0.30
SD6522	7.95 ± 1.96	5.53 ± 2.14	4.67 ± 1.68	2.84 ± 0.49

Table 10.7: Recovered average hydrodynamic radii for diluted sodium silicate samples at different R6G concentrations.

At 5 µM dye concentration (Figure 10.4A), the diluted samples reveal a relatively large and similar R_H for all three silicates, with SD6524 exhibiting the largest radius, followed by SD6521, with SD6522 being the smallest. In contrast, the case of undiluted samples revealed a different size, with SD6524 having the smallest radius. This trend supports the view that reducing the particle concentration allows the labelling of larger dye–particle complexes, which then dominate the recovery dynamics. Namely, at low dye concentrations, larger particles have a higher probability of being labelled due to their greater surface area and longer residence time in the bleached region. At higher dye concentrations, more of the smaller particles are labelled, shifting the recovered

radius downward. Dilution further amplifies this effect by lowering the total particle concentration, effectively increasing the dye-to-particle ratio, doubling it, in the case of a 50% dilution. As a result, smaller particles, which were underrepresented in low-dye conditions, are now more readily labelled and contribute more to the recovery signal.

Additionally, the impact of diffusion kinetics must be considered. In dense samples, the recovery signal is often dominated by small, fast-moving particles, which rapidly restore fluorescence and can mask the contribution from slower, larger aggregates. In contrast, in diluted samples, the fast-diffusing species may recover fluorescence within the first few seconds, leaving the slower components, such as large aggregates, to dominate the later stages of the recovery curve. Consequently, FRAP fitting in diluted samples may return slower average diffusion rates, interpreted as larger apparent sizes.

Finally, dilution may itself modify the supramolecular structure of the silicates. Although NMR shows no disruption of the primary silicate framework, dilution could weaken interparticle interactions, disrupt loosely bound aggregates, or alter the colloidal equilibrium. These subtle structural shifts may change how the dye interacts with the particles and how diffusion manifests in the system, further complicating interpretation. Moreover, some recovery curves show an increasing hydrodynamic radius with repeated measurements, which may indicate laser-induced aggregation or ongoing silicate growth during the experiment. This will be discussed in more detail in Section 10.3.3.

However, as the dye concentration increases, the samples start showing more variability, but less consistency when compared with undiluted samples, nonetheless, the trend of decreasing size with increasing dye concentration is somewhat present here as well. For example, SD6521 becomes unstable, displaying extreme values and large error bars, especially at the intermediate concentrations. A similar phenomenon was observed with SD6522 in the case of undiluted samples. At 20 µM, the hydrodynamic radii for all samples collapse to values below 5 nm, which is analogous to the overall decrease in the recovered radii for undiluted samples. This again highlights the dominance of free dye in the recovery signal, as a mono-exponential model is unable to separate multiple diffusive species.

Nonetheless, in the case of diluted samples, FRAP can still reliably differentiate

between the three silicate samples under those conditions. At certain dye concentrations, particularly intermediate values (e.g., 10 and 15 µM, panels B and C), the differences between samples are still observable, suggesting that FRAP retains discriminatory power under carefully chosen conditions. However, the absolute recovered sizes differ from those obtained in undiluted samples, and the trends can become inconsistent, as seen with SD6521. This raises the concern that dilution alters not just measurement sensitivity, but also the dominant diffusion behaviour captured in the analysis.

However, as the dilution reduces the total particle concentration, this results in increased relative dye concentration, which although it improves S/N ratio, reduces the average recovered particle size. Furthermore, dilution also introduces experimental and data analysis challenges, which can also contribute to the observed inconsistencies between stock and diluted samples. The main drawback is that it decreases the overall viscosity of the sample, thus altering the overall mobility of all species, and reducing the confinement of the bleached spot as a result. This undermines the assumption of a well-defined initial condition in FRAP analysis and can introduce substantial errors, particularly, when the spatial gradient of the bleach is insufficiently sharp.

Although dilution was initially expected to improve FRAP size estimates by reducing interparticle interactions, suppressing transient aggregates, and reducing turbidity, the results indicate that this approach introduces significant drawbacks. Most notably, the size trends become inconsistent across different dye concentrations. For example, at 5 µM, all three samples have comparable sizes, while at 10 µM and 15 µM, SD6521 shows significantly higher values than the other two samples, and does not follow the pattern of decreasing size with increasing dye concentration. This lack of consistency undermines the reliability of sample dilution.

Furthermore, the error bars in the diluted measurements are considerably larger across nearly all samples in all concentrations, since the sharp drop of viscosity upon dilution leads to faster diffusion of both the dye and labelled nanoparticles. Given that there is an unavoidable 1 s delay between bleaching and the image acquisition, this becomes a critical issue. As described in Section 9.3.2 of Chapter 9, in low-viscosity en-

vironments, a substantial portion of the fluorescence recovery can occur during this gap, especially for free dye, making it extremely difficult to resolve the early fast component of the decay. This limitation makes the bi-exponential fitting approaches unfeasible in the diluted samples without involving time-resolved measurements.

The above issues suggest that sample dilution, while potentially useful for reducing artefacts in some systems, such as those exhibiting high turbidity, is not an optimal strategy for studying diffusion in sodium silicates by classical, intensity-based FRAP. The undiluted systems, despite their higher turbidity and structural complexity, provide more consistent size trends across dye concentrations and retain sufficient viscosity to allow meaningful separation of fast and slow diffusion components. For future applications, particularly where a multi-exponential model is desired, maintaining a moderately high sample concentration, to ensure high viscosity, which is essential in capturing nuanced diffusion characteristics, appears to be essential.

Bi-Exponential Model To assess whether a more complex model can aid in separating the diffusion behaviour of multiple species present in the samples, the FRAP recovery curves were fitted to a bi-exponential model as in the case of neat samples. The results of fitting to a bi-exponential model are shown in Figure 10.5.
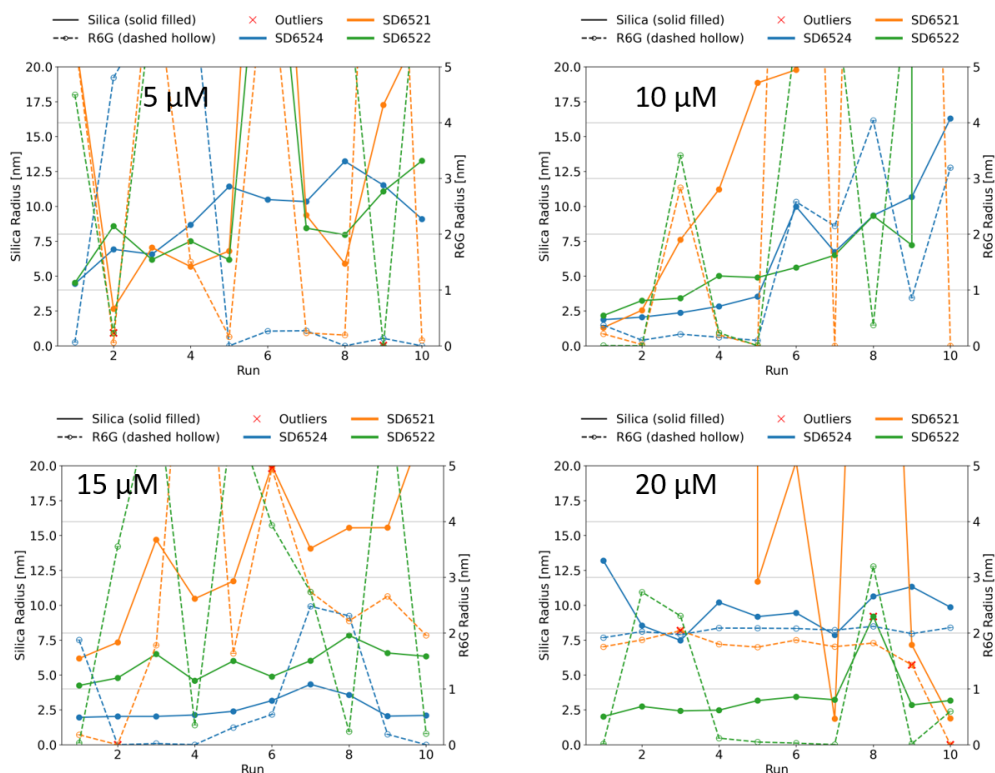
Figure 10.5: Hydrodynamic radii recovered from bi-exponential fits of FRAP recovery curves for diluted sodium silicate samples (SD6521, SD6522, SD6524) across dye concentrations of 5, 10, 15, and 20 µM. Solid lines denote the slow component (attributed to dye bound to silicate particles), and dashed lines represent the fast component (presumed to correspond to free R6G dye). Each data point reflects one of ten replicate runs.

Overall, the recovered R_H values obtained from fitting the data for the diluted silicates to the bi-exponential model exhibit identical features as seen in the case of undiluted samples. Namely, the values for the shorter component exhibit significant oscillations, and in the majority of the cases report values significantly larger than the known radius of R6G equal to ~ 0.6 nm, even when the oscillations start to settle down at higher dye concentrations.

Despite its theoretical advantage in capturing multiple diffusion components, the bi-exponential model fails to produce reliable or physically meaningful results in diluted samples, similar to what was observed in undiluted silicates. The fits yielded unstable

parameters, which showed substantial variability between runs. In many cases, the model appeared over-parametrised relative to the data quality, leading to inconsistent trends, similar to those observed in the case of undiluted samples. These issues suggest that, under current experimental conditions, the added complexity of the bi-exponential model in intensity-based FRAP measurements does not translate into clearer insights and may instead obscure the underlying diffusion behaviour.

10.3.3   Potential Laser-Induced Effects on Silicate Systems in FRAP

In some FRAP measurements, the postbleach fluorescence intensity exceeded the pre-bleach baseline. This effect was predominantly observed in the diluted sodium silicate samples, and less frequently in the undiluted ones, and was not limited to only a specific sample, but rather present in all of them. Exemplar curves exhibiting such behaviour are shown in Figure 10.6.
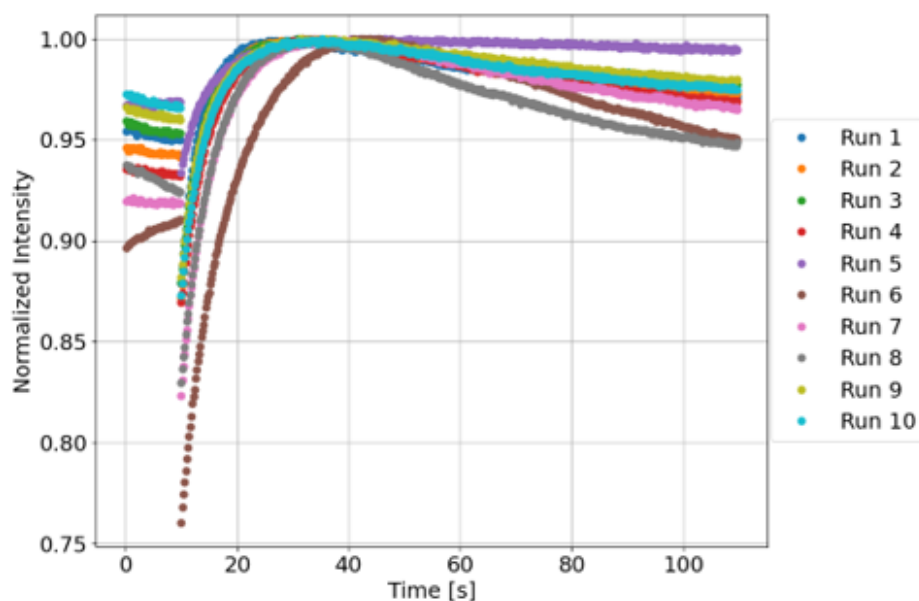
Figure 10.6: Anomalous FRAP recovery curves for diluted SD6524 sample labelled with 15 µM of R6G.

While such behaviour is typically attributed to artefacts, such as drift, focus shifts, or normalisation errors, it may also reflect the real photophysical or photochemical

changes occurring during the bleaching phase. The fact that this effect is most pronounced in the diluted sodium silicate samples may be tied to the intrinsic stability of silica nanoparticles in solution. Silica colloids require a certain equilibrium concentration of silicate and sodium ions to maintain their surface charge and hydration shell; upon dilution, this balance can be disrupted, leading to partial dissolution or restructuring of the nanoparticle surface and a greater susceptibility to heat- or charge-induced aggregation. Given the relatively high laser power (150 mW) and duration (3 s) of the 532 nm bleaching pulse used in these experiments, it is possible that the laser induced localised heating in the sample. This may have destabilised the electrostatic double layer surrounding the silicate nanoparticles or disrupted hydration shells, as a result, promoting interparticle interactions or aggregation in the affected area. In addition to thermal effects on the nanoparticle environment, it is also conceivable that laser excitation disrupts pre-existing non-fluorescent R6G dimers, converting them into fluorescent monomers and altering the observed signal. Furthermore, elevated temperatures may accelerate chemical reactions or promote physical processes such as Ostwald ripening, contributing further to structural changes during the experiment [366]. Such laser-induced aggregation is particularly plausible in sodium silicate systems, which are known to have marginal colloidal stability and are sensitive to local heating. Similar to the laser-induced gelation observed in silica aerogel synthesis [367], localised thermal energy from the 532 nm pulse could reduce the energy barrier for silanol condensation, promoting the formation of larger Si–O–Si aggregates. If these newly formed clusters have a higher affinity for dye molecules, as suggested by MD simulations (See Chapter 6, Section 6.3.4), this could lead to enhanced fluorescence in the bleached region, falsely mimicking the recovery above baseline. Therefore, the apparent recovery above the baseline may not be a simple artefact, but a photothermally induced restructuring of the nanoparticle–dye system within the region of interest.

Moreover, intense irradiation might cause photo-induced changes in the dye itself, potentially altering its binding affinity or causing redistribution between nanoparticle surfaces. Under intense 532 nm irradiation, R6G molecules populate long-lived triplet states that transfer energy to dissolved oxygen, generating singlet oxygen which irre-

versibly oxidises the xanthene core and cleaves the fluorophore [368]. Furthermore, R6G can exhibit photoblinking through radical dark states formed via intermolecular charge transfer, introducing transient "off" periods that can artifactually boost apparent recovery above baseline when dark-state dyes reactivate [369]. Together, these effects highlight that under certain conditions, the bleach pulse in FRAP experiments is not simply a passive photobleaching step, but can actively perturb the colloidal structure of complex systems like sodium silicates. Such findings underscore the importance of careful power calibration, control measurements, and complementary structural analysis when interpreting FRAP data in chemically reactive or unstable systems.

FRAP and ^{29}Si NMR Comparison

The findings from ^{29}Si NMR measurements indicate that the silicate network remains chemically stable and well-conserved, even upon significant dilution. The absence of notable spectral differences confirms that the primary connectivity of silicon tetrahedra, i.e., the degree of polymerisation, remains unaffected. In other words, the dilution procedure does not break down or restructure the silicate network on the atomic level.

FRAP experiments reveal a clear distinction between the silicate samples. Even in the undiluted state, where NMR shows nearly identical spectra, FRAP consistently detected differences in the recovery profiles and resulting hydrodynamic radii (see Table 10.6). This discrepancy suggests that while the silicate network structure is chemically similar across the samples, as indicated by virtually identical NMR spectra, their physical states, such as particle aggregation, dye-binding environments, or colloidal interactions, differ in ways that strongly influence dynamic measurements such as FRAP.

The hydrodynamic radii derived by FRAP for the neat samples were found to follow the order SD6524 < SD6521 < SD6522 at all dye concentrations (Table 10.6). The smallest radii (0.57 to 2.83 nm) were measured for SD6524, which also exhibited the highest viscosity (304 cP) and turbidity (14 NTU) in its undiluted form, consistent with a system in which many small particles are formed. In contrast, SD6522 was found to display the largest radii (6.45 to 10.73 nm) despite viscosities and turbidities (46 cP and 5.8 NTU) comparable to those of SD6521 (48 cP and 8.8 NTU), implying that its

greater impurity content promotes aggregation into fewer larger particles. Intermediate radii (1.82 to 7.98 nm) were recorded for SD6521, reflecting its moderate viscosity and turbidity and lower aggregation propensity. Given that all three samples share nearly identical molar ratios and NMR spectra, these size variations must be attributed to secondary supramolecular factors such as particle packing, network entanglement and dye surface interactions to which FRAP is sensitive.

Upon dilution, FRAP reveals a further silicate complexity. While NMR still shows no visible changes, the FRAP-measured hydrodynamic radii fluctuate unpredictably throughout the different R6G concentrations, with significant variability and loss of reproducibility between individual experiment repetitions. Those differences between structural stability as revealed by NMR and dynamic variability reported by FRAP underscore the sensitivity of the silicate system to environmental conditions that alter interparticle dynamics without disrupting the underlying silicate framework.

It is important to note, that minor variations in recovered hydrodynamic radii were observed between successive experimental runs. In neat silicate samples, there is a slight trend of decreasing radii over the course of repeated measurements, whereas in dilute samples, a small increase is sometimes seen. These effects likely arise from subtle changes in local dye distribution, transient particle rearrangements, or minor laser-induced artefacts, rather than systematic changes in the silicate network itself. Given the limited dataset, these variations cannot be definitively attributed to run sequence effects, but they highlight the sensitivity of FRAP to dynamic sample conditions.

Together, these results highlight the distinct yet complementary insights provided by FRAP and NMR. The NMR spectra confirm that dilution and sample differences do not alter the silicate network structure; however, FRAP exposes a more nuanced picture of sample behaviour, sensitive to viscosity, aggregation and dye-particle interactions. These differences are not easily inferred from composition alone, reinforcing the importance of using multi-modal approaches when characterising complex, multiscale colloidal systems.

10.4 Conclusions

This chapter explored the structural and dynamic behaviour of sodium silicate liquids using a combination of ^{29}Si NMR spectroscopy and FRAP. The primary aim was to understand how the silicate network polymerisation, particle size, and mobility vary with composition and dilution, and whether these differences manifest consistently across structural and dynamic measurement techniques.

The NMR analysis of samples SD6521, SD6522, and SD6524, revealed no substantial differences in the distribution of Q-species across the three silicates in both undiluted and diluted conditions. The findings suggest that the core silicate framework remains chemically and structurally intact regardless of dilution or subtle composition differences. No significant shifts in Q^0–Q^4 intensities were observed, confirming the stability of the silicate network at the molecular level.

In contrast, FRAP measurements revealed clear differences in hydrodynamic radii. Mono-exponential fits yielded sample sizes spanning 0.57–2.83 nm for SD6524 (smallest), 1.82–7.98 nm for SD6521 (intermediate), and 6.45–10.73 nm for SD6522 (largest), with bi-exponential modelling proving unreliable due to errors arising from overlapping recovery kinetics. These results point to sample-specific variations in silicate speciation, dye-surface interactions, and mesoscale organisation that are invisible to NMR. When NMR and FRAP outcomes are combined, a complementary picture emerges: while NMR confirms a uniform silicate speciation in all samples, FRAP uniquely resolves differences in particle packing and dynamic behaviour, demonstrating that formulations chemically indistinguishable by NMR can be dynamically distinct under FRAP.

Additionally, FRAP measurements on samples diluted to 50% revealed increased variability and, at low dye concentrations, larger apparent radii, highlighting how reduced particle concentration amplifies the free-dye contribution and complicates accurate size recovery. Furthermore, dilution lowers the viscosity, accelerating diffusion and compromising the spatial confinement of the bleached spot, which in turn undermines the reliability of multiexponential models in low-viscosity environments.

Together, the findings demonstrate that while NMR provides detailed insights into

the chemical and structural connectivity of silicate networks, it is largely insensitive to dynamic and supramolecular differences that can strongly influence particle behaviour. FRAP captures this missing dimension, revealing aggregation, size, and diffusion behaviour that directly impact functional performance. Importantly, FRAP offers key practical advantages over commonly used techniques like SAXS or SANS: it is faster, more cost-effective and widely accessible, with CLSM equipped for FRAP being standard in many biological and materials science laboratories. While scattering techniques can provide detailed and quantitative size distributions and even shed some light on the particle shape and structure, FRAP can rapidly identify trends and anomalies in complex or evolving colloidal systems, making it a valuable and powerful screening tool. Moreover, the observed differences in FRAP-recovered sizes between silicates with nominally identical molar ratios may reflect not only aggregation states or experimental conditions but also intrinsic variations in source materials, such as differences in sand purity, trace ion content, or synthesis protocols. These findings underline the potential of FRAP as a practical and sensitive method for probing the functional dynamics of industrial silicate solutions where compositional control may be limited. The combination of methods reveals a coherent picture: silicate polymerisation decreases systematically with decreasing molar ratio, but the dynamic behaviour (e.g., mobility, dye binding, aggregate disruption) is influenced by composition, concentration-dependent effects, and particle interactions.

The insights presented in this chapter are particularly relevant for industrial and geochemical applications, where silicate-based formulations' performance often depends on their molecular composition and mesoscale structural organisation.

Chapter 11

Final Remarks and Future Outlook

11.1 Conclusions

The central hypothesis of this thesis was that fluorescence-based techniques, when combined with molecular simulations, provide a reliable and scalable framework for characterising silica colloids and sodium silicate systems. Specifically, it was proposed that FRAP could distinguish particle size differences in sodium silicate solutions that remain invisible to ^{29}Si NMR. This hypothesis has been broadly supported, though the work has also highlighted important limitations and avenues for improvement.

The work began with molecular simulations (Chapter 6), where the dynamics of xanthene dyes, mainly R6G, in the presence of silica nanoparticles were investigated. These studies achieved the objective of establishing a molecular-scale picture of dye–surface interactions. Adsorption was shown to depend strongly on nanoparticle curvature, crystallinity, and pH, with van der Waals forces revealed to play a more significant role than commonly assumed. While these simulations were limited in system size and timescale, they nonetheless provided crucial mechanistic insight into dye binding, directly informing the later experimental design. However, the simulations were restricted to spherical nanoparticles, whereas literature indicates that sodium silicate species may adopt ellip-

246

soidal or more irregular shapes. This geometrical simplification may have overlooked anisotropic adsorption effects. Furthermore, binding free energy profiles were not computed, meaning adsorption strength could only be inferred indirectly. Such profiles would have provided a thorough thermodynamic analysis of adsorption to complement the kinetic insights from residence times. Although considerable effort was invested in calculating dimer binding energies using SMD and DFT, the strength of monomer–SNP binding was not directly measured, which prevented a rigorous comparison of dye–dye and dye–surface affinities in terms of binding strength.

Nevertheless, residence time analysis offered an indirect route to quantify binding strength. By applying Eyring transition state theory, adsorption lifetimes in the range of 1–100 ns were mapped onto activation free energies of $\sim$5–8 kcal·mol^{-1}. These barriers fall in the range characteristic of hydrogen bonds and weak electrostatic interactions, aligning with the expected silanol–R6G chemistry. Importantly, this represents the kinetic barrier to desorption rather than the full equilibrium binding free energy. A rigorous ΔG_{bind} would require free energy methods such as PMF or metadynamics, which remain a clear direction for future work.

Chapter 7 addressed the second objective by exploring R6G dimerisation in solution and on nanoparticle surfaces. The results showed that dimerisation is favoured in solution, competing with adsorption but rarely coexisting stably. Importantly, a new methodology for estimating aromatic dimer binding energies using SMD was validated against high-level DFT. This offered a computationally efficient tool for analysing non-covalent interactions, though it remains approximate compared to *ab initio* methods. Together, these studies confirmed the initial hypothesis that dye–dye and dye–surface equilibria are key to understanding fluorescence signals in nanoparticle systems.

The comparison between SMD-derived work values and DFT also underscored a systematic limitation. According to the Jarzynski equality, the true free energy is always lower than the average non-equilibrium work, meaning SMD estimates should systematically overbind relative to equilibrium values. This was consistent with the observed overestimation of some dimer stabilities. Nevertheless, applying the same protocol across systems ensured meaningful relative comparisons with DFT, even if

absolute binding energies remain inflated.

The third objective, experimental validation through fluorescence methods, was pursued in Chapters 8 and 9. Time-resolved anisotropy demonstrated that dye probes can provide reproducible average particle sizes for sodium silicate oligomers, with results in close agreement with SAXS. The method proved robust, cost-effective, and non-invasive, benefiting from the electrostatic labelling ability of R6G, which avoids complex chemical modification. However, anisotropy was inherently limited to reporting mean hydrodynamic radii and could not resolve size heterogeneity. Moreover, dye-to-particle ratios were not explicitly considered, which is now recognised as a critical limitation. A naive calculation assuming dense spherical SNPs suggested unphysical ratios ($<10^{-5}$ dyes per particle), whereas correcting for polydispersity, porosity, and anisotropy bias yields far more realistic values (0.01–1). This highlights that only a subset of particles contributes to anisotropy signals and that labelling efficiency must be carefully considered in future studies.

FRAP was then developed and validated as a nanometrology tool. In silica colloids (LUDOX), FRAP successfully resolved distinct particle populations, outperforming anisotropy in capturing polydispersity. The method's sensitivity to viscosity, dye concentration, and model selection was both a strength and a limitation: when carefully optimised, FRAP gave highly reliable results, but poor parameter choices introduced artefacts. The work thus met the objective of establishing FRAP as a complementary characterisation method, while also clarifying the conditions under which it is most effective. One critical caveat, however, is that FRAP implicitly assumes stable dye adsorption during the recovery period. Simulations demonstrated that adsorption is in fact dynamic, with desorption occurring on nanosecond timescales. Fortunately, because this is several orders of magnitude faster than FRAP's seconds-scale recovery, the data still represent reliable ensemble averages. Nevertheless, at high dye concentrations, rapid adsorption–desorption cycles may increase the contribution of free dye to recovery curves, subtly biasing apparent size estimates.

Finally, the hypothesis was directly tested in Chapter 10, where FRAP was applied to chemically similar sodium silicate samples. NMR confirmed consistent Q-

species distributions across samples, yet FRAP revealed clear differences in particle sizes and diffusion behaviour, supporting the hypothesis that FRAP captures structural dynamics invisible to conventional methods. These results are significant, showing that supramolecular differences arising from synthesis or impurities can be resolved by FRAP, even when local chemical composition remains unchanged.

Taken together, the thesis objectives were achieved as follows:

- Provided mechanistic insights through molecular-scale modelling, though restricted by scale. Future work should incorporate non-spherical particle models and compute binding free energies directly.

- Validated dye behaviour through photophysical characterisation and produced reliable average size estimates, though unable to resolve heterogeneity. Explicit treatment of dye/particle ratios remains necessary.

- Established FRAP as a powerful method for probing size distributions, with limitations rooted in dye concentration and fitting models. The implicit assumption of stable adsorption, although practically valid, should be treated with caution in systems with higher dye exchange.

- Benchmarked fluorescence-obtained results against SAXS and NMR, demonstrating complementarity and highlighting FRAP's unique sensitivity to mesoscale dynamics.

Despite the limitations identified, such as resolution constraints in anisotropy measurements, parameter sensitivity in FRAP, simplified simulation geometries, missing data on monomer–SNP binding, unconsidered dye–particle ratios, and absence of binding free energy profiles, the thesis makes significant contributions. It demonstrates that simple fluorescence techniques can uncover nanoscale features beyond the reach of more traditional methods, and that computational and experimental approaches can be effectively integrated to provide a multiscale picture of dye–silicate systems.

Future improvements could include adopting lifetime-gated FRAP, expanding molecular dynamics simulations to larger assemblies with free energy calculations, and

conducting systematic dye-labelling studies.

Ultimately, the core hypothesis has been confirmed: fluorescence-based nanometrology, especially FRAP, offers a distinctive, affordable, and scalable method for characterising silica colloids and sodium silicates. While not replacing established techniques, it provides complementary insights into dynamics and particle size heterogeneity, thereby expanding the range of tools available for both academic and industrial use.

11.2 Future Outlook

With the core objectives of this thesis addressed, spanning molecular-level dye-nanoparticle interactions to the practical application of fluorescence-based nanometrology in industrial silicate systems, the final section outlines several directions for future research building on the methodologies and insights developed here.

11.2.1 Future Directions in Computational Modelling of Dye–SNP Interactions

This thesis has established a computational framework for understanding dye-dye and dye-SNP interactions using classical MD, SMD and DFT approaches. While these methods provided valuable insights into curvature-dependent adsorption, dye dimerisation and the magnitude of binding energies, they were necessarily constrained by assumptions of idealised geometry and force field accuracy. One clear direction for future work involves extending the nanoparticle models beyond spherical approximations used here. In reality, SNPs, especially sodium silicates, often adopt ellipsoidal morphologies, which can be either oblate (flattened) or prolate (elongated) [261]. Incorporating these anisotropic shapes into simulations would provide a more realistic representation of surface curvature heterogeneity and its influence on dye binding, orientation, and mobility.

In addition to improved geometric realism, future studies could benefit from advanced sampling techniques and higher-level electronic structure methods. For instance, the use of *ab initio* MD would allow explicit treatment of electronic effects

during adsorption events, particularly important for charged dyes like R6G. Furthermore, enhanced sampling methods, such as umbrella sampling or metadynamics, can be employed to map free energy profiles along dye-surface interaction coordinates, yielding deeper insights into thermodynamic and kinetic effects of adsorption, desorption, and orientation. This would help overcome the limitations of conventional MD, which can miss rare events or underestimate energy barriers due to sampling of configurational space.

Another key limitation of the present work is the assumption that the dye molecule retains its charge state and molecular structure across all pH conditions. In reality, pH-induced protonation or deprotonation could alter both the electronic distribution and geometry of the dye, therefore influencing its interaction with the SNP surface. Future computational studies should explicitly account for these protonation equilibria using pKa prediction, quantum chemical tautomer scans, or constant-pH MD techniques to more accurately model the pH-dependent behaviour.

To further improve the accuracy of the binding energy calculations, especially in weakly bound or charge-transfer systems, methods beyond DFT should be considered. In particular, CCSD(T), often referred to as the "gold standard" in quantum chemistry, can provide benchmark-quality interaction energies for selected dye–dye or dye–surface configurations. Additionally, similarity-transformed equation-of-motion coupled-cluster theory (STEOM-CCSD(T)) offers an appealing balance between computational cost and excited-state accuracy, and can be used in conjunction with time-dependent DFT to enhance the theoretical understanding of fluorescence spectra and excited-state processes [370]. These methods would enable direct connections between predicted electronic transitions and experimental observables, such as adsorption or quenching effects, offering atomistic insight into the photophysics of dye–SNP systems and dye aggregation mechanics.

Lastly, a crucial direction for future modelling involves the role of impurities in nanoparticle formation and aggregation. Experimental FRAP results suggest that seemingly identical silicate samples can differ significantly in diffusion behaviour, possibly due to uncontrollable trace elements or synthesis-related variability. Computa-

tional studies could therefore explore the early-stage formation of silicate network from individual silicon-oxygen tetrahedra in the presence of metal contaminants, such as magnesium, aluminium, or iron, which may act as aggregation seeds. Understanding how these ions affect network growth, structural compactness and dye-binding affinity would provide much-needed context for interpreting differences in experimental mobility data and help identify hidden artefacts behind nanoparticle behaviour in industrial silicate solutions.

11.2.2   Experimental Outlook: Enhancing Dye–Nanoparticle Characterisation Techniques

While current work demonstrated that R6G can serve as a reliable probe for fluorescence-based nanometrology due to the simple labelling procedure and its high stability, one clear direction for experimental refinement involves the development and use of dyes that covalently bind to silica nanoparticle surfaces. The current approach, based on physisorption, inherently introduces free dye into the sample, which can significantly bias diffusion measurements, particularly in low-viscosity or diluted systems, by contributing faster-moving fluorescent species to the recovery signal. This artificially lowers the measured hydrodynamic radii and complicates model selection. Employing silane-functionalised fluorophores, which form stable Si–O–Si bonds with the nanoparticle surface, would eliminate this issue by ensuring that all fluorescence originates from particle-bound dye. This would improve measurement precision, reduce background signal variability, and ultimately enhance the reliability of FRAP-based size determination across a wide range of systems.

A more advanced experimental direction involves the integration of time-resolved FRAP (TR-FRAP) using SPAD array detectors. This approach would leverage the distinct fluorescence lifetimes of free versus bound dye to decouple their contributions during the recovery phase. Free dye, typically exhibiting shorter lifetimes, could be selectively excluded or de-emphasised in the data analysis, allowing more accurate quantification of nanoparticle-bound diffusion kinetics. Moreover, combining TR-FRAP with fluorescence anisotropy imaging would yield a powerful hybrid platform capable

of simultaneously determining rotational and translational diffusion. This would allow for the extraction of both viscosity and particle size from a single measurement, eliminating the need for independent viscosity calibration or prior knowledge of the sample's physical properties. Such a self-contained TR-FRAP-anisotropy setup would dramatically streamline data acquisition and analysis, and make the method more broadly applicable, particularly in high-throughput or industrial settings.

In parallel with these methodological developments, several key instrumental improvements could substantially enhance experimental performance. Replacing the current mirror in the bypass path with a beamsplitter would eliminate the ∼1 s delay between the bleaching and imaging, thereby reducing measurement artefacts caused by early-stage diffusion. Similarly, a more powerful laser source would allow for faster and more complete bleaching, minimising motion blur and initial recovery during the photobleaching phase. Sample cooling could also be introduced to slow down molecular diffusion, particularly useful for low-viscosity or highly dynamic samples, further improving spatial confinement and measurement accuracy.

Beyond the optical setup, the development of a dedicated graphical user interface for FRAP data analysis would greatly increase the accessibility and reproducibility of the method, especially for non-expert users. Lastly, given the ease and speed with which FRAP data can be generated, training ML models on a large, curated dataset of silicate measurements could enable fast, automated prediction and classification of nanoparticle sizes based on raw recovery curves. This would be particularly valuable for industrial control workflows, where quick feedback is essential.

Finally, recent observations from SAXS and steady-state fluorescence measurements have revealed the presence of intrinsic fluorescence in certain industrial silicate formulations, likely originating from trace impurities such as iron (Fe^{3+}) or chromium (Cr^{3+}) [371]. These metal ions are known to exhibit fluorescence under specific conditions and may complicate the interpretation of dye-based measurements [372]. Their presence also raises deeper questions about their role in the structural and dynamic behaviour of silicate networks, potentially acting as nucleation points, aggregation centres, or quenching agents. Future experimental work should focus on systematically

characterising the photophysical properties of these impurities across different formulations, perhaps using spectrally resolved lifetime imaging or elemental analysis (e.g., ICP-MS) to quantify and isolate their effects. Understanding the contribution of these metal impurities would not only improve data accuracy in fluorescence-based techniques but also help establish impurity thresholds for quality control in industrial silicate production. Such investigations could lead to better-defined specifications for raw material sourcing and processing, and might even reveal opportunities for deliberately tuning silicate properties via controlled impurity incorporation. Moreover, with the recent rise in the accessibility and popularity of SPAD detectors, there is promising potential to develop a novel, high-sensitivity fluorescence-based method for impurity quantification in silicate systems, offering a fast, optical alternative to traditional elemental analysis.

11.3 Final Remarks

Taken together, the work presented in this thesis establishes a comprehensive and versatile platform for the characterisation of silica-based nanomaterials, grounded in both theoretical modelling and experimental innovation. From elucidating fundamental dye-nanoparticle interactions at the molecular scale to developing practical, fluorescence-based techniques for resolving particle sizes in chemically complex systems, this research bridges critical gaps between computational chemistry, spectroscopy, and applied nanometrology. The integration of FRAP and fluorescence anisotropy as accessible, cost-effective alternatives to traditional techniques represents a significant step forward in the field, particularly for systems where standard methods fall short. The computational strategies and experimental methodologies developed here not only improve our understanding of silica nanomaterials but also provide a foundation for future exploration of diverse soft-matter and colloidal systems. As nanotechnology continues to intersect with industrial processing, biomedical diagnostics, and environmental monitoring, the tools and insights introduced in this thesis will remain relevant, adaptable, and impactful in both academic and applied contexts.

Appendix A: Additional Data for Chapter 6

TCL Script for Measuring COM Coordinates

The following TCL script is used to calculate and save the coordinates of the COM for two selected residues during a molecular dynamics trajectory in VMD.

```
# Daniel Doveiko January 6th 2022
# daniel.doveiko.2018@uni.strath.ac.uk
# script to save coordinates of 2 COM of any selected residues
# it creates a file coordinates.dat with the data
# to use: >source COMcoord.tcl
#         >measure_coordinates "protein and resid X" "protein and resid Y"

proc measure_coordinates { selstring1 selstring2 {molID {top}} {weight {}} } {

  set sel1 [atomselect $molID $selstring1]
  set sel2 [atomselect $molID $selstring2]
  set numframes [molinfo top get numframes]
  set output [open "coordinates.dat" w]

  puts $output "Frame\tx-coord\ty-coord\tz-coord\tx-coord\ty-coord\tz-coord"

  for {set i 0} {$i < $numframes} {incr i} {
    animate goto $i
    if {![llength $weight]} {
      set cent_sel1 [measure center $sel1]
      set cent_sel2 [measure center $sel2]
    } else {
```

```
    set cent_sel1 [measure center $sel1 weight $weight]

    set cent_sel2 [measure center $sel2 weight $weight]

  }

  puts $output "$i\t$cent_sel1 $i\t$cent_sel2"

}


$sel1 delete

$sel2 delete

unset numframes

unset output

}
```

System composition for simulations used in subsection 6.3.3

System	# of R6G	R6G	# of SNP	SNP	Cl$^-$	# of Na$^+$ per NP / SNP charge	Water	Total
40qSNP7	6	64	1	3,141	6	51	80,118	83,700
40qSNP12	6	64	1	3,077	6	116	80,612	84,195
40cSNP7	6	64	1	2,725	6	58	81,832	85,005
40cSNP12	6	64	1	2,638	6	155	80,292	83,475
20qSNP7	6	64	3	436	6	11	82,731	84,462
20qSNP12	6	64	3	421	6	27	84,153	85,887
20cSNP7	6	64	3	376	6	17	83,325	84,894
20cSNP12	6	64	3	354	6	39	81,861	83,430

Table 1: System composition. From left to right: the number of R6G molecules, the number of atoms within one R6G molecule, the number of SNPs added into the system and number of atoms involved in SNPs, number of Cl$^-$ ions, number of Na$^+$ ions and number of water atoms are listed.

Appendix B: Additional Data for Chapter 8

Dilution Measurements
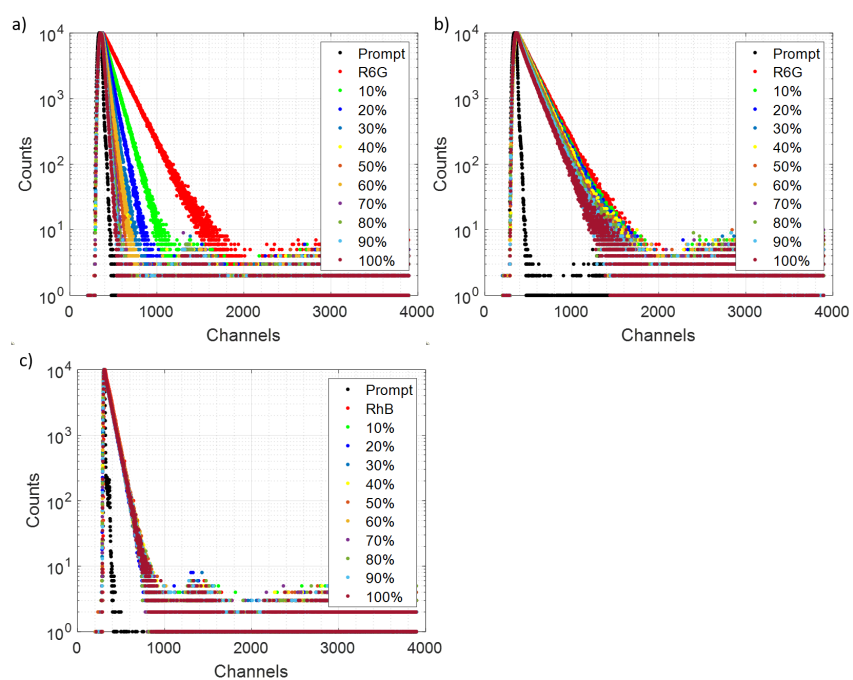
Figure 1: Fluorescence intensity decays of (a) R6G in NaOH, (b) R6G-silicate complex; (c) RB in sodium silicate.

SiO$_2$ (%)	[NaOH] (M)	T_1 (ns)	B_1 (%)	T_2 (ns)	B_2 (%)	C (%)	χ^2
27.0	2.0	3.42	82.43	0.94	8.01	9.56	1.23
24.3	1.8	3.46	88.30	0.79	5.19	6.50	1.13
21.6	1.6	3.51	93.43	0.58	3.43	3.14	1.18
18.9	1.4	3.55	93.06	0.57	3.59	3.35	1.12
16.2	1.2	3.55	95.23	0.45	3.63	1.15	1.05
13.5	1.0	3.65	94.19	0.59	2.16	3.65	1.09
10.8	0.8	3.73	93.98	0.69	1.14	4.58	1.16
8.1	0.6	3.81	93.39	1.43	1.66	4.95	1.19
5.4	0.4	3.89	93.58	1.78	2.53	3.89	1.18
2.7	0.2	3.98	95.87	0.61	1.40	2.73	1.13
0.0	0.0	4.18	97.20	-	-	2.80	1.07

Table 2: Fitting results for the R6G intensity decays in sodium silicate

SiO$_2$ (%)	[NaOH] (M)	T_1 (ns)	B_1 (%)	T_2 (ns)	B_2 (%)	C (%)	χ^2
27.0	2.0	1.69	90.62	0.38	5.62	3.76	0.97
24.3	1.8	1.70	90.25	0.38	5.94	3.81	1.08
21.6	1.6	1.69	92.47	0.24	4.58	2.94	1.04
18.9	1.4	1.69	91.54	0.31	5.36	3.09	0.99
16.2	1.2	1.72	93.32	0.22	3.23	3.45	1.08
13.5	1.0	1.71	94.33	0.30	2.12	3.55	1.04
10.8	0.8	1.73	92.31	0.33	3.78	3.91	1.13
8.1	0.6	1.69	93.84	0.16	2.78	3.38	1.17
5.4	0.4	1.65	93.85	0.22	1.87	4.28	1.16
2.7	0.2	1.68	94.49	0.18	2.03	3.48	0.97
0.0	0.0	1.67	94.15	0.17	2.78	3.06	0.95

Table 3: Fitting results for RB intensity decays in sodium silicate.

SiO$_2$ (%)	[NaOH] (M)	Φ (ns)	R_0	χ^2
27.0	2.0	1.16	0.17	1.10
24.3	1.8	0.84	0.13	1.10
21.6	1.6	0.40	0.31	1.11
18.9	1.4	0.44	0.21	1.05
16.2	1.2	0.27	0.29	1.07
13.5	1.0	0.19	0.33	1.26
10.8	0.8	0.24	0.28	1.08
8.1	0.6	0.17	0.34	1.18
5.4	0.4	0.19	0.22	1.19
2.7	0.2	0.14	0.35	1.12
0.0	0.0	0.16	0.20	1.06

Table 4: Anisotropy fitting results for the R6G-silicate complex.

SiO$_2$ (%)	[NaOH] (M)	Φ (ns)	R_0	χ^2
27.0	2.0	0.54	0.17	1.00
24.3	1.8	0.46	0.19	1.00
21.6	1.6	0.41	0.20	1.07
18.9	1.4	0.35	0.20	0.96
16.2	1.2	0.32	0.18	1.02
13.5	1.0	0.40	0.15	1.14
10.8	0.8	0.30	0.18	1.22
8.1	0.6	0.25	0.21	1.03
5.4	0.4	0.26	0.15	1.07
2.7	0.2	0.22	0.16	1.19
0.0	0.0	0.22	0.22	1.01

Table 5: Anisotropy fitting results for RB in silicate solutions.

Dye Hydrodynamic Radii

Counts	Φ (ns)	R_0	χ^2	R_H (Å)
5000	0.211	0.31	1.08	5.88
10000	0.178	0.38	0.98	5.56
15000	0.212	0.32	1.06	5.89
20000	0.227	0.31	1.05	6.03
25000	0.208	0.34	1.05	5.85
30000	0.220	0.32	1.00	5.96

Table 6: R6G hydrodynamic radius (R_H) at different photon count levels with corresponding anisotropy parameters and goodness-of-fit χ^2.

Counts	Φ (ns)	R_0	χ^2	R_H (Å)
5000	0.189	0.31	1.08	5.67
10000	0.194	0.33	1.09	5.72
15000	0.195	0.34	1.02	5.73
20000	0.195	0.31	1.08	5.73
25000	0.190	0.31	1.11	5.68
30000	0.197	0.30	1.14	5.75

Table 7: RB hydrodynamic radius (R_H) at different photon count levels with corresponding anisotropy parameters and goodness-of-fit χ^2.

Temperature-Controlled Measurements
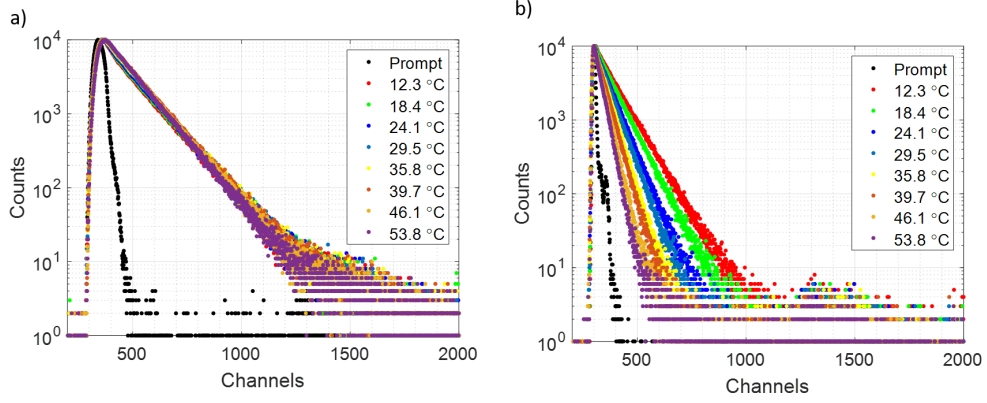
Figure 2: Fluorescence intensity decays at different temperatures (a) R6G-Silicate complex; (b) RB in Sodium Silicate.

T (°C)	T_1 (ns)	B_1 (%)	T_2 (ns)	B_2 (%)	C (%)	χ^2
12	3.47	75.88	1.01	10.73	10.72	1.19
18	3.45	81.34	0.89	9.40	9.27	1.29
24	3.42	84.90	0.82	6.30	8.80	1.20
29	3.41	86.69	0.96	5.31	8.00	1.21
35	3.35	89.23	0.95	3.01	7.75	1.23
39	3.33	90.74	1.16	3.06	6.21	1.18
46	3.22	92.52	0.88	2.09	5.38	1.15
53	3.11	94.46	–	–	5.54	1.18

Table 8: R6G fluorescence intensity decay fitting parameters across a temperature range. The parameters T_1 and T_2 represent decay times, B_1 and B_2 the corresponding amplitudes, C is the scattered light contribution, and χ^2 indicates the goodness of fit.

T (°C)	T_1 (ns)	B_1 (%)	T_2 (ns)	B_2 (%)	C (%)	χ^2
12	2.25	87.51	0.59	8.73	3.76	1.07
18	1.93	88.01	0.48	8.04	3.94	0.98
24	1.56	88.30	0.35	6.73	4.97	1.19
29	1.39	87.98	0.33	5.88	6.14	1.01
35	1.15	87.13	0.27	6.85	6.02	1.24
39	1.06	82.52	0.43	9.18	8.30	1.21
46	0.90	68.53	0.47	19.91	11.57	1.09
53	1.13	7.51	0.65	79.36	13.14	1.25

Table 9: RB fluorescence intensity decay fitting parameters across a temperature range. T_1 and T_2 represent decay times, B_1 and B_2 the respective amplitude contributions, C is the scattered light contribution, and χ^2 indicates the goodness of fit.

T (°C)	Φ (ns)	R_0	χ^2
12	1.17	0.17	1.11
18	0.76	0.13	1.06
24	0.82	0.10	1.09
29	0.51	0.15	1.05
35	0.44	0.17	1.14
39	0.32	0.22	1.05
46	0.18	0.34	1.10
53	0.22	0.25	1.05

Table 10: Anisotropy fitting results for the R6G–silicate complex across a temperature range. Φ represents the rotational time, R_0 is the initial anisotropy, and χ^2 denotes the goodness of fit.

T (°C)	Φ (ns)	R_0	χ^2
12	0.72	0.17	1.15
18	0.53	0.17	1.12
24	0.54	0.12	1.10
29	0.37	0.13	1.12
35	0.23	0.12	1.16
39	0.29	0.11	1.15
46	0.19	0.10	1.18
53	0.14	0.09	1.16

Table 11: Anisotropy fitting results for RB in sodium silicate as a function of temperature. Φ is the rotational time, R_0 the initial anisotropy, and χ^2 denotes the goodenss of fit.

Multiplexed Time-Resolved Measurements
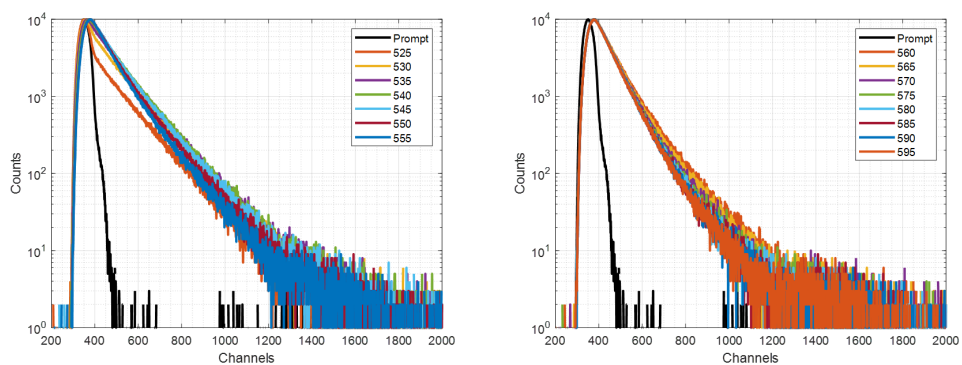
Figure 3: Fluorescence intensity decays for the multiplexed measurements.
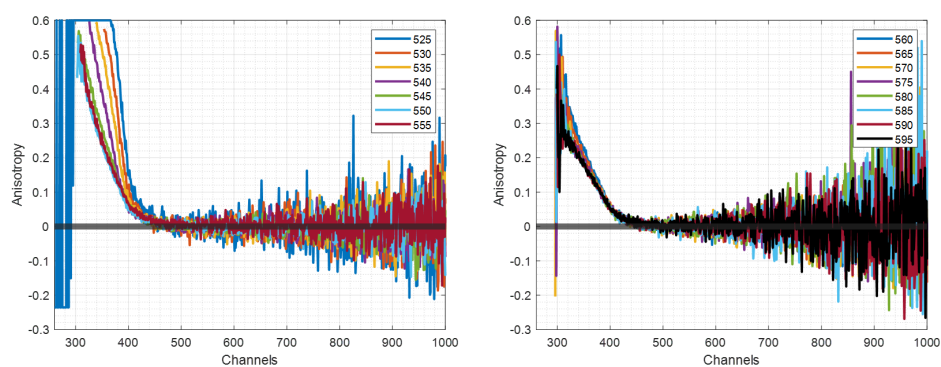
Figure 4: Anisotropy decays for the multiplexed measurements.

Appendix C: Additional Data for Chapter 10

Element	SD6521	SD6522	SD6524
Al	118	146	121
Ba	1.2	1.4	5.1
Ca	7	9.4	8.3
Cd	0.01	0.01	<0.02
Co	0.05	0.07	0.1
Cr	0.12	0.27	0.33
Cu	0.07	0.12	0.16
Fe	16.7	31.6	76
K	42.6	–	46
Mg	2.1	5.5	5.4
Mn	0.24	0.51	0.58
Mo	0	0	<0.02
Ni	0.03	0.04	0.14
PO_4	3.1	3.8	15.1
Pb	0.11	0.11	0.14
Ti	17.6	39.1	40
Zn	0.18	0.22	0.41
As	0.03	0.05	0.36
Hg	–	0	<0.02
Se	0.01	–	<0.02
Sb	–	0	<0.02
V	–	0.13	0.48

Table 12: Elemental analysis by ICP in parts per million (ppm) for three silicate samples. Data provided by PQ Silicas in private correspondence.

Bibliography

[1] Healy, J. F., <u>Pliny the Elder on science and technology</u>, Clarendon Press, 1999.

[2] Pliny, <u>Natural History</u>, Vol. X:, Harvard University Press, Books 36-37. Translated by D. E. Eichholz. Loeb Classical Library 419. Cambridge, MA, 1962.

[3] Goethe, J. W., <u>The Auto-Biography of Goethe: Truth and Poetry: From My Own Life</u>, BoD–Books on Demand, 2022.

[4] Fuchs, J., "Ueber ein neues Product aus Kieselerde und Kali; und dessen n ü zzliche Anwendung als Schuzmittel gegen schnelle Verbreitung des Feuers in Theatern, als Bindemittel, zu firni ß artigen Anstrichen usw Dinglers Polytech," <u>Dinglers Polytechnisches J</u>, Vol. 17, 1825, pp. 465–481.

[5] de Lucas, A., Rodríguez, L., Sánchez, P., and Lobato, J., "Synthesis of Crystalline Layered Sodium Silicate from Amorphous Silicate for Use in Detergents," <u>Industrial & Engineering Chemistry Research</u>, Vol. 39, No. 5, 2000, pp. 1249–1255.

[6] Song, L., Liu, W., Xin, F., and Li, Y., "Study of adhesion properties and mechanism of sodium silicate binder reinforced with silicate fume," <u>International Journal of Adhesion and Adhesives</u>, Vol. 106, 2021, pp. 102820.

[7] Thompson, J. L., Silsbee, M., Gill, P., and Scheetz, B., "Characterization of silicate sealers on concrete," <u>Cement and Concrete Research</u>, Vol. 27, No. 10, 1997, pp. 1561–1567.

[8] "Sodium Silicate Market Size, Share & Growth Report, 2030 — grandviewresearch.com," `https://www.grandviewresearch.com/industry-analysis/sodium-silicate-market`, [Accessed 24-06-2025].

[9] Shi, F., Zhang, Q., Li, D., and Deng, Y., "Silica-gel-confined ionic liquids: a new attempt for the development of supported nanoliquid catalysis," Chemistry–A European Journal, Vol. 11, No. 18, 2005, pp. 5279–5288.

[10] Barbe, C., Bartlett, J., Kong, L., Finnie, K., Lin, H. Q., Larkin, M., Calleja, S., Bush, A., and Calleja, G., "Silica particles: a novel drug-delivery system," Advanced Materials, Vol. 16, No. 21, 2004, pp. 1959–1966.

[11] Yoshida, K., "Abrasive properties of nano silica particles prepared by a sol–gel method for polishing silicon wafers," Journal of Sol-Gel Science and Technology, Vol. 43, 2007, pp. 9–13.

[12] Miyashita, N., Uekusa, S.-i., Kodera, M., Matsui, Y., and Katsumata, H., "Development of dishing-less slurry for polysilicon chemical-mechanical polishing process," Japanese Journal of Applied Physics, Vol. 42, No. 9R, 2003, pp. 5433.

[13] Matinfar, M. and Nychka, J. A., "A review of sodium silicate solutions: Structure, gelation, and syneresis," Advances in Colloid and Interface Science, Vol. 322, 2023, pp. 103036.

[14] Van der Donck, J. and Stein, H., "Viscosity of silicate solutions," Langmuir, Vol. 9, No. 9, 1993, pp. 2276–2280.

[15] Harris, R. K., Knight, C. T. G., and Hull, W. E., "NMR Studies of the Chemical Structure of Silicates in Solution," Soluble Silicates, Vol. 194 of ACS Symposium Series, chap. 6, American Chemical Society, 1982, pp. 79–93.

[16] Lentz, C. W., "Silicate minerals as sources of trimethylsilyl silicates and silicate structure analysis of sodium silicate solutions," Inorganic Chemistry, Vol. 3, No. 4, 1964, pp. 574–579.

[17] Fortnum, D. and Edwards, J. O., "The Raman spectrum and the structure of the aqueous silicate ion," Journal of Inorganic and Nuclear Chemistry, Vol. 2, No. 4, 1956, pp. 264–265.

[18] Marsmann, H., "29Si-Kernresonanzuntersuchungen an wäßrigen Silicatlösungen/29Si NMR Studies on Silicate Solutions in Water," Zeitschrift für Naturforschung B, Vol. 29, No. 7-8, 1974, pp. 495–499.

[19] Knight, C. T. and Harris, R. K., "Silicon-29 nuclear magnetic resonance studies of aqueous silicate solutions. 8 spin–lattice relaxation times and mechanisms," Magnetic Resonance in Chemistry, Vol. 24, No. 10, 1986, pp. 872–874.

[20] Knight, C. T., Balec, R. J., and Kinrade, S. D., "The structure of silicate anions in aqueous alkaline solutions," Angewandte Chemie, Vol. 119, No. 43, 2007, pp. 8296–8300.

[21] Engelhardt, G., Jancke, H., Hoebbel, D., and Wieker, W., "Structural studies in aqueous solutions of silicate anions by ^{29}Si NMR spectroscopy," Zeitschrift für Chemie, Vol. 14, No. 3, 1974, pp. 109–110.

[22] Nordström, J., Sundblom, A., Jensen, G. V., Pedersen, J. S., Palmqvist, A., and Matic, A., "Silica/alkali ratio dependence of the microscopic structure of sodium silicate solutions," Journal of Colloid and Interface Science, Vol. 397, 2013, pp. 9–17.

[23] Böschel, D., Janich, M., and Roggendorf, H., "Size distribution of colloidal silica in sodium silicate solutions investigated by dynamic light scattering and viscosity measurements," Journal of Colloid and Interface Science, Vol. 267, No. 2, 2003, pp. 360–368.

[24] Jansson, H., Bernin, D., and Ramser, K., "Silicate species of water glass and insights for alkali-activated green cement," AIP Advances, Vol. 5, No. 6, 06 2015, pp. 067167.

[25] Bass, J. L., Turner, G. L., and Morris, M. D., "Vibrational and 29Si NMR spectroscopies of soluble silicate oligomers," Macromolecular Symposia, Vol. 140, Wiley Online Library, 1999, pp. 263–270.

[26] Halasz, I., Agarwal, M., Li, R., and Miller, N., "Molecular spectroscopy of alkaline silicate solutions," Studies in Surface Science and Catalysis, Vol. 174, Elsevier, 2008, pp. 787–792.

[27] Halasz, I., Agarwal, M., Li, R., and Miller, N., "What can vibrational spectroscopy tell about the structure of dissolved sodium silicates?" Microporous and Mesoporous Materials, Vol. 135, No. 1-3, 2010, pp. 74–81.

[28] Dupuis, R., Rodrigues, D. G., Champenois, J.-B., Pellenq, R. J., and Poulesquen, A., "Time resolved alkali silicate decondensation by sodium hydroxide solution," Journal of Physics: Materials, Vol. 3, No. 1, 2020, pp. 014012.

[29] Wijnen, P., Beelen, T. P., and Van Santen, R. A., "Silica gels from aqueous silicate solutions," The Colloid Chemistry of Silica, Vol. 234, 1994, pp. 26–517.

[30] Uskoković, V., "Dynamic light scattering based microelectrophoresis: main prospects and limitations," Journal of Dispersion Science and Technology, Vol. 33, No. 12, 2012, pp. 1762–1786.

[31] Nordström, J., Nilsson, E., Jarvol, P., Nayeri, M., Palmqvist, A., Bergenholtz, J., and Matic, A., "Concentration-and pH-dependence of highly alkaline sodium silicate solutions," Journal of Colloid and Interface Science, Vol. 356, No. 1, 2011, pp. 37–45.

[32] Lunevich, L., Sanciolo, P., Smallridge, A., and Gray, S., "Silica scale formation and effect of sodium and aluminium ions-29 Si NMR study," Environmental Science: Water Research & Technology, Vol. 2, No. 1, 2016, pp. 174–185.

[33] Tleugabulova, D., Zhang, Z., and Brennan, J. D., "Evolution of sodium silicate sols through the sol-to-gel transition assessed by the fluorescence-based nanopar-

ticle metrology approach," <u>The Journal of Physical Chemistry B</u>, Vol. 107, No. 37, 2003, pp. 10127–10133.

[34] Tleugabulova, D., Zhang, Z., Chen, Y., Brook, M. A., and Brennan, J. D., "Fluorescence anisotropy in studies of solute interactions with covalently modified colloidal silica nanoparticles," <u>Langmuir</u>, Vol. 20, No. 3, 2004, pp. 848–854.

[35] Yip, P., Karolin, J., and Birch, D. J., "Fluorescence anisotropy metrology of electrostatically and covalently labelled silica nanoparticles," <u>Measurement Science and Technology</u>, Vol. 23, No. 8, 2012, pp. 084003.

[36] Zehentbauer, F. M., Moretto, C., Stephen, R., Thevar, T., Gilchrist, J. R., Pokrajac, D., Richard, K. L., and Kiefer, J., "Fluorescence spectroscopy of Rhodamine 6G: Concentration and solvent effects," <u>Spectrochimica Acta Part A: Molecular and Biomolecular Spectroscopy</u>, Vol. 121, 2014, pp. 147–151.

[37] Kubin, R. F. and Fletcher, A. N., "Fluorescence quantum yields of some rhodamine dyes," <u>Journal of Luminescence</u>, Vol. 27, No. 4, 1982, pp. 455–462.

[38] Doveiko, D., Kubiak-Ossowska, K., and Chen, Y., "Impact of the Crystal Structure of Silica Nanoparticles on Rhodamine 6G Adsorption: A Molecular Dynamics Study," <u>ACS Omega</u>, Vol. 9, No. 3, 2024, pp. 4123–4136.

[39] Doveiko, D., Martin, A. R., Vyshemirsky, V., Stebbing, S., Kubiak-Ossowska, K., Rolinski, O., Birch, D. J., and Chen, Y., "Nanoparticle Metrology of Silicates Using Time-Resolved Multiplexed Dye Fluorescence Anisotropy, Small Angle X-ray Scattering, and Molecular Dynamics Simulations," <u>Materials</u>, Vol. 17, No. 7, 2024, pp. 1686.

[40] Sen, T. and Patra, A., "Resonance energy transfer from rhodamine 6G to gold nanoparticles by steady-state and time-resolved spectroscopy," <u>The Journal of Physical Chemistry C</u>, Vol. 112, No. 9, 2008, pp. 3216–3222.

[41] Barzan, M. and Hajiesmaeilbaigi, F., "Effect of gold nanoparticles on the optical properties of Rhodamine 6G," The European Physical Journal D, Vol. 70, 2016, pp. 1–6.

[42] Vogel, R., Meredith, P., Harvey, M., and Rubinsztein-Dunlop, H., "Absorption and fluorescence spectroscopy of rhodamine 6G in titanium dioxide nanocomposites," Spectrochimica Acta Part A: Molecular and Biomolecular Spectroscopy, Vol. 60, No. 1-2, 2004, pp. 245–249.

[43] Ren, H., Kulkarni, D. D., Kodiyath, R., Xu, W., Choi, I., and Tsukruk, V. V., "Competitive adsorption of dopamine and rhodamine 6G on the surface of graphene oxide," ACS Applied Materials & Interfaces, Vol. 6, No. 4, 2014, pp. 2459–2470.

[44] Zhang, K., Yu, S., Jv, B., and Zheng, W., "Interaction of Rhodamine 6G molecules with graphene: a combined computational–experimental study," Physical Chemistry Chemical Physics, Vol. 18, No. 41, 2016, pp. 28418–28427.

[45] Chen, J., Zheng, A., Chen, A., Gao, Y., He, C., Kai, X., Wu, G., and Chen, Y., "A functionalized gold nanoparticles and Rhodamine 6G based fluorescent sensor for high sensitive and selective detection of mercury (II) in environmental water samples," Analytica Chimica Acta, Vol. 599, No. 1, 2007, pp. 134–142.

[46] Dhanya, S., Joy, J., and Rao, T. P., "Fabrication and characterization of rhodamine 6G entrapped sol–gel film test strip for virtually specific and sensitive sensing of nitrite," Sensors and Actuators B: Chemical, Vol. 173, 2012, pp. 510–516.

[47] Trinh, T. T., Jansen, A. P., and van Santen, R. A., "Mechanism of oligomerization reactions of silica," The Journal of Physical Chemistry B, Vol. 110, No. 46, 2006, pp. 23099–23106.

[48] Trinh, T. T., Jansen, A. P., van Santen, R. A., and Meijer, E. J., "Role of water in silica oligomerization," The Journal of Physical Chemistry C, Vol. 113, No. 7, 2009, pp. 2647–2652.

[49] White, C. E., Provis, J. L., Kearley, G. J., Riley, D. P., and Van Deventer, J. S., "Density functional modelling of silicate and aluminosilicate dimerisation solution chemistry," Dalton Transactions, Vol. 40, No. 6, 2011, pp. 1348–1355.

[50] Malani, A., Auerbach, S. M., and Monson, P. A., "Probing the mechanism of silica polymerization at ambient temperatures using Monte Carlo simulations," The Journal of Physical Chemistry Letters, Vol. 1, No. 21, 2010, pp. 3219–3224.

[51] Jing, Z., Xin, L., and Sun, H., "Replica exchange reactive molecular dynamics simulations of initial reactions in zeolite synthesis," Physical Chemistry Chemical Physics, Vol. 17, No. 38, 2015, pp. 25421–25428.

[52] Zhang, X.-Q., Trinh, T. T., van Santen, R. A., and Jansen, A. P., "Mechanism of the initial stage of silicate oligomerization," Journal of the American Chemical Society, Vol. 133, No. 17, 2011, pp. 6613–6625.

[53] Pereira, J., Catlow, C., and Price, G., "Silica condensation reaction: an ab initio study," Chemical Communications, , No. 13, 1998, pp. 1387–1388.

[54] Henschel, H., Schneider, A. M., and Prosenc, M. H., "Initial Steps of the Sol-Gel Process: Modeling Silicate Condensation in Basic Medium," Chemistry of Materials, Vol. 22, No. 17, 2010, pp. 5105–5111.

[55] Pereira, J., Catlow, C., and Price, G., "Ab initio studies of silica-based clusters. Part I. Energies and conformations of simple clusters," The Journal of Physical Chemistry A, Vol. 103, No. 17, 1999, pp. 3252–3267.

[56] Pavlova, A., Trinh, T. T., van Santen, R. A., and Meijer, E. J., "Clarifying the role of sodium in the silica oligomerization reaction," Physical Chemistry Chemical Physics, Vol. 15, No. 4, 2013, pp. 1123–1129.

[57] Rao, N. Z. and Gelb, L. D., "Molecular Dynamics Simulations of the Polymerization of Aqueous Silicic Acid and Analysis of the Effects of Concentration on Silica Polymorph Distributions, Growth Mechanisms, and Reaction Kinetics," The Journal of Physical Chemistry B, Vol. 108, No. 33, 2004, pp. 12418–12428.

[58] Kamińska, M., Gruy, F., and Valente, J., "dynamics of non-dense sodium silicate - water system studied by molecular dynamics," Colloids and Surfaces A: Physicochemical and Engineering Aspects, Vol. 603, 2020, pp. 125226.

[59] Emami, F. S., Puddu, V., Berry, R. J., Varshney, V., Patwardhan, S. V., Perry, C. C., and Heinz, H., "Force Field and a Surface Model Database for Silica to Simulate Interfacial Properties in Atomic Resolution," Chemistry of Materials, Vol. 26, No. 8, 2014, pp. 2647–2658.

[60] Axelrod, D., Koppel, D., Schlessinger, J., Elson, E., and Webb, W. W., "Mobility measurement by analysis of fluorescence photobleaching recovery kinetics," Biophysical Journal, Vol. 16, No. 9, 1976, pp. 1055–1069.

[61] Periasamy, N., Bicknese, S., and Verkman, A., "Reversible photobleaching of fluorescein conjugates in air-saturated viscous solutions: singlet and triplet state quenching by tryptophan," Photochemistry and Photobiology, Vol. 63, No. 3, 1996, pp. 265–271.

[62] Weiss, M., "Challenges and artifacts in quantitative photobleaching experiments," Traffic, Vol. 5, No. 9, 2004, pp. 662–671.

[63] Lippincott-Schwartz, J., Altan-Bonnet, N., and Patterson, G. H., "Photobleaching and photoactivation: following protein dynamics in living cells." Nature Cell Biology, 2003, pp. S7–14.

[64] Sprague, B. L., Pego, R. L., Stavreva, D. A., and McNally, J. G., "Analysis of binding reactions by fluorescence recovery after photobleaching," Biophysical Journal, Vol. 86, No. 6, 2004, pp. 3473–3495.

271

[65] Blonk, J., Don, A., Van Aalst, H., and Birmingham, J., "Fluorescence photobleaching recovery in the confocal scanning light microscope," Journal of Microscopy, Vol. 169, No. 3, 1993, pp. 363–374.

[66] Kusumi, A., Nakada, C., Ritchie, K., Murase, K., Suzuki, K., Murakoshi, H., Kasai, R. S., Kondo, J., and Fujiwara, T., "Paradigm shift of the plasma membrane concept from the two-dimensional continuum fluid to the partitioned fluid: high-speed single-molecule tracking of membrane molecules," Annu. Rev. Biophys. Biomol. Struct., Vol. 34, No. 1, 2005, pp. 351–378.

[67] Schwille, P. and Haustein, E., "Fluorescence correlation spectroscopy: a tutorial for the biophysics textbook online (BTOL)," Rockville: Biophysical Society, 2002.

[68] Ellenberg, J., Lippincott-Schwartz, J., and Presley, J. F., "Dual-colour imaging with GFP variants," Trends in Cell Biology, Vol. 9, No. 2, 1999, pp. 52–56.

[69] Phair, R. D. and Misteli, T., "Kinetic modelling approaches to in vivo imaging," Nature Reviews Molecular Cell Biology, Vol. 2, No. 12, 2001, pp. 898–907.

[70] Saxton, M. J. and Jacobson, K., "Single-particle tracking: applications to membrane dynamics," Annual Review of Biophysics and Biomolecular Structure, Vol. 26, No. 1, 1997, pp. 373–399.

[71] Reits, E. A. and Neefjes, J. J., "From fixed to FRAP: measuring protein mobility and activity in living cells," Nature Cell Biology, Vol. 3, No. 6, 2001, pp. E145.

[72] Alder, B. J. and Wainwright, T. E., "Studies in Molecular Dynamics. I. General Method," The Journal of Chemical Physics, Vol. 31, No. 2, 08 1959, pp. 459–466.

[73] Karplus, M. and McCammon, J. A., "Molecular dynamics simulations of biomolecules," Nature Structural Biology, Vol. 9, No. 9, 2002, pp. 646–652.

[74] Wüthrich, K., "Protein structure determination in solution by NMR spectroscopy." Journal of Biological Chemistry, Vol. 265, No. 36, 1990, pp. 22059–22062.

[75] Ilari, A. and Savino, C., Protein Structure Determination by X-Ray Crystallography, Humana Press, Totowa, NJ, 2008, pp. 63–87.

[76] Jumper, J., Evans, R., Pritzel, A., Green, T., Figurnov, M., Ronneberger, O., Tunyasuvunakool, K., Bates, R., Žídek, A., Potapenko, A., et al., "Highly accurate protein structure prediction with AlphaFold," Nature, Vol. 596, No. 7873, 2021, pp. 583–589.

[77] Abramson, J., Adler, J., Dunger, J., Evans, R., Green, T., Pritzel, A., Ronneberger, O., Willmore, L., Ballard, A. J., Bambrick, J., et al., "Accurate structure prediction of biomolecular interactions with AlphaFold 3," Nature, Vol. 630, No. 8016, 2024, pp. 493–500.

[78] Hansson, T., Oostenbrink, C., and van Gunsteren, W., "Molecular dynamics simulations," Current Opinion in Structural Biology, Vol. 12, No. 2, 2002, pp. 190–196.

[79] Feller, S. E., "Molecular dynamics simulations of lipid bilayers," Current Opinion in Colloid & Interface Science, Vol. 5, No. 3-4, 2000, pp. 217–223.

[80] Zeng, Q., Yu, A., Lu, G., and Standish, R., "Molecular dynamics simulation of organic- inorganic nanocomposites: layering behavior and interlayer structure of organoclays," Chemistry of Materials, Vol. 15, No. 25, 2003, pp. 4732–4738.

[81] Salomon-Ferrer, R., Gotz, A. W., Poole, D., Le Grand, S., and Walker, R. C., "Routine microsecond molecular dynamics simulations with AMBER on GPUs. 2. Explicit solvent particle mesh Ewald," Journal of Chemical Theory and Computation, Vol. 9, No. 9, 2013, pp. 3878–3888.

[82] Sampath, J., Kullman, A., Gebhart, R., Drobny, G., and Pfaendtner, J., "Molecular recognition and specificity of biomolecules to titanium dioxide from molecular dynamics simulations," npj Computational Materials, Vol. 6, No. 1, 2020, pp. 34.

[83] Patwardhan, S. V., Patwardhan, G., and Perry, C. C., "Interactions of biomolecules with inorganic materials: principles, applications and future

prospects," Journal of Materials Chemistry, Vol. 17, No. 28, 2007, pp. 2875–2884.

[84] Born, M. and Oppenheimer, R., "Zur Quantentheorie der Molekeln," Annalen der Physik, Vol. 84, 1927, pp. 457–484.

[85] Levine, I. N., Busch, D. H., and Shull, H., Quantum Chemistry, Vol. 6, Pearson Prentice Hall Upper Saddle River, NJ, 2009.

[86] Jensen, F., Introduction to Computational Chemistry, John wiley & sons, 2017.

[87] Lifson, S. and Warshel, A., "Consistent force field for calculations of conformations, vibrational spectra, and enthalpies of cycloalkane and n-alkane molecules," The Journal of Chemical Physics, Vol. 49, No. 11, 1968, pp. 5116–5129.

[88] Vanommeslaeghe, K., Hatcher, E., Acharya, C., Kundu, S., Zhong, S., Shim, J., Darian, E., Guvench, O., Lopes, P., Vorobyov, I., et al., "CHARMM general force field: A force field for drug-like molecules compatible with the CHARMM all-atom additive biological force fields," Journal of Computational Chemistry, Vol. 31, No. 4, 2010, pp. 671–690.

[89] Huang, J. and MacKerell Jr, A. D., "CHARMM36 all-atom additive protein force field: Validation based on comparison to NMR data," Journal of Computational Chemistry, Vol. 34, No. 25, 2013, pp. 2135–2145.

[90] MacKerell Jr, A. D., Bashford, D., Bellott, M., Dunbrack Jr, R. L., Evanseck, J. D., Field, M. J., Fischer, S., Gao, J., Guo, H., Ha, S., et al., "All-atom empirical potential for molecular modeling and dynamics studies of proteins," The Journal of Physical Chemistry B, Vol. 102, No. 18, 1998, pp. 3586–3616.

[91] Huang, J., Rauscher, S., Nawrocki, G., Ran, T., Feig, M., De Groot, B. L., Grubmüller, H., and MacKerell Jr, A. D., "CHARMM36m: an improved force field for folded and intrinsically disordered proteins," Nature Methods, Vol. 14, No. 1, 2017, pp. 71–73.

[92] Wang, J., Wolf, R. M., Caldwell, J. W., Kollman, P. A., and Case, D. A., "Development and testing of a general amber force field," Journal of Computational Chemistry, Vol. 25, No. 9, 2004, pp. 1157–1174.

[93] Scott, W. R., Hünenberger, P. H., Tironi, I. G., Mark, A. E., Billeter, S. R., Fennen, J., Torda, A. E., Huber, T., Krüger, P., and Van Gunsteren, W. F., "The GROMOS biomolecular simulation program package," The Journal of Physical Chemistry A, Vol. 103, No. 19, 1999, pp. 3596–3607.

[94] Jorgensen, W. L., Maxwell, D. S., and Tirado-Rives, J., "Development and testing of the OPLS all-atom force field on conformational energetics and properties of organic liquids," Journal of the American Chemical Society, Vol. 118, No. 45, 1996, pp. 11225–11236.

[95] Heinz, H., Vaia, R., Farmer, B., and Naik, R., "Accurate simulation of surfaces and interfaces of face-centered cubic metals using 12- 6 and 9- 6 Lennard-Jones potentials," The Journal of Physical Chemistry C, Vol. 112, No. 44, 2008, pp. 17281–17290.

[96] Heinz, H., Lin, T.-J., Kishore Mishra, R., and Emami, F. S., "Thermodynamically consistent force fields for the assembly of inorganic, organic, and biological nanostructures: the INTERFACE force field," Langmuir, Vol. 29, No. 6, 2013, pp. 1754–1765.

[97] Montagna, M., Bruckner, S. I., Dianat, A., Gutierrez, R., Daus, F., Geyer, A., Brunner, E., and Cuniberti, G., "Interactions of long-chain polyamines with silica studied by molecular dynamics simulations and solid-state NMR spectroscopy," Langmuir, Vol. 36, No. 39, 2020, pp. 11600–11609.

[98] Martín-Moldes, Z., Barreiro, D. L., Buehler, M. J., and Kaplan, D. L., "Effect of the silica nanoparticle size on the osteoinduction of biomineralized silk-silica nanocomposites," Acta Biomaterialia, Vol. 120, 2021, pp. 203–212.

[99] Bruckner, S. I., Donets, S., Dianat, A., Bobeth, M., Gutierrez, R., Cuniberti, G., and Brunner, E., "Probing silica–biomolecule interactions by solid-state NMR and molecular dynamics simulations," Langmuir, Vol. 32, No. 44, 2016, pp. 11698–11705.

[100] Bhandarkar, M., Brunner, R., Chipot, C., Dalke, A., Dixit, S., Grayson, P., Gullingsrud, J., Gursoy, A., Hardy, D., Humphrey, W., et al., "NAMD user's guide," Urbana, Vol. 51, 2003, pp. 61801.

[101] Girifalco, L. A. and Weizer, V. G., "Application of the Morse potential function to cubic metals," Physical Review, Vol. 114, No. 3, 1959, pp. 687.

[102] Vanommeslaeghe, K., Guvench, O., and MacKerell, A. D. J., "Molecular Mechanics," Current Pharmaceutical Design, Vol. 20, No. 20, 2014, pp. 3281–3292.

[103] Alekseev, A. and Yakimets, V., "Electromagnetic Radiation in an Absorbing Medium," Sov. Phys. JETP, Vol. 24, No. 5, 1967.

[104] Hermann, J., DiStasio Jr, R. A., and Tkatchenko, A., "First-principles models for van der Waals interactions in molecules and materials: Concepts, theory, and applications," Chemical Reviews, Vol. 117, No. 6, 2017, pp. 4714–4758.

[105] Keesom, W. H., "The second viral coefficient for rigid spherical molecules, whose mutual attraction is equivalent to that of a quadruplet placed at their centre," Proc. R. Acad. Sci, Vol. 18, 1915, pp. 636–646.

[106] Debye, P., "Van der Waals cohesion forces," Physikalische Zeitschrift, Vol. 21, 1920, pp. 178–187.

[107] London, F., "The general theory of molecular forces," Transactions of the Faraday Society, Vol. 33, 1937, pp. 8b–26.

[108] Vaccarelli, O., Fedorov, D. V., Stöhr, M., and Tkatchenko, A., "Quantum-mechanical force balance between multipolar dispersion and Pauli repulsion in

atomic van der Waals dimers," Physical Review Research, Vol. 3, No. 3, 2021, pp. 033181.

[109] Andersson, Y., Hult, E., Rydberg, H., Apell, P., Lundqvist, B. I., and Langreth, D. C., "Van der Waals interactions in density functional theory," Electronic Density Functional Theory: Recent Progress and New Directions, 1998, pp. 243–260.

[110] Gasteiger, J. and Saller, H., "Calculation of the charge distribution in conjugated systems by a quantification of the resonance concept," Angewandte Chemie International Edition in English, Vol. 24, No. 8, 1985, pp. 687–689.

[111] Doveiko, D., Kubiak-Ossowska, K., and Chen, Y., "Estimating binding energies of π-stacked aromatic dimers using force field-driven molecular dynamics," International Journal of Molecular Sciences, Vol. 25, No. 11, 2024, pp. 5783.

[112] Martyna, G. J., Tuckerman, M. E., Tobias, D. J., and Klein, M. L., "Explicit reversible integrators for extended systems dynamics," Molecular Physics, Vol. 87, No. 5, 1996, pp. 1117–1157.

[113] Berendsen, H. J., Postma, J. v., Van Gunsteren, W. F., DiNola, A., and Haak, J. R., "Molecular dynamics with coupling to an external bath," The Journal of Chemical Physics, Vol. 81, No. 8, 1984, pp. 3684–3690.

[114] Andersen, H. C., "Molecular dynamics simulations at constant pressure and/or temperature," The Journal of Chemical Physics, Vol. 72, No. 4, 1980, pp. 2384–2393.

[115] NOSÉ, S. U. I., "A molecular dynamics method for simulations in the canonical ensemble," Molecular Physics, Vol. 100, No. 1, 2002, pp. 191–198.

[116] Hoover, W. G., "Canonical dynamics: Equilibrium phase-space distributions," Physical Review A, Vol. 31, No. 3, 1985, pp. 1695.

[117] Bussi, G., Donadio, D., and Parrinello, M., "Canonical sampling through velocity rescaling," The Journal of Chemical Physics, Vol. 126, No. 1, 2007.

[118] Heyes, D., "Molecular dynamics at constant pressure and temperature," <u>Chemical Physics</u>, Vol. 82, No. 3, 1983, pp. 285–301.

[119] Allen, M. P. and Tildesley, D. J., <u>Computer Simulation of Liquids</u>, Oxford University Press, 2017.

[120] Hoover, W. G., Ladd, A. J., and Moran, B., "High-strain-rate plastic flow studied via nonequilibrium molecular dynamics," <u>Physical Review Letters</u>, Vol. 48, No. 26, 1982, pp. 1818.

[121] Evans, D. J., "Computer "experiment"for nonlinear thermodynamics of Couette flow," <u>The Journal of Chemical Physics</u>, Vol. 78, No. 6, 1983, pp. 3297–3302.

[122] Mark, P. and Nilsson, L., "Structure and dynamics of the TIP3P, SPC, and SPC/E water models at 298 K," <u>The Journal of Physical Chemistry A</u>, Vol. 105, No. 43, 2001, pp. 9954–9960.

[123] Abascal, J. L. F. and Vega, C., "A general purpose model for the condensed phases of water: TIP4P/2005," <u>The Journal of Chemical Physics</u>, Vol. 123, No. 23, 2005, pp. 234505.

[124] Andersen, H. C., "Rattle: A "velocity" version of the shake algorithm for molecular dynamics calculations," <u>Journal of Computational Physics</u>, Vol. 52, No. 1, 1983, pp. 24–34.

[125] Hess, B., Bekker, H., Berendsen, H. J. C., and Fraaije, J. G. E. M., "LINCS: A linear constraint solver for molecular simulations," <u>Journal of Computational Chemistry</u>, Vol. 18, No. 12, 1997, pp. 1463–1472.

[126] Jorgensen, W. L., Chandrasekhar, J., Madura, J. D., Impey, R. W., and Klein, M. L., "Comparison of simple potential functions for simulating liquid water," <u>The Journal of Chemical Physics</u>, Vol. 79, No. 2, 1983, pp. 926–935.

[127] Tokarczyk, K., Kubiak-Ossowska, K., Jachimska, B., and Mulheran, P. A., "Energy landscape of negatively charged BSA adsorbed on a negatively charged silica

surface," The Journal of Physical Chemistry B, Vol. 122, No. 14, 2018, pp. 3744–3753.

[128] Peng, Q., Zhuang, S., Wang, M., Cao, Y., Khor, Y., and Li, H., "Mechanical design of the third FnIII domain of tenascin-C," Journal of Molecular Biology, Vol. 386, No. 5, 2009, pp. 1327–1342.

[129] Kubiak-Ossowska, K. and Mulheran, P. A., "Protein diffusion and long-term adsorption states at charged solid surfaces," Langmuir, Vol. 28, No. 44, 2012, pp. 15577–15585.

[130] Sugita, Y. and Okamoto, Y., "Replica-exchange molecular dynamics method for protein folding," Chemical Physics Letters, Vol. 314, No. 1-2, 1999, pp. 141–151.

[131] Torrie, G. M. and Valleau, J. P., "Nonphysical sampling distributions in Monte Carlo free-energy estimation: Umbrella sampling," Journal of Computational Physics, Vol. 23, No. 2, 1977, pp. 187–199.

[132] Laio, A. and Parrinello, M., "Escaping free-energy minima," Proceedings of the National Academy of Sciences, Vol. 99, No. 20, 2002, pp. 12562–12566.

[133] Batatia, I., Kovacs, D. P., Simm, G., Ortner, C., and Csányi, G., "MACE: Higher order equivariant message passing neural networks for fast and accurate force fields," Advances in Neural Information Processing Systems, Vol. 35, 2022, pp. 11423–11436.

[134] Kovács, D. P., Batatia, I., Arany, E. S., and Csányi, G., "Evaluation of the MACE force field architecture: From medicinal chemistry to materials science," The Journal of Chemical Physics, Vol. 159, No. 4, 2023.

[135] Hohenberg, P. and Kohn, W., "Inhomogeneous electron gas," Physical Review, Vol. 136, No. 3B, 1964, pp. B864.

[136] Kohn, W. and Sham, L. J., "Self-consistent equations including exchange and correlation effects," Physical Review, Vol. 140, No. 4A, 1965, pp. A1133.

[137] Schrödinger, E., "An undulatory theory of the mechanics of atoms and molecules," Physical Review, Vol. 28, No. 6, 1926, pp. 1049.

[138] Jain, A., Shin, Y., and Persson, K. A., "Computational predictions of energy materials using density functional theory," Nature Reviews Materials, Vol. 1, No. 1, 2016, pp. 1–13.

[139] Hartree, D. R., "The wave mechanics of an atom with a non-Coulomb central field. Part I. Theory and methods," Mathematical Proceedings of the Cambridge Philosophical Society, Vol. 24, Cambridge University Press, 1928, pp. 89–110.

[140] Slater, J. C., "Note on Hartree's method," Physical Review, Vol. 35, No. 2, 1930, pp. 210.

[141] Perdew, J. P. and Schmidt, K., "Jacob's ladder of density functional approximations for the exchange-correlation energy," AIP Conference Proceedings, Vol. 577, American Institute of Physics, 2001, pp. 1–20.

[142] Perdew, J. P., Ruzsinszky, A., Tao, J., Staroverov, V. N., Scuseria, G. E., and Csonka, G. I., "Prescription for the design and selection of density functional approximations: More constraint satisfaction with fewer fits," The Journal of Chemical Physics, Vol. 123, No. 6, 2005.

[143] Perdew, J. P. and Wang, Y., "Accurate and simple analytic representation of the electron-gas correlation energy," Physical Review B, Vol. 45, No. 23, 1992, pp. 13244.

[144] Perdew, J. P., Burke, K., and Ernzerhof, M., "Generalized gradient approximation made simple," Physical Review Letters, Vol. 77, No. 18, 1996, pp. 3865.

[145] Tao, J., Perdew, J. P., Staroverov, V. N., and Scuseria, G. E., "Climbing the density functional ladder: Nonempirical meta–generalized gradient approximation designed for molecules and solids," Physical Review Letters, Vol. 91, No. 14, 2003, pp. 146401.

[146] Becke, A. D., "Density-functional thermochemistry. III. The role of exact exchange," The Journal of Chemical Physics, Vol. 98, No. 7, 1993, pp. 5648–5652.

[147] Becke, A. D., "A new mixing of Hartree-Fock and local density-functional theories," Journal of Chemical Physics, Vol. 98, No. 2, 1993, pp. 1372–1377.

[148] Lee, C., Yang, W., and Parr, R. G., "Development of the Colle-Salvetti correlation-energy formula into a functional of the electron density," Physical Review B, Vol. 37, No. 2, 1988, pp. 785.

[149] Stephens, P. J., Devlin, F. J., Chabalowski, C. F., and Frisch, M. J., "Ab initio calculation of vibrational absorption and circular dichroism spectra using density functional force fields," The Journal of Physical Chemistry, Vol. 98, No. 45, 1994, pp. 11623–11627.

[150] Iikura, H., Tsuneda, T., Yanai, T., and Hirao, K., "A long-range correction scheme for generalized-gradient-approximation exchange functionals," The Journal of Chemical Physics, Vol. 115, No. 8, 2001, pp. 3540–3544.

[151] Chai, J.-D. and Head-Gordon, M., "Long-range corrected hybrid density functionals with damped atom–atom dispersion corrections," Physical Chemistry Chemical Physics, Vol. 10, No. 44, 2008, pp. 6615–6620.

[152] Chai, J.-D. and Head-Gordon, M., "Systematic optimization of long-range corrected hybrid density functionals," The Journal of Chemical Physics, Vol. 128, No. 8, 2008.

[153] Grimme, S., "Semiempirical GGA-type density functional constructed with a long-range dispersion correction," Journal of Computational Chemistry, Vol. 27, No. 15, 2006, pp. 1787–1799.

[154] Grimme, S. and Neese, F., "Double-hybrid density functional theory for excited electronic states of molecules," The Journal of Chemical Physics, Vol. 127, No. 15, 2007.

281

[155] Hehre, W. J., Stewart, R. F., and Pople, J. A., "Self-consistent molecular-orbital methods. I. Use of Gaussian expansions of Slater-type atomic orbitals," The Journal of Chemical Physics, Vol. 51, No. 6, 1969, pp. 2657–2664.

[156] Ditchfield, R., Hehre, W. J., and Pople, J. A., "Self-consistent molecular-orbital methods. IX. An extended Gaussian-type basis for molecular-orbital studies of organic molecules," The Journal of Chemical Physics, Vol. 54, No. 2, 1971, pp. 724–728.

[157] Schäfer, A., Horn, H., and Ahlrichs, R., "Fully optimized contracted Gaussian basis sets for atoms Li to Kr," Journal of Chemical Physics, Vol. 97, No. 4, 1992, pp. 2571–2577.

[158] Miertuš, S., Scrocco, E., and Tomasi, J., "Electrostatic interaction of a solute with a continuum. A direct utilizaion of AB initio molecular potentials for the prevision of solvent effects," Chemical Physics, Vol. 55, No. 1, 1981, pp. 117–129.

[159] Klamt, A. and Schüürmann, G., "COSMO: a new approach to dielectric screening in solvents with explicit expressions for the screening energy and its gradient," J. Chem. Soc., Perkin Trans. 2, 1993, pp. 799–805.

[160] Barone, V. and Cossi, M., "Quantum calculation of molecular energies and energy gradients in solution by a conductor solvent model," The Journal of Physical Chemistry A, Vol. 102, No. 11, 1998, pp. 1995–2001.

[161] Mulliken, R. S., "Electronic population analysis on LCAO–MO molecular wave functions. I," The Journal of Chemical Physics, Vol. 23, No. 10, 1955, pp. 1833–1840.

[162] Reed, A. E., Weinstock, R. B., and Weinhold, F., "Natural population analysis," The Journal of Chemical Physics, Vol. 83, No. 2, 1985, pp. 735–746.

[163] Bayly, C. I., Cieplak, P., Cornell, W., and Kollman, P. A., "A well-behaved electrostatic potential based method using charge restraints for deriving atomic

charges: the RESP model," <u>The Journal of Physical Chemistry</u>, Vol. 97, No. 40, 1993, pp. 10269–10280.

[164] Klimeš, J. and Michaelides, A., "Perspective: Advances and challenges in treating van der Waals dispersion forces in density functional theory," <u>The Journal of Chemical Physics</u>, Vol. 137, No. 12, 2012.

[165] Tao, J. and Perdew, J. P., "Test of a nonempirical density functional: Short-range part of the van der Waals interaction in rare-gas dimers," <u>The Journal of Chemical Physics</u>, Vol. 122, No. 11, 2005.

[166] Johnson, E. R. and Becke, A. D., "A post-Hartree–Fock model of intermolecular interactions," <u>The Journal of Chemical Physics</u>, Vol. 123, No. 2, 2005.

[167] Grimme, S., Antony, J., Ehrlich, S., and Krieg, H., "A consistent and accurate ab initio parametrization of density functional dispersion correction (DFT-D) for the 94 elements H-Pu," <u>The Journal of Chemical Physics</u>, Vol. 132, No. 15, 2010.

[168] Nygaard, C. R. and Olsen, J., "A second-order unconstrained optimization method for canonical-ensemble density-functional methods," <u>The Journal of Chemical Physics</u>, Vol. 138, No. 9, 2013.

[169] Gritsenko, O., Ensing, B., Schipper, P., and Baerends, E., "Comparison of the accurate Kohn- Sham solution with the generalized gradient approximations (GGAs) for the SN2 Reaction F-+ CH3F$\rightarrow$ FCH3+ F-: a qualitative rule to predict success or failure of GGAs," <u>The Journal of Physical Chemistry A</u>, Vol. 104, No. 37, 2000, pp. 8558–8565.

[170] Kresse, G. and Hafner, J., "Ab initio molecular dynamics for liquid metals," <u>Physical Review B</u>, Vol. 47, No. 1, 1993, pp. 558.

[171] Marx, D. and Hutter, J., <u>Ab initio molecular dynamics: basic theory and advanced methods</u>, Cambridge University Press, 2009.

[172] Valeur, B. and Berberan-Santos, M. N., <u>Molecular fluorescence: principles and applications</u>, John Wiley & Sons, 2013.

283

[173] Kasha, M., "Characterization of electronic transitions in complex molecules," Discussions of the Faraday society, Vol. 9, 1950, pp. 14–19.

[174] Demchenko, A. P., "The red-edge effects: 30 years of exploration," Luminescence: The Journal of Biological and Chemical Luminescence, Vol. 17, No. 1, 2002, pp. 19–42.

[175] Lakowicz, J. R., Principles of fluorescence spectroscopy, Springer, 2006.

[176] Andrews, D. L., Photonics, Volume 4: Biomedical Photonics, Spectroscopy, and Microscopy, Vol. 4, John Wiley & Sons, 2015.

[177] Birch, D. J., Chen, Y., and Rolinski, O. J., "Fluorescence," Photonics: Biomedical Photonics, Spectroscopy, and Microscopy, 2015, pp. 1–58.

[178] Pettersen, J. M. and Robinson, A. S., "Ligand binding kinetics of A2AR nanodiscs using fluorescence anisotropy," Biophysical Journal, Vol. 123, No. 3, 2024, pp. 344a.

[179] Jensen, L. and Schatz, G. C., "Resonance Raman Scattering of Rhodamine 6G as Calculated Using Time-Dependent Density Functional Theory," The Journal of Physical Chemistry A, Vol. 110, No. 18, 2006, pp. 5973–5977, PMID: 16671663.

[180] Gavrilenko, V. I. and Noginov, M. A., "Ab initio study of optical properties of rhodamine 6G molecular dimers," The Journal of Chemical Physics, Vol. 124, No. 4, 01 2006, pp. 044301.

[181] Karpiuk, J., Grabowski, Z. R., and Schryver, F. C. D., "Fluorescence kinetics study of rhodamine B lactone in polar aprotic solvents — a global analysis approach," Proceedings of the Indian Academy of Sciences - Chemical Sciences, Vol. 104, No. 2, 1992, pp. 133–142.

[182] Davydov, A. S., "The theory of molecular excitons," Soviet Physics Uspekhi, Vol. 7, No. 2, Feb. 1964, pp. 145–178.

[183] Setiawan, D., Kazaryan, A., Martoprawiro, M. A., and Filatov, M., "A first principles study of fluorescence quenching in rhodamine B dimers: how can quenching occur in dimeric species?" Phys. Chem. Chem. Phys., Vol. 12, 2010, pp. 11238–11244.

[184] Förster, H., "UV/vis spectroscopy," Characterization I: -/-, 2004, pp. 337–426.

[185] Becker, W., Advanced time-correlated single photon counting applications, Vol. 111, Springer, 2015.

[186] O'Connor, D., Time-correlated single photon counting, Academic Press, 2012.

[187] Brochon, J.-C., "[13] Maximum entropy method of data analysis in time-resolved spectroscopy," Methods in Enzymology, Vol. 240, Elsevier, 1994, pp. 262–311.

[188] Bharill, S., Sarkar, P., Ballin, J. D., Gryczynski, I., Wilson, G. M., and Gryczynski, Z., "Fluorescence intensity decays of 2-aminopurine solutions: lifetime distribution approach," Analytical Biochemistry, Vol. 377, No. 2, 2008, pp. 141–149.

[189] Bajzer, Ž., Therneau, T. M., Sharp, J. C., and Prendergast, F. G., "Maximum likelihood method for the analysis of time-resolved fluorescence decay curves," European Biophysics Journal, Vol. 20, 1991, pp. 247–262.

[190] Li, Y., Natakorn, S., Chen, Y., Safar, M., Cunningham, M., Tian, J., and Li, D. D.-U., "Investigations on average fluorescence lifetimes for visualizing multi-exponential decays," Frontiers in Physics, Vol. 8, 2020, pp. 576862.

[191] Luchowski, R., Gryczynski, Z., Sarkar, P., Borejdo, J., Szabelski, M., Kapusta, P., and Gryczynski, I., "Instrument response standard in time-resolved fluorescence," Review of Scientific Instruments, Vol. 80, No. 3, 2009.

[192] Lakowicz, J. R., Shen, B., Gryczynski, Z., D'Auria, S., and Gryczynski, I., "Intrinsic fluorescence from DNA can be enhanced by metallic particles," Biochemical and Biophysical Research Communications, Vol. 286, No. 5, 2001, pp. 875–879.

[193] Selanger, K., Falnes, J., and Sikkeland, T., "Fluorescence lifetime studies of Rhodamine 6G in methanol," The Journal of Physical Chemistry, Vol. 81, No. 20, 1977, pp. 1960–1963.

[194] Press, W. H., Numerical recipes 3rd edition: The art of scientific computing, Cambridge University Press, 2007.

[195] Kasche, V. and Lindqvist, L., "Reactions between the Triplet State of Fluorescein and Oxygen," The Journal of Physical Chemistry, Vol. 68, No. 4, 1964, pp. 817–823.

[196] Zheng, Q., Jockusch, S., Zhou, Z., and Blanchard, S. C., "The Contribution of Reactive Oxygen Species to the Photobleaching of Organic Fluorophores," Photochemistry and Photobiology, Vol. 90, No. 2, 2014, pp. 448–454.

[197] Eggeling, C., Widengren, J., Rigler, R., and Seidel, C. A. M., "Photobleaching of Fluorescent Dyes under Conditions Used for Single-Molecule Detection: Evidence of Two-Step Photolysis," Analytical Chemistry, Vol. 70, No. 13, 1998, pp. 2651–2659, PMID: 21644785.

[198] Cheng, Y., Prud'Homme, R. K., and Thomas, J. L., "Diffusion of mesoscopic probes in aqueous polymer solutions measured by fluorescence recovery after photobleaching," Macromolecules, Vol. 35, No. 21, 2002, pp. 8111–8121.

[199] Tsien, R. Y., "The green fluorescent protein," Annual Review of Biochemistry, Vol. 67, No. 1, 1998, pp. 509–544.

[200] Sinnecker, D., Voigt, P., Hellwig, N., and Schaefer, M., "Reversible photobleaching of enhanced green fluorescent proteins," Biochemistry, Vol. 44, No. 18, 2005, pp. 7085–7094.

[201] Swaminathan, R., Hoang, C. P., and Verkman, A., "Photobleaching recovery and anisotropy decay of green fluorescent protein GFP-S65T in solution and cells: cytoplasmic viscosity probed by green fluorescent protein translational and rotational diffusion," Biophysical Journal, Vol. 72, No. 4, 1997, pp. 1900–1907.

[202] Zhang, J., Campbell, R. E., Ting, A. Y., and Tsien, R. Y., "Creating new fluorescent probes for cell biology," Nature Reviews Molecular Cell Biology, Vol. 3, No. 12, 2002, pp. 906–918.

[203] Panchuk-Voloshina, N., Haugland, R. P., Bishop-Stewart, J., Bhalgat, M. K., Millard, P. J., Mao, F., Leung, W.-Y., and Haugland, R. P., "Alexa dyes, a series of new fluorescent dyes that yield exceptionally bright, photostable conjugates," Journal of Histochemistry & Cytochemistry, Vol. 47, No. 9, 1999, pp. 1179–1188.

[204] Song, L., Hennink, E., Young, I. T., and Tanke, H. J., "Photobleaching kinetics of fluorescein in quantitative fluorescence microscopy," Biophysical Journal, Vol. 68, No. 6, 1995, pp. 2588–2600.

[205] Dahan, M., Levi, S., Luccardini, C., Rostaing, P., Riveau, B., and Triller, A., "Diffusion dynamics of glycine receptors revealed by single-quantum dot tracking," Science, Vol. 302, No. 5644, 2003, pp. 442–445.

[206] Michalet, X., Pinaud, F. F., Bentolila, L. A., Tsay, J. M., Doose, S., Li, J. J., Sundaresan, G., Wu, A., Gambhir, S., and Weiss, S., "Quantum dots for live cells, in vivo imaging, and diagnostics," Science, Vol. 307, No. 5709, 2005, pp. 538–544.

[207] Clapp, A. R., Medintz, I. L., Uyeda, H. T., Fisher, B. R., Goldman, E. R., Bawendi, M. G., and Mattoussi, H., "Quantum dot-based multiplexed fluorescence resonance energy transfer," Journal of the American Chemical Society, Vol. 127, No. 51, 2005, pp. 18212–18221.

[208] Medintz, I. L., Uyeda, H. T., Goldman, E. R., and Mattoussi, H., "Quantum dot bioconjugates for imaging, labelling and sensing," Nature Materials, Vol. 4, No. 6, 2005, pp. 435–446.

[209] Alivisatos, P., "The use of nanocrystals in biological detection," Nature Biotechnology, Vol. 22, No. 1, 2004, pp. 47–52.

[210] Resch-Genger, U., Grabolle, M., Cavaliere-Jaricot, S., Nitschke, R., and Nann, T., "Quantum dots versus organic dyes as fluorescent labels," Nature Methods, Vol. 5, No. 9, 2008, pp. 763–775.

[211] Carnell, M., Macmillan, A., and Whan, R., "Fluorescence recovery after photobleaching (FRAP): acquisition, analysis, and applications," Methods in Membrane Lipids, 2015, pp. 255–271.

[212] Schneider, C. A., Rasband, W. S., and Eliceiri, K. W., "NIH Image to ImageJ: 25 years of image analysis," Nature Methods, Vol. 9, No. 7, 2012, pp. 671–675.

[213] Abràmoff, M. D., Magalhães, P. J., and Ram, S. J., "Image processing with ImageJ," Biophotonics International, Vol. 11, No. 7, 2004, pp. 36–42.

[214] Schindelin, J., Rueden, C. T., Hiner, M. C., and Eliceiri, K. W., "The ImageJ ecosystem: An open platform for biomedical image analysis," Molecular Reproduction and Development, Vol. 82, No. 7-8, 2015, pp. 518–529.

[215] Lubelski, A. and Klafter, J., "Fluorescence recovery after photobleaching: the case of anomalous diffusion," Biophysical Journal, Vol. 94, No. 12, 2008, pp. 4646–4653.

[216] Bhushan, B., Introduction to Nanotechnology, Springer, 2007.

[217] Buzea, C., Pacheco, I. I., and Robbie, K., "Nanomaterials and nanoparticles: sources and toxicity," Biointerphases, Vol. 2, No. 4, 2007, pp. MR17–MR71.

[218] El-Sayed, M. A., "Some interesting properties of metals confined in time and nanometer space of different shapes," Accounts of Chemical Research, Vol. 34, No. 4, 2001, pp. 257–264.

[219] Nel, A. E., Mädler, L., Velegol, D., Xia, T., Hoek, E. M., Somasundaran, P., Klaessig, F., Castranova, V., and Thompson, M., "Understanding biophysico-chemical interactions at the nano–bio interface," Nature Materials, Vol. 8, No. 7, 2009, pp. 543–557.

[220] Geddes, C. D., Karolin, J., and Birch, D. J., "Fluorescence Anisotropy in Sol-Gels: Microviscosities or Growing Silica Nanoparticles Offering a New Approach to Sol-Gel Structure Elucidation?" Journal of Fluorescence, Vol. 12, 2002, pp. 135–137.

[221] Birch, D. J. and Geddes, C. D., "Sol-gel particle growth studied using fluorescence anisotropy: an alternative to scattering techniques," Physical Review E, Vol. 62, No. 2, 2000, pp. 2977.

[222] Geddes, C. and Birch, D., "Nanometre resolution of silica hydrogel formation using time-resolved fluorescence anisotropy," Journal of Non-Crystalline Solids, Vol. 270, No. 1-3, 2000, pp. 191–204.

[223] Apperson, K., Karolin, J., Martin, R. W., and Birch, D. J., "Nanoparticle metrology standards based on the time-resolved fluorescence anisotropy of silica colloids," Measurement Science and Technology, Vol. 20, No. 2, 2009, pp. 025310.

[224] Stewart, H. L., Yip, P., Rosenberg, M., Sørensen, T. J., Laursen, B. W., Knight, A. E., and Birch, D. J., "Nanoparticle metrology of silica colloids and super-resolution studies using the ADOTA fluorophore," Measurement Science and Technology, Vol. 27, No. 4, 2016, pp. 045007.

[225] Kushida, Y., Nagano, T., and Hanaoka, K., "Silicon-substituted xanthene dyes and their applications in bioimaging," Analyst, Vol. 140, No. 3, 2015, pp. 685–695.

[226] Eggeling, C., Volkmer, A., and Seidel, C. A., "Molecular photobleaching kinetics of rhodamine 6G by one-and two-photon induced confocal fluorescence microscopy," ChemPhysChem, Vol. 6, No. 5, 2005, pp. 791–804.

[227] Ahmad, M., King, T. A., Ko, D.-K., Cha, B. H., and Lee, J., "Performance and photostability of xanthene and pyrromethene laser dyes in sol-gel phases," Journal of Physics D: Applied Physics, Vol. 35, No. 13, 2002, pp. 1473.

[228] Wang, Z., Yang, M., Chen, C., Zhang, L., and Zeng, H., "Selectable ultrasensitive detection of Hg2+ with rhodamine 6G-modified nanoporous gold optical sensor," Scientific Reports, Vol. 6, No. 1, 2016, pp. 29611.

[229] Milton, K. L., Durrant, T. R., Cobos Freire, T., and Shluger, A. L., "Difference in structure and electronic properties of oxygen vacancies in α-quartz and α-cristobalite phases of sio2," Materials, Vol. 16, No. 4, 2023, pp. 1382.

[230] Phillips, J. C., Braun, R., Wang, W., Gumbart, J., Tajkhorshid, E., Villa, E., Chipot, C., Skeel, R. D., Kale, L., and Schulten, K., "Scalable molecular dynamics with NAMD," Journal of Computational Chemistry, Vol. 26, No. 16, 2005, pp. 1781–1802.

[231] Phillips, J. C., Hardy, D. J., Maia, J. D., Stone, J. E., Ribeiro, J. V., Bernardi, R. C., Buch, R., Fiorin, G., Hénin, J., Jiang, W., et al., "Scalable molecular dynamics on CPU and GPU architectures with NAMD," The Journal of Chemical Physics, Vol. 153, No. 4, 2020.

[232] Jo, S., Kim, T., Iyer, V. G., and Im, W., "CHARMM-GUI: a web-based graphical user interface for CHARMM," Journal of Computational Chemistry, Vol. 29, No. 11, 2008, pp. 1859–1865.

[233] Neubauer, H., Gaiko, N., Berger, S., Schaffer, J., Eggeling, C., Tuma, J., Verdier, L., Seidel, C. A., Griesinger, C., and Volkmer, A., "Orientational and dynamical heterogeneity of rhodamine 6G terminally attached to a DNA helix revealed by NMR and single-molecule fluorescence spectroscopy," Journal of the American Chemical Society, Vol. 129, No. 42, 2007, pp. 12746–12755.

[234] Jo, S., Cheng, X., Islam, S. M., Huang, L., Rui, H., Zhu, A., Lee, H. S., Qi, Y., Han, W., Vanommeslaeghe, K., et al., "CHARMM-GUI PDB manipulator for advanced modeling and simulations of proteins containing nonstandard residues," Advances in Protein Chemistry and Structural Biology, Vol. 96, 2014, pp. 235–265.

[235] Park, S.-J., Kern, N., Brown, T., Lee, J., and Im, W., "CHARMM-GUI PDB manipulator: various PDB structural modifications for biomolecular modeling and simulation," Journal of Molecular Biology, Vol. 435, No. 14, 2023, pp. 167995.

[236] Chuichay, P., Vladimirov, E., Siriwong, K., Hannongbua, S., and Rösch, N., "Molecular-dynamics simulations of pyronine 6G and rhodamine 6G dimers in aqueous solution," Journal of Molecular Modeling, Vol. 12, 2006, pp. 885–896.

[237] Vaiana, A. C., Schulz, A., Wolfrum, J., Sauer, M., and Smith, J. C., "Molecular mechanics force field parameterization of the fluorescent probe rhodamine 6G using automated frequency matching," Journal of Computational Chemistry, Vol. 24, No. 5, 2003, pp. 632–639.

[238] Bartasun, P., Cieśliński, H., Bujacz, A., Wierzbicka-Woś, A., and Kur, J., "A study on the interaction of rhodamine B with methylthioadenosine phosphorylase protein sourced from an Antarctic soil metagenomic library," PLoS One, Vol. 8, No. 1, 2013, pp. e55697.

[239] O'Boyle, N. M., Banck, M., James, C. A., Morley, C., Vandermeersch, T., and Hutchison, G. R., "Open Babel: An open chemical toolbox," Journal of Cheminformatics, Vol. 3, 2011, pp. 1–14.

[240] Neese, F., "The ORCA program system," Wiley Interdisciplinary Reviews: Computational Molecular Science, Vol. 2, No. 1, 2012, pp. 73–78.

[241] Neese, F., "Software update: the ORCA program system, version 4.0," Wiley Interdisciplinary Reviews: Computational Molecular Science, Vol. 8, No. 1, 2018, pp. e1327.

[242] Neese, F., Wennmohs, F., Becker, U., and Riplinger, C., "The ORCA quantum chemistry program package," The Journal of Chemical Physics, Vol. 152, No. 22, 2020.

[243] Caldeweyher, E., Mewes, J.-M., Ehlert, S., and Grimme, S., "Extension and evaluation of the D4 London-dispersion model for periodic systems," Physical Chemistry Chemical Physics, Vol. 22, No. 16, 2020, pp. 8499–8512.

[244] Weigend, F. and Ahlrichs, R., "Balanced basis sets of split valence, triple zeta valence and quadruple zeta valence quality for H to Rn: Design and assessment of

accuracy," Physical Chemistry Chemical Physics, Vol. 7, No. 18, 2005, pp. 3297–3305.

[245] Breneman, C. M. and Wiberg, K. B., "Determining atom-centered monopoles from molecular electrostatic potentials. The need for high sampling density in formamide conformational analysis," Journal of Computational Chemistry, Vol. 11, No. 3, 1990, pp. 361–373.

[246] Choi, Y. K., Kern, N. R., Kim, S., Kanhaiya, K., Afshar, Y., Jeon, S. H., Jo, S., Brooks, B. R., Lee, J., Tadmor, E. B., et al., "CHARMM-GUI nanomaterial modeler for modeling and simulation of nanomaterial systems," Journal of Chemical Theory and Computation, Vol. 18, No. 1, 2021, pp. 479–493.

[247] Kern, N. R., Lee, J., Choi, Y. K., and Im, W., "CHARMM-GUI Multicomponent Assembler for modeling and simulation of complex multicomponent systems," Nature Communications, Vol. 15, No. 1, 2024, pp. 5459.

[248] Humphrey, W., Dalke, A., and Schulten, K., "VMD: visual molecular dynamics," Journal of Molecular Graphics, Vol. 14, No. 1, 1996, pp. 33–38.

[249] Brooks, B. R., Bruccoleri, R. E., Olafson, B. D., States, D. J., Swaminathan, S. a., and Karplus, M., "CHARMM: a program for macromolecular energy, minimization, and dynamics calculations," Journal of Computational Chemistry, Vol. 4, No. 2, 1983, pp. 187–217.

[250] Levy, Y. and Onuchic, J. N., "Water mediation in protein folding and molecular recognition," Annu. Rev. Biophys. Biomol. Struct., Vol. 35, No. 1, 2006, pp. 389–415.

[251] Chaplin, M., "Do we underestimate the importance of water in cell biology?" Nature Reviews Molecular Cell Biology, Vol. 7, No. 11, 2006, pp. 861–866.

[252] Higham, D. J. and Higham, N. J., MATLAB guide, SIAM, 2016.

[253] Arbeloa, F. L., Gonzalez, I. L., Ojeda, P. R., and Arbeloa, I. L., "Aggregate formation of rhodamine 6G in aqueous solution," Journal of the Chemical Society, Faraday Transactions 2: Molecular and Chemical Physics, Vol. 78, No. 7, 1982, pp. 989–994.

[254] Marini, L., "Chapter 5—The Product Solid Phases," Developments in Geo-Chemistry; Elsevier: Amsterdam, The Netherlands, Vol. 11, 2007, pp. 79–167.

[255] Chen, Z., Tang, Y.-J., Xie, T.-T., Chen, Y., and Li, Y.-Q., "Fluorescence spectral properties of rhodamine 6G at the silica/water interface," Journal of Fluorescence, Vol. 18, 2008, pp. 93–100.

[256] Avnir, D., Levy, D., and Reisfeld, R., "The nature of the silica cage as reflected by spectral changes and enhanced photostability of trapped rhodamine 6G," The Journal of Physical Chemistry, Vol. 88, No. 24, 1984, pp. 5956–5959.

[257] Tleugabulova, D., Duft, A. M., Zhang, Z., Chen, Y., Brook, M. A., and Brennan, J. D., "Evaluating formation and growth mechanisms of silica particles using fluorescence anisotropy decay analysis," Langmuir, Vol. 20, No. 14, 2004, pp. 5924–5932.

[258] Hinckley, D. A. and Seybold, P. G., "A spectroscopic/thermodynamic study of the rhodamine B lactone/zwitterion equilibrium," Spectrochimica Acta Part A: Molecular Spectroscopy, Vol. 44, No. 10, 1988, pp. 1053–1059.

[259] Chang, T. L. and Cheung, H. C., "Solvent effects on the photoisomerization rates of the zwitterionic and the cationic forms of rhodamine B in protic solvents," The Journal of Physical Chemistry, Vol. 96, No. 12, 1992, pp. 4874–4878.

[260] Dare-Doyen, S., Doizi, D., Guilbaud, P., Djedaini-Pilard, F., Perly, B., and Millié, P., "Dimerization of xanthene dyes in water: Experimental studies and molecular dynamic simulations," The Journal of Physical Chemistry B, Vol. 107, No. 50, 2003, pp. 13803–13812.

[261] Hu, G., Jin, S., and Liu, K., "Structure-Directing Effect on Silica Nanoparticle Growth in Sodium Silicate Solutions through Small-Angle X-ray Scattering," The Journal of Physical Chemistry C, Vol. 127, No. 22, 2023, pp. 10585–10593.

[262] Steiner, T., "The Hydrogen Bond in the Solid State," Angewandte Chemie International Edition, Vol. 41, No. 1, 2002, pp. 48–76.

[263] Moutoussamy, E. E., Khan, H. M., Roberts, M. F., Gershenson, A., Chipot, C., and Reuter, N., "Standard Binding Free Energy and Membrane Desorption Mechanism for a Phospholipase C," Journal of Chemical Information and Modeling, Vol. 62, No. 24, 2022, pp. 6602–6613, PMID: 35343689.

[264] Al Masum, A., Chakraborty, M., Ghosh, S., Laha, D., Karmakar, P., Islam, M. M., and Mukhopadhyay, S., "Biochemical activity of a fluorescent dye rhodamine 6G: Molecular modeling, electrochemical, spectroscopic and thermodynamic studies," Journal of Photochemistry and Photobiology B: Biology, Vol. 164, 2016, pp. 369–379.

[265] Ilich, P., Mishra, P., Macura, S., and Burghardt, T., "Direct observation of rhodamine dimer structures in water," Spectrochimica Acta Part A: Molecular and Biomolecular Spectroscopy, Vol. 52, No. 10, 1996, pp. 1323–1330.

[266] Toptygin, D., Packard, B. Z., and Brand, L., "Resolution of absorption spectra of rhodamine 6G aggregates in aqueous solution using the law of mass action," Chemical Physics Letters, Vol. 277, No. 5-6, 1997, pp. 430–435.

[267] Parr, R. G., "Density functional theory of atoms and molecules," Horizons of Quantum Chemistry: Proceedings of the Third International Congress of Quantum Chemistry Held at Kyoto, Japan, October 29-November 3, 1979, Springer, 1989, pp. 5–15.

[268] Burke, K., "Perspective on density functional theory," The Journal of Chemical Physics, Vol. 136, No. 15, 2012.

[269] Raghavachari, K., Trucks, G. W., Pople, J. A., and Head-Gordon, M., "A fifth-order perturbation comparison of electron correlation theories," Chemical Physics Letters, Vol. 157, No. 6, 1989, pp. 479–483.

[270] Bartlett, R. J. and Musiał, M., "Coupled-cluster theory in quantum chemistry," Reviews of Modern Physics, Vol. 79, No. 1, 2007, pp. 291–352.

[271] Pople, J., Head-Gordon, M., and Raghavachari, K., "Corrections to correlations energies beyond fourth order moller-plesset (mp4) perturbation theory. Contributions of single, double, and triple substitutions," International Journal of Quantum Chemistry, Vol. 34, No. S22, 1988, pp. 377–382.

[272] Møller, C. and Plesset, M. S., "Note on an approximation treatment for many-electron systems," Physical Review, Vol. 46, No. 7, 1934, pp. 618.

[273] Kossmann, S. and Neese, F., "Efficient structure optimization with second-order many-body perturbation theory: The RIJCOSX-MP2 method," Journal of Chemical Theory and Computation, Vol. 6, No. 8, 2010, pp. 2325–2338.

[274] Riplinger, C., Sandhoefer, B., Hansen, A., and Neese, F., "Natural triple excitations in local coupled cluster calculations with pair natural orbitals," The Journal of Chemical Physics, Vol. 139, No. 13, 2013.

[275] Riplinger, C. and Neese, F., "An efficient and near linear scaling pair natural orbital based local coupled cluster method," The Journal of Chemical Physics, Vol. 138, No. 3, 2013.

[276] Grimme, S., Ehrlich, S., and Goerigk, L., "Effect of the damping function in dispersion corrected density functional theory," Journal of Computational Chemistry, Vol. 32, No. 7, 2011, pp. 1456–1465.

[277] Grimme, S., "Accurate description of van der Waals complexes by density functional theory including empirical corrections," Journal of Computational Chemistry, Vol. 25, No. 12, 2004, pp. 1463–1473.

[278] Bursch, M., Mewes, J.-M., Hansen, A., and Grimme, S., "Best-practice DFT protocols for basic molecular computational chemistry," Angewandte Chemie, Vol. 134, No. 42, 2022, pp. e202205735.

[279] Neese, F., "An improvement of the resolution of the identity approximation for the formation of the Coulomb matrix," Journal of Computational Chemistry, Vol. 24, No. 14, 2003, pp. 1740–1747.

[280] Izsák, R., Neese, F., and Klopper, W., "Robust fitting techniques in the chain of spheres approximation to the Fock exchange: The role of the complementary space," The Journal of Chemical Physics, Vol. 139, No. 9, 2013.

[281] Plessow, P. and Weigend, F., "Seminumerical calculation of the Hartree–Fock exchange matrix: Application to two-component procedures and efficient evaluation of local hybrid density functionals," Journal of Computational Chemistry, Vol. 33, No. 7, 2012, pp. 810–816.

[282] Furche, F., Ahlrichs, R., Hättig, C., Klopper, W., Sierka, M., and Weigend, F., "Turbomole," Wiley Interdisciplinary Reviews: Computational Molecular Science, Vol. 4, No. 2, 2014, pp. 91–100.

[283] Becke, A. D., "Density-functional exchange-energy approximation with correct asymptotic behavior," Physical Review A, Vol. 38, No. 6, 1988, pp. 3098.

[284] Perdew, J. P., "Density-functional approximation for the correlation energy of the inhomogeneous electron gas," Physical Review B, Vol. 33, No. 12, 1986, pp. 8822.

[285] Zhao, Y. and Truhlar, D. G., "The M06 suite of density functionals for main group thermochemistry, thermochemical kinetics, noncovalent interactions, excited states, and transition elements: two new functionals and systematic testing of four M06-class functionals and 12 other functionals," Theoretical Chemistry Accounts, Vol. 120, No. 1, 2008, pp. 215–241.

[286] Caldeweyher, E., Bannwarth, C., and Grimme, S., "Extension of the D3 dispersion coefficient model," The Journal of Chemical Physics, Vol. 147, No. 3, 2017.

[287] Caldeweyher, E., Ehlert, S., Hansen, A., Neugebauer, H., Spicher, S., Bannwarth, C., and Grimme, S., "A generally applicable atomic-charge dependent London dispersion correction," The Journal of Chemical Physics, Vol. 150, No. 15, 2019.

[288] Boys, S. F. and Bernardi, F., "The calculation of small molecular interactions by the differences of separate total energies. Some procedures with reduced errors," Molecular Physics, Vol. 19, No. 4, 1970, pp. 553–566.

[289] Weigend, F., "Accurate Coulomb-fitting basis sets for H to Rn," Physical Chemistry Chemical Physics, Vol. 8, No. 9, 2006, pp. 1057–1065.

[290] Neese, F., Wennmohs, F., Hansen, A., and Becker, U., "Efficient, approximate and parallel Hartree–Fock and hybrid DFT calculations. A 'chain-of-spheres' algorithm for the Hartree–Fock exchange," Chemical Physics, Vol. 356, No. 1-3, 2009, pp. 98–109.

[291] Kubiak-Ossowska, K., Tokarczyk, K., Jachimska, B., and Mulheran, P. A., "Bovine serum albumin adsorption at a silica surface explored by simulation and experiment," The Journal of Physical Chemistry B, Vol. 121, No. 16, 2017, pp. 3975–3986.

[292] Hudek, M., Kubiak-Ossowska, K., Johnston, K., Ferro, V. A., and Mulheran, P. A., "Chitin and chitosan binding to the α-chitin crystal: a molecular dynamics study," ACS Omega, Vol. 8, No. 3, 2023, pp. 3470–3477.

[293] Malfatti, L., Kidchob, T., Aiello, D., Aiello, R., Testa, F., and Innocenzi, P., "Aggregation states of rhodamine 6G in mesostructured silica films," The Journal of Physical Chemistry C, Vol. 112, No. 42, 2008, pp. 16225–16230.

[294] Leonenko, E., Telbiz, G., Bogoslovskaya, A., and Manoryk, P., "Effect of aggregation of Rhodamine 6G on the spectral and luminescence characteristics of hybrid

mesostructured silica films," Theoretical and Experimental Chemistry, Vol. 50, 2015, pp. 358–363.

[295] Cohen, A. J., Mori-Sánchez, P., and Yang, W., "Challenges for density functional theory," Chemical Reviews, Vol. 112, No. 1, 2012, pp. 289–320.

[296] Grimme, S., "Density functional theory with London dispersion corrections," Wiley Interdisciplinary Reviews: Computational Molecular Science, Vol. 1, No. 2, 2011, pp. 211–228.

[297] Goerigk, L. and Grimme, S., "Efficient and Accurate Double-Hybrid-Meta-GGA Density Functionals – Evaluation with the Extended GMTKN30 Database for General Main Group Thermochemistry, Kinetics, and Noncovalent Interactions," Journal of Chemical Theory and Computation, Vol. 7, No. 2, 2011, pp. 291–309.

[298] Peverati, R. and Truhlar, D. G., "Exchange–correlation functional with good accuracy for both structural and energetic properties while depending only on the density and its gradient," Journal of Chemical Theory and Computation, Vol. 8, No. 7, 2012, pp. 2310–2319.

[299] Lin, Y.-S., Li, G.-D., Mao, S.-P., and Chai, J.-D., "Long-range corrected hybrid density functionals with improved dispersion corrections," Journal of Chemical Theory and Computation, Vol. 9, No. 1, 2013, pp. 263–272.

[300] Peverati, R. and Truhlar, D. G., "Improving the accuracy of hybrid meta-GGA density functionals by range separation," The Journal of Physical Chemistry Letters, Vol. 2, No. 21, 2011, pp. 2810–2817.

[301] Doveiko, D., Kubiak-Ossowska, K., and Chen, Y., "Binding energy calculations of anthracene and Rhodamine 6G H-type dimers: a comparative study of DFT and SMD methods," The Journal of Physical Chemistry A, 2025.

[302] Heyd, J., Scuseria, G. E., and Ernzerhof, M., "Hybrid functionals based on a screened Coulomb potential," The Journal of Chemical Physics, Vol. 118, No. 18, 2003, pp. 8207–8215.

[303] Oostenbrink, C., Villa, A., Mark, A. E., and Van Gunsteren, W. F., "A biomolecular force field based on the free enthalpy of hydration and solvation: the GROMOS force-field parameter sets 53A5 and 53A6," Journal of Computational Chemistry, Vol. 25, No. 13, 2004, pp. 1656–1676.

[304] Cornell, W. D., Cieplak, P., Bayly, C. I., Gould, I. R., Merz, K. M., Ferguson, D. M., Spellmeyer, D. C., Fox, T., Caldwell, J. W., and Kollman, P. A., "A second generation force field for the simulation of proteins, nucleic acids, and organic molecules," Journal of the American Chemical Society, Vol. 117, No. 19, 1995, pp. 5179–5197.

[305] Hornak, V., Abel, R., Okur, A., Strockbine, B., Roitberg, A., and Simmerling, C., "Comparison of multiple Amber force fields and development of improved protein backbone parameters," Proteins: Structure, Function, and Bioinformatics, Vol. 65, No. 3, 2006, pp. 712–725.

[306] Schweiker, G., "Sodium silicates and sodium aluminosilicates," Journal of the American Oil Chemists' Society, Vol. 55, 1978, pp. 36–40.

[307] Khan, M. I., Azizli, K., Sufian, S., and Man, Z., "Sodium silicate-free geopolymers as coating materials: Effects of Na/Al and water/solid ratios on adhesion strength," Ceramics International, Vol. 41, No. 2, 2015, pp. 2794–2805.

[308] Yang, X., Zhu, W., and Yang, Q., "The viscosity properties of sodium silicate solutions," Journal of Solution Chemistry, Vol. 37, 2008, pp. 73–83.

[309] Tsai, M.-S., "The study of formation colloidal silica via sodium silicate," Materials Science and Engineering: B, Vol. 106, No. 1, 2004, pp. 52–55.

[310] Gurav, J. L., Rao, A. V., Rao, A. P., Nadargi, D., and Bhagat, S., "Physical properties of sodium silicate based silica aerogels prepared by single step sol–gel process dried at ambient pressure," Journal of Alloys and Compounds, Vol. 476, No. 1-2, 2009, pp. 397–402.

[311] Katoueizadeh, E., Rasouli, M., and Zebarjad, S. M., "A comprehensive study on the gelation process of silica gels from sodium silicate," Journal of Materials Research and Technology, Vol. 9, No. 5, 2020, pp. 10157–10165.

[312] Owusu, Y. A., "Physical-chemistry study of sodium silicate as a foundry sand binder," Advances in Colloid and Interface Science, Vol. 18, No. 1-2, 1982, pp. 57–91.

[313] Ünlü, N. and Odabaş, A., "Development and evaluation of a new eco-friendly sodium silicate-based binder system," International Journal of Metalcasting, Vol. 12, No. 4, 2018, pp. 765–771.

[314] Pouretedal, H. and Kazemi, M., "Characterization of modified silica aerogel using sodium silicate precursor and its application as adsorbent of Cu 2+, Cd 2+, and Pb 2+ ions," International Journal of Industrial Chemistry, Vol. 3, 2012, pp. 1–8.

[315] Loncki, S. B., Cook, L. M., Shen, J., and Pierce, K. G., "Polishing silicon wafers with improved polishing slurries," Jan. 19 1999, US Patent 5,860,848.

[316] Stebbins, J. F., "Identification of multiple structural species in silicate glasses by 29Si NMR," Nature, Vol. 330, No. 6147, 1987, pp. 465–467.

[317] Pauw, B. R., "Everything SAXS: small-angle scattering pattern collection and correction," Journal of Physics: Condensed Matter, Vol. 25, No. 38, 2013, pp. 383201.

[318] Birch, D. J. and Yip, P., "Nanometrology," Fluorescence Spectroscopy and Microscopy: Methods and Protocols, Springer, 2013, pp. 279–302.

[319] Birch, D. J. and Imhof, R. E., "Time-domain fluorescence spectroscopy using time-correlated single-photon counting," Topics in Fluorescence Spectroscopy: Techniques, Springer, 1991, pp. 1–95.

[320] Phillips, D., Drake, R., O'Connor, D., and Christensen, R., Time correlated single-photon counting (TCSPC) using laser excitation, Taylor & Francis, 1985.

[321] McGuinness, C., Sagoo, K., McLoskey, D., and Birch, D., "A new sub-nanosecond LED at 280 nm: application to protein fluorescence," Measurement Science and Technology, Vol. 15, No. 11, 2004, pp. L19.

[322] Fuertes, G., Banterle, N., Ruff, K. M., Chowdhury, A., Mercadante, D., Koehler, C., Kachala, M., Estrada Girona, G., Milles, S., Mishra, A., et al., "Decoupling of size and shape fluctuations in heteropolymeric sequences reconciles discrepancies in SAXS vs. FRET measurements," Proceedings of the National Academy of Sciences, Vol. 114, No. 31, 2017, pp. E6342–E6351.

[323] Okada, K., Watanabe, K., Wataoka, I., Toda, A., Sasaki, S., Inoue, K., and Hikosaka, M., "Size distribution and shape of nano-nucleus of polyethylene simultaneously determined by SAXS," Polymer, Vol. 48, No. 1, 2007, pp. 382–392.

[324] Ren, Y., Ma, Z., and Bruce, P. G., "Ordered mesoporous metal oxides: synthesis and applications," Chemical Society Reviews, Vol. 41, No. 14, 2012, pp. 4909–4927.

[325] Pilz, I., Glatter, O., and Kratky, O., "Small-angle x-ray scattering," Methods in Enzymology, Vol. 61, Elsevier, 1979, pp. 148–249.

[326] Hopkins, J. B., Gillilan, R. E., and Skou, S., "BioXTAS RAW: improvements to a free open-source program for small-angle X-ray scattering data reduction and analysis," Applied Crystallography, Vol. 50, No. 5, 2017, pp. 1545–1553.

[327] Anedda, A., Carbonaro, C., Corpino, R., Ricci, P., Grandi, S., and Mustarelli, P., "Formation of fluorescent aggregates in Rhodamine 6G doped silica glasses," Journal of Non-Crystalline Solids, Vol. 353, No. 5-7, 2007, pp. 481–485.

[328] Haimerl, J. M., Ghosh, I., König, B., Lupton, J. M., and Vogelsang, J., "Chemical photocatalysis with rhodamine 6g: investigation of photoreduction by simultaneous fluorescence correlation spectroscopy and fluorescence lifetime measurements," The Journal of Physical Chemistry B, Vol. 122, No. 47, 2018, pp. 10728–10735.

[329] Smith, T., Irwanto, M., Haines, D., Ghiggino, K., and Millar, D., "Time-resolved fluorescence anisotropy measurements of the adsorption of Rhodamine-B and a labelled polyelectrolyte onto colloidal silica," Colloid and Polymer Science, Vol. 276, 1998, pp. 1032–1037.

[330] Müller, C., Loman, A., Pacheco, V., Koberling, F., Willbold, D., Richtering, W., and Enderlein, J., "Precise measurement of diffusion by multi-color dual-focus fluorescence correlation spectroscopy," Europhysics Letters, Vol. 83, No. 4, 2008, pp. 46001.

[331] Gumy, J.-C. and Vauthey, E., "Picosecond polarization grating study of the effect of excess excitation energy on the rotational dynamics of rhodamine 6G in different electronic states," The Journal of Physical Chemistry, Vol. 100, No. 21, 1996, pp. 8628–8632.

[332] D'Arrigo, J. S., "Screening of membrane surface charges by divalent cations: an atomic representation," American Journal of Physiology-Cell Physiology, Vol. 235, No. 3, 1978, pp. C109–C117.

[333] Trease, N. M., Clark, T. M., Grandinetti, P. J., Stebbins, J. F., and Sen, S., "Bond length-bond angle correlation in densified silica—Results from 17O NMR spectroscopy," The Journal of Chemical Physics, Vol. 146, No. 18, 2017.

[334] Aguilar-Caballos, M. P., Gómez-Hens, A., and Pérez-Bendito, D., "Simultaneous stopped-flow determination of butylated hydroxyanisole and propyl gallate using a T-format luminescence spectrometer," Journal of Agricultural and Food Chemistry, Vol. 48, No. 2, 2000, pp. 312–317.

[335] Sutherland, J. C., "Simultaneous measurement of circular dichroism and fluorescence polarization anisotropy," Clinical Diagnostic Systems: Technologies and Instrumentation, Vol. 4625, SPIE, 2002, pp. 126–136.

[336] Birch, D., Holmes, A., Gilchrist, J., Imhof, R., Al Alawi, S., and Nadolski, B., "A multiplexed single-photon instrument for routine measurement of time-resolved

fluorescence anisotropy," Journal of Physics E: Scientific Instruments, Vol. 20, No. 4, 1987, pp. 471.

[337] Kufcsák, A., Erdogan, A., Walker, R., Ehrlich, K., Tanner, M., Megia-Fernandez, A., Scholefield, E., Emanuel, P., Dhaliwal, K., Bradley, M., et al., "Time-resolved spectroscopy at 19,000 lines per second using a CMOS SPAD line array enables advanced biophotonics applications," Optics Express, Vol. 25, No. 10, 2017, pp. 11103–11123.

[338] Tande, B. M., Wagner, N. J., Mackay, M. E., Hawker, C. J., and Jeong, M., "Viscosimetric, hydrodynamic, and conformational properties of dendrimers and dendrons," Macromolecules, Vol. 34, No. 24, 2001, pp. 8580–8585.

[339] Eichler, H., Klein, U., and Langhans, D., "Measurement of orientational relaxation times of rhodamine 6G with a streak camera," Chemical Physics Letters, Vol. 67, No. 1, 1979, pp. 21–23.

[340] Karolin, J., Geddes, C., Wynne, K., and Birch, D., "Nanoparticle metrology in sol-gels usingmultiphoton excited fluorescence," Measurement Science and Technology, Vol. 13, No. 1, 2001, pp. 21.

[341] Lippincott-Schwartz, J., Snapp, E. L., and Phair, R. D., "The Development and Enhancement of FRAP as a Key Tool for Investigating Protein Dynamics," Biophysical Journal, Vol. 115, No. 7, 2018, pp. 1146–1155.

[342] Chalfie, M., Tu, Y., Euskirchen, G., Ward, W. W., and Prasher, D. C., "Green fluorescent protein as a marker for gene expression," Science, Vol. 263, No. 5148, 1994, pp. 802–805.

[343] Lorén, N., Hagman, J., Jonasson, J. K., Deschout, H., Bernin, D., Cella-Zanacchi, F., Diaspro, A., McNally, J. G., Ameloot, M., Smisdom, N., et al., "Fluorescence recovery after photobleaching in material and life sciences: putting theory into practice," Quarterly Reviews of Biophysics, Vol. 48, No. 3, 2015, pp. 323–387.

[344] Singer, J., "NMR diffusion and flow measurements and an introduction to spin phase graphing," Journal of Physics E: Scientific Instruments, Vol. 11, No. 4, 1978, pp. 281.

[345] Bernin, D. and Topgaard, D., "NMR diffusion and relaxation correlation methods: New insights in heterogeneous materials," Current Opinion in Colloid & Interface Science, Vol. 18, No. 3, 2013, pp. 166–172.

[346] Liebman, P. and Entine, G., "Lateral diffusion of visual pigment in photoreceptor disk membranes," Science, Vol. 185, No. 4149, 1974, pp. 457–459.

[347] Stenoien, D. L., Patel, K., Mancini, M. G., Dutertre, M., Smith, C. L., O'Malley, B. W., and Mancini, M. A., "FRAP reveals that mobility of oestrogen receptor-α is ligand-and proteasome-dependent," Nature Cell Biology, Vol. 3, No. 1, 2001, pp. 15–23.

[348] Bulinski, J. C., Odde, D. J., Howell, B. J., Salmon, T. D., and Waterman-Storer, C. M., "Rapid dynamics of the microtubule binding of ensconsin in vivo," Journal of Cell Science, Vol. 114, No. 21, 2001, pp. 3885–3897.

[349] Sarkar, P. and Chattopadhyay, A., "Exploring membrane lipid and protein diffusion by FRAP," Analysis of Membrane Lipids, 2020, pp. 119–141.

[350] Mueller, F., Mazza, D., Stasevich, T. J., and McNally, J. G., "FRAP and kinetic modeling in the analysis of nuclear protein dynamics: what do we really know?" Current Opinion in Cell Biology, Vol. 22, No. 3, 2010, pp. 403–411.

[351] Giakoumakis, N. N., Rapsomaniki, M. A., and Lygerou, Z., "Analysis of protein kinetics using fluorescence recovery after photobleaching (FRAP)," Light Microscopy: Methods and Protocols, 2017, pp. 243–267.

[352] Xia, Y., Wu, J., Wei, W., Du, Y., Wan, T., Ma, X., An, W., Guo, A., Miao, C., Yue, H., et al., "Exploiting the pliability and lateral mobility of Pickering emulsion for enhanced vaccination," Nature Materials, Vol. 17, No. 2, 2018, pp. 187–194.

[353] Lee, D. and Weitz, D. A., "Double emulsion-templated nanoparticle colloidosomes with selective permeability," Advanced Materials, Vol. 20, No. 18, 2008, pp. 3498–3503.

[354] Singh, V. K., Yadav, I., Kulanthaivel, S., Roy, B., Giri, S., Maiti, T. K., Banerjee, I., and Pal, K., "Groundnut oil based emulsion gels for passive and iontophoretic delivery of therapeutics," Designed Monomers and Polymers, Vol. 19, No. 4, 2016, pp. 297–308.

[355] Brake, J. M., Daschner, M. K., and Abbott, N. L., "Formation and characterization of phospholipid monolayers spontaneously assembled at interfaces between aqueous phases and thermotropic liquid crystals," Langmuir, Vol. 21, No. 6, 2005, pp. 2218–2228.

[356] Pihl, M., Kolman, K., Lotsari, A., Ivarsson, M., Schüster, E., Lorén, N., and Bordes, R., "Silica-based diffusion probes for use in FRAP and NMR-diffusometry," Journal of Dispersion Science and Technology, Vol. 40, No. 4, 2019, pp. 555–562.

[357] Van Rossum, G., Drake, F. L., et al., Python reference manual, Vol. 111, Centrum voor Wiskunde en Informatica Amsterdam, 1995.

[358] Harris, C. R., Millman, K. J., Van Der Walt, S. J., Gommers, R., Virtanen, P., Cournapeau, D., Wieser, E., Taylor, J., Berg, S., Smith, N. J., et al., "Array programming with NumPy," Nature, Vol. 585, No. 7825, 2020, pp. 357–362.

[359] Friedman, J. H., "Greedy function approximation: a gradient boosting machine," Annals of Statistics, 2001, pp. 1189–1232.

[360] Hastie, T., Tibshirani, R., Friedman, J., Hastie, T., Tibshirani, R., and Friedman, J., "Boosting and additive trees," The Elements of Statistical Learning: Data Mining, Inference, and Prediction, 2009, pp. 337–387.

[361] Doveiko, D., Kubiak-Ossowska, K., and Chen, Y., "Nanoparticles as adsorbents for hydrophobic molecules: Exploring size, pH, and structural dependencies," The Journal of Chemical Physics, Vol. 163, No. 2, 2025.

[362] Mori, I., Terasaka, S., Yamaguchi, S., and Otosu, T., "Diffusion of Multiple Species Resolved by Fluorescence Lifetime Recovery after Photobleaching (FLRAP)," Analytical Chemistry, Vol. 96, No. 12, 2024, pp. 4854–4859.

[363] Vail, J. G., Soluble silicates in industry, Vol. 46, Chemical Catalog Company, 1928.

[364] Toda, K. and Furuse, H., "Extension of Einstein's viscosity equation to that for concentrated dispersions of solutes and particles," Journal of Bioscience and Bioengineering, Vol. 102, No. 6, 2006, pp. 524–528.

[365] van Beek, T. A., "Low-field benchtop NMR spectroscopy: status and prospects in natural product analysis," Phytochemical Analysis, Vol. 32, No. 1, 2021, pp. 24–37.

[366] Madras, G. and McCoy, B. J., "Temperature effects during Ostwald ripening," The Journal of Chemical Physics, Vol. 119, No. 3, 2003, pp. 1683–1693.

[367] Saeed, S., Al Soubaihi, R. M., White, L. S., Bertino, M. F., and Saoud, K. M., "Rapid fabrication of cross-linked silica aerogel by laser induced gelation," Microporous and Mesoporous Materials, Vol. 221, 2016, pp. 245–252.

[368] Zondervan, R., Kulzer, F., Kol'chenk, M. A., and Orrit, M., "Photobleaching of rhodamine 6G in poly (vinyl alcohol) at the ensemble and single-molecule levels," The Journal of Physical Chemistry A, Vol. 108, No. 10, 2004, pp. 1657–1665.

[369] Zondervan, R., Kulzer, F., Orlinskii, S. B., and Orrit, M., "Photoblinking of rhodamine 6G in poly (vinyl alcohol): Radical dark state formed through the triplet," The Journal of Physical Chemistry A, Vol. 107, No. 35, 2003, pp. 6770–6776.

[370] Nooijen, M. and Bartlett, R. J., "Similarity transformed equation-of-motion coupled-cluster theory: Details, examples, and comparisons," The Journal of Chemical Physics, Vol. 107, No. 17, 1997, pp. 6812–6830.

[371] Müller-Buschbaum, P., "A basic introduction to grazing incidence small-angle X-ray scattering," Applications of Synchrotron Light to Scattering and Diffraction in Materials and Life Sciences, Springer, 2009, pp. 61–89.

[372] Henke, B. L., Gullikson, E. M., and Davis, J. C., "X-ray interactions: photoabsorption, scattering, transmission, and reflection at E= 50-30,000 eV, Z= 1-92," Atomic Data and Nuclear Data Tables, Vol. 54, No. 2, 1993, pp. 181–342.